UNIVERSITY OF SOUTHAMPTON

FACULTY OF ENGINEERING AND THE ENVIRONMENT
Aerodynamics and Fluid Mechanics

Presumed pdf modelling for turbulent spray combustion

by

Tomas Matheson

Thesis for the degree of Doctor of Philosophy

31st March 2016

ABSTRACT

Theory and modelling for turbulent reacting flows is presented in the framework of the presumed-probability density function (pdf) approach. The presumed-pdf method accounts for the stochastic nature of composition fluctuations in a turbulent flow by relating the composition to the statistical distribution of a small number of reference variables. Partially-premixed combustion is most commonly modelled with reference to the distribution of two variables: the mixture fraction is used to describe the fuel-air ratio, and the progress variable is used to describe the extent of reaction. However, the use of alternative reference variables is also investigated in this thesis – the scalar dissipation rate, in order to account for the effect of turbulent mixing on combustion, and residence time-based variables, in order to numerically resolve slow chemical processes for which the progress variable is ill-conditioned. It is common to assume that mixture fraction and progress variable are statistically independent, however there is previous evidence that this assumption gives poor predictions in some important partially-premixed applications involving flame stabilisation. In order to account for the possibility of statistical dependence between reference variables, this thesis focusses on the use of copulas in order to construct joint-pdfs from the marginal pdfs of reference variables, and a numerical implementation for presumed-pdf modelling using copulas is developed in this thesis.

The presumed-pdf approach relies upon models for the shape of the pdf of the reference variables as a function of their statistical moments, which must themselves be modelled. Transport equations for the statistical moments involve unclosed source terms, however, integration of the presumed-pdf provides a means to obtain closure for these source terms. Similarly, unclosed terms appear in the models for momentum exchange and evaporation of the liquid fuel spray, and the presumed-pdf can provide the necessary information about the state of the fluid *seen* by the droplets. The novel aspects of the modelling developed include a method for modelling the temperature and velocity fluctuations experienced by individual fuel droplets; alternative reference variables based on fluid residence time that may improve modelling of autoigniting flow; and rigorous and robust numerical procedures for handling the copulas in combustion simulations.

The first results chapter examines the form of the joint-pdf of normalised progress variable and mixture fraction in three different partially premixed flows: a direct numerical simulation (DNS) of fuel air ratio-stratified flame propagation; a series of non-premixed laboratory flames featuring significant extinction and reignition; and an lifted autoigniting jet flame DNS. This confirms that the dependence between progress variable and mixture fraction is most important in lifted flame structures, and the second and third results chapters go on to investigate the performance of the presumed-pdf modelling formulation in the autoigniting lifted jet flame DNS and an autoigniting spray flame experiment.

Contents

List of Figures

List of Tables

Declaration of Authorship

I, Tomas Matheson, declare that the thesis entitled *Presumed pdf modelling for turbulent spray combustion* and the work presented in the thesis are both my own, and have been generated by me as the result of my own original research. I confirm that:

- this work was done wholly or mainly while in candidature for a research degree at this University;
- where any part of this thesis has previously been submitted for a degree or any other qualification at this University or any other institution, this has been clearly stated;
- where I have consulted the published work of others, this is always clearly attributed;
- where I have quoted from the work of others, the source is always given. With the exception of such quotations, this thesis is entirely my own work;
- I have acknowledged all main sources of help;
- where the thesis is based on work done by myself jointly with others, I have made clear exactly what was done by others and what I have contributed myself;
- none of this work has been published before submission

Signed:..

Date:..

Acknowledgements

There are many people to whom I am deeply grateful for their help in preparing this thesis. I would like to thank firstly my supervisor, Dr Edward Richardson, for his endless support, encouragement, and guidance during this study. His openness to new ideas, and the enthusiasm to pursue them, have been hugely motivating. This thesis would not have come to fruition without the help of Dr Richardson and the turbulent combustion research group he has built at Southampton.

To my friends and colleagues Nabil Meah, Mark Picciani and Bruno Soriano: thank you for the many hours we have shared huddled around whiteboards, the late night and early morning discussions (both academic and otherwise), and the strong sense of camaraderie in our office. Together we fostered a collaborative and supportive work environment that I will miss dearly.

I am grateful to Dr John Shrimpton for the insight and advice he has lent at several key stages of this project. Funding for the present work was provided by EPSRC with support from Rolls-Royce plc.

Finally I would like to thank my father, for his continued support and words of encouragement. And to Kirsten, for her unbounded patience and understanding.

Chapter 1

Introduction

1.1 Motivation

Conflicting demands for increased energy supply and reduced environmental impact present important challenges for energy technologies based on fossil fuel combustion. Fossil fuel combustion currently supplies 85% of world primary energy (*BP Statistical Review of World Energy June 2015* 2015) and more than 75% of anthropogenic greenhouse gas emissions (*Climate Analysis Indicators Tool* 2009). Both the vast scale of pollutant emission from current fossil fuel use and diminishing reserves of fossil fuels motivate the development of more efficient and less-polluting combustion technology.

Two modes of pollution need to be distinguished: greenhouse gas emissions (mostly CO2) which contribute to global climate change; and air-quality pollutants (e.g. oxides of nitrogen (NO_x), CO, unburned-hydrocarbons (UHC), and particulates) which are harmful to human health in the region of emission and harmful to the ozone layer if emitted high in the atmosphere by aircraft. CO_2 emissions are tied to the amount of hydrocarbon fuel consumed which depends on thermal efficiency of combustion devices. Emissions of air-quality pollutants, in contrast, depend on how the fuel is burned. Formation of NO_x, for example, can be greatly reduced by burning fuel at low-temperature (less than 1800K). NO_x emissions are important as the UK is failing to meet EU air quality standards for nitrogen dioxide (NO_2) (McGrath 2014).

Technology for reducing emissions of air-quality pollutants, however, frequently acts to increase fuel consumption and life-cycle emission of CO_2: this is the case with popular exhaust after-treatment systems such as catalytic converters, diesel particle filters, and selective catalytic reduction. Indeed, the performance penalties associated with after-treatment systems entirely rule them out from consideration for aircraft applications. Instead of costly after-treatment, a preferable approach would be to burn fuel without producing the air-quality pollutants in the first place. However, practical application of low-emission combustion technology has so far eluded engineers. For example, in urban driving conditions the NO_x performance of diesel passenger cars has been shown to have changed little in the past 20 years (Carslaw et al. 2011).

Prospective technologies for low-emission power and propulsion systems rely on highly dilute, low-temperature combustion. Low temperature combustion prevents thermal formation of oxides of nitrogen and, with careful control of the combustion process, it is possible to achieve very low levels of particulates, CO and UHC at the same time (Opat et al. 2007). This mode of combustion requires high levels of dilution (for example with cool exhaust gas or with excess air) that can cause the fuel to burn slowly making it difficult to ignite and stabilise the combustion process (Arghode and Gupta 2010). In instances of extreme dilution, the fuel may even burn in a distributed manner without any visible flame. Low temperature combustion technologies researched increasingly since the 1990s include lean-burn gas turbine technologies, the Homogeneous Charge Compression Ignition (HCCI) engine (Yao et al. 2009) and a number of concepts for sustaining flameless-oxidation in industrial furnaces (Cavaliere and Joannon 2004). Implementation of these concepts continues to present significant technical challenges however.

In addition to utilisation of traditional fossil fuels, combustion technology needs to be developed in order to fully exploit emerging low-carbon fuels, and in order to work in conjunction with prospective carbon capture technologies. In one example, both coal and solid bio-fuels may be gassified for use in more efficient or carbon capture-compatible power plants. The gas produced has a low calorific value and is rich in hydrogen and carbon monoxide, and these fuel properties affect how combustion systems should be designed (Prins et al. 2007). In a second example, oxy-fuel combustion involves combustion in the absence of nitrogen, in order to facilitate post-combustion capture of carbon dioxide, again leading to very different design requirements for the combustion system (Wall 2007).

The high energy density and low specific costs of liquid hydrocarbon fuels, in comparison with electrochemical, thermal and mechanical means of energy storage, suggests that liquid fuels will remain an important energy source in the transport sector. This is particularly true in aviation where the weight and volume of the fuel or alternative energy storage media has a large knock-on impact on the overall energy consumption (Epstein 2012). Supply of fuel in liquid form is a further complicating factor in the understanding, modelling and design of combustion systems. Methods that facilitate better design of liquid-fuelled combustion systems in particular will therefore continue to have significant value.

Despite the long history of combustion technology, and the pressing need to move beyond global reliance on fossil fuels, there remains a requirement for very substantial further development of combustion technology in order to support anticipated changes in fuel types, energy usage and energy technology, some of which have been introduced above.

In particular, the drive to utilise new fuels in new energy technologies may lead to exploitation of alternative modes of combustion that are neither fully understood nor well modelled by established engineering design tools.

1.2 Combustion processes

Combustion systems are classically described in terms of two limits: fully premixed flames and non-premixed or diffusion flames (Bilger et al. 2005). The former assumes perfect mixing of fuel and air prior to combustion while the latter assumes that combustion occurs at the interface where the fuel and oxidiser first meet. Neither limit holds strictly in modern combustion devices for propulsion and power generation. A broad spectrum of flame structures arise in practice, including edge flames (Buckmaster 1996), triple flames (Domingo and Vervisch 1996) and fuel air ratio-stratified flames (Masri 2015). Such flames exhibit features of both premixed and non-premixed flames, leading to complex interactions between multiple combustion modes. These intermediate *partially-premixed* combustion modes arise in particular when a combustion system undergoes ignition (Mastorakos 2009) and extinction (Barlow and Frank 1998) processes, during unsteady operation, and in spray-fuelled combustion. Combustion may also proceed, wholly or in part, without the occurrence of a flame: autoignition and so-called flameless combustion being key examples in which chemical reaction proceeds relatively slowly compared to relevant mixing processes such that combustion is not limited by diffusion or propagation (i.e. coupled reaction-diffusion) processes.

The diesel engine provides an illustrative example of the many competing combustion modes that can co-exist in a single, nominally non-premixed, combustion application. Following compression of air and residual exhaust gas to a temperature of the order of 1000K, liquid diesel fuel is injected in one or more injection pulses. Jets of the liquid fuel break up into small droplets as they leave the injector and penetrate into the compressed oxidiser, and start to evaporate. The relatively cold evaporated fuel begins to mix with the hot oxidiser and spontaneous chemical reactions, that are the first stages of autoignition, occur between the oxidiser and the fuel within the inhomogeneous mixture of gas and spray. Because the oxidiser is substantially hotter than the fuel, the combustion process progresses more rapidly in fuel-lean mixtures. After an *ignition delay* during which sufficient concentrations of radicals and of heat are generated by the pre-ignition chemical reactions, the combustion proceeds rapidly to produce an ignition kernel (Glassman et al. 2014). Given the variation of temperature with fuel-air ratio, the composition that requires the shortest *ignition delay time* in order to autoignite under quiescent conditions is described as the *most reactive* mixture (Mastorakos 2009). In a subsequent period that is conventionally described as the premixed phase of diesel combustion, the region of burnt fuel expands through the generation of further ignition kernels by autoignition and through partially-premixed flame propagation. The progress of the reaction front towards the injector is inhibited by the convection of flow away from the injector, the lack of fully-evaporated fuel, the shorter residence time and therefore less reacted fuel, and by higher mixing rates near the injector that tend to quench combustion processes, so that the reaction front appears to stabilise as a *lifted flame* some distance away from the injector (L. Pickett 2005). Upstream of the lifted flame base there is some pre-mixing of fuel and oxidiser leading to partially-reacted autoigniting mixture. Downstream of the flame base there are reaction fronts extending through both fuel-rich and fuel-lean mixture that may resemble either fuel air ratio-stratified flames or ignition fronts, depending on the operating conditions, and also diffusion flame fronts aligned with the surface of *stoichiometric* fuel-air ratio, where stoichiometric describes the condition where fuel and oxidiser are mixed in exact proportions needed to achieve complete combustion.

The combustion processes in the diesel engine are also affected by the turbulent flow in which they take place, adding further complexity. A key feature of turbulent flow is that it strains the fluid in which combustion is taking place. The laminar counterflow has been used in numerous combustion studies as a simple model in which to examine how combustion phenomena respond to strain. Along the symmetry axis of the counterflow the property variation is one-dimensional, making the counterflow configuration relatively straightforward to characterise using either laboratory measurements or numerical simulations. In the case of non-premixed counterflow flames, involving opposed flows of fuel and oxidiser, there is a critical strain rate above which the counterflow will not autoignite, and a second, higher critical strain rate above which an initially burning flame will extinguish, depending on the temperatures and compositions of the two streams (Linan 1974; Seiser et al. 2000). The strain has the effect of compressing the mixing layer which separates the fuel and oxidiser and thereby increasing the rate of molecular transport. In combustion theory and modelling it is common to refer to the scalar dissipation rate $\chi = 2\mathscr{D}|\nabla(\xi)|^2$ which is related to the square of the mixture fraction gradient magnitude $|\nabla(\xi)|$ and diffusivity $\mathscr{D}$ of the mixture fraction, and provides a more direct measure of the mixing rate resulting from a given flow. The critical strain rates for a given fuel-oxidiser pair therefore correspond to critical scalar dissipation rates. High scalar dissipation rates imply fast diffusive mixing so that heat, products or intermediate species produced within the reactive mixing layer are rapidly dissipated. Below the critical dissipation rate for autoignition, high scalar dissipation rates tend to retard the onset of ignition, and hence in a turbulent flow featuring a range of scalar dissipation rates autoignition is most likely to occur in regions of low scalar dissipation rate. The preference for autoignition to occur in fluid with relatively low scalar dissipation rate and in lean mixtures of relatively high temperature is confirmed by numerical simulations of turbulent flows involving either simple (Mastorakos et al. 1997) or detailed (Yoo, Richardson, et al. 2011) chemistry models, and in turbulent fuel plumes (Markides and Mastorakos 2010).

The species profiles in non-premixed and premixed laminar counterflow provide a simple model for the thermochemical states encountered in a wide range of turbulent flows. This model both provides insight into mechanisms that are at play in turbulent flames and, in the context of flamelet modelling approaches, can be used to model both composition and reaction rates in turbulent flames. Gopalakrishnan and Abraham (2004) used non-premixed laminar counterflow simulations to demonstrate the significant role of preferential transport on ignition delay times. Knudsen, Richardson, Chen, et al. (2011) show that in Large Eddy Simulations with the flamelet modelling approach it is necessary to include preferential transport effects in Large Eddy Simulations based on the flamelet modelling approach in order to achieve satisfactory predictions of the ignition location in an autoigniting lifted turbulent jet flame.

Investigation of turbulent autoignition using either computational simulations or experimental measurements presents considerable practical challenges, however the few studies reported provide valuable insight. Yoo *et al.* have done several numerical studies of autoigniting turbulent jets, including a hydrogen flame (Yoo, Sankaran, et al. 2009) and an ethylene flame (Yoo, Richardson, et al. 2011), in order to investigate the stabilisation mechanism. There is also Kerkemeier et al. (2009) which is a numerical study of an autoigniting fuel plume experiment (Markides and Mastorakos 2010). In each of these studies autoignition points are observed upstream from the main flame and then propagate. This continual statistical process forms the stabilisation mechanism that holds the flame at its lift-off height. It also explains the fluctuation of the lift-off height around its mean value. This implies that height of the flame base is strongly linked to the autoignition time and the upstream conditions, particularly the scalar dissipation rate distribution and the convective time of the fluid mixture between the fuel nozzle and the ignition location. For relatively higher coflow temperatures the flame base fluctuations caused by independent ignition kernels forming tend to reduce but the flame is still predominantly stabilised by autoignition, as shown by the presence of autoignition precursors (HO2 for hydrogen and H2O2 or formaldehyde for hydrocarbons) and displacement speeds of the reaction front orders of magnitude greater than relevant laminar flame speeds (Yoo, Sankaran, et al. 2009; Yoo, Richardson, et al. 2011).

A second valuable contribution of the full resolution numerical studies of turbulent autoigniting jets contributed by Yoo *et al.* has been that they can serve as numerical experiments against which less costly engineering models may be tested and developed, as in Knudsen *et al.* (Knudsen, Richardson, Chen, et al. 2011) Numerical experiments offer several advantages for model development, such as exact knowledge of the experimental conditions that were simulated. In the case of autoigniting flows, in which an $\mathcal{O}(10\text{K})$ difference in the flow temperature can lead to a $\mathcal{O}(100\%)$ difference in the location of ignition, there may be an $\mathcal{O}(10\text{K})$ experimental uncertainty in laboratory measurements of temperature (Cabra et al. 2005).

1.3 Simulation in design

The development of technology that exploits the complex physics of combustion in order to meet the challenges introduced above can be greatly facilitated by simulation. Simulations can provide insight into detailed mechanisms as well as overall behaviour of practical devices. This enables evaluation and refinement of innovative design concepts. Without these tools the development of these advanced combustion systems will depend on many more expensive rig tests, which both reduces the pace at which new designs may be evaluated and provides less information about the flow field.

For a physical system where the governing equations are known exactly and accurate numerical methods are available, it is possible to conduct Direct Numerical Simulation (DNS) of the system. In this situation, the simulation results involve no modelling and they may be considered exact observations in a numerical experiment. While full resolution DNS of spray combustion has been demonstrated in very simple (laminar) configurations (Sirignano 2010), the computational cost of the technique prevents its application in the design process of practical combustion systems. The fundamental reason for the high computational cost of directly simulating sprays and spray combustion is the wide range of length-scales which must be considered and the large number of droplets involved. Noting that full-resolution simulation of turbulent and reactive multiphase flows found in most engineering applications is considerably beyond the computing resources anticipated for the coming decades, alternative modelling strategies are sought.

The turbulent flow field may be partially-resolved using Large Eddy Simulation (LES), where the large energy-containing scales of turbulent motion are resolved and smaller scale processes, including viscous dissipation and most combustion phenomena, are modelled. Alternatively the turbulent flow field may be ensemble averaged and modelled through the Reynolds-Averaged Navier Stokes approach, in which only selected fields of ensemble statistics are resolved and higher-order statistics affecting these statistical moments are modelled. In both LES and RANS, moments of the chemical reaction rates must be modelled and the irregular nature of turbulent flow lends itself to a statistical modelling approach (Pope 2000) and several statistical approaches have been proposed. Broadly these approaches may be described as either presumed probability density function (pdf) approaches or transported-pdf approaches. In the presumed-pdf approach, the properties of the fluid are related to a smaller number of reference variables, for example using flamelet (Peters 1984a) or Conditional Moment Closure approaches (Klimenko and Bilger 1999), and then the shape of the reference variables' probability density function is modelled based on modelled values for a number of its moments. In transported-pdf methods (Pope 1985; Pope 1994) a transport equation for the pdf is solved, typically with a Monte Carlo-type numerical method. Although chemical source terms appear in closed form once the joint-pdf of composition is determined, diffusive fluxes appearing in the pdf transport equation must still be modelled. Simulation using the transported pdf approach demands greater computational resources than presumed-pdf methods typically.

Transport equations for the statistical moments required in the presumed-pdf approach involve unclosed source terms, however, integration of the presumed-pdf provides a means to obtain closure for these source terms. Similarly, unclosed terms appear in the models for momentum exchange and evaporation of the liquid fuel spray, and the presumed-pdf can provide the necessary information about the state of the fluid *seen* by the droplets. Partially-premixed combustion is most commonly modelled with reference to the distribution of two variables: the mixture fraction is used to describe the fuel-air ratio, and the progress variable is used to describe the extent of reaction. However, the use of alternative reference variables has also been investigated, such as the scalar dissipation rate (Bushe 1996; Grout 2009), in order to account for the effect of turbulent mixing on combustion. It is common to assume that mixture fraction and progress variable or scalar dissipation rate are statistically independent, however there is previous evidence that this assumption gives poor predictions in some important partially-premixed applications involving flame stabilisation, and presumed-pdf modelling accounting for such dependence of the reference variables requires further investigation.

1.4 Outline

This thesis is motivated by the important role of numerical simulation in the development of future combustion technology, and the need for computational simulation methods with high predictive accuracy and low computational cost across a wide range of combustion phenomena. The thesis contributes to statistical modelling of turbulent combustion using the presumed-pdf approach, and focusses on its application to partially-premixed combustion modes, and autoignition and fuel spray effects in particular. The central modelling aspect developed in this work is the application of models for the presumed joint-pdf in order to obtain improved modelling of chemical reaction and spray effects.

In Chapter 2, theory and modelling for turbulent reacting flows is presented in the framework of presumed-pdf modelling. In Chapter 3, modelling for the presumed joint-pdf of reference variables used in combustion modelling is introduced, focussing on the copula approach introduced to combustion modelling by Darbyshire and Swaminathan (Darbyshire and Swaminathan 2012). Chapter 4 sets out methods that address challenges concerning the numerical implementation of presumed-pdf modelling employing joint-pdfs based on copulas. The novel aspects of the modelling developed include a method for modelling the temperature and velocity fluctuations experienced by individual fuel droplets; alternative reference variables based on fluid residence time that may improve modelling of autoigniting flow; and rigorous and robust numerical procedures for handling the copulas in combustion simulations.

Chapter 5 examines the form of the joint-pdf of reaction progress variable and mixture fraction in three archetypal partially premixed flows: in a DNS of fuel air ratio-stratified flame propagation (Richardson and Chen 2016); in a laboratory experiment involving extinction and reignition of a nominally non-premixed flame (Barlow and Frank 1998); and in an autoigniting lifted jet flame (Yoo, Richardson, et al. 2011). This confirms that the dependence between progress variable and mixture fraction is most important in lifted flame structures, and Chapters 6 and 7 go on to investigate the performance of the presumed-pdf modelling formulation in the autoigniting lifted jet flame case (Yoo, Richardson, et al. 2011) and autoigniting spray flame (Idicheria and Pickett 2007a; M. Pickett 2016).

Chapter 2

Theory and Model Development

Combustion usually occurs in a turbulent mixing field in practical devices. Turbulence can have a beneficial effect of enhancing the rate of mixing between fuel and oxidiser, and between reactants and products. The interaction between turbulence and combustion is integral to modelling of combustion systems.

In this chapter, the governing equations describing reacting flow will be presented. Since it is generally not possible to resolve these equations fully in numerical simulations, ensemble averaged equations with closure models will be introduced. Modelling for a dilute fuel spray, and its interactions with the turbulent flow are then introduced.

The modelling approach that is presented characterises the thermochemical state of the fluid in terms of a limited number of reference variables, and accounts for the statistics of the fluctuations of composition in the turbulent flow by presuming a particular functional form for the (joint-) probability density functions (pdfs) of the reference variables. Methods for modelling the relationship between the thermochemical state and the reference variables through an analogy between turbulent flames and laminar *flamelets* are presented, and approaches for modelling joint-pdfs of reference variables using *copulas* are presented in the subsequent chapter.

2.1 Governing equations

The dynamics of a viscous, continuum fluid, are governed by coupled set of partial differential equations. Conservation of mass can be stated by the continuity equation given by

$$\frac{\partial \rho}{\partial t} + \frac{\partial \rho u_j}{\partial x_j} = \rho \dot{S} \tag{2.1}$$

where ρ is the gas phase density, u_i is the velocity along the co-ordinate x_i, and $\dot{S}$ represents a source term which can be used to represent the change in the mass of gas, for example due to evaporation of a fuel spray. The conservation of momentum can be stated as

$$\frac{\partial \rho u_i}{\partial t} + \frac{\partial \rho u_j u_i}{\partial x_j} = -\frac{\partial p}{\partial x_i} + \frac{\partial \tau_{ij}}{\partial x_j} + \rho f_i \tag{2.2}$$

in which p is the pressure, f_i are the body forces, and τ_{ij} is the viscous stress tensor. For a Newtonian fluid, the viscous stress tensor can be expressed as

$$\tau_{ij} = -\frac{2}{3}\mu \frac{\partial u_k}{\partial x_k}\delta_{ij} + \mu \left(\frac{\partial u_i}{\partial x_j} - \frac{\partial u_j}{\partial x_i} \right) \tag{2.3}$$

where μ is the dynamic viscosity of the mixture. The momentum equations solved in the principle coordiate diections are know as the Navier-Stokes equations. Together, Equation 2.1 and Equation 2.2 fully describe flow of a Newtonian fluid.

In addition to the mass, momentum equations, the transport of a generic passive scalar can be expressed as,

$$\frac{\partial \rho \phi}{\partial t} + \frac{\partial \rho u_j \phi}{\partial x_j} = \frac{\partial}{\partial x_j}\left(\rho \mathcal{D}_\phi \frac{\partial \phi}{\partial x_j} \right) + \rho \dot{S}_\phi, \tag{2.4}$$

where $\mathcal{D}_\phi$ is the diffusivity of the scalar and $\dot{S}_\phi$ is the source term of the scalar due, for example, to evaporation.

In the case of chemically reactive systems, additional transport equations are required for each chemical species. The temporal evolution of the mass fraction Y of species α is

$$\frac{\partial \rho Y_\alpha}{\partial t} + \frac{\partial \rho u_i Y_\alpha}{\partial x_i} = -\frac{\partial}{\partial x_i}\left(\rho Y_\alpha V_\alpha \right) + \dot{\omega}_\alpha \tag{2.5}$$

where $\dot{\omega}_\alpha$ is the reaction rate of Y_α with units $kg/m^3/s$ representing the net production and consumption of a species due to chemical reaction, and V_α is the diffusion velocity. Using the Hirschfelder and Curtis (Poinsot and Veynante 2005) approximation, the diffusion flux $Y_\alpha V_\alpha$ can be approximated as

$$Y_\alpha V_\alpha = -\rho D_\alpha \frac{\partial Y_\alpha}{\partial x_i} \tag{2.6}$$

where D_α is the diffusion coefficient of species α. This approximation would normally not satisfy global mass conservation in the case of unequal species diffusivities, and correction velocity would need to be introduced to Equation 2.5, however, in this thesis equal species diffusivities is assumed and global mass conservation is conserved. The final form of the species transport equation is

$$\frac{\partial \rho Y_\alpha}{\partial t} + \frac{\partial \rho u_i Y_\alpha}{\partial x_i} = \frac{\partial}{\partial x_i}\left(\rho \mathcal{D}_\alpha \frac{\partial Y_\alpha}{\partial x_i} \right) + \dot{\omega}_\alpha \tag{2.7}$$

In non-isothermal flows, the energy of the flow must be accounted for using a relevant thermodynamic variable. In this thesis, static enthalpy is used. The entalpy of the mixture is the sum of the individual enthalpies of all N chemical species present in the mixture.

$$h = \sum_{\alpha=1}^{N} Y_\alpha h_\alpha = \sum_{\alpha=1}^{N} Y_\alpha \left[\Delta h_f^\circ (T_{ref}) + \int_{T_{ref}}^{T} c_{p_\alpha} dT \right], \tag{2.8}$$

where Δh_f° is the enthalpy of formation at a reference temperature T_{ref} and c_{p_α} is the isobaric specific heat capacity of the species. The energy balance equation is given by

$$\frac{\partial \rho h}{\partial t} + \frac{\partial \rho u_j h}{\partial x_j} = \frac{Dp}{Dt} + \tau_{ij} \frac{\partial u_i}{\partial x} + \frac{\partial q_i}{\partial x} - \dot{q} \tag{2.9}$$

where the second term on the RHS represnets viscous heating and $\dot{q}$ is any source term associate with heat exchange into the gas, for example from a spray or from radiation. The enthalpy flux q_i is given by

$$q_i = -\lambda \frac{\partial T}{\partial x} + \rho \sum_{\alpha=1}^{N} h_\alpha Y_\alpha V_\alpha \tag{2.10}$$

where λ is the thermal conductivity of the mixture. The first term represents heat diffusion by Fourier's Law and the second term represents the enthalpy flux generated by diffusion of species.

$$\frac{\partial \rho h}{\partial t} + \frac{\partial \rho u_j h}{\partial x_j} = \frac{Dp}{Dt} + \tau_{ij} \frac{\partial u_i}{\partial x} - \frac{\partial}{\partial x} \left(\lambda \frac{\partial T}{\partial x} - \rho \sum_{\alpha=1}^{N} h_\alpha Y_\alpha V_\alpha \right) - \dot{q} \tag{2.11}$$

2.1.1 Turbulence

Turbulent flows governed by Equations 2.1 and 2.2 are characterised by unsteady and irregular three-dimensional rotational motions across a wide range of scales. The largest length scales of the turbulent motions is often denoted as the integral length scale, L_T, and may have a similar order of magnitude to the main geometric features driving the flow. These structures are said to be within the energy containing range and contain most of the kinetic energy k of the turbulence of order ${u'}^2$. Here u' is the root mean square (rms) of the turbulent velocity fluctuations. If no energy is added to the flow, these structures will eventually begin to break down into smaller structures, transferring their kinetic energy in the process. This range of scales is known as the inertial range. The rate of kinetic energy transfer to the smaller scales is determined by the kinetic energy dissipation rate

$$\varepsilon \approx \frac{{u'}^3}{L_T} \tag{2.12}$$

and is assumed to be constant in the inertial range. The dissipation of larger scale kinetic energy to the smaller structures is known as the turbulence cascade (Pope 2000). This process continues until all the kinetic energy is dissipated by the smallest scales into heat in the dissipation range.

The turbulent Reynolds number (which represents the ratio of inertial to viscous forces) is defined as:

$$\mathrm{Re}_t = \frac{u' L_T}{\nu} \tag{2.13}$$

where ν is the kinematic viscosity. The smallest length scale of the turbulence is known as the Kolmogorov length scale (Kolmogorov 1991). Using dimensional analysis, the length scale can be approximated as

$$\eta = \left(\frac{\nu^3}{\varepsilon}\right)^{1/4} \tag{2.14}$$

With the assumption of constant kinetic energy dissipation to the smallest scales, the ratio between the smallest and largest length scales in the flow can be approximated as a function of the turbulent Reynolds number Re_t according to

$$L_T/\eta \sim \mathrm{Re}_t^{3/4}. \tag{2.15}$$

2.1.2 Turbulence Modelling

The scaling argument for L_T/η above indicates that the range of scales in a turbulent flow increases with Reynolds number. Since the turbulent Reynolds number in practical combustion systems is large (estimated as $\mathcal{O}(10^5)$-$\mathcal{O}(10^7)$ in gas turbine combustors) it can become impractical to solve the governing equations for the entire range of scales. The high computational cost of fully-resolved turbulence simulations, called Direct Numerical Simulations (DNS), means that DNS is restricted to relatively low turbulent Reynolds number flows. DNS is used mostly as a research tool in order to investigate in detail the physical processes arising in turbulent flows, rather than to obtain practical predictions. In order to obtain useful predictions at a lower computational cost, a portion of the flow dynamics must be modelled. There are two methods to achieve this: Large Eddy Simulation (LES) and Reynolds Averaged Navier-Stokes (RANS).

LES is an intermediate modelling approach between RANS and full-resolution DNS. In LES, the governing equations are spatially filtered at a specified filter width, with a scale lying somewhere within the inertial range. The filter operates as a low-pass filter removing the small scales, eliminating the necessity to resolve them. Consequently, the smallest scales are modelled with models known as sub-grid scale (SGS) models. Since LES models the scales below the filter width, it allows the spatial resolution of the discritized governing equations to be more coarse than with DNS, allowing the simulation of more complex, higher Reynolds number flows.

The RANS approach is the opposite extreme of DNS. It considers an ensemble average of the governing equations, such that it is only necessary to resolve gradients of the ensemble averaged flow quantities, and to completly model the unresolved physical processes. Since the ensemble-averaged flow features typically exhibit length scales on the order of L_T, rather than η, the computational cost of simulating high Reynolds number turbulent flow is vastly reduced. The draw back is that the validity of the predictions is dependent on the accuracy of the modelling for the unresolved processes.

Both RANS and LES are used by engineers in industry and the use of either depends on the application and the level of fidelity required from the solution. In terms of turbulent (spray) combustion modelling, RANS and LES present similar challenges concerning modelling of unresolved processes, and some modelling approaches may be applied in either the RANS and LES contexts. The burden of modelling is generally greater in RANS, since a greater range of processes must be modelled, and this thesis focusses exclusively on RANS modelling, however it may be noted that many of the approaches developed are equally applicable in the LES context.

2.1.3 Reynolds-Averaged Governing Equations

Ensemble averaging of the governing equations is achieved by decomposing the flow properties into two components

$$\phi = \overline{\phi} + \phi' \tag{2.16}$$

where $\overline{\phi}$ and ϕ' are the ensemble average and fluctuating components respectively. Due to the substantial density variation in combusting flows, density-weighted averaging is used more commonly,

$$\rho\phi = \overline{\rho\phi} + (\rho\phi)'. \tag{2.17}$$

Defining Favre variables as

$$\tilde{\phi} = \frac{\overline{\rho\phi}}{\overline{\rho}}, \phi'' = \frac{(\rho\phi)'}{\overline{\rho}} \tag{2.18}$$

gives the decomposition as

$$\frac{\rho\phi}{\overline{\rho}} = \tilde{\phi} + \phi''. \tag{2.19}$$

The Favre averaged mass conservation equation may be written

$$\frac{\partial\overline{\rho}}{\partial t} + \frac{\partial\overline{\rho}\widetilde{u_i}}{\partial x_j} = \overline{\rho\dot{S}} \tag{2.20}$$

The Favre averaged momentum equation (neglecting body forces) may be written

$$\frac{\partial\overline{\rho}\widetilde{u_i}}{\partial t} + \frac{\partial\overline{\rho}\widetilde{u_j}\widetilde{u_i}}{\partial x_j} = -\frac{\partial\overline{p}}{\partial x_i} - \frac{\partial}{\partial x}\left(\overline{\rho}\widetilde{u_i''u_j''}\right) + \frac{\partial\widetilde{\tau_{ij}}}{\partial x_j} + \frac{\partial\tau_{ij}''}{\partial x_j} \tag{2.21}$$

where $\widetilde{\tau_{ij}}$ is the viscous stress tensor as a function of the Favre filtered quantities, and following Vreman et al. (1995), τ''_{ij} is often neglected. The Reynolds stresses $\overline{\rho u''_i u''_j}$ are modelled using an eddy viscosity model:

$$-\overline{\rho u''_i u''_j} \approx 2\mu_t S_{ij} - \frac{2}{3}\left(\mu_t \frac{\partial u_k}{\partial x_k} + \rho k \delta_{ij}\right) \tag{2.22}$$

where μ_t is a turbulent viscosity, S_{ij} is the mean rate of strain tensor, δ_{ij} is the Kronecker delta, and k is the turbulent kinetic energy:

$$k = \frac{1}{2}\widetilde{u''_j u''_j} \tag{2.23}$$

To obtain the turbulent viscosity in a RANS simulation, the k-ε model is commonly employed, in which additional transport equations for the turbulent kinetic energy k and the turbulent dissipation rate ε are solved. In this thesis, the realisable form of the $k-\varepsilon$ equations are used (Shih et al. 1995).

$$\frac{\partial \rho k}{\partial t} + \frac{\partial \rho k u_j}{\partial x_j} - \frac{\partial}{\partial x_j}\left(\frac{\mu_t}{\sigma_k}\frac{\partial k}{\partial x_j}\right) = \mu_t S_{ij}\frac{\partial u_j}{\partial x_j} - \rho\varepsilon - \frac{2}{3}\left(\mu_t \frac{\partial u_j}{\partial x_j} + \rho k\right)\frac{\partial u_j}{\partial x_j} \tag{2.24}$$

$$\frac{\partial \rho \varepsilon}{\partial t} + \frac{\partial \rho \varepsilon u_j}{\partial x_j} - \frac{\partial}{\partial x_j}\left(\frac{\mu_t}{\sigma_\varepsilon}\frac{\partial \varepsilon}{\partial x_j}\right) = \rho C_1 S\varepsilon - \rho C_2 \frac{\varepsilon^2}{k + \sqrt{\nu\varepsilon}} + C_{\varepsilon_4}\rho\varepsilon\frac{\partial u_j}{\partial x_j} \tag{2.25}$$

where the constants are $C_2 = 1.9$, $C_{\varepsilon_4} = -0.33$ and

$$C_1 = \max\left(0.43, \frac{\eta}{\eta + 5}\right), \text{ where} \tag{2.26}$$

$$\eta = S\frac{k}{\varepsilon} \tag{2.27}$$

$$S = \sqrt{2S_{ij}S_{ij}} \tag{2.28}$$

and buoyancy terms and laminar viscosity have been neglected. This modification of the standard $k - \varepsilon$ equations provides better predictions for the spread rate of planar jets that are studied in this work. Aside from a slight modification of the ε equation, the primary difference between the Realizable and standard $k-\varepsilon$ are in the calculation of the turbulent viscosity μ_t, specifically that the coefficient C_μ is no longer constant but variable, which avoids the problem of non-realisable values of the Reynolds stresses (*StarCD 4.20 Methodology Manual* 2013):

The turbulent viscosity μ_t is given in terms of a variable C_μ as:

$$\mu_t = \rho C_\mu \frac{k^2}{\varepsilon}, \text{ where} \tag{2.29}$$

$$C_\mu = \left(A_0 + A_S U^* \frac{k}{\varepsilon}\right)^{-1} \tag{2.30}$$

$$U^* = \sqrt{S_{ij}S_{ij} + \Omega_{ij}\Omega_{ij}} \tag{2.31}$$

$$A_0 = 4.0 \tag{2.32}$$

$$A_S = \sqrt{6}\cos(\phi) \tag{2.33}$$

$$\phi = \frac{1}{3}\arccos\left(\sqrt{6}\frac{S_{ij}S_{jk}S_{ki}}{\sqrt{S_{ij}S_{ij}}^3}\right) \tag{2.34}$$

The turbulent Schmidt numbers are taken as $\sigma_k = 1.0$ and $\sigma_\varepsilon = 1.2$. The mean rate of strain tensor S_{ij} and vorticity tensor Ω_{ij} are given by

$$S_{ij} = \frac{1}{2}\left(\frac{\partial u_i}{\partial x_j} + \frac{\partial u_j}{\partial x_i}\right) \tag{2.35}$$

$$\Omega_{ij} = \frac{1}{2}\left(\frac{\partial u_i}{\partial x_j} - \frac{\partial u_j}{\partial x_i}\right) \tag{2.36}$$

The Favre averaged equation for a generic scalar, as described by Equation 2.4, may be written

$$\frac{\partial \overline{\rho}\tilde{\phi}}{\partial t} + \frac{\partial \overline{\rho}\tilde{u}_j\tilde{\phi}}{\partial x_j} = \frac{\partial}{\partial x_j}\left(\overline{\rho}\mathcal{D}_\phi \frac{\partial \tilde{\phi}}{\partial x_j}\right) - \frac{\partial}{\partial x_j}\left(\overline{\rho}\widetilde{u_j''\phi''}\right) + \overline{\rho\dot{S}_\phi}, \tag{2.37}$$

where $\overline{\rho}\widetilde{u_j''\phi''}$ is the scalar flux commonly modelled through a gradient transport assumption by

$$\overline{\rho}\widetilde{u_j''\phi''} = -\overline{\rho}\frac{\mu_t}{\sigma_\phi}\frac{\partial \tilde{\phi}}{\partial x_j} \tag{2.38}$$

where σ_ϕ is the turbulent Schmidt number, and μ_t is the turbulent viscosity given by Equation 2.29. The final transport equation for a passive scalar is given by

$$\frac{\partial \overline{\rho}\tilde{\phi}}{\partial t} + \frac{\partial \overline{\rho}\tilde{u}_j\tilde{\phi}}{\partial x_j} = \frac{\partial}{\partial x_j}\left(\overline{\rho}\mathcal{D}_e \frac{\partial \tilde{\phi}}{\partial x_j}\right) + \overline{\rho\dot{S}_\phi}, \tag{2.39}$$

where $\mathcal{D}_e$ is the effective diffusion coefficient given by

$$\mathcal{D}_e = \mathcal{D}_\phi + \frac{\mu_t}{\sigma_\phi} \tag{2.40}$$

2.1.4 Reference variables

In a typical chemically reacting system with complex hydrocarbon fuels, there may be hundreds or thousands of species present. In DNS, each of these requires the solution of a transport equation which imposes a substantial computational cost on finding the solution. If the thermochemical state of the system is described by a set of species mass fractions Y_α and enthalpy h, the full set of states is embedded in $(\alpha + 1)$-dimensional space. However, not every point in thermochemical space is realisable – due to the physical properties of the system, additional restrictions are placed on the state and hence the total number of degrees of freedom is less than $\alpha + 1$. Firstly, the mass fractions are subject to the restriction

$$\sum_\alpha Y_\alpha = 1, \tag{2.41}$$

which restricts the set of realisable states to an α-dimensional manifold embedded in $\alpha + 1$-dimensional space. The elemental masses must be conserved, and therefore the initial composition restricts the composition to those that meet this criteria.

More specifically, in most combustion applications the range of realisable states forms a thin manifold in thermochemical space (Pope 2013), and by approximating this thin manifold by a similar low dimensional manifold the realisable states may be be described using a coordinate system of much lower dimension. A set of n such coordinates are referred to as *reference variables*. Techniques exist, such as Principal Component Analysis (Sutherland and Parente 2009), to automatically determine the optimal n-dimensional coordinate system (the principal components) for a given set of observations either from DNS or experiment, where n may be chosen based on the acceptable error in the approximation. This approach however relies on having sufficient data a-priori to apply the analysis to. Alternatively, reference variables based on physical arguments about turbulent combustion processes have been defined, and then a corresponding manifold in thermochemical space is generated either by physical considerations (for example, the Burke-Schumann limit (Burke and Schumann 1948)) or from the solution to canonical combustion problems such as premixed or diffusion flames.

Examples of reference variables used in turbulent combustion include the mixture fraction, progress variable, scalar dissipation rate, enthalpy, temperature, entropy, residence time or age, and many others. In this thesis, the two main reference variables that will be considered are the mixture fraction, which describes the degree of mixing between fuel and oxidiser streams, and the normalised progress variable, which describes the progress of the reaction from unburned to fully burned. In addition, two new reference quantities based on residence time will be introduced. Mixture fraction and progress variable are an appropriate choice for partially-premixed systems which exhibit varying degrees of reactedness and variations in local equivalence ratio. Their combination is appropriate as the effects of inert mixing and reaction are typically orthogonal in thermochemical space and therefore provide a useful set of coordinates to parametrise the a wide range of possible states.

This thesis will focus on methods in which a series of solutions of premixed or non-premixed laminar flamelets are used to populate the thermochemical state in composition space.

2.1.4.1 Reference variables for partially-premixed flames

In non-premixed combustion the fuel and oxidiser are initially separated in different streams and must mix at the molecular level in order to react. In order to characterise the degree of mixing that has occurred, the concept of a *mixture fraction* was introduced (Bilger 1977). The mixture fraction may be defined as the fraction of mass that originated from the fuel stream. In the limits of infinitely fast chemistry or equilibrium chemistry, the thermochemical state in an adiabatic non-premixed combustion system is uniquely defined by the mixture fraction. Experimental measurements of non-premixed flames commonly exhibit a strong dependence of the thermochemical state on mixture fraction, and this motivates the use of mixture fraction as a reference variable for non-premixed combustion (Barlow and Frank 1998; Klimenko and Bilger 1999; Peters 2000).

In premixed combustion flame fronts propagate through unburned mixture due to the combined effects of reaction and diffusion. In the flamelet combustion regime, the composition through the reaction-diffusion layer approaches a one-dimensional manifold in composition space, and a reaction progress variable can be used to describe the extent of the reaction process along this trajectory through composition space (Knudsen, Kim, et al. 2010). Furthermore, in partially-premixed combustion involving variation of reaction progress and equivalence ratio, a progress variable may be used in combination with a mixture fraction to characterise the thermochemical state.

Mixture fraction and progress variable are both thermochemical properties of the flow, and provide a useful basis for modelling the thermochemical state of a range of turbulent reacting flows. However, there is not necessarily a unique mapping between a pair of mixture fraction and progress variable values and the thermochemical state: for example, the same mixture fraction/progress variable pair may be realised during either an extinction or an ignition event, between which there are differences in composition. In terms of realisable thermochemical state, mixture fraction and progress variable are no longer sufficient coordinate system to describe the thin composition manifold in thermochemical space, which now requires at least 3 coordinates to closely approximate. In this example it is useful to refer to information that can indicate the direction of the trajectory through this mixture fraction/progress variable state. Mixture fraction dissipation rate in particular is a useful measure of how the flow affects extinction and ignition processes, and it has been used as a reference variable in a number of modelling approaches (Bushe 1996; Knudsen, Richardson, Doran, et al. 2012).

For kinetically-limited processes such as autoignition or post-combustion NOx formation, measures of the flow residence time have been used as reference variables (Shin et al. 2016). Therefore it is relevant to consider how variables providing information about the flow and mixing dynamics can supplement the use of variables describing the fuel-oxidiser ratio and extent of reaction.

This thesis focusses in large part on the application of mixture fraction and progress variable to autoigniting combustion problems. In the following Sections, the definitions of mixture fraction and progress variable used in this thesis will be formalised, and two new residence time-based reference variable for autoigniting problems are defined and the motivation for its application explained.

2.1.4.2 Definitions of the mixture fraction

For the purposes of modelling, it is convenient to define mixture fraction Z based on its transport equation

$$\frac{\partial \rho Z}{\partial t} + \frac{\partial \rho u_i Z}{\partial x_j} = \frac{\partial}{\partial x_i}\left(\rho D_Z \frac{\partial Z}{\partial x_i}\right) \tag{2.42}$$

setting the initial/boundary value of mixture fraction equal to unity in the fuel stream and equal to zero in the oxidiser stream. However Z is a fictitious fluid property which can be simulated numerically but cannot be measured directly. In order to evaluate the mixture fraction from experimental data it is necessary to provide a definition of mixture fraction as a function of the thermochemical state.

Since elemental mass fractions are conserved during chemical reaction, mixture fraction may be evaluated by considering the elemental mass fractions in a mixture. Hydrocarbon combustion in air involves predominantly carbon, hydrogen, oxygen and nitrogen atoms and, assuming that all chemical species have equal diffusivities, the mixture fraction can be evaluated equivalently from the elemental mass fraction of any of these elements, or from a linear combination of them. It can be shown that, given the assumption of equal thermal and species diffusivities, the mixture fraction based on any linear combination of elemental mass fractions and enthalpy is consistent with Equation 2.42. In general however, chemical species do have different diffusivities and, in particular, atomic and molecular hydrogen have substantially higher diffusivities than other species in hydrocarbon flames. Therefore a particular linear combination of elemental mass fractions must be specified in order to define mixture fraction. Following (Bilger 1989a), it is conventional to specify the weighting of the carbon, hydrogen and oxygen based on the elemental ratios in a stoichiometric global chemical equation between the fuel (F) and oxidiser (O) streams, yielding a product mixture (P),

$$\mu_F Y_F + \mu_O Y_O \rightarrow \mu_P Y_P \tag{2.43}$$

where μ are stoichiometric coefficients. The mixture fraction is given by

$$Z = \frac{Y_F - (Y_O - Y_{O,2})(\mu_F W_F/\mu_O W_O)}{Y_{F,1} - Y_{O,2}(\mu_F W_F/\mu_O W_O)} \tag{2.44}$$

where W_α are the molar masses and the indices 1 and 2 indicate the fuel and oxidiser streams, respectively. It should be noted that mixture fractions defined based on elemental mass fractions are not strictly conserved scalars when considering differential diffusion.

The mixture fraction is a measure of the fuel-oxidiser ratio and, assuming equal diffusivities, there is a simple relationship between the mixture fraction and the fuel-air equivalence ratio. The fuel-air equivalence ratio is the gravimetric fuel-air ratio normalised so that it is equal to unity in stoichiometric mixtures. It can be related to the mixture fraction by,

$$\phi = \frac{Z}{1-Z}\frac{(1-Z_{st})}{Z_{st}} \tag{2.45}$$

where Z_{st} is the stoichiometric mixture fraction.

The mixture fraction turbulent dissipation rate is a measure of the rate of decay of mixture fraction variance due to molecular diffusion, given by

$$\tilde{\chi} = 2\mathcal{D}\widetilde{\left(\frac{\partial Z''}{\partial x_j}\right)^2}. \tag{2.46}$$

$\tilde{\chi}$ is potentially useful as a reference variable since its magnitude characterises the effect of turbulent mixing on non-premixed flames.

2.1.4.3 Definitions of the progress variable

We require a definition that gives a monotonic variation of progress variable from the reactant mixture composition through to the product composition. In this study we focus on species-based progress variable definitions rather than considering equally-valid temperature or sensible enthalpy-based definitions. The non-normalised progress variable Y_c is defined as a linear combination of a the reactive species,

$$Y_c = \sum_{\alpha}^{N} a_\alpha Y_\alpha \tag{2.47}$$

where a_α are constant weighting applied to each of the N species in the mixture. Due to the fact that there is often a significant quantity of hydrogen and carbon monoxide in the products of fuel-rich flames, a common definition for non-normalised progress variable is $Y_c = Y_{\mathrm{CO_2}} + Y_{\mathrm{H_2O}} + Y_{\mathrm{H_2}} + Y_{\mathrm{CO}}$.

Conventionally progress variable in premixed flames is normalised using the fully burnt value of Y_c in order to obtain a parameter varying between zero in the reactants and unity in the products. In flows involving variation of the fuel-oxidiser ratio, there is not a unique product composition, and the normalising value is taken as a function of the mixture fraction,

$$c = \frac{Y_c - Y_{c,u}(Z)}{Y_{c,b}(Z) - Y_{c,u}(Z)} \tag{2.48}$$

where subscripts u and b denote the unburnt and burnt conditions for a given value of mixture fraction. The transport equation for c may be derived from Equation 2.7 (Bray, Domingo, et al. 2005):

$$\frac{\partial \rho c}{\partial t} + \frac{\partial \rho u_i c}{\partial x_i} = \frac{\partial}{\partial x_i}\left(\rho D_c \frac{\partial c}{\partial x_i}\right) + \dot{\omega}_c \tag{2.49}$$

where $\dot{\omega}_c$ is the reaction rate of normalised progress variable. The mixture fraction progress variable cross-dissipation terms have been neglected (Bray, Domingo, et al. 2005).

2.1.4.4 Residence time-based reference variables

It is noted that the rapid change of a progress variable c through a premixed flame or autoignition implies that the variation of thermochemical state is well resolved in progress variable space during this process, but poorly resolved around $c = 0$ or 1. Hence modelling using progress variables based on the major species may be ill-conditioned and sensitive to numerical integration. Close to the fully burned state, this limits the ability of the progress variable approach to predict slow processes such as NO_x formation. The present work addresses autoigniting flows, in which there is a very limited increase in progress variables based on major reactants or products during the early stages of the ignition delay. In Section 6.2, it is demonstrated that this causes problems for the accurate time integration of the progress variable. The use of residence time-based quantities as reference variables is investigated and shown to avoid this problem.

The fluid-age (a_M) is a continuum property of a fluid that is defined by a transport equation in the form proposed by Sandberg (1981) which was later generalised by Ghirelli and Leckner (2004) and Shin et al. (2016) to variable property flow. For flow of a fluid consisting of one or more chemical species with equal diffusivities, the fluid-age transport equation is given by

$$\frac{\partial a}{\partial t} + u_i \frac{\partial a}{\partial x_i} = \frac{1}{\rho}\frac{\partial}{\partial x_i}\left(D_a \frac{\partial a}{\partial x_i}\right) + 1 \tag{2.50}$$

The first term in Equation 2.50 represents unsteadiness of the local fluid-age, the second term represents advection by the convective velocity u_i, the third term represents the effects of diffusive flux of material between regions with different values of fluid-age, and the final source term represents the process of age increasing due to the passage of time.

Note that the fluid-age may be interpreted as an instantaneous mass-weighted average of the elementary-age of atoms in an infinitesimal volume within the flow (Shin et al. 2016). The fluid-age a_M is not a convenient reference variable for use as a tabulated reference variable because it is not bounded, and may tend to infinity with increasing time, such as in a recirculation zone. This differs from the case of scalar dissipation rate, for example, for which an arbitrary upper bound may be chosen to represent a value unlikely to be achieved in the flow field of interest. Therefore an alternative approach is developed in this work.

In order to obtain a bounded scalar a that is age-dependent, the source term in Equation 2.50 is substituted for a non-linear source term. The transport equation for a is given by

$$\frac{\partial \rho a}{\partial t} + \frac{\partial \rho u_i a}{\partial x_i} = \frac{\partial}{\partial x_i}\left(\rho D_a \frac{\partial a}{\partial x_i}\right) + \rho \frac{2}{t_1}\sqrt{1-a} \tag{2.51}$$

where t_1 is a characteristic timescale that can be related to the fully burned thermochemical state. Provided that the initial and boundary conditions are restricted to $a \in [0,1]$, the source term on the right hand side of Equation 2.51 has the desirable property that as $a \to 0$, $\sqrt{1-a} \approx 1$ and hence a increases linearly with time; and as $a \to 1$ then $\sqrt{1-a} \to 0$ so that a will not exceed 1 (given initial conditions $a \in [0,1]$). Hence, in the limit of zero advection and diffusion, the variable a essentially constitutes a remapping of a_M from $R^+ \to [0,1]$. The plot of $a(t)$ over time is quadratic, as seen by the integration of the source term over time while neglecting convection and assuming constant ρ:

$$\begin{aligned} a(t) &= 2\frac{t}{c} - \frac{t^2}{c^2} && (2.52)\\ \sqrt{1-a} &= \{\frac{t}{c} - 1, 1 - \frac{t}{c}\} && (2.53)\\ \frac{\partial a}{\partial t} &= \frac{2}{c}(1 - \frac{t}{c}) && (2.54)\\ &= \frac{2}{c}\sqrt{1-a} && (2.55) \end{aligned}$$

where $\sqrt{1-a} = 1 - \frac{t}{c}$ is chosen for consistency.

Alternatively this could be interpreted as a remapping from normalised progress variable c to a. Over the course of a homogeneous ignition event, $c_t = c(t)$ and $a_t = a(t)$, and therefore we may write

$$a_t = a(c^{-1}(c_t))) \tag{2.56}$$

where the inverse function $c^{-1}(t)$ is guaranteed to exist due to the requirement that c is strictly monotonic in time.

Therefore, in the homogeneous reactor case, a may be considered an equivalent reference quantity to c. It will however have different mixing characteristics: whereas c is based on normalised mass fractions and therefore has the same linear mixing behaviour as Y_α, a has a non-linear source term and will exhibit different mixing.

One advantage of a progress variable over a in its current form is that species mass fraction profiles may change rapidly through a flame. The gradient of the progress variable varies most strongly through the flame and therefore there intermediate species are well resolved in progress variable space (i.e. $\frac{\partial \phi}{\partial c}$ is small). In order to maintain adequate resolution in reference variable space to describe intermediate species, the reference variable a is combined with the progress variable to give a new reference variable, $b = (a + c)/2$, with transport equation

$$\frac{\partial \rho b}{\partial t} + \frac{\partial \rho u_i b}{\partial x_i} = \frac{\partial}{\partial x_i}\left(\rho D_b \frac{\partial b}{\partial x_i}\right) + \rho \frac{1}{t_1}\sqrt{1-a} + \rho \frac{1}{2}\dot{\omega}_c \tag{2.57}$$

that can achieve both accurate ignition delay times ($\frac{\partial b}{\partial t} \to 1$ as $b \to 0$) and sufficient resolution in reference variable space ($\frac{\partial Y_\alpha}{\partial b}$ remains small through flame). Here, D_b is the laminar diffusivity of the scalar b and may be a function of x and scalar gradients $\frac{\partial a}{\partial x}$ and $\frac{\partial c}{\partial x}$.

In the Section 4.6, the reference variables a and b are shown to successfully avoid the problems discussed above which are inherent in using a progress variable approach for autoigniting flows.

2.1.4.5 Mapping reference variables to quantities of interest

Once the instantaneous reference variables described above are solved for, the problem remains of linking these reference variables to quantities of interest such as species mass fractions. In this thesis, the approach taken is to tabulate the quantities of interest as a function of chosen reference variables using a laminar flamelet table. Quantities such as mass fractions or temperature are determined from the values of reference variables through the flamelet function. For two reference variables η and ζ, this has the form

$$\phi(x,t) = \phi^*(\eta(x,t), \zeta(x,t)), \tag{2.58}$$

which links the value of the instantaneous quantity $\phi(x,t)$ at point x and time t with the values from the flamelet table $\phi^*(\eta,\zeta)$ which correspond to the values of η and ζ at the space-time point (x,t). The choice of reference variables will depend on the type of flamelet to be stored in the table.

Such a laminar flamelet table may be populated using existing combustion codes. Several such codes were used throughout this thesis, depending on the application of the flamelet table. In addition, for the turbulent autoigniting flamelet solutions required for tabulation in Chapter 6, a singly-conditioned Conditional Moment Closure (CMC) code was written to provide the solutions.

CMC (Klimenko and Bilger 1999) is a combustion model which solves a transport equation for the evolution of composition as a function of mixture fraction. In the zero-dimensional formulation, the following transport equations are solved for the conditional species mass fractions $\langle Q_k|\eta\rangle$:

$$\frac{\partial\langle Q_k|\eta\rangle}{\partial t} = \langle\chi|\eta\rangle\frac{\partial^2\langle Q_k|\eta\rangle}{\partial\eta^2} + \langle\dot{\omega}_k|\eta\rangle \tag{2.59}$$

Here, $\langle\chi|\eta\rangle$ is the conditional scalar dissipation rate and $\langle\dot{\omega}_k|\eta\rangle$ is the conditional reaction rate of species k. In the current implementation, no conditional energy equation is solved, since the conditional averaged enthalpy equation is conserved by chemical reaction, and the profile remains linear and unchanged under the diffusion operator in Equation 2.59; instead, temperature is calculated from fixed conditional enthalpy by means of a Newton-Raphson iteration.

The conditional scalar dissipation rate $\langle\chi|\eta\rangle$ is given by the AMC model (O'Brien and Jiang 1991) as a constant function of mixture fraction:

$$\langle\chi|\eta\rangle = \chi_{max}\exp\left(-2\left[\mathrm{erf}^{-1}(2\eta-1)\right]^2\right) \tag{2.60}$$

where χ_{max} is the peak scalar dissipation rate.

Equation 2.59 is solved in mixture fraction space over time, starting from an initial condition in which linear mixing of species and enthalpy is assumed between the boundary conditions, and with appropriate conditions produces a solution $\phi(\eta, t)$ for an autoigniting flamelet. To create a two dimensional laminar flamelet table, the time coordinate is then mapped to the appropriate second reference variable. In the case of progress variable, $c(\eta, t)$ is calculated for each point in mixture fraction space and time, and then the solution interpolated onto a mixture fraction-progress variable grid. In the CMC calculations both a and c are known and therefore b is known, and the same interpolation process can be applied in order to generate a laminar flamelet table parametrised by either of these two reference variables. Any relevant source terms in the reference variable transport equations may also be tabulated and therefore be available when solving the transport equation.

A requirement for the remapping from time to a reference variable is that the reference variable is monotonically increasing in time in the CMC simulation for all mixture fractions. This property is satisfied by both reference variables a and c and therefore is automatically satisfied for b.

2.1.4.6 Reference variable moment equations

The Favre averaged transport equations for $\widetilde{Z}$, $\tilde{c}$, $\widetilde{Z''^2}$, $\widetilde{c''^2}$ are given here in the form presented by Darbyshire and Swaminathan (2012):

$$\frac{\partial \bar{\rho}\widetilde{Z}}{\partial t} + \frac{\partial \bar{\rho}\widetilde{u_i}\widetilde{Z}}{\partial x_i} = \frac{\partial}{\partial x_i}\left(\overline{\rho D_t \frac{\partial Z''^2}{\partial x_i}} - \overline{\rho u_i'' Z''}\right) \tag{2.61}$$

$$\frac{\partial \bar{\rho}\tilde{c}}{\partial t} + \frac{\partial \bar{\rho}\widetilde{u_i}\tilde{c}}{\partial x_i} = \frac{\partial}{\partial x_i}\left(\overline{\rho D_t \frac{\partial c''^2}{\partial x_i}} - \overline{\rho u_i'' c''}\right) + \overline{\dot{\omega}_c} \tag{2.62}$$

$$\begin{aligned}\frac{\partial \bar{\rho}\widetilde{Z''^2}}{\partial t} + \frac{\partial \bar{\rho}\widetilde{u_i}\widetilde{Z''^2}}{\partial x_i} = \frac{\partial}{\partial x_i}\left(\overline{\rho D_t \frac{\partial Z''^2}{\partial x_i}} - \overline{\rho u_i'' Z''}\right)\\ - 2\overline{\rho u_i'' Z''}\frac{\partial \widetilde{Z}}{\partial x_i} - 2\overline{\rho D \frac{\partial Z''}{\partial x_i}\frac{\partial Z''}{\partial x_i}}\end{aligned} \tag{2.63}$$

$$\begin{aligned}\frac{\partial \bar{\rho}\widetilde{c''^2}}{\partial t} + \frac{\partial \bar{\rho}\widetilde{u_i}\widetilde{c''^2}}{\partial x_i} = \frac{\partial}{\partial x_i}\left(\overline{\rho D_t \frac{\partial c''^2}{\partial x_i}} - \overline{\rho u_i'' c''}\right)\\ - 2\overline{\rho u_i'' c''}\frac{\partial \tilde{c}}{\partial x_i} - 2\overline{\rho D \frac{\partial c''}{\partial x_i}\frac{\partial c''}{\partial x_i}} + 2\overline{c''\dot{\omega}_c}\end{aligned} \tag{2.64}$$

$$\begin{aligned}\frac{\partial \bar{\rho}\widetilde{Z''c''}}{\partial t} + \frac{\partial \bar{\rho}\widetilde{u_i}\widetilde{Z''c''}}{\partial x_i} = \frac{\partial}{\partial x_i}\left(\overline{\rho D_t \frac{\partial Z''c''}{\partial x_i}} - \overline{\rho u_i'' Z''c''}\right)\\ - \overline{\rho u_i'' Z''}\frac{\partial \tilde{c}}{\partial x_i} - \overline{\rho u_i'' c''}\frac{\partial \widetilde{Z}}{\partial x_i} - 2\overline{\rho D \frac{\partial Z''}{\partial x_i}\frac{\partial c''}{\partial x_i}} + \overline{Z''\dot{\omega}_c}\end{aligned} \tag{2.65}$$

The first term in each of Equations 2.61-2.65 represents unsteadiness of the local Favre averaged quantity, the second term represents advection by the convective velocity $\widetilde{u_i}$, and the third term represents the combined effect of molecular diffusion and turbulent transport. The turbulent fluxes may be modelled through the gradient approximation (Poinsot and Veynante 2005):

$$\overline{\rho u_i'' Z''} = -\bar{\rho}\frac{\mu_t}{\sigma_t}\frac{\partial \widetilde{Z}}{\partial x_i} \tag{2.66}$$

$$\overline{\rho u_i'' Z''^2} = -\bar{\rho}\frac{\mu_t}{\sigma_t}\frac{\partial \widetilde{Z''^2}}{\partial x_i} \tag{2.67}$$

$$\tag{2.68}$$

and similarly for $\tilde{c}$ and $\widetilde{c''^2}$. Here σ_t is the turbulent Schmidt number for the scalar and μ_t is the turbulent viscosity. The scalar dissipation rates in the Favre variance and covariance equations are modelled by the variance and the inverse turbulence timescale:

$$\overline{\rho}\widetilde{\chi_Z} = 2\overline{\rho D \frac{\partial Z''}{\partial x_i}\frac{\partial Z''}{\partial x_i}} = 2\rho\frac{\tilde{\varepsilon}}{\tilde{k}}\widetilde{Z''^2} \tag{2.69}$$

$$\overline{\rho}\widetilde{\chi_c} = 2\overline{\rho D \frac{\partial c''}{\partial x_i}\frac{\partial c''}{\partial x_i}} = 2\rho\frac{\tilde{\varepsilon}}{\tilde{k}}\widetilde{c''^2} \tag{2.70}$$

$$\overline{\rho}\widetilde{\chi_{Zc}} = 2\overline{\rho D \frac{\partial Z''}{\partial x_i}\frac{\partial c''}{\partial x_i}} = 2\rho\frac{\tilde{\varepsilon}}{\tilde{k}}\widetilde{Z''c''} \tag{2.71}$$

The transport equation for the Favre averaged scalars $\tilde{a}$ and $\tilde{b}$ are given by:

$$\frac{\partial\overline{\rho}\tilde{\phi}}{\partial t} + \frac{\partial\overline{\rho}\widetilde{u_i}\tilde{\phi}}{\partial x_i} = \frac{\partial}{\partial x_i}\left(\overline{\rho D_t\frac{\partial\phi''^2}{\partial x_i}} - \overline{\rho u_i{}''\phi''}\right) + \overline{\rho\dot{S}_\phi} \tag{2.72}$$

for $\phi \in \{a, b\}$ with $\dot{S}_a = \sqrt{1-a}/t_1$ and $\dot{S}_b = \sqrt{1-a}/t_1 + \dot{\omega}_c/2$. The corresponding variance transport equations are given by

$$\begin{aligned}\frac{\partial\overline{\rho}\widetilde{\phi''^2}}{\partial t} + \frac{\partial\overline{\rho}\widetilde{u_i}\widetilde{\phi''^2}}{\partial x_i} &= \frac{\partial}{\partial x_i}\left(\overline{\rho D_t\frac{\partial\phi''^2}{\partial x_i}} - \overline{\rho u_i{}''\phi''}\right)\\ &\quad - 2\overline{\rho u_i{}''\phi''}\frac{\partial\tilde{\phi}}{\partial x_i} - 2\overline{\rho D\frac{\partial\phi''}{\partial x_i}\frac{\partial\phi''}{\partial x_i}} + 2\overline{\rho\phi''\dot{S}_\phi}\end{aligned} \tag{2.73}$$

In each case, the same modelling steps as described for the mixture fraction and progress variable moment transport equations are applied.

2.2 Liquid phase

Many combustion systems use liquid fuels, particularly internal combustion engines and gas turbines in transport applications. Computational simulation of fuel injection and atomisation is particularly challenging because liquid fuels have high density ratios compared to the vapour and they are injected at high velocity, resulting in high Reynolds and Weber numbers (We $= \rho u^2 D_d/\sigma$, where D_d is the droplet diameter and ρ and σ are the density and surface tension of the liquid, respectively) — implying impractically fine-scale resolution is required. More commonly, heuristic models are used for spray injection and atomisation, and the two-phase simulation is restricted to the dilute spray processes after the contiguous liquid injected has broken into relatively small and widely spaced droplets.

A number of alternative approaches have emerged for modelling the transport of dispersed liquid droplets in a gaseous carrier phase and these may be characterised broadly by whether both the gaseous flow and the statistical moments of the liquid spray are represented in an Eulerian sense, or whether a Lagrangian description of the dispersed liquid spray is combined with an Eulerian description of the gas. In this work a Lagrangian approximation is adopted for the spray. Since the number of physical droplets in a computational cell can be very large, physical droplets with similar properties are grouped into a *parcel* representing an ensemble of droplets. Another interpretation of the Discrete Droplet Model is to consider that the ensemble of numerical parcels corresponds to a Monte Carlo representation of the probability density function of spray properties, or *droplet distribution function* (Williams 1958). In either case, the particle trajectories are solved in a Lagrangian sense according to modelled momentum source terms representing drag from movement through the gas, and the droplet mass and temperature are modelled by source terms representing the exchange of mass and thermal energy between phases. The counterparts of the spray mass, momentum and heat exchange appear as source terms in the governing equations for the gas phase, Equations 2.1, 2.2, 2.11 and 2.4. The rate of mass, momentum and energy exchange depends on the properties of both the droplet and of the gaseous fluid surrounding the droplet, and the properties of the fluid seen by a given droplet vary over time as the droplet traverses a turbulent flow. The dependence on the droplet source terms on *seen* gas properties is illustrated in the case of droplet evaporation source terms in the following section.

2.2.1 Droplet evaporation

The droplet modelling in this thesis assumes that droplets may be accurately represented by Lagrangian particles, an assumption that is widely made in RANS and DNS simulations of a dispersed liquid phase. The governing equations for the position $\mathbf{x}_d$, velocity $\mathbf{u}_d$, mass m_d and temperature T_d of a droplet are given by the following Lagrangian equations (De and Kim 2013):

$$\frac{d\mathbf{x}_d}{dt} = \mathbf{u}_d \tag{2.74}$$

$$\frac{d\mathbf{u}_d}{dt} = \frac{3}{4}\frac{C_D}{D_d}\frac{\rho_{\text{seen}}}{\rho_d}|\mathbf{u}_{\text{seen},i} - \mathbf{u}_d|(\mathbf{u}_{\text{seen},i} - \mathbf{u}_d) \tag{2.75}$$

$$\frac{dm_d}{dt} = -\pi D_d (\rho D)_{\text{seen}} B_M \text{Sh}_d \tag{2.76}$$

$$\frac{dT_d}{dt} = \frac{\dot{Q}_d + \dot{m}_d L_v}{m_d c_{p,d}} \tag{2.77}$$

Here, $\mathbf{u}_{\text{seen}}$ is the gas phase velocity at the droplet position $\mathbf{x}_d$, ρ_{seen} is the seen gas phase density, ρ_d is the density of the liquid fuel, and C_D is the drag coefficient which is given by the model of Schiller and Naumann (1933) as

$$C_D = \begin{cases} 0.44 & ; \text{Re}_d > 1000 \\ \frac{24}{\text{Re}_d}\left(1 + 0.15\text{Re}_d^{0.687}\right) & ; 0 < \text{Re}_d \leq 1000 \end{cases} \tag{2.78}$$

where Re_d is the droplet Reynolds number defined as

$$\mathrm{Re}_d = \frac{\rho_{\mathrm{seen}} D |\mathbf{u}_{\mathrm{seen}} - \mathbf{u}_d|}{\mu_{\mathrm{seen}}}. \tag{2.79}$$

The diameter of the droplet D_d is determined by its mass m_d, temperature T_d and ρ_d. With the assumption of a spherical droplet, the diameter is calculated as

$$D_d = 2\left(\frac{3m_d}{4\pi\rho_d}\right)^{\frac{1}{3}} \tag{2.80}$$

In Equation 2.77, L_v and $c_{p,d}$ are the latent heat of vaporization and the specific heat of the liquid fuel respectively, and $\dot{Q}_d$ is the convective heat transfer rate at the droplet surface, which is given by

$$\dot{Q}_d = \rho_{\mathrm{seen}} D_d k_{\mathrm{seen}} (T_{\mathrm{seen}} - T_d) \mathrm{Nu}_d. \tag{2.81}$$

where, k_{seen} and T_{seen} are the thermal conductivity and temperature of the surrounding gas phase seen by the particle.

Nu_d and Sh_d present in the above equations are the Nusselt and Sherwood numbers which represent the ratios of convective to conductive transfer of heat and mass respectively. In their present form in the above equations, they represent the aforementioned ratios for a stationary droplet. In the presence of a mean flow, the enhancement of convective transfer must be accounted for through modification of these numbers. The convective Nusselt, Nu_d^c, and Sherwood, Sh_d^c, numbers are given by the empirical correlations (Sazhin 2006)

$$\mathrm{Nu}_d^c = (2 + 0.6{\mathrm{Re}_d}^{1/2}{\mathrm{Pr}_d}^{1/3}) \tag{2.82}$$

$$\mathrm{Sh}_d^c = (2 + 0.6{\mathrm{Re}_d}^{1/2}{\mathrm{Sc}_d}^{1/3}) \tag{2.83}$$

$$\mathrm{Pr}_d = \frac{\mu_{\mathrm{film}} c_{p,\mathrm{film}}}{\lambda_{\mathrm{film}}} \tag{2.84}$$

$$\mathrm{Sc}_d = \frac{\mu_{\mathrm{film}}}{(\rho D)_{\mathrm{film}}} \tag{2.85}$$

Here, Pr_d and Sc_d are the Prandtl and Schmidt numbers. The subscript film denotes thermophysical properties of the vapour film or boundary layer surrounding the droplet, which are evaluated using the one-third rule (Sparrow and Gregg 1958):

$$T_{\mathrm{ref}} = T_{\mathrm{surf}} + \frac{1}{3}(T_{\mathrm{seen}} - T_{\mathrm{surf}}) \tag{2.86}$$

$$Y_{f,\mathrm{ref}} = Y_{f,\mathrm{surf}} + \frac{1}{3}(Y_{f,\mathrm{seen}} - Y_{f,\mathrm{surf}}). \tag{2.87}$$

where Y_f is the fuel mass fraction and the surface fuel mass fraction $Y_{f,\mathrm{surf}}$ is calculated via the Clausius–Clapeyron rule. In this droplet formulation, infinite thermal conductivity is assumed and as a consequence, the entire droplet has a uniform temperature. Therefore, the surface temperature T_{surf} is assumed equal to the droplet temperature T_d.

In cases where there is strong evaporation, advection of the evaporated fuel away from the droplet surface that is generated by the bulk motion of this vapour must be accounted for in some manner. This phenomena is known as Stefan flow. Similar to convective effects, the effects of Stefan flow are accounted for through additional modification of the Sherwood and Nusselt numbers (Sazhin 2006)

$$\mathrm{Nu}_d^s = \mathrm{Nu}_d^c \frac{\log(1 + B_T)}{B_T} \tag{2.88}$$

$$\mathrm{Sh}_d^s = \mathrm{Sh}_d^c \frac{\log(1 + B_M)}{B_M} \tag{2.89}$$

$$\tag{2.90}$$

in which B_M and B_T are the Spalding mass and heat transfer numbers (Spalding 1953).

2.2.2 Droplet Boiling

For a droplet temperature lower than the boiling point of the fuel at a given pressure, a droplet in hot surroundings will experience heat transfer from the surrounding gas raising its temperature. The total amount of fuel evaporated from the droplet surface will depend on how quickly the vapour is carried away from the surface. If the vapour remains at the surface, the film surrounding the droplet will saturate, and evaporation will cease. Therefore, the evaporation of a non-boiling droplet is limited by mass transfer to the gas phase. When the droplet reaches its boiling temperature, the liquid is rapidly converted to vapour, and the surrounding vapour film quickly becomes saturated. In order to sustain boiling (and evaporation) the temperature of the droplet must remain above its boiling temperature and sufficient heat must continue to be supplied though the film to the droplet. Therefore, in the case of boiling droplets, the evaporation of liquid fuel is governed by heat transfer.

In some cases we may wish to look at the steady state evaporation of the droplet, in order to simplify analysis by removing the dependence on droplet temperature. To do this, we may look at the steady-state boiling of a single component fuel droplet. Chin and Lefebvre (1983) model the evaporation rate $\dot{m}_d$ of a boiling droplet as

$$\dot{m}_d = -\frac{\pi}{4} \rho_d D_d \lambda_{st} \tag{2.91}$$

where $\dot{m}_d$ is dependent on the the droplet liquid density ρ_d, the droplet diameter D_d, and a steady-state evaporation parameter λ_{st}, which is dependent both the droplet properties and on the seen properties of the surrounding flow. The liquid density is approximately constant for a given fuel, therefore the droplet property with the main influence on the evaporation rate is the diameter D_d. Chin and Lefebvre (1983) then model the steady-state evaporation parameter λ_{st} for a boiling droplet as

$$\lambda_{st} = \frac{8\log(1 + B_T)}{\rho_d \frac{c_{p,\text{film}}}{k_{\text{film}}}} \tag{2.92}$$

where $c_{p,\text{film}}$ and k_{film} are vapour film values of heat capacity and thermal conductivity.

Since it is assumed that the droplet is at the boiling temperature T_b, B_T is given by Spalding (1953),

$$B_T = \frac{c_{p,\text{film}}(T_{\text{seen}} - T_b)}{L_v} \tag{2.93}$$

where T_b is the boiling temperature of the liquid, and T_{seen} is the far-field temperature seen by the droplet. This is based on a gas-phase Prandtl number Pr which is representative of the fluid properties in the boundary layer surrounding the droplet, where ρ_{seen} and μ_{seen} represent instantaneous values of gas-phase density and viscosity outside the droplet boundary layer and hence depend on the seen composition.

In this thesis, the full set of Lagrangian equations Equations 2.74-2.77 will be used for CFD simulations of sprays, but *a-priori* analysis of the effect of stochastic fluctuations of seen quantities on the evaporation rate will be studied directly through the effect on the steady-state evaporation parameter given in Equation 2.92.

2.2.3 Droplets' seen properties

In turbulent combustion the seen properties, such as the seen velocity and temperature, fluctuate over time due to turbulent convection, the influence of flames, and the proximity of other droplets. In Reynolds Averaged and Large Eddy Simulation (RANS and LES) approaches, droplet-scale processes are not resolved and any effects of fluctuations of the seen properties on evaporation should be modelled.

Therefore the evaporation rate of a boiling droplet depends on the instantaneous values of the gas-phase properties seen by a given droplet, in addition to the droplet's own properties. Furthermore, the evaporation rate has a non-linear dependence on these properties, implying that the effects of gas-phase property fluctuations in a turbulent flow tend not to cancel over a droplet's lifetime.

In the equations presented in Section 2.2.1, the seen velocity $\mathbf{u}_{\text{seen}}$ appears in both the momentum equation (2.75) and in the droplet temperature and mass equations through the Reynolds number (2.79). The seen velocity magnitude for a droplet fluctuates as the droplet traverses turbulent motions. Dukovicz (Dukowicz 1980) proposed modelling for the fluctuating seen velocity vector in the form,

$$\mathbf{u}_{\text{seen}} = \overline{\mathbf{u}}(\mathbf{x}_d) + \mathbf{u}' \tag{2.94}$$

where $\overline{\mathbf{u}}(\mathbf{x}_d)$ is the mean gas phase velocity at the droplet location $\mathbf{x}_p$. The second term, $\mathbf{u}'$, represents turbulent fluctuations. Noting that the velocity fluctuations in homogeneous isotropic turbulence decay towards a Gaussian distribution (Pope 2000), Dukowicz (1980) modelled the instantaneous velocity components of $\mathbf{u}'$ as Gaussian random variables with zero mean and with variance given by

$$\sigma^2_{u'} = \frac{2}{3}k(x_p) \tag{2.95}$$

where k is the turbulent kinetic energy at the particle position. The Dukovicz model, or similar Gaussian dispersion models, are implemented in many widely used Computational Fluid Dynamics codes.

Modelling for the effect of composition and temperature fluctuations on the evaporation rate is less common, even though their effect on the evaporation rate may be greater than the effect of velocity fluctuations (De, Lakshmisha, et al. 2011). Bilger (Bilger 2011) developed a mixture fraction framework for modelling of spray combustion which is able to take account of temperature and composition fluctuations associated with mixture fraction fluctuations. Mixture fraction is a conserved scalar, bounded by zero and unity, which represents the local fraction of fluid mass which originated from the fuel stream (Peters 2000). Bilger's approach has been tested in turbulent spray flames by De *et al.* (De, Lakshmisha, et al. 2011; De and H. 2013), showing that mixture fraction fluctuations have a significant influence on the overall turbulent flame properties. The mixture fraction fluctuations are simulated by sampling new values of mixture fraction from a presumed beta distribution (Libby and Williams 2000). The approach of De *et al.* (De, Lakshmisha, et al. 2011) carries an implicit assumption that mixture fraction and velocity fluctuations are independent. In general the velocity and mixture fraction will not be independent. Indeed the mixture fraction-velocity covariance (i.e. the turbulent flux of mixture fraction) are more commonly modelled using a linear gradient approximation (Poinsot and Veynante 2005),

$$\widetilde{u_i'' Z''} = -D_t \frac{\partial \widetilde{Z}}{\partial x} \tag{2.96}$$

where D_t is a turbulent or sub-grid-scale diffusivity (Peters 2000) — indicating that the correlation is likely to be non-zero in the presence of mean mixture fraction gradients. The correlation of the seen mixture fraction and velocity arises naturally in transported-pdf simulations, provided that the seen mixture fraction and velocity are included in the joint-pdf, for example Liu *et al.* (Z. Liu et al. 2002), however the author is not aware of prior spray combustion modelling which accounts for this correlation by sampling the seen mixture fraction and velocity from a presumed bivariate-pdf.

This thesis will develop modelling for seen quantities that is compatible with the lookup table approach for combustion modelling. Once an appropriate presumed joint pdf has been chosen, the seen reference quantities will be sampled from this presumed distribution. Specifically, in the case of the joint mixture fraction–velocity presumed pdf, samples of $\mathbf{u}_{\text{seen}}$ and Z_{seen} will be generated; in the case of a joint progress variable–mixture fraction presumed pdf, samples of c_{seen} and Z_{seen} will be generated. In each of these cases, the sampled values of the reference quantities c_{seen} and Z_{seen} will be used to determine the seen quantities used in the evaporation model, such as T_{seen} and $Y_{f,\text{seen}}$. (The seen velocity $\mathbf{u}_{\text{seen}}$ is not a reference quantity and the samples are therefore used directly.)

2.3 The presumed pdf approach

The RANS modelling approach considers transport equations for ensemble statistics of the flow properties, such as velocity, enthalpy and composition. Turbulent reacting flows exhibit irregular unsteady fluctuations of composition and temperature around their ensemble average values. The reaction rates in combustion and evaporation rates in sprays depend on composition and temperature in a non-linear way. In particular, the Arrhenius equation indicates that reaction rate constants typically exhibit an exponential dependence on the temperature,

$$k = Ae^{-E_a/R_u T} \tag{2.97}$$

where A is a pre-exponential factor, E_a is the molar activation energy and R_u is the Universal Gas Constant. This implies that the ensemble averaged reaction rate constant is not necessarily well modelled as a function of the ensemble averaged temperature:

$$\overline{Ae^{(-E_a/R_u T)}} \neq Ae^{(-E_a/R_u \overline{T})}. \tag{2.98}$$

The statistics of the gas-phase properties at one point in the flow are fully described by their joint one-point pdf $P(\boldsymbol{\psi})$, where $\boldsymbol{\psi}$ is the vector of sample space variables for the gas-phase properties. Knowledge of the one-point joint-pdf of the relevant gas-phase properties, in addition to algebraic expressions for the elementary reaction rates, provides a closure for the ensemble-averaged reaction rates appearing in the Reynolds-averaged species equations. For example, the ensemble-averaged reaction rate constants can be evaluated by considering the probability-weighted contributions from all the different temperatures in the turbulent flow,

$$\overline{Ae^{(-E_a/R_u T)}} = \int Ae^{(-E_a/R_u \tau)} P_T(\tau) d\tau. \tag{2.99}$$

where $P_T(\tau)$ is the marginal pdf of temperature and τ is sample space variable for temperature.

Two approaches for obtaining the joint-pdf of gas-phase properties are employed in the context of RANS modelling: first the joint-pdf may be modelled and simulated through the transported-pdf approach (Pope 2000) or, second, the shape of the pdf may be *presumed* in a manner that is consistent with a set of moments of the pdf (Veynante and Vervisch 2002). Modelling or simulation of the full joint-pdf of composition, temperature, and potentially also velocity is challenging due to its high dimensionality (i.e. one dimension for each fluid property). Fortunately, the compositions observed in turbulent combusting flows tend to lie close to a relatively low-dimensional manifold (Pope 2013) on account of relatively short time scales of many chemical processes, and this observation motivates attempts to relate the full joint-pdf of gas-phase properties to the joint-pdf of a set of reference variables. The presumed-pdf approach is compatible with several turbulent combustion modelling approaches such as flamelet methods (Peters 2000) and conditional moment closure methods (Klimenko and Bilger 1999). In its general form, the presumed-pdf approach is extremely powerful and in certain turbulent combustion applications the presumed-pdf approach achieves acceptable predictions with only a single well-chosen reference variable. Presumed-pdf modelling is adopted as the general modelling approach pursued in this thesis. This section proceeds by introducing reference variables that can describe the thermochemical state in non-premixed, premixed, and autoigniting flows; presenting transport equations for moments of these reference variables; and flamelet approaches for mapping between the thermochemical state and the reference variables.

2.4 Summary

The modelling approach taken in this thesis to predict mean quantities of interest may be summarised as follows. First, Favre averaged transport equations (Section 2.1.3) for the statistical moments of appropriate reference variables are solved. The connection between instantaneous reference variables and instantaneous quantities of interest is given via a laminar flamelet table (Section 2.1.4.5). The unresolved distribution of reference variables is modelled using a presumed pdf (Section 2.3), based on the transported moments. The flamelet table is then applied to this modelled distribution of reference variables, to calculate mean quantities of interest. In the case of turbulent combusting sprays, the spray is solved using a Lagrangian approach (Section 2.2.1) and the distribution of seen reference variables is modelled using the same presumed pdf as the gas phase. Individual realisations of the seen quantities are sampled from the presumed pdf on an appropriate timescale. Seen quantities such as fuel mass fraction and gas phase temperature are then obtained from the laminar flamelet as functions of the seen reference variables. Further details on this sampling process will be given in Chapter 3, which elaborates on the modelling of the presumed pdf.

Chapter 3

Modelling joint-probability density functions

Due to restrictions in computational cost, it is not possible to solve the fully resolved set of instantaneous equations for momentum, mass conservation, and thermochemical transport in a reasonable time-frame. Therefore, in industrial contexts, turbulent reacting flows are only partially resolved and the physical phenomena in the unresolved scales is modelled. Since the unresolved chemical state is not available, it must be modelled. Due to the statistical nature of turbulent flows, one potential approach to this problem is modelling of the distribution of unresolved quantities. This is referred to generally as pdf modelling. Once a model for the distribution is chosen (for example, transported pdf or presumed pdf), the effect on mean reaction rates or evaporation may be determined. For mean reaction rates, this takes the form of integration of conditional thermochemical properties $\phi(\psi)$ together with the pdf $p(\psi)$:

$$\overline{\phi} = \int_{-\infty}^{\infty} \phi(\psi)p(\psi)d\psi \tag{3.1}$$

For the case of a stochastic evaporation model, the seen thermochemical quantities $\phi_{\text{seen}}(\psi)$ are determined from samples of the reference variables ψ_i which are drawn from the pdf:

$$\psi_i \sim p(\psi) \tag{3.2}$$

This chapter will introduce the relevant nomenclature and theoretical background on random variables and stochastic processes that will be used to formulate the stochastic evaporation model based on a presumed pdf model.

The irregular and seemingly random nature of the fluctuations in turbulent reacting flows lends itself to a statistical description of the fluid state in terms of probability density functions (pdfs). The pdf may be used either in order to evaluate statistical moments such as means, by integration of relevant state variables such as reaction rates over the domain of the pdf or, in stochastic models, in order to sample individual states from the pdf.

The pdf of fluid properties in a turbulent reacting flow may evolve in both time and space, and it becomes necessary to model the evolution of the pdf in some way. Two main approaches may be distinguished: (1) transported-pdf methods involving integration of the equation governing the transport of the pdf; and (2) presumed-pdf methods involving integration of transport equations for moments of the pdf along with sufficient assumptions about the form of the distribution in order to evaluate a pdf that is consistent with the transported moments.

The first method involving transport of a joint-pdf equation presents numerical challenges. The number of dimensions in the pdf is equal to the number of properties whose distribution it describes. In a simple Cartesian discretisation of the Eulerian joint-pdf transport equation, the number of grid points required to represent state-space would increase exponentially with the number of properties. Since the numbers of properties needed to characterise either turbulent evaporating sprays or chemically-reacting turbulent flow fully are typically large, the evolution of the pdf transport equation is usually simulated in a Lagrangian manner using stochastic differential equations. In order to introduce the modelling of turbulent sprays developed in this thesis that involves the use of stochastic processes, this Chapter starts by introducing necessary mathematics of stochastic processes and stochastic differential equations.

The second method involving presumed pdfs relies upon assumptions about the form of the pdf that provide a reasonably close approximation to the physical behaviour of the actual pdf. This requires both an adequate description for the distribution of the individual properties or reference variables used to describe the fluid state, and for the statistical dependence between these parameters. This Chapter discusses how univariate-pdfs may be presumed both for individual reference variables introduced in Chapter 2 (mixture fraction, progress variable, residence time parameters, and dissipation rate), and how multi-variate pdfs may be constructed in order to account for their dependence. The Chapter concludes with a summary of how presumed-pdfs and stochastic processes will be used in turbulent spray combustion modelling in this thesis.

3.1 Background

This section outlines the mathematical background for the discussion joint probability density functions, by introducing concepts such as random variables, joint distributions, statistical moments and marginal distributions. These concepts will be referenced in Section 3.2 when the notion of presumed probability density functions is introduced.

3.1.1 Random variables and vectors

A random variable is a mathematical object which consists of a set S of possible values together with a probability density function $f(x)$, $x \in S$ describing the probability of each value (Kampen 1992). This definition is general enough to encompass both discrete and continuous random variables, where the set S is naturally a discrete or continuous set, respectively. The probability density function (pdf) $f(x)$ associated with such a random variable may be defined as having the property

$$\Pr[x \leq X \leq x + dx] = f(x)dx \tag{3.3}$$

where dx is a small increment and $\Pr[Q]$ denotes the probability of event Q. This is the probability that the value will lie in the range $[x, x + dx]$. Similarly, the probability X taking a value lying below a given point determines the cumulative density function (cdf) of the distribution, denoted F:

$$\Pr[X \leq x] = F(x) \tag{3.4}$$

We have that $dF/dx = f(x)$. From the cdf we may define the moments of a probability distribution. The nth *raw moment* of X is given by

$$\overline{X^n} = \int_S x^n dF(x) \tag{3.5}$$

Note that expressing the moments as Riemann-Stieltjes integrals avoids a restriction to continuous distributions. The first raw moment of a random variable is its mean or expected value:

$$\overline{X} = \int_S x dF(x) \tag{3.6}$$

We may also define the *central moments* of the distribution, of which the second ($n = 2$) is the variance:

$$\overline{\left(X - \overline{X}\right)^n} = \int_S \left(x - \overline{X}\right)^n dF(x) \tag{3.7}$$

The idea of a random variable may be extended to include multiple components in a random vector $(X_1, \ldots, X_r)$ where the components are random variables governed by a joint probability distribution and hence may include some dependence between components. In this case the moments are defined element-wise and are themselves vector quantities.

3.1.2 Types of pdf

The *marginal probability* of a subset of random variables $(X_1, \ldots, X_s)$ where $s < r$ is found by integrating over the variables $X_{s+1}, \ldots, X_r$ as per

$$f(x_1, \ldots, x_s) = \int f(x_1, \ldots, x_r) dx_{s+1} \ldots dx_r \tag{3.8}$$

Here we have assumed that the cdf is well behaved.

The *conditional probability* $f(x_1, \ldots, x_s | x_{s+1}, \ldots, x_r)$ of a subset of the random variables $(X_1, \ldots, X_s)$ is the new probability distribution produced when a subset $(X_{s+1}, \ldots, X_r)$ are assigned specific values $(x_{s+1}, \ldots, x_r)$. For a simple joint-pdf of variables X and Y, this is written

$$f(X = x | Y = y) = \frac{f(x, y)}{f_Y(x)} \tag{3.9}$$

where $f_Y(x)$ denotes the marginal probability of f over Y. For a general pdf this becomes the following relationship between marginal and conditional probability distributions:

$$f(x_1, \ldots, x_r) = f(x_{s+1}, \ldots, x_r) f(x_1, \ldots, x_s \mid x_{s+1}, \ldots, x_r) \tag{3.10}$$

i.e. the full pdf is recovered by multiplying the conditional probability (the probability of observing the values $x_1, \ldots, x_s$) with the marginal pdf of $X_{s+1}, \ldots, X_r$ (the pdf given the values $x_1, \ldots, x_s$).

A substantial simplification arises in the special case where subsets of random variables $(X_1, \ldots, X_s)$ and $(X_{s+1}, \ldots, X_r)$ are *statistically independent*. In this instance the joint-pdf for all r variables is given by the product of the marginal pdfs,

$$f(x_1, \ldots, x_r) = f(x_{s+1}, \ldots, x_r) f(x_1, \ldots, x_s) \tag{3.11}$$

Density-weighted pdfs

The (thermodynamic) *density-weighted* pdf, or *Favre* pdf, is used in combustion modelling due to the large temperature and density variations in the flow (Yun et al. 2005). The Favre pdf (Bilger 1975) is given by

$$\tilde{p}(\boldsymbol{\psi}) = \frac{\rho(\boldsymbol{\psi}) p(\boldsymbol{\psi})}{\overline{\rho}} \tag{3.12}$$

where $p(\boldsymbol{\psi})$ is the unweighted pdf and $\boldsymbol{\psi}$ is the sample space vector. Reynolds and Favre averages can then be evaluated from,

$$\overline{\phi} = \overline{\rho} \int \frac{\phi(\boldsymbol{\psi})}{\rho(\boldsymbol{\psi})} \tilde{p}(\boldsymbol{\psi}) d\boldsymbol{\psi} \tag{3.13}$$

$$\tilde{\phi} = \int \phi(\psi) \tilde{p}(\psi) d\boldsymbol{\psi} \tag{3.14}$$

and the mean density may be recovered via

$$\frac{1}{\overline{\rho}} = \int \frac{\tilde{p}(\boldsymbol{\psi})}{\rho(\boldsymbol{\psi})} d\boldsymbol{\psi} \tag{3.15}$$

When transporting and tabulating Favre averaged quantities it is convenient to work with the Favre averaged pdf $\tilde{p}$.

3.2 Presumed probability density functions

The use of presumed pdfs underpins a number of distinct turbulent combustion modelling approaches, including flamelet (Peters 1984b) and conditional moment closure (Klimenko and Bilger 1999) approaches. In simpler cases, one reference variable may provide adequate predictions – usually mixture fraction in the case of non-premixed combustion and progress-variable in the case of perfectly-premixed combustion. This section starts by introducing approaches that have been used to model the marginal pdfs of the main reference variables used in combustion modelling. This section then proceeds to deal with modelling of joint-pdfs for more complex cases where more than one reference variable may be needed.

3.2.1 Marginal distributions of reference variables

This thesis focusses on partially premixed combustion, and hence places emphasis on the modelling of the joint mixture fraction – progress variable distribution. Due to the simplicity of assuming independence between the two, there is extensive literature on the marginal distributions of each, and this will be discussed below. Additionally, in both diffusion flame and premixed flame structures the scalar dissipation rate is an important parameter and hence it too is discussed. Finally, a summary of literature on marginal distributions for residence time based parameters is presented, since the development of new residence time based reference variables is also a focus of this thesis. The fact that each reference variable represents a distinct physical quantity represented by each reference variable requires that each be

3.2.1.1 Mixture fraction distribution

In presumed-pdf modelling for combustion applications, the mixture fraction pdf $p(\eta)$ is most commonly presumed based on its mean $\widetilde{Z}$ and variance $\widetilde{Z''^2}$ using the beta distribution (Poinsot and Veynante 2005),

$$\begin{aligned}
\tilde{p}(\eta) &= \frac{\eta^{\alpha-1}(1-\eta)^{\beta-1}}{B(\alpha,\beta)} \\
B &\equiv \int_0^1 \eta^{\alpha-1}(1-\eta)^{\beta-1} d\eta \\
\alpha &= \widetilde{Z}\left(\widetilde{Z}\frac{1-\widetilde{Z}}{\widetilde{Z''^2}}-1\right); \beta = \alpha\frac{1-\widetilde{Z}}{\widetilde{Z}}.
\end{aligned} \tag{3.16}$$

$\widetilde{Z}$ is positive and $\widetilde{Z''^2}$ lies in the range $0 \leq \widetilde{Z}(1-\widetilde{Z}) \leq 1$. Prediction of the pdf of conserved scalar variables is still an active subject of research.

The beta distribution provides a poor representation of the bimodal pdf shapes that arise towards the edges of free shear flows due to external intermittency. Gampert *et al.* (Gampert et al. 2013) achieve excellent agreement with the mixture fraction pdf throughout a turbulent round jet using a hybrid model that combines the beta distribution with a model for the mixture distribution in the viscous layer at the turbulent/non-turbulent interface. In the context of conditional moment closure modelling, Wright *et al.* (Wright et al. 2005) switch between a beta distribution and a clipped Gaussian pdf in order to account for instances of high variance, however this approach appears to be motivated by difficulties with the numerical implementation of the beta distribution-based approach rather than any physical validation of the clipped Gaussian pdf.

Mortensen analyses the relationship between presumed pdfs that enforce an arbitrary number of moments and conditional scalar dissipation rates (Mortensen 2005) and sets out a methodology for achieving consistency between their modelling, but without showing that general presumed pdfs ensure realisable (i.e. positive) conditional dissipation rates. However the beta distribution does correspond to positive conditional scalar dissipation rates in the results presented. With Andersson (Mortensen and Andersson 2006), Mortensen went on to present a *presumed mapping function* approach that relates mixing to a Gaussian reference field, and implies a presumed pdf that performs well in comparison to the beta distribution when considering single scalar mixing in DNS. The presumed mapping function approach also provides advantages in that it allows derivation of consistent conditional statistics models needed, for example, in conditional moment closure modelling.

Evaporation of a liquid fuel spray also affects the form of the mixture fraction pdf. One of the main observations (Demoulin and Borghi 2000; Réveillon and Vervisch 2000; Duret et al. 2012) is that the peak mixture fraction in a spray-fuelled mixture fraction pdf can be substantially less than unity. The maximum value is generally less than the saturation concentration, because the fuel mixes rapidly to a much lower concentration by the time it leaves the droplet boundary layer. Hollmann and Gutheil (Hollmann and Gutheil 1996) extended the beta-pdf model for spray evaporation by scaling the presumed pdf between the mixture fraction limits found in the spray, specifically the oxidizer conditions and the saturation conditions of the fuel. Since the saturation mixture fraction depends on temperature at the liquid-gas interface, and because this temperature can be different on every droplet in the flow, and it is not defined in regions of the flow where there are no droplets, it is not straightforward to apply the scaled beta distribution model. Demoulin and Borghi (Demoulin and Borghi 2000) present a transport equation for the saturation mixture fraction which does not account for the variation between droplets but does give a representative value for the saturation conditions in a cell. In analysis of their resolved spray DNS, Duret *et al.* (Duret et al. 2012) found that the beta distribution model (effectively in its scaled form) performs badly for dense sprays. It is also unclear how this model should be applied in the context of multi-component evaporation, because the value of mixture fraction does not distinguish the range of compositions which are evaporated during the droplet lifetime.

The difficulty of formulating a generally applicable algebraic model for the mixture fraction pdf and corresponding models for its moment equations motivates the use of numerical models, such as the transported-pdf approach, for the mixture fraction pdf of the mixture fraction, or other reference variables. For example, Ge and Gutheil (Ge and Gutheil 2008) used particle-based Monte Carlo integration for the transport of the mixture fraction pdf in a spray-fuelled flow, relying upon the interaction by exchange with the mean mixing model to account for molecular diffusion in the fluid. The transported-pdf gives similar results to the rescaled beta pdf in that spray combustion case. It must be appreciated that the transported-pdf approach itself relies upon models for conditional diffusion fluxes (also described as micromixing effects) and conditional evaporation rates, and the established models such as the exchange with the mean mixing model and evaporation to the mean composition used by Ge and Gutheil (Ge and Gutheil 2008) have clear deficiencies in terms of their ability to represent that actual physics of turublent mixing and spray evaporation, some aspects of which are discussed in Ref. (Subramaniam and Pope 1998).

In principle, realistic pdfs could be sampled from experimental measurements and DNS, however if such data are available then RANS or LES modelling itself becomes redundant. In its stead, the Linear Eddy Model (LEM) (Kerstein 1988; Kerstein 1991) is a numerical simulation approach for idealised turbulent flow from which it is possible to sample probability density functions for use in other presumed-pdf simulations. Indeed, although the solution approach is quite different from the conventional particle-based Monte Carlo solution methods, the LEM is itself a form of closure for the transported-pdf in which information concerning spatial profiles is included (Pope 2013). The LEM approach considers a line passing through a turbulent flow, with full resolution of all turbulence and scalar length scales, and represents the effects of turbulent mixing on the scalar profile by stochastic application of multi-scale rearrangements of the one-dimensional solution using so-called triplet mappings. The LEM can be used to sample pdfs by performing many simulations for various input parameters and parametrising the resultant pdfs based on a finite set of their lower moments (Goldin 1996; Goldin and Menon 1997)). The initial distribution is taken as double-delta (half fuel, half oxidiser in a slab configuration) thus making the model applicable to non-premixed combustion. Goldin and Menon (Goldin 1996; Goldin and Menon 1998) show an improvement over algebraic presumed-pdfs in comparison to experimental-pdfs when using a joint mixture fraction-progress variable LEM distribution.

There is currently no consensus concerning what constitutes an acceptable model for the mixture fraction pdf, since the accuracy of the pdf models, and the sensitivity of the overall combustion predictions to the pdf models depends on the application. There is also a trade off in terms of complexity and cost of execution versus the accuracy. In particular, it is generally convenient to use a mixture fraction pdf model that can be expressed algebraically, rather than as a discretised numerical solution, especially since this facilitates the construction of some forms of joint-pdf, as discussed later in this section. Due to its ubiquity in combustion modelling and its simple algebraic formulation, the beta distribution is adopted as the default model for mixture fraction pdf in this thesis. In order to test the sensitivity to the shape presumed for the mixture fraction pdf in subsequent chapters, the simpler top-hat distribution (Borghi and Moreau 1977) is used as a comparison.

3.2.1.2 Progress variable distribution

General modelling of reactive scalar pdfs is more challenging than for censored scalars because, in addition to all of the factors influencing the pdfs of conserved scalars, chemical reaction also contributes various effects, depending on the combustion regime. In the distributed combustion regime, the form of the progress variable pdf may resemble that of a passive scalar, whereas in the flamelet regime the flame fronts containing intermediate progress variables become relatively thin, yielding bi-modal progress variable pdfs containing high probabilities only for burnt and/or unburnt compositions. Bray *et al.* (Bray, Champion, et al. 2006) assess three presumed pdf models through comparison with DNS data representative of combustion in the flamelet regime: a beta distribution; a twin δ-function pdf; and a pdf based on unstrained laminar flame profiles. In this comparison, the flamelet-based pdf performs best since it contains information about the expected physical form of the flame structure that is absent in the other models, however one may anticipate that the relative performance of the beta distribution would improve moving towards a distributed combustion regime.

In turbulent combustion dominated by autoignition it is important to model the evolution of the progress variable in the pre-ignition region, in which there is no flame at all. In this situation the twin δ-function pdf or the flamelet-based pdf models appear entirely inappropriate and beta distribution (Cha and Pitsch 2002) or even single-δ function pdfs (Knudsen, Richardson, Chen, et al. 2011; Ihme, Cha, et al. 2005) have been used.

The progress variable presumed-pdf approaches discussed so far rely upon some form of information about the form of the pdf a priori. The maximum entropy pdf, or the statistically most likely distribution (SMLD) (Pope 1979) is defined in a way that approximates the true distribution from a reduced set of known (or assumed) higher moments subject to the constraint that the resulting PDF, denoted by $p_{\mathrm{SMLD},i}$, contains a minimum of statistical information. Here, the subscript i indicates the number of enforced moments. The SMLD produces a PDF of the following form:

$$\widetilde{p}_{\mathrm{SMLD},i}(\psi) = Q(\psi)\exp\left\{\sum_{j=0}^{i} a_j \psi^j\right\} \tag{3.17}$$

where there are i moments available and $\mathbf{a}$ is a vector of Lagrangian multipliers. The corresponding Lagrangian constraints are

$$\begin{aligned}\int_{\psi} \widetilde{p}_{\mathrm{SMLD},i}(\psi)d\psi &= 1\\ \int_{\psi} \psi\widetilde{p}_{\mathrm{SMLD},i}(\psi)d\psi &= \widetilde{\psi}\\ \int_{\psi} (\psi-\widetilde{\psi})^j\widetilde{p}_{\mathrm{SMLD},i}(\psi)d\psi &= \widetilde{(\psi-\widetilde{\psi})^j}.\end{aligned}$$

The main draw back of the SMLD in comparison to other algebraic presumed pdf models is the need for a non-linear root solve to find the coefficients in Eq. 3.17.

Ihme and Pitsch (Ihme and Pitsch 2008a; Ihme and Pitsch 2008b) use a SMLD for the conditional progress variable pdf and conclude that use of more than two moments is required in order to achieve adequate performance in cases where there is a lot of local extinction and re-ignition, and similarly more than two moments are required in order to model the mixture fraction distribution in free shear flows.

Given the additional challenges of modelling the progress variable pdf compared to conserved scalars, the Linear Eddy Model is also a candidate for modelling of the progress variable, and has proven successful in work by Tsui and Bushe (Tsui and Bushe 2014).

3.2.1.3 Dissipation rate distribution

It is well established that the correct functional form for the scalar dissipation rate pdf for passive scalars is log-normal (Lentini 1994; Liew et al. 1984). The scalar dissipation rate distribution for progress variable in flamelet-regime combustion tends to show an additional likelihood of dissipation rates scales on the order of those found in stretched laminar flames.

Models for the mean scalar dissipation rate are presented by Sanders and Gökalp (1998). The simplest model is based on the assumption of proportionality between mechanical mixing and scalar mixing time scales,

$$\chi_T = C_\chi \widetilde{Z''^2} \frac{\tilde{\epsilon}}{\tilde{k}}. \tag{3.18}$$

Swaminathan and co-workers (Swaminathan and Bray 2005; Kolla et al. 2009) have developed algebraic modelling for the mean progress variable dissipation rate that accounts for effects of thermal expansion within the propagating flame fronts. Modelled transport equations for the progress variable dissipation rate have also been developed, as reviewed by Gao *et al.* (Gao et al. 2015).

Construction of the log-normal dissipation rate pdf also requires specification of a second scale parameter σ. Lentini (Lentini 1994) uses $\sigma = 2$, while Liew *et al.* (Liew et al. 1984) developed an algebraic model with geometry dependent coefficients. However the more common approach in the combustion modelling literature is to neglect fluctuations of the dissipation rate entirely and impose a δ-function pdf for the dissipation rate, for example in (Knudsen, Richardson, Chen, et al. 2011).

3.2.1.4 Residence time distribution

The distribution of residence time is widely used in process engineering to characterise the state of fluid exiting a vessel (Levenspiel 1999), and a wide range of distributions may arise depending on the flow configuration, and also depending on the measure of residence time used. There is also a lack of published information concerning the distribution of the residence time at a specific point within a turbulent flow, rather than at the exit of the vessel. Shin *et al.* (Shin et al. 2016) provide one such investigation, demonstrating that certain measures of residence time exhibit statistically stationary and self-similar statistics in turbulent round jets which suggests that presumed-pdf modelling may be applicable, however the probability density functions observed do not correspond to shapes that are readily modelled by any of the common functions used for presumed pdf modelling (e.g. β, δ, Gaussian, top hat, log-normal).

3.2.2 Joint distributions of reference variables

The special case where the reference variables used for combustion modelling are statistically independent leads to a particularly simple model for their joint-pdf, given by the product of the variables' marginal pdfs. Possibly due to the lack of simple models for the statistical interdependence of mixture fraction and progress variable, rather than strong evidence that there is absence of dependence between mixture fraction and progress variable, the assumption that progress variable and mixture fraction are independent is very common in published modelling for partially-premixed flames. The assumption of statistical independence between mixture fraction and normalised progress variable appears to give adequate performance in a number of partially-premixed modelling attempts however Ruan *et al.* (Ruan et al. 2014) show that the statistical interdependence has a substantial influence on modelling around the stabilisation point in lifted flames, which is a situation in which there are strong variations of mixture fraction and progress variable in the same region.

The statistically most likely distribution can be applied to the joint distribution of any number of reference variables. Calculation of the bivariate SMLD based on first and second moments requires evaluation of the roots of six non-linear equations (five moments and the condition that the pdf integrates to unity), as in (Doran 2012).

The most basic representation of the pdf is given by one or more delta functions but unless a large number of delta functions, and hence moments, are used this typically provides a poor model for pdfs that in reality are continuous. The use of delta-functions has found use as a means to achieve a crude modelling of multi-variate distributions (Marchisio et al. 2003; Fox 2003; Raman et al. 2005), and such a representation is the basis of the direct quadrature method of moments (DQMOM) approach.

Although the SMLD provides the maximum entropy for a given set of moments, implying that any other form of pdf imposes incorrect information about higher moments, it is found in practice that the beta distribution distribution performs better as a marginal distribution for mixture fraction, given the first two moments. This is because the higher moments implicit in specification of the beta distribution distribution happen to add some useful information concerning the physical distribution. The simplest extensions of the beta distribution to bivariate distributions is the Dirichlet distribution, involving three parameters, as used by Girmiaji (Girimaji 1991). However three parameters are not sufficient even to enforce the means and variances of the two reference variables. Doran presents a five parameter bi-variate beta distribution distribution that enforces all of the first and second moments (Doran 2012). Since Doran considers mixing in terms of multiple mixture fractions, the proposed bi-variate beta distribution distribution is supported on a domain on which reference variables sum to unity. Whereas the mixture fraction-progress variable distribution is not subject to the same constraint, making the model by Doran unsuitable for describing the mixture fraction-progress variable joint-pdf. Following Cha and Pitsch (Cha and Pitsch 2002), De Paola (Paola 2007) used the beta distribution to model the conditional progress variable pdf conditioned on mixture fraction within the framework of second-order conditional moment closure modelling, in which conditional means and conditional variances of progress variable are both provided. The second-order conditional moment closure approach provides many advantages in general although it is rather specialised and has seen limited uptake, and for this reason the present focus is on pdfs presumed in terms of unconditional moments. Finally, Darbyshire and Swaminathan (Darbyshire and Swaminathan 2012) proposed the use of copulas for combining mixture fraction and progress variable marginal distributions in a manner that imposes a particular co-dependence. Darbyshire and Swaminathan solve transport equations for the mixture fraction, reaction progress variable and their variances, and the covariance $\overline{\rho c'' Z''}$. The marginal pdfs of mixture fraction and progress variable are assumed to be beta-distributed with mean and variances provided by the corresponding transport equations. Together with the transported covariance, these marginal PDFs are used to construct a joint-PDF for mixture fraction and progress variable by using the *Plackett* family of copulas. In general the copula approach has the ability to combine any combination of marginal distributions and to impose a range of different dependence structures, and it is not yet clear that the Plackett copula is the most appropriate structure. Due to these properties, the copula approach is adopted for further investigation in this thesis and details of the copula approach are set out below.

3.2.3 Copulas

3.2.3.1 Mathematical description of copulas

For a bivariate distribution with cumulative density function cdf $P(x, y)$, the marginal distribution functions are defined as

$$P_x(x) = \int_{-\infty}^{\infty} P(x, y) dy \tag{3.19}$$

$$P_y(y) = \int_{-\infty}^{\infty} P(x, y) dx \tag{3.20}$$

The marginal cdf $P_x(x)$ is thus the cumulative probability that the random variable x will take the value ξ, regardless of the value of y. For a given distribution function P, the copula C is defined (Nelsen 1999) such that

$$P(x, y) = C(P_x(x), P_y(y)) \tag{3.21}$$

This illustrates how the copula relates to the joint distribution function, but the restrictions on the form of the copula remain unspecified. The general form is quite broad in scope. By definition (Nelsen 1999), a two-dimensional copula C is a two dimensional function with domain $[0, 1]^2$ and the following properties:

- C is *grounded*:

$$C(u, 0) = C(0, v) = 0 \ \ \forall u, v \in [0, 1] \tag{3.22}$$

- The limits of C reproduce the marginal distributions:

$$C(u,1) = u \text{ and } C(1,v) = v \;\; \forall u, v \in [0,1] \tag{3.23}$$

- C is *two increasing*:

$$\begin{aligned} & C(u_2, v_2) - C(u_2, v_1) - C(u_1, v_2) + C(u_1, v_1) \geq 0 \\ & \forall \{u_1, u_2, v_1, v_2 \in [0,1] : u_2 \geq u_1, v_2 \geq v_1\}. \end{aligned} \tag{3.24}$$

This definition is easily extended to higher dimensional copulas. However, this thesis considers only two dimensional copulas. Essentially, the copula provides a direct connection between the two marginal distribution functions $u = P_x(x)$ and $v = P_y(y)$ (where x and y are the sample space variables of the underlying distribution $P(x,y)$) and the full joint distribution, $P(x,y)$, through Equation 3.21.

In other words, the copula relates the values of the marginal cumulative distribution functions to the joint cumulative distribution function. Such a copula is not uniquely determined for all joint distributions, however its existence is guaranteed by Sklar's theorem (Sklar 1959). When constructing a multivariate PDF from several known marginal PDFs, the choice of copula determines the type of dependence between the random variables. Looking at the underlying copula of a distribution is a convenient way to study the dependence of two parameters without the marginal distributions clouding the issue.

3.2.3.2 Plackett copula

Since the Plackett copula (Plackett 1965) has been used previously in the literature (Darbyshire and Swaminathan 2012), a brief description is given here. The Plackett copula was originally designed to replace bivariate normal distribution for statistical tables. The Plackett family of copulas (Plackett 1965) provide both joint cdf and pdf as algebraic functions of the marginal distributions. The co-dependence between variables is specified by an odds parameter θ. The pdf and cdf of a Plackett copula with given marginal pdfs f and g and marginal cdfs F and G are given by

$$CDF = \begin{cases} \frac{S - \sqrt{S^2 - 4\theta(\theta-1)FG}}{2(\theta-1)} & \theta \neq 1 \\ FG & \theta = 1 \end{cases} \tag{3.25}$$

$$PDF = \begin{cases} \frac{\theta f g \{1 + (\theta-1)[F + G - FG]\}}{[S^2 - 4\theta(\theta-1)FG]^{\frac{3}{2}}} & \theta \neq 1 \\ fg & \theta = 1 \end{cases} \tag{3.26}$$

where θ is the "odds-parameter" which specifies the degree of dependence between the two random variables, and where $S = 1 + (\theta - 1)(F(x) + G(y))$. The relationship

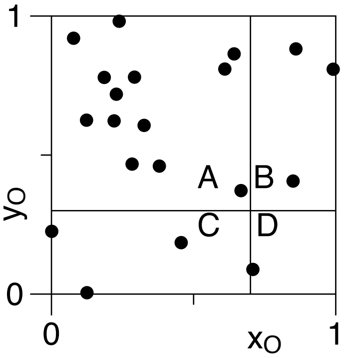

Figure 3.1: Contingency diagram for a set of random samples on $[0,1]^2$. Here, $A = 13$, $B = 3$, $C = 3$ and $D = 1$ (with $x_O = 0.7$ and $y_O = 0.3$) and hence the odds parameter is $\theta = 1.44$.

between the odds parameter and the covariance is discussed in Section 4.4. The odds parameter is defined for a point (x_O, y_O) as the ratio $\theta = AD/BC$, where

$$A = Pr(x < x_O, y > y_O) \tag{3.27}$$

$$B = Pr(x > x_O, y > y_O) \tag{3.28}$$

$$C = Pr(x < x_O, y < y_O) \tag{3.29}$$

$$D = Pr(x > x_O, y < y_O) \tag{3.30}$$

where Pr denotes the probability of an event occurring. This is illustrated in Figure 3.1. Since the choice of (x_O, y_O) is arbitrary, the odds parameter is not uniquely determined by a given bivariate distribution, because different choices of (x_O, y_O) will lead to different values of θ in the general case. The Plackett family of copulas is the set of copulas for which the odds parameter θ is independent of the choice of (x_O, y_O). This restriction is sufficient to uniquely determine the copula. When the data about the distribution to be modelled is presented in the form of a contingency table, the odds parameter is a convenient estimator. However, when the data about the distribution to be modelled is in the form of moments of the distribution, this estimator is less useful as samples must be generated with the desired correlation and then the odds ratio calculated manually. Additionally, this imposes an arbitrary restriction on the structure of the copula, which holds no obvious physical meaning when applied to modelling of the $Z - c$ distribution.

3.2.4 Summary

For presumed pdf modelling in more advanced combustion systems that have multidimensional state space, we need presumed joint pdfs. The available multidimensional pdf models are restrictive and may perform poorly for a limited number of moments, or fail to respect other physical constants. The copula approach is attractive as it can combine arbitrary marginals that respect relevant constraints and that use appropriate numbers of moments. The Plackett copula has been previously applied (Darbyshire and Swaminathan 2012) to the problem of constructing from two marginal distributions a joint distribution with the specified correlation; this correlation may be controlled through the free parameter θ in the Plackett copula's definition and supplied via a transport equation. However, the choice of the Plackett copula to model the dependence between mixture fraction and progress variable imposes a very particular dependence structure on the joint distribution, which is not based on physical reasoning.

The copula approach (that is, using a copula together with two predefined marginal distributions) is an attractive approach to joint pdf modelling for several reasons. Firstly, it may build upon the established literature on marginal distributions and elegantly extend them to the multidimensional case. Secondly, it isolates the dependence structure of the joint distribution and therefore allows development of dependence modelling to proceed disconnected from marginal distribution model development. Finally, it allows the full range of potential distribution structures to be captured. In contrast, the use of existing analytical bivariate or multivariate distributions for modelling the joint distribution is often overly restrictive: the choice of marginal distribution can not be easily changed; the marginal distributions depend on the specified joint distribution are are thus inherently linked; and the realisable dependence structures are usually limited to a small subset of what is possible. It should be noted, however, that the two approaches are mathematically equivalent; any given analytical joint distribution may be separated into its component parts of marginal distributions and copula.

In the following chapter, the numerical implementation of applying a presumed copula in conjunction with two presumed marginal distributions will be discussed, including the application to both calculation of mean quantities and stochastic modelling of seen quantities for fuel droplet evaporation. Then, the separate issue of how appropriate the choice of Plackett copula is for modelling the dependence between mixture fraction and progress variable will be investigated in the following chapters, by analysing data from experiments and DNS simulations of partially premixed flames.

Chapter 4

Numerical details of the copula method

4.1 Introduction

In order to calculate a table of mean values of scalars which depend on the sub-grid distribution of mixture fraction and progress variable, an integration over the joint-pdf must be performed. Here methods are considered for the numerical evaluation of the integral

$$\overline{\phi} = \int \int \phi(\eta, \zeta) p(\eta, \zeta) d\eta d\zeta \tag{4.1}$$

where $\phi = (\eta, \zeta)$ is a scalar, $p(\eta, \zeta)$ is a joint pdf and η and ζ are sample space variables.

In Chapter 3, the mathematical framework for a copula based presumed joint-pdf model was described. However, details of the numerical algorithms for integration and sampling from the resultant joint-pdf were not discussed. There are several subtleties involved in the calculation of the joint-pdfs, and in the integration of the pdf with and without a scalar.

It was noted that the transport equation for $\widetilde{Z''c''}$ can be used to provide a measure of the dependence between c and Z, but how to actually apply this in the presumed pdf was not discussed. Many copulas, particularly the single parameter copulas of interest for this application, take a parameter θ which determines the strength of the dependence. Typically there is no analytical expression for the mapping from $\widetilde{Z''c''}$ to θ.

Additionally, there is the difficulty of using a quantity such as $\widetilde{Z''c''}$ as a tabulation parameter, since (unlike the mean or variance) has no clear upper and lower bounds. It is necessary to establish the upper and lower bounds for $\widetilde{Z''c''}$ in order to ensure that control parameter space covered by the look up table corresponds to realisable pdfs.

The upper bound of the variance is a well known function of the mean:

$$\sigma^2 \leq \mu - \mu^2 \tag{4.2}$$

This is often used as a realisability check for the transport equation for the variance, which due to modelling assumptions and numerical accuracy is does not enforce this limit. The same issue is found with the covariance transport equation; therefore, knowledge of the upper and lower bounds of covariance are required for the equivalent realisability check on the convergence.

In turbulent combustion applications where the integration of a pdf is a requirement, the pdf may be obtained in a variety of different forms. For example, empirical distributions from DNS or experimental results, or via a parametrised analytical function. Such analytical functions may contain singularities which can be difficult for numerical integration schemes to handle. Additionally, sampling from an arbitrary joint distribution poses a difficult problem, and no generally applicable efficient algorithm is available.

In this chapter, a discussion of the above considerations is given, and a full description of the algorithms used in the accurate implementation of these statistical models is presented. A robust, accurate and efficient integration of arbitrary distributions with analytical expressions for the cdf is presented as an alternative to simple integration or advanced quadrature methods. The method for calculating the upper and lower bounds of covariance and the tabulation scheme used are explained. And finally, the issue of mapping a statistical moment such as the covariance to a copula parameter θ is elaborated on and a solution proposed.

4.2 Numerical integration of distribution functions

Liu *et al.* (F. Liu et al. 2002) discuss the “robust and accurate” integration of the beta pdf with respect to gas turbine combustion, using the work of Chen *et al.* (Chen et al. 1994) as a starting point. They consider two problems simultaneously: the correct evaluation of the beta pdf, avoiding floating point underflow; and the integration of the pdf with a scalar, assuming the pdf is known. The present work does not concern the correct calculation of the beta pdf, as this has been discussed in statistical literature (Majumder and Bhattacharjee 1973; Cran et al. 1977) and several robust libraries are available (Lozier and Olver 1994). A summary of the integration method they propose is as follows:

1. The beta distribution integral is split into three parts as

$$\begin{aligned}\int_0^1 \phi(\eta)\eta^{\alpha-1}(1-\eta)^{\beta-1}d\eta = & \int_0^\varepsilon \phi(\eta)\eta^{\alpha-1}(1-\eta)^{\beta-1}d\eta \\ & + \int_\varepsilon^{1-\varepsilon} \phi(\eta)\eta^{\alpha-1}(1-\eta)^{\beta-1}d\eta \\ & + \int_{1-\varepsilon}^1 \phi(\eta)\eta^{\alpha-1}(1-\eta)^{\beta-1}d\eta \qquad (4.3)\end{aligned}$$

   where $\eta^{\alpha-1}(1-\eta)^{\beta-1}/B(\alpha,\beta)$ is the beta pdf (the constant normalisation factor $B(\alpha,\beta)$ has been omitted in the above integrals).

2. The outer integrals, where there are potentially singularities depending on the values of α and β, are replaced with the approximations

$$\int_0^\varepsilon \phi(\eta)\eta^{\alpha-1}(1-\eta)^{\beta-1}d\eta \approx \phi_{ox}\frac{\varepsilon^\alpha}{\alpha} \qquad (4.4)$$

$$\int_{1-\varepsilon}^1 \phi(\eta)\eta^{\alpha-1}(1-\eta)^{\beta-1}d\eta \approx \phi_{fu}\frac{\varepsilon^\beta}{\beta} \qquad (4.5)$$

For two- or higher-dimensional joint-pdfs, particularly if specified by a presumed copula with strong dependence, there may be sharp gradients of the pdf inside the domain which can introduce errors if the integration grid is not appropriately refined around these points. Such points can appear anywhere in the domain.

Even in the 1D case, the two limits of the variance must also be treated specially. In the limit as the variance approaches 0 or $(1-\mu)\mu$, the beta distribution approaches a delta distribution or double delta distribution, respectively. Particularly for the two delta distribution case, there is the problem of estimating the weights of each of the delta distributions in such a way that the integration remains continuous in (α, β) space. When applying alternative marginal pdfs, such as the top-hat pdf considered in this work, the special cases are different and must be implemented separately. For higher dimensional cases, the number of special cases increases with the number of dimensions. Even for a two dimensional case, the use one beta pdf marginal and one top-hat pdf marginal together with a presumed copula is desirable, the number of special cases is huge. Using the pdf based approach, each these cases must be specially handled in a separate code path, complicating the implementation details and expanding the potential for coding errors.

There exist well established, general purpose, well tested quadrature/cubature integration algorithms that can handle singularities in the integrand (see Dooren and Ridder (1976) and Berntsen et al. (1991) for example). In the focus of this work, the integration of a scalar with the pdf is decoupled from the solution of the flow field and therefore the computational cost of this integration is not a major concern. However, if these techniques are to be applied in other contexts where the integration is coupled to the flow field calculation (such as the RIF or CMC models) the computational cost becomes important. For this reason, general purpose quadrature algorithms are avoided in favour of a more efficient algorithm.

The remainder of this section presents a new algorithm for the integration of numerical pdfs. This method depends on the existence of an expression for the cumulative density function for the distribution in question. For most of the presumed pdfs considered in combustion and fluid dynamics (such as the beta, Normal, maximum entropy, and top-hat distributions), these are available. The proposed algorithm has the following desirable properties:

- Applicable to both analytical cdfs and discretely computed distributions (from Lagrangian methods or DNS data)
- Integrates well with the mathematical formulation of copulas
- Easily extendible to N dimensions
- Computation time is predictable and $O(n^N)$, where n is the resolution of state space
- Identically preserves the relation $\int p(\eta)d\eta = 1$
- Does not depend on any parameters such as ε

The 1D implementation is described first, followed by the extension to 2D.

4.2.1 One dimensional case

The simplest approach to this problem of integrating the pdf numerically is to apply the trapezoidal rule of integration. Here, the 1 dimensional case is demonstrated for ease of illustration:

$$\int_a^b f(\eta)d\eta \approx \sum_{i=1}^{n} (\eta_{k+1} - \eta_k)\frac{(f(\eta_{k+1}) - f(\eta_k))}{2} \tag{4.6}$$

where the interval $[a, b]$ is divided up into n equal length segments where the kth segment is $[\eta_k, \eta_{k+1}]$. This is illustrated graphically by the red segment in Figure 4.1.

For the applications listed above, the function will be $f(\eta) = \phi(\eta)p(\eta)$ where $p(\eta)$ is a univariate pdf and $\phi(\eta)$ is an arbitrary scalar. The algorithm for finding the mean of scalar ϕ based on the trapezoidal rule is then to find $p_k = p(\eta_k)$ and $\phi_k = \phi(\eta_k)$ and let

$$\overline{\phi} \approx \sum_{k=1}^{n} (\eta_{k+1} - \eta_k)\frac{(f(\eta_{k+1}) - f(\eta_k))}{2} \tag{4.7}$$

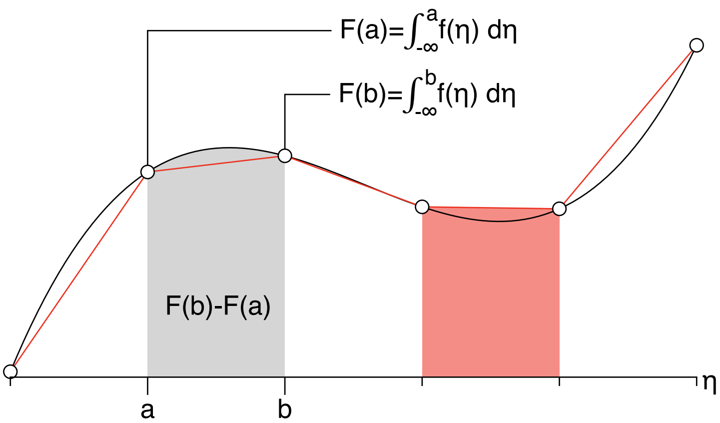

Figure 4.1: Equivalence of integration of pdf over interval and difference in cdf

However, the accuracy of this approach depends on the behaviour of the function $f(\eta)$. Since the marginal distributions in consideration can potentially contain singularities, this causes several problems for the trapezoidal rule:

- It is impossible to make use of the value of the pdf at the singularity in the trapezoidal rule, because it is undefined.
- Avoiding this problem might be attempted by taking a value close to the singularly point but not actually on it. However, the value of the pdf sampled there will vary rapidly depending on how exactly how close.
- Furthermore, the high value of the pdf "close" to the singularity will then be applied by the trapezoidal rule to the whole interval, resulting in a large integration error.
- These errors will be high enough that the after generation of the discretised pdf, the integration of this pdf will not be 1. This problem is usually solved by normalising the pdf by dividing by its own numerical integral, producing a new "pdf" which integrates to 1. However, now the error from the boundaries has been spread throughout the entire discretised pdf.

Note that all of the scalars of relevance in practice come from laminar flamelet calculations and are well behaved near the boundaries. The difficulties stem from the evaluation of the pdf p. To avoid these problems, rather than integrating the pdf directly, the cdf $P(\eta)$ is employed to find an approximation. The cdf has a number of desirable properties for this purpose:

- It is monotonically increasing
- It is bounded between 0 and 1

- Its values at the limits of the domain are known ($P(-\infty) = 0$ and $P(\infty) = 1$)
- For many marginal distributions, it can be evaluated analytically

This approach depends on the availability of the cdf function. Again, accurate numerical evaluation of cdfs is not the focus of the current work, as many existing statistical libraries already implement these for standard distributions (e.g. (Brown et al. 2002)). For a pdf in which no functional form of the cdf is available this technique cannot be applied, because in order to find the cdf $P(\eta) = \int_{-\infty}^{\eta} p(\eta')d\eta'$ a numerical integration needs to be performed. By considering only distributions where both the pdf and the cdf are known, the cdf based approach can be applied.

The integral of the pdf over a small interval ε can be written in terms of the cdf:

$$\int_{-\infty}^{\eta} p(\eta')d\eta' = P(\eta) \tag{4.8}$$

$$\int_{-\infty}^{\eta+\varepsilon} p(\eta')d\eta' = P(\eta+\varepsilon) \tag{4.9}$$

$$\Rightarrow \int_{\eta}^{\eta+\varepsilon} p(\eta')d\eta' = P(\eta+\varepsilon) - P(\eta) \tag{4.10}$$

This is illustrated by the grey area in Figure 4.1. For a grid η_k this provides a simple way to evaluate the value of the integral of the pdf over each interval using the analytical expressions for the cdf. This expression is *exact* and contains no error, even at the intervals on the boundary where the pdf has a singularity. Therefore there is no need to normalise the discretised pdf generated in this way, because (to machine precision) the values of the integrals found in this way will sum to 1.

Assuming that the values of $\phi(\eta)$ are available at each η_k, define a set of n intervals I_k on which to perform the integration, defined by the midpoints between the grid coordinates η_k as shown in Figure 4.2:

$$I_1 = [\eta_1, \eta_{1+\frac{1}{2}}] \tag{4.11}$$

$$I_k = [\eta_{k-\frac{1}{2}}, \eta_{k+\frac{1}{2}}],\ k \in \{2, \dots, n-1\} \tag{4.12}$$

$$I_n = [\eta_{n-\frac{1}{2}}, \eta_n] \tag{4.13}$$

where grid half-points which form the endpoints of these intervals are given by

$$\eta_{k-\frac{1}{2}} = \frac{1}{2}(\eta_k - \eta_{k-1}) \tag{4.14}$$

$$\eta_{k+\frac{1}{2}} = \frac{1}{2}(\eta_{k+1} - \eta_k) \tag{4.15}$$

Note that the intervals around $k = 1$ and $k = n$ are treated specially.

Two simple approaches are to take the value of the scalar for the interval as either the mean of the two end values, or the value of the scalar at the midpoint. The former was chosen over the alternative, namely

$$\int_{\eta_1}^{\eta_n} \phi(\eta)p(\eta)d\eta \approx \sum_{k=1}^{n_g} \phi(\eta_{k+\frac{1}{2}})\left(P(\eta_{k+1}) - P(\eta_k)\right) \tag{4.16}$$

because in typically in the generation of flamelet tables, scalar values are available from the laminar flamelet simulations on a grid which includes the boundary points. The values of the scalar on these grid points were chosen to represent the value of the scalar on the interval associated with that point. Therefore our integration grid is such that the intervals at the boundaries are half of the size of the other intervals (assuming a uniform grid). In comparison, the cdf may be easily evaluated at any point without approximation or interpolation.

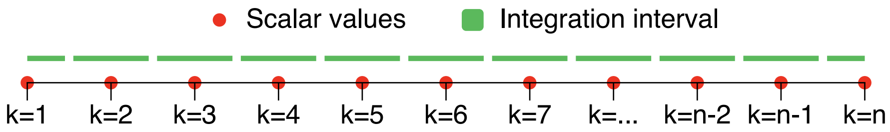

Figure 4.2: Location of scalar values and integration intervals used in the integration of a scalar with a pdf. Boundary intervals are half of the size of the central domain intervals.

Therefore the integral of $\phi(\eta)p(\eta)$ over this interval is approximated by the mean value of ϕ in each of these intervals and multiplied by the integral of the pdf:

$$\int_{I_k} \phi(\eta)p(\eta)d\eta = \phi(\eta_k)\int_{I_k} p(\eta)d\eta \tag{4.17}$$

This is illustrated graphically in Figure 4.3. Though the pdf has a strong gradient near the boundary, the scalar is assumed to vary gradually for all η. The value of the integration for the interval shown is approximated by $p(\eta)d\eta$ (the grey area) multiplied by the approximate value of the scalar over that interval. This value is obtained using the values of the cdf at the endpoints of the intervals:

$$W_1 = \int_{I_1} p(\eta')d\eta' = P(\eta_{1+\frac{1}{2}}) - P(\eta_1) \tag{4.18}$$

$$W_k = \int_{I_k} p(\eta')d\eta' = P(\eta_{k+\frac{1}{2}}) - P(\eta_{k-\frac{1}{2}}),\ k \in \{2, \dots, n-1\} \tag{4.19}$$

$$W_n = \int_{I_n} p(\eta')d\eta' = P(\eta_n) - P(\eta_{n-\frac{1}{2}}) \tag{4.20}$$

In the particular case where integration is performed at a boundary with a singularity, suggests that there will be a large error resulting from the fact that the values of ϕ very close to a should be weighted much higher by the pdf than values close to b. Hence the

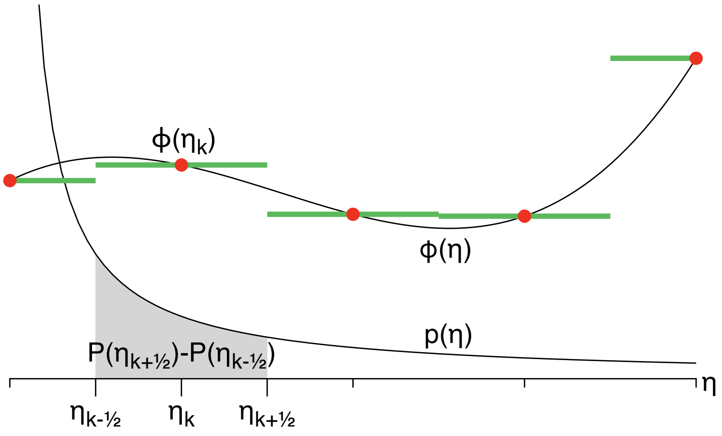

Figure 4.3: Integration of $\phi(\eta)p(\eta)$ over a small interval.

underlying assumption of this approach is that *the values of* ϕ *vary slowly enough to be considered constant across the interval* $[a, b]$. This is a reasonable assumption; if it does not hold then it is implied that the grid is not refined enough to capture the profile of ϕ.

To summarise, the process for the one-dimensional case is as follows:

- A grid η_k of size n_g over the domain $[\eta_1, \eta_{n_g}]$ of the distribution
- A corresponding set of intervals I_k defined in Equation 4.11
- Scalar values $\phi_k = \phi(\eta_k)$ which are known at each point η_k, either directly or by interpolation
- The values of the cdf calculated at $P(\eta_{k\pm\frac{1}{2}})$
- The value of the integral of the pdf over the interval I_k is given by Equation 4.18
- The value of the mean scalar is approximated as

$$\overline{\phi} \approx \sum_{k=1}^{n_g} \phi_k W_k \tag{4.21}$$

4.2.2 Two-dimensional case

This approach easily translates to the n-dimensional case. In this section, the extension of integration method for a bivariate pdf $p(\eta, \zeta)$ is described. The two dimensional grid, the location of the scalar values and the areas integrated over are shown in Figure 4.4. For this section, it is assumed that the joint-pdf has domain $(\eta, \zeta) \in [\eta_1, \eta_n] \times [\zeta_1, \zeta_m]$

which is discretised by an $n \times m$ Cartesian grid (η_k, ζ_l) where

$$\eta_k \in \{\eta_1, \dots, \eta_n\}, \tag{4.22}$$

$$\zeta_l \in \{\zeta_1, \dots, \zeta_m\} \tag{4.23}$$

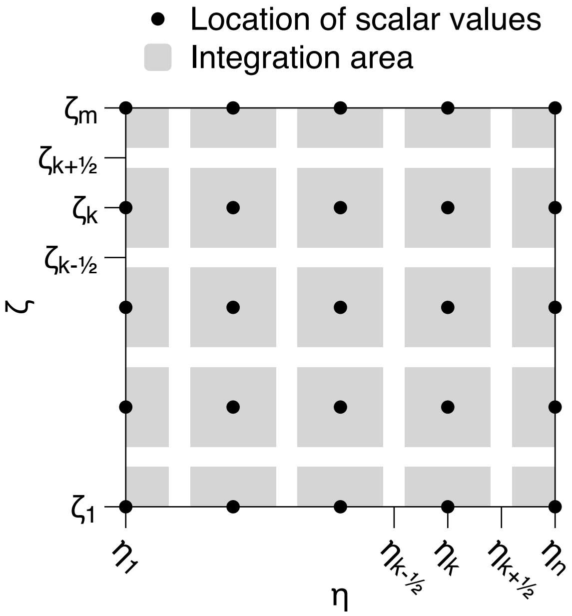

Figure 4.4: Location of scalar values and integration areas used in the integration of a scalar with a joint-pdf.

In comparison with the 1D version, the intervals on which integration is done are now areas, and there are three different sizes and 4 different shapes to consider: each area on a boundary is half of the size of a full area and each area at a corner is quarter of a full size, i.e.:

$$A_{kl} = [\eta_{k-\frac{1}{2}}, \eta_{k+\frac{1}{2}}] \times [\zeta_{l-\frac{1}{2}}, \zeta_{l+\frac{1}{2}}] \tag{4.24}$$

where the grid points are given by

$$\eta_{1-\frac{1}{2}} = \eta_1 \quad (4.25) \qquad \zeta_{1-\frac{1}{2}} = \zeta_1 \quad (4.28)$$

$$\eta_{k+\frac{1}{2}} = \frac{1}{2}(\eta_{k+1} + \eta_k) \quad (4.26) \qquad \zeta_{l+\frac{1}{2}} = \frac{1}{2}(\zeta_{l+1} + \zeta_l) \quad (4.29)$$

$$\eta_{n+\frac{1}{2}} = \eta_n \quad (4.27) \qquad \zeta_{m+\frac{1}{2}} = \zeta_m \quad (4.30)$$

The value of the integral $\int_{A_{kl}} p(\eta, \zeta) d\eta d\zeta$ over the area A_{kl} can be calculated by using the values of the joint cdf at each of the four corners, as shown in Figure 4.5. The value of $P(a)$ is the integral $\int_0^a p(\eta, \zeta) d\eta d\zeta$, from the origin to that point, and similarly for the other points. Therefore the integral of the joint-pdf over the area defined by the

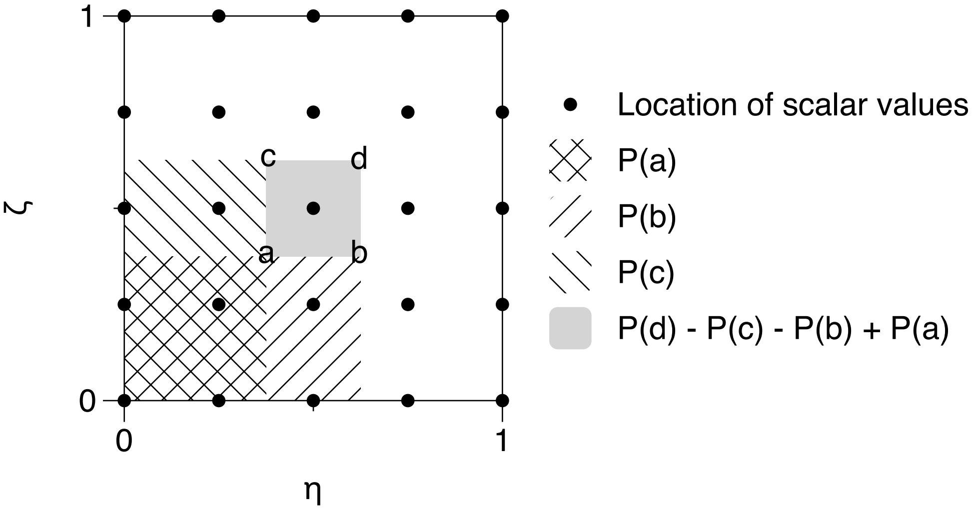

Figure 4.5: Calculation of $\int p(\eta,\zeta)d\eta d\zeta$ using values of the joint cdf P at points a, b, c and d.

points a, b, c, d can be calculated by the differences of such integrals:

$$W_{kl} = \int_{A_{kl}} p(\eta,\zeta)d\eta d\zeta \tag{4.31}$$

$$= P(d) - P(c) - P(b) + P(a) \tag{4.32}$$

This is equivalent to the H-volume of the integration area (Nelsen 1999):

$$V_H(B) = H(x_2,y_2) - H(x_1,y_2) - H(x_2,y_1) + H(x_1,y_1) \tag{4.33}$$

where $B = [x_1,y_1]\times[x_2,y_2]$. One of the requirements of a copula is that it is *2-increasing*, defined as having a positive H-volume for all rectangular subsets of the domain. Hence it is possible to show analytically that this quantity W_{kl} cannot be negative, and this forms a simple validation that there are no problems with the numerical evaluation of the cdf at these points. As with the 1D case, this equation is exact and contains no approximations.

To summarise, the two dimensional algorithm is as follows:

- A Cartesian grid (η_k,ζ_l) of size $n \times m$ over the domain $[\eta_1,\eta_n] \times [\zeta_1,\zeta_m]$.
- A corresponding staggered grid as defined in Equations 4.25-4.30
- A corresponding set of areas A_{jl} as defined in Equation 4.24, which are half-sized at the boundary and quarter sized at the corners
- The scalar values $\phi_{kl} = \phi(\eta_k,\zeta_l)$ which are known at each point (η_k,ζ_l)

- The value of the integral of the pdf over the area A_{kl} is calculated exactly as

$$W_{kl} = \int_{A_{kl}} p(\eta,\zeta)d\eta d\zeta \tag{4.34}$$

$$= P(\eta_{k+\frac{1}{2}},\zeta_{l+\frac{1}{2}}) - P(\eta_{k+\frac{1}{2}},\zeta_{l-\frac{1}{2}}) \tag{4.35}$$

$$- P(\eta_{k-\frac{1}{2}},\zeta_{l+\frac{1}{2}}) + P(\eta_{k-\frac{1}{2}},\zeta_{l-\frac{1}{2}}) \tag{4.36}$$

- The value of the mean scalar is approximated as

$$\overline{\phi} = \int_{\zeta_1}^{\zeta_m}\int_{\eta_1}^{\eta_n} \phi(x,y)p(\eta,\zeta)d\eta d\zeta \tag{4.37}$$

$$\approx \sum_{l=1}^{m}\sum_{k=1}^{n} \phi_{kl}W_{kl} \tag{4.38}$$

From the above formulations, it is possible to find several important quantities from the pdf by choosing different ϕ:

The marginal mean and variances are approximated by (ζ version omitted for brevity)

$$\mu_\eta = \int_{\zeta_1}^{\zeta_m}\int_{\eta_1}^{\eta_n} \eta p(\eta,\zeta)d\eta d\zeta \tag{4.39}$$

$$\approx \sum_{l=1}^{m}\sum_{k=1}^{n} \eta_k W_{kl} \tag{4.40}$$

$$\sigma_\eta^2 = \int_{\zeta_1}^{\zeta_m}\int_{\eta_1}^{\eta_n} \eta^2 p(\eta,\zeta)d\eta d\zeta - \mu_\eta^2 \tag{4.41}$$

$$\approx \sum_{l=1}^{m}\sum_{k=1}^{n} \eta_k^2 W_{kl} - \mu_\eta^2 \tag{4.42}$$

The covariance can be recovered via

$$\sigma_{\eta\zeta} = \int_{\zeta_1}^{\zeta_m}\int_{\eta_1}^{\eta_n} \eta\zeta p(\eta,\zeta)d\eta d\zeta - \mu_\eta\mu_\zeta \tag{4.43}$$

$$\approx \sum_{l=1}^{m}\sum_{k=1}^{n} \eta_k\zeta_l W_{kl} - \mu_\eta\mu_\zeta \tag{4.44}$$

One can even calculate the odds parameter numerically for an arbitrary cross-point (η_x, ζ_y):

$$\theta = AD/BC \tag{4.45}$$

$$= \frac{\left[\int_{\zeta_1}^{\zeta_y}\int_{\eta_1}^{\eta_x} p(\eta,\zeta)d\eta d\zeta\right]\left[\int_{\zeta_y}^{\zeta_m}\int_{\eta_x}^{\eta_n} p(\eta,\zeta)d\eta d\zeta\right]}{\left[\int_{\zeta_1}^{\zeta_y}\int_{\eta_x}^{\eta_n} p(\eta,\zeta)d\eta d\zeta\right]\left[\int_{\zeta_y}^{\zeta_m}\int_{\eta_1}^{\eta_x} p(\eta,\zeta)d\eta d\zeta\right]} \tag{4.46}$$

$$\approx \frac{\left[\sum_{l=1}^{y}\sum_{k=1}^{x} W_{kl}\right]\left[\sum_{l=y}^{m}\sum_{k=x}^{n} W_{kl}\right]}{\left[\sum_{l=1}^{y}\sum_{k=x}^{n} W_{kl}\right]\left[\sum_{l=y}^{m}\sum_{k=1}^{x} W_{kl}\right]} \tag{4.47}$$

4.3 Upper and lower bounds of covariance

The upper and lower bounds of the covariance of a bivariate distribution $H(\eta, \zeta)$ with known marginal distributions $F(\eta)$ and $G(\zeta)$ are given by the Hoeffding-Frechet bounds (Nelsen 1999; Hoeffding 1940; Fréchet 1951):

$$H^- = \max(F(\eta) - G(\zeta) - 1, 0) \tag{4.48}$$

$$H^+ = \min(F(\eta), G(\zeta)) \tag{4.49}$$

where + and − denote the upper and lower bounds, respectively.

$$H^-(\eta,\zeta) \le H(\eta,\zeta) \le H^+(\eta,\zeta) \tag{4.50}$$

As discussed in (Avellana 2006), Hoeffding (Hoeffding 1940) derived an expression for the covariance and then showed that the correlation coefficient r_H was bounded by

$$r^- \le r_H \le r^+ \tag{4.51}$$

where r^- and r^+ correspond to H^- and H^+ above. These are only equal to −1 and 1, respectively, when

$$H(\eta,\zeta) = H^-(\eta,\zeta) \Rightarrow F(\eta) = 1 - G(\zeta) \tag{4.52}$$

$$H(\eta,\zeta) = H^+(\eta,\zeta) \Rightarrow F(\eta) = G(\zeta) \tag{4.53}$$

i.e. that the two marginals are either equal to each other or reflections of each other. This can be demonstrated (Demirtas and Hedeker 2011) through considering the Wasserstein metric for two random variables η and ζ:

$$W(F,G) = E[(\eta-\zeta)^2] \tag{4.54}$$

$$= E[\eta^2] + E[\zeta^2] - 2E[\eta\zeta] \tag{4.55}$$

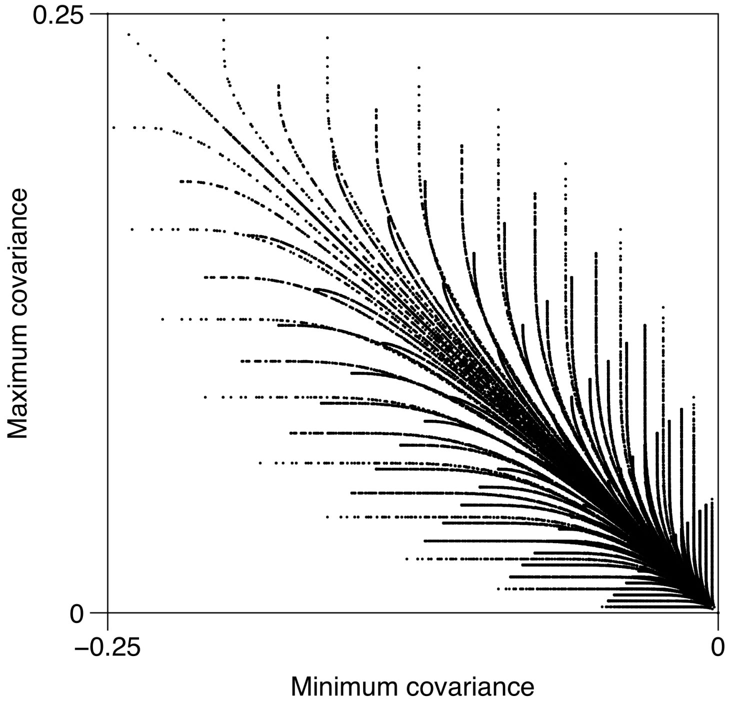

Figure 4.6: Upper and lower bounds of covariance for a full range of marginal beta distributions.

This gives a measure of the difference between the distributions of the two random variables η and ζ. Since the first two terms on the right hand side of Equation 4.55 depend only on the marginal distributions, the term $E[\eta\zeta]$ (and hence the covariance) is maximised when $W(F, G)$ is minimised, which occurs when $\eta = F^{-1}(t)$ and $\zeta = G^{-1}(t)$ for a uniform random variable t. Conversely the covariance will be minimised when $W(F, G)$ is maximised, which is done by taking $\eta = F^{-1}(t)$ and $\zeta = G^{-1}(1 - t)$. Equations 4.52 and 4.53 follow from these observations. Note that in the case of equally distributed marginals, the upper limit on correlation is always 1, while the lower limit needs to be determined.

For two marginal distributions which are not mathematically related as above, the correlation coefficient cannot reach 1 or -1. Such upper and lower bounds are shown in Figure 4.6. Discrete values of the four marginal distribution parameters (two means, two variances) were taken at regular intervals over their valid ranges. For each set of parameters, the minimum and maximum covariance were plotted. Only in particular cases is the upper bound equal to the negation of the lower bound. However, these bounds are difficult to evaluate for arbitrary distributions. For the case of two identically distributed marginals, Dukic *et al.* (Dukic and Marić 2013) present analytical limits for a very restricted subset of distributions with beta marginals, and numerically obtained limits for slightly less restrictive conditions (but still assuming identically distributed marginals). They also present an algorithm for sampling from such joint distributions.

Demirtas and Hedeker (Demirtas and Hedeker 2011) discuss the problems associated with obtaining the upper and lower bounds of correlation or covariance.

The Hoeffding representation of covariance (Lin et al. 2014) is

$$\sigma_{\eta\zeta} = \int_{-\infty}^{\infty}\int_{-\infty}^{\infty} H(\eta,\zeta) - F(\eta)G(\zeta)d\eta d\zeta \tag{4.56}$$

and with the above observations the maximum and minimum covariance are given by

$$\sigma^{+}_{\eta\zeta} = \int_{0}^{1} F^{-1}(t)G^{-1}(t)dt - \mu_{\eta}\mu_{y} \tag{4.57}$$

$$\sigma^{-}_{\eta\zeta} = \int_{0}^{1} F^{-1}(t)G^{-1}(1-t)dt - \mu_{\eta}\mu_{y} \tag{4.58}$$

The corresponding correlations reach the values of 1 and -1 only in the case of $F(x) = G(ax+b)$ for some a and b. For beta distributed marginals with shape parameters $\{\alpha_1, \beta_1\}$ and $\{\alpha_2, \beta_2\}$, these become

$$\sigma^{+}_{\eta\zeta} = \int_{0}^{1} I_t^{-1}(\alpha_1,\beta_1)I_t^{-1}(\alpha_2,\beta_2)dt - \mu_{\eta}\mu_{y} \tag{4.59}$$

$$\sigma^{-}_{\eta\zeta} = \int_{0}^{1} I_t^{-1}(\alpha_1,\beta_1)I_{1-t}^{-1}(\alpha_2,\beta_2)dt - \mu_{\eta}\mu_{y} \tag{4.60}$$

where here $I_t(\alpha,\beta)$ is the regularised incomplete beta function (the cdf of a beta distribution). These may be integrated using a numerical integration scheme such as the Gauss–Kronrod quadrature method (Laurie 1997).

In Appendix A, some upper and lower bounds on the covariance are derived for a some special cases. However, based on numerical evaluation of the covariance from Plackett copulas using the methods described in Section 4.2 (specifically, Equation 4.43), these bounds are not sufficiently strict. The numerical integration of the Hoeffding-Frechet bounds (Equation 4.50) was found to match the values found by integrating the Plackett copula directly. However, in certain cases the numerical integration of Equation 4.50 failed, and producing an anomalous result that did not fit the trend. The direct integration using Equation 4.43 had no such problems, and was therefore the chosen method for calculating the upper and lower bounds, both because it proved the more robust method and because it is consistent with the method used to generate the copula during the application. The agreement between this method and the direct integration of the Hoeffding-Frechet bounds, in the cases where that method worked, gives confidence that the results are accurate.

4.3.1 Scaled covariance as tabulation parameter

As seen in the preceding section, for the purposes of tabulation, the correlation is a poor choice of tabulation parameter because the limits $[-1, 1]$ are not always realisable. Therefore new quantity σ^*_{xy} is defined which is normalised by the minimum and maximum covariances for a given set of marginal distributions:

$$\sigma^*_{\eta\zeta} = \frac{\sigma_{\eta\zeta} - \sigma^-_{\eta\zeta}}{\sigma^+_{\eta\zeta} - \sigma^-_{\eta\zeta}} \tag{4.61}$$

4.4 Linking odds parameter to covariance

The covariance of two random variables Z and c with marginal distribution functions $F(\eta)$ and $G(\zeta)$, respectively, may be written in terms of their joint distribution function $P(\eta, \zeta)$ as

$$\sigma_{Zc} = \int_c \int_Z P(\eta, \zeta) - F(\eta)G(\zeta) d\eta d\zeta \tag{4.62}$$

$$= \int_c \int_Z C[F(\eta), G(\zeta)] - F(\eta)G(\zeta) d\eta d\zeta \tag{4.63}$$

where C is the copula for the joint-cdf P with marginals F and G. For the Plackett copula, this becomes

$$\sigma_{\eta\zeta} = \int\int \frac{S - \sqrt{S^2 - 4\theta(\theta-1)FG}}{2(\theta-1)} - F(\eta)G(\zeta) d\eta d\zeta \tag{4.64}$$

$$S = 1 + (\theta - 1)(F(\eta) + G(\zeta)) \tag{4.65}$$

This integration depends on the choice of θ as well as the two marginal distribution functions F and G. Presuming beta distributions for the marginals, i.e.

$$F(\eta) = I_\eta(\alpha_\eta, \beta_\eta) \tag{4.66}$$

$$G(\zeta) = I_\zeta(\alpha_\zeta, \beta_\zeta) \tag{4.67}$$

where $I_\eta(\alpha_\eta, \beta_\eta)$ is the regularised incomplete beta function. Then

$$\sigma_{\eta\zeta} = \int\int \frac{S - \sqrt{S^2 - 4\theta(\theta-1)I_\eta(\alpha_\eta, \beta_\eta)I_\zeta(\alpha_\zeta, \beta_\zeta)}}{2(\theta-1)} - I_\eta(\alpha_\eta, \beta_\eta)I_\zeta(\alpha_\zeta, \beta_\zeta) d\eta d\zeta \tag{4.68}$$

$$S(\theta) = 1 + (\theta - 1)(I_\eta(\alpha_\eta, \beta_\eta) + I_\zeta(\alpha_\zeta, \beta_\zeta)) \tag{4.69}$$

where α_η, β_η, α_ζ, β_η are determined by the marginal distributions and hence known constants. This can be integrated to find an expression for the covariance. However, inverting this relation to obtain an expression for θ in terms of $\sigma_{\eta\zeta}$ is difficult due to the inability to find an analytical solution to the integral.

Hence there is no direct relationship between the odds parameter and the correlation, because the correlation depends on the marginal distributions whereas the odds parameter is purely a function of the copula. To determine the odds parameter for a distribution with Normal marginal distributions, Nelsen (Nelsen 1999) suggests the following procedure:

1. Generate two sets of correlated Gaussian random numbers (X, Y)
2. Transform these Gaussian random numbers into uniform random numbers through $U_i = \phi^{-1}(X_i)$ and $V_i = \phi^{-1}(X_i)$ where ϕ^{-1} is the Gaussian inverse cumulative distribution function
3. Plot these correlated uniform random numbers on a contingency diagram
4. Calculate the odds parameter as $\theta = ad/bc$, where a, b, c and d are the number of points found in the upper left, upper right, lower left and lower right quadrants of the plane, respectively

This method is only valid for Normal marginals, as it relies on the known result that transforming marginals from uniform distributions to Normal distributions (and vice versa) does not significantly change the correlation.

The following method proposed by Johnson (Johnson 2013; Nelsen 1999) generates two samples (u, v) of the joint cdfs from a Plackett distribution:

1. Generate two independent uniform $(0, 1)$ variates u, t.
2. Set

$$\begin{aligned}
a &= t(1-t) \\
b &= \theta + a(\theta-1)^2 \\
c &= 2a(u\theta^2 + 1 - u) + \theta(1-2a) \\
d &= \sqrt{\theta}\sqrt{\theta + 4au(1-u)(1-\theta)^2} \\
v &= \frac{[c-(1-2t)d]}{2b}
\end{aligned}$$

3. The desired pair is (u, v)

These samples of the cdf (u, v) can then be transformed via the desired inverse marginal pdfs to obtain samples from the joint distribution. This is correct and a viable approach for generating samples, but it relies on knowing the odds parameter in advance.

Darbyshire and Swaminathan (Darbyshire and Swaminathan 2012) use the following procedure to find the odds parameter from covariance:

1. The desired RMSs and covariance σ_η, σ_ζ and $\sigma_{\eta\zeta}$ are known (from CFD)
2. The desired *Pearson* correlation coefficient $r_{\eta\zeta} = \sigma_{\eta\zeta}/(\sigma_\eta \sigma_\zeta)$ is therefore known
3. The Pearson correlation coefficient $r_{\eta\zeta}$ of the required distribution (η, ζ) can be related to the Pearson correlation coefficient r_{XY} of a pair of Normally distributed variables (X, Y) through
$$r_{XY} = 2\sin(\frac{\pi r_{\eta\zeta}}{6}), \tag{4.70}$$
4. A set of correlated *Normally distributed* random variables (X, Y) are generated with Pearson correlation coefficient r_{XY}
5. A pair of random variates (η, ζ) are then calculated using the standard Normal distribution cdf $\eta = \phi(X)$, $\zeta = \phi(Y)$
6. The odds parameter θ is then calculated based on (η, ζ)

However, step 3 above is not generally valid. In step 3, Equation 4.70 is actually the relationship between the *Pearson correlation* $r_{\eta\zeta}$ and *Spearman's rank correlation coefficient* $\rho_{\eta\zeta}$ and is only correct for the Gaussian copula:

$$\rho_{\eta\zeta} = \frac{6}{\pi}\arcsin(\frac{r_{\eta\zeta}}{2}) \tag{4.71}$$
$$r_{\eta\zeta} = 2\sin(\frac{\pi \rho_{\eta\zeta}}{6}) \tag{4.72}$$

This relationship will not be correct for any marginal pdfs besides the normal distribution, and is not correct for the Plackett copula used in (Darbyshire and Swaminathan 2012; Ruan et al. 2014) which is not a Normal copula (the copula of a multivariate normal distribution).

To summarise, there are two issues with the approach in (Darbyshire and Swaminathan 2012): the conflation of Spearman's ρ and the Pearson correlation coefficient (step 3); and the assumption that the correlation coefficient will be unchanged by a change of marginals (step 6). The final samples (η, ζ) will indeed have uniform marginals, and they will have Pearson correlation coefficient r_{XY}.

In the context of stochastic evaporation modelling for sprays, a further consideration with methods that rely on sampling to obtain the odds parameter is that they are typically inefficient when large numbers of samples are required. As the correlation between the two variables approaches its extremes, large numbers of samples are required to avoid insufficient numbers of samples in the less populated diagonal quadrants of the contingency diagram. Ruan *et al.* (Ruan et al. 2014) suggest 5000 samples to achieve

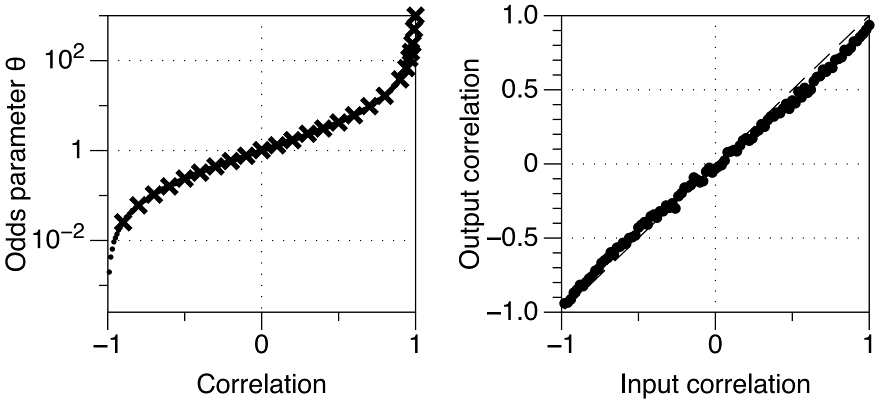

Figure 4.7: Left: Odds-parameter as a function of correlation (·) as predicted by the method outlined above. The piecewise linear fit (×) which is used in the code is illustrated. Right: The reproduction of the correlation between pairs of random variates generated using the copula method. There is a slight under-prediction. Dashed line: $y = x$.

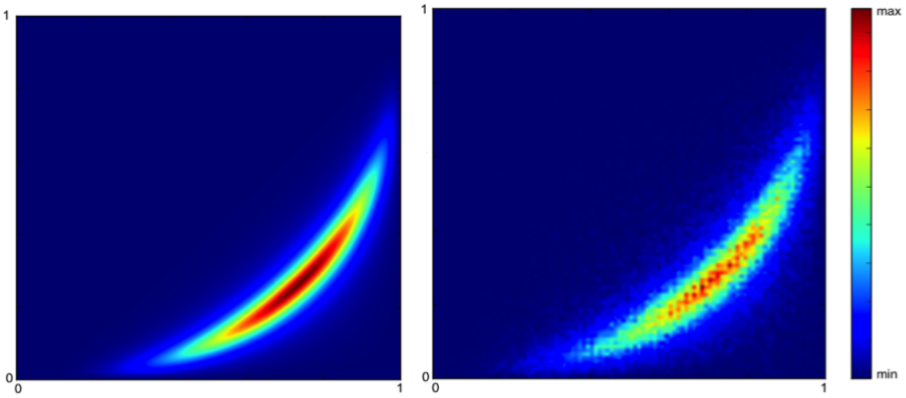

Figure 4.8: Left: Original joint-pdf, Right: Pdf reconstructed from random multivariate samples. The marginal distributions are both beta in this case and the correlation is 0.7.

around 1% error. If the objective is to randomly sample values from the presumed droplet or particle in a turbulent flow, a new joint distribution must be constructed at every timestep in every CFD cell. Therefore a more efficient approach for constructing and sampling from the joint distribution is desired. A lookup table approach is developed in this work, in which the odds ratio has been pre-calculated for a range of values of correlation (see Figure 4.7) and a piecewise linear interpolation is performed to obtain the odds parameter from the correlation.

The implementation of the Plackett copula has been verified by confirming that it produces the requested correlation, and marginal pdfs. The sampling procedure has been validated by demonstrating its convergence towards the appropriate analytical joint and marginal pdfs, as illustrated in Figures 4.8 and 4.9.

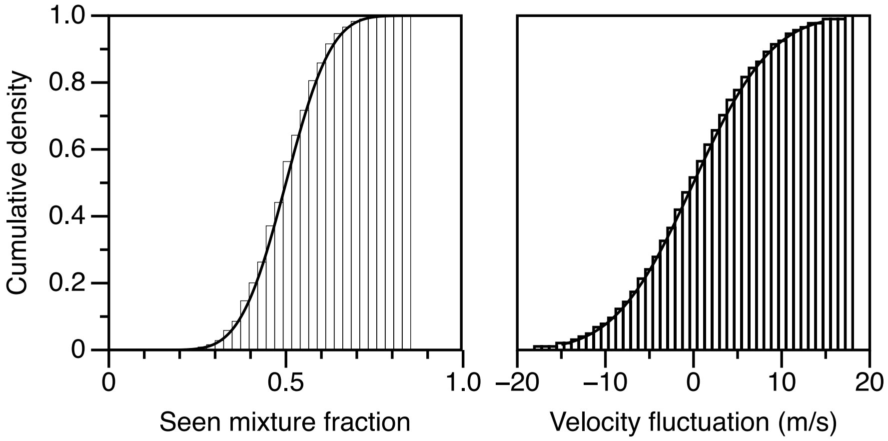

Figure 4.9: Comparison of the analytical marginal CDFs (solid line) and the numerically reconstructed CDFs produced by the copula method (bars).

4.4.1 Copula-invariant approaches

The numerical approach described in the preceding chapter involves a costly interpolation to find the odds parameter from a given covariance. This section briefly explores the potential alternative approaches to obtaining the odds parameter.

The covariance of a joint distribution $h(\eta,\zeta)$ may be written as

$$\begin{aligned}\sigma_{\eta\zeta} &= \int_{\Omega_{\eta\zeta}} (\eta-\mu_\eta)(\zeta-\mu_\zeta)h(\eta,\zeta)d\eta d\zeta && (4.73)\\ &= E[(\eta-\mu_\eta)(\zeta-\mu_\zeta)] && (4.74)\\ &= E[\eta\zeta]-\mu_\eta\mu_\zeta && (4.75)\end{aligned}$$

where $h(\eta,\zeta)$ is the joint-pdf of η and ζ defined on the domain $\Omega_{\eta\zeta}$, μ_ζ and μ_ζ are the mean values of these scalars and E indicates the expected value of a random variable.

The quantity $\sigma_{\eta\zeta}$ cannot be expressed solely as a function of the copula $C(u,v)$. This is because $\sigma_{\eta\zeta}$ also depends on the marginal distributions. Recall that the copula binds the two marginal cdfs $u=F(\eta)$ and $v=G(\zeta)$ to form the joint cdf according to

$$C(u,v)=H(\eta,\zeta) \tag{4.76}$$

where H is the joint cdf corresponding to the joint-pdf h. Then the dependence of the covariance on the choice of marginal distributions can be observed:

$$\sigma_{\eta\zeta} = \int_{\Omega_{\eta\zeta}} \eta\zeta h(\eta,\zeta) d\eta d\zeta - \mu_\eta \mu_\zeta \tag{4.77}$$

$$= \int_{\Omega_{\eta\zeta}} \eta\zeta \frac{\partial^2 C(u,v)}{\partial u \partial v} d\eta d\zeta - \mu_\eta \mu_\zeta \tag{4.78}$$

$$= \int_{I^2} F^{-1}(u) G^{-1}(v) dC(u,v) - \mu_\eta \mu_\zeta \tag{4.79}$$

$$\tag{4.80}$$

Alternative measures of dependence, such as Spearman's rank correlation coefficient or Kendal's tau, depend only on the copula and not on the joint distribution function. Hence, finding a mapping between them and the odds ratio may be easier. The population version of Spearman's rank correlation coefficient is (Nelsen 1999)

$$\rho_{\eta\zeta} = 12 \int_{I^2} uv dC(u,v) - 3 \tag{4.81}$$

$$= 12 \int_{I^2} C(u,v) du dv - 3 \tag{4.82}$$

Fredricks and Nelsen (Fredricks and Nelsen 2007) give Spearman's ρ for the Plackett copula ($\theta \neq 0$) as

$$\rho(\theta) = \frac{2\theta + \theta^2 - 2(\theta+1)\log(\theta+1)}{\theta^2} \tag{4.83}$$

This is arrived at by noting that C is defined implicitly by the quadratic (in C)

$$\theta C^2 - [1 + \theta(F+G)]C + (\theta+1)FG = 0 \tag{4.84}$$

If the error (discussed in Section 4.4) associated with assuming $\rho_{\eta\zeta} = r_{\eta\zeta}$ is acceptable for a given application, then the inversion of Equation 4.83 provides an attractive alternative to the sampling approach of linking $\sigma_{\eta\zeta}$ and θ. One could attempt to derive an analytical expression for $\sigma_{\eta\zeta}$ as a function of θ, beginning by substituting the expression for the Plackett pdf into the definition of covariance and solve for θ. This quickly becomes intractable due to the combined complexity of the Plackett distribution and the beta pdf marginals. Alternatively a transport equation could be derived for a quantity which depends only on the copula, not on the marginal distributions. One example of such a quantity is the odds parameter; another, more standard option is Spearman's ρ. However, the problem still remains of finding a transport equation for Spearman's ρ, since that depends on the marginal pdfs. Neither of these approaches seems viable.

4.4.2 Numerical evaluation of the copula parameters

In order to avoid the use of sampling techniques for the generation of the copula parameter θ, the mapping between odds parameter and covariance is numerically tabulated. This approach can be generalised to arbitrary table parameters and copula parameters. Here, the process is outlined by the following steps to generate a mapping from mixture fraction progress variable covariance σ_{Zc} to odds parameter θ for a regular flamelet table parametrised on $\Theta = \{\widetilde{Z},\ \widetilde{Z''^2},\ \tilde{c},\ \widetilde{c''^2}\}$ and a fifth parameter, the min/max normalised covariance σ^*_{Zc}:

1. For each combination of Θ in the table,
    (a) find the two presumed marginal distributions from their moments,
    (b) generate two joint distributions based on these marginals and the Hoeffding-Frechet bounds (Equation 4.50) (equivalent to Plackett distributions with odds parameters $\theta = \infty$ and $\theta = -1$),
    (c) from these two joint distributions, numerically calculate the covariance via Equation 4.43. These are the minimum and maximum possible covariances for the given marginal moments.
    (d) for an arbitrary set of odds parameters θ_k spanning the full range $[0, \infty]$ (see Equation 4.86), numerically calculate the corresponding covariance σ_{Zc_k} and the min/max scaled covariance $\sigma^*_{Zc_k}$ as defined in Section 4.3.1. This gives a discrete mapping m such that $\sigma^*_{Zc_k} = m(\theta_k)$
2. For each desired σ^*_{Zc} on a regular grid, calculate the appropriate odds parameter θ by a linear interpolation of the inverse of the mapping from step 1d,

$$\theta = m^{-1}(\sigma^*_{Zc}) \tag{4.85}$$

This process produces a set of odds parameters θ given as a function of the table parameters $\Theta \cup \{\sigma^*_{Zc}\}$, which can then be used to generate the appropriate Plackett copula for each set of table parameters.

The choice of the values of θ_k must be made carefully in order to ensure that the mapping m has sufficient resolution in σ^*_{Zc} space to make the linear interpolation accurate. In the present study, through trial and error it was found that $n_\theta = 31$ values of θ_k given by

$$\sigma^{*\ guess}_{Zc_k} = \begin{cases} 0.0 & \text{if } k = 1 \\ 0.0 + \varepsilon & \text{if } k = 2 \\ 1.0 - \varepsilon & \text{if } k = n_\theta - 1 \\ 1.0 & \text{if } k = n_\theta \\ \varepsilon + (1 - 2\varepsilon)\frac{k-2}{n_\theta - 3} & \text{otherwise} \end{cases} \tag{4.86}$$

$$\theta_k = \frac{1}{1 - \sigma^{*\ guess}_{Zc_k}} - 1 \tag{4.87}$$

where $\varepsilon = 1 \times 10^{-6}$ produced appropriate results. This mapping uses a $1/x$ shape profile as a guess for θ as a function of σ^*_{Zc}, with values placed very close to $\theta = 0$ and $\theta = \infty$ to ensure the full range is covered. The resulting table was tested by comparing the numerically calculated σ^*_{Zc} with the input σ^*_{Zc}, and the error was found to be satisfactory.

Finally, it is noted that the expression for the Plackett copula (Equation 3.25) is sensitive to numerical accuracy problems when the odds parameter is close to zero. This was avoided in the present work by simply assuming independence for $|\theta - 1| < 10^{-10}$.

4.5 Sampling from a joint-pdf

4.5.1 Sampling from joint distributions (application to spray)

To evaluate the droplet evaporation rate it is necessary to select a pair of seen fluid properties from their joint-probability distribution so that T_∞ and $Y_{f,\infty}$ can be obtained. Efficient sampling from multivariate distributions with specified correlations remains a difficult problem (Gentle 2003). Several methods exist, but the methods are intended for sampling large numbers of random values from a single distribution. The requirements for evaporation modelling are somewhat different: the mixture fraction – progress variable distribution varies in space and time, so that a new joint distribution should be constructed at every grid point and every time-step. The number of samples required from each distribution is then equal to the number of particles in that cell at that time, which may be as few as one. Established sampling schemes rely on Monte Carlo approaches, as in (Chang et al. 1994) or (Lurie and Goldberg 1998), which aim to find the transformation from the multivariate normal correlation matrix to the correct correlation matrix of the joint distribution after an inverse transform. These Monte Carlo approaches are inefficient if only a few samples are required from each joint-distribution. In this section, a new computational algorithm is developed, designed to efficiently generate a single sample from an arbitrary multi-variate probability distribution.

Sampling from a univariate distribution where the inverse cdf is available is simple and efficient using the inverse transform sampling method:

1. Generate uniformly distributed random variates X_i
2. Obtain arbitrarily distributed random variates as $Q\left(X_i\right)$, where Q is the distribution's quantile function, the inverse of the cumulative distribution function.

However, for a multivariate distribution this approach is not possible as the cdf is a function mapping a vector to a scalar (more specifically, it is not one-to-one) and hence has no inverse. Algorithms exist for drawing from specific bivariate distributions; for example, many algorithms are available for the bivariate Normal distribution and an algorithm for sampling from the Plackett copula was described in Section 4.4.

In the case where the bivariate distribution is expressed as an empirical joint cdf, a numerical approach can be taken to efficiently generate samples. Consider a distribution with probability density function $f(x,y)$ defined on the domain $(x,y) \in [0,1] \times [0,1]$. Allow an $n \times n$ discretisation of this domain into cells of size $n^{-1} \times n^{-1}$ with centres at points

$$(x_i, y_i) = \left(\frac{i-0.5}{n}, \frac{j-0.5}{n}\right) \tag{4.88}$$

where $i, j \in \{1, \dots, n\}$. Further, subdivide the central value $f_{ij} = f(x_i, y_j)$ of the pdf in each of these cells into sections of length n^{-1}, effectively discretising the integral under the curve $z = f(x,y)$ into equal volumes $V_{ijk} = n^{-3}$. As $n \to \infty$, the total sum of these volumes approaches 1, which is the integral of $f(x,y)$ over the whole domain. Selecting one of these volumes at random (each having equal probability) will give a pair of random numbers — the domain coordinates (x_i, y_j) — which will exhibit the desired joint distribution. This selection is done in practice by generating a uniform random number ξ and stepping through the volumes V_{ijk} in a predefined order, summing them until the total volume exceeds ξ. The exact order of traversal is not important as long as it is consistent between samples, because the traversal path is essentially a mapping the discrete set of volumes to a one-dimensional set of integers, from which a random selection is made. Thus a mapping from a univariate random number ξ to a multivariate random vector (x,y) with $n \times n$ discrete values is achieved. This procedure is possible due to the discretisation — it is not possible to traverse a continuous two or three dimensional field in this way.

A simple improvement to this sampling procedure is possible wherever the joint cdf is available. For any point $(X_i, Y_i) = (i/n, j/n)$, the cdf $F_{ij} = F(X_i, Y_j)$ is equal to the integral of the pdf up to (X_i, Y_i):

$$F_{ij} = \int_0^{X_i} \int_0^{Y_j} f(x,y)dxdy \tag{4.89}$$

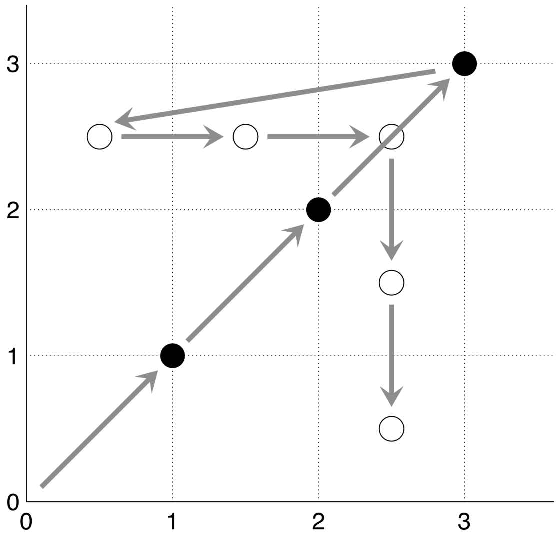

Figure 4.10: Algorithm for searching distribution space.

which is approximately equal to the sum of the value of the PDF at the centre of the cells, multiplied by the area of the cells:

$$F_{ij} \approx \sum_{U=0}^{i} \sum_{J=0}^{j} f_{IJ} A_{IJ} \tag{4.90}$$

Therefore the cost of searching for the point where accumulated probability exceeds ξ can be reduced by traversing the diagonals (x_a, y_a) until two CDF values are found F_{aa} and $F_{(a+1)(a+1)}$ such that

$$F_{aa} \leq \xi < F_{(a+1)(a+1)} \tag{4.91}$$

Then, beginning from the lower value of the CDF, perimeter of the $a \times a$ square is traversed, as indicated in Figure 4.10, accumulating probability from $f(x_i, y_i)$. When the total probability exceeds ξ the coordinates (x, y) of the last point give the pair of random variates.

It is possible that the joint-PDF will contain sharp gradients if it is numerically evaluated from a joint cdf, rather than from observed empirical samples; for example when the marginal beta-pdf contains a singularity at 0 as can happen with the beta distribution with low mean and high variance. In this case a uniform grid is not sufficient and numerical error leads to over prediction of the mean mixture fraction. A simple refinement which has proven to be effective in avoiding this error is to discretise the grid according to points $G^{-1}(y_i)$ where y_i are evenly spaced points on the interval $[0, 1]$ and $G^{-1}(y_i)$ is the value of the inverse marginal beta-pdf at these points. Hence the point $G^{-1}(0.01)$ is the point at which 1% of the distribution has been accumulated. This leads to a refinement of the grid where the marginal distribution changes most rapidly.

This efficient method of sampling from the joint distribution is necessary for application of this evaporation model in the context of Eulerian-Lagrangian simulations, where droplets will move through computational cells and the mean velocity and mixture fraction seen by the droplet will vary rapidly over time. This motivates the need for a computationally cheap method to generate random samples from each presumed joint distribution encountered, as the next seen distribution is likely to be different. Using only the pdf in the above sampling technique results in $O(n^2)$ computational cost, where n is the resolution of the grid; making use of the cdf reduces this to $O(n)$ computational cost. In the case where multiple Lagrangian particles are present in the same Eulerian cell further optimizations can be made by using an ordered list of uniform random numbers (see Bentley and Saxe (1980) for an example of an algorithm for generating such a list) and starting the search location of each from the position where the last was found.

4.6 Time integration of reference variables

The Reynolds averaged simulations presented in this thesis employ lookup tables generated from an autoigniting laminar flamelet to provide thermochemical fluid properties conditioned on the reference variables. The *laminar table* is then multiplied by a set of presumed pdfs and integrated to give a *turbulent lookup table* which provides Favre averaged quantities such as composition, temperature and density to the CFD code as functions of the Favre averaged reference variable moments. A simple test case to ensure that the lookup table is working correctly is to reproduce the flamelet solution by integrating the lookup table in time using the CFD code. Here this test is performed with the CFD code by setting up a 1-dimensional solution domain $x \in [0, 1]$, in which the velocity field is held equal to zero so that the mixture fraction distribution given in the initial condition $(\widetilde{Z}, \tilde{c}) = (x, 0) \forall x$ does not change over time. The variances and covariance are initialised to zero and remain so, effectively making this a laminar calculation where $\tilde{c} = c$ and $\widetilde{Z} = Z$. The Favre averaged progress variable $\tilde{c}$ evolves according to its reaction rate, as this is the only non-zero term in the transport equation:

$$\frac{\partial \tilde{c}(\widetilde{Z})}{\partial t} = \overline{\dot{\omega}_c}(\widetilde{Z}) \tag{4.92}$$

While the flamelet solution is calculated by considering the evolution of all species in the chemical mechanism, the CFD solution with tabulated chemistry solves only for $\tilde{c}$. The 0D flamelet solution is a solution in conditional mass fraction space (plus enthalpy or temperature, but here $\partial \langle h|\eta \rangle / \partial t = 0$ and therefore temperature is uniquely determined by mass fractions). The solution is a set of mass fractions at a given mixture fraction and time: $Y_k = Y_k(Z, t)$. Therefore the solution represents a two dimensional manifold in k-dimensional composition space. Defining c and Z as a reference variables implies a coordinate system in $[0, 1]^2$ for this manifold. Another coordinate system is already

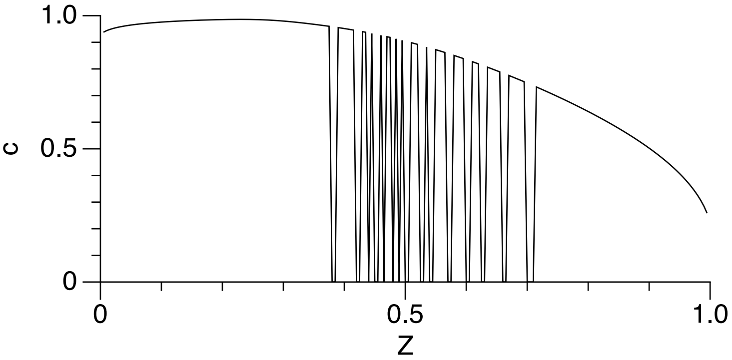

Figure 4.11: Value of c from the CFD case at $t = 0.1 \times t_{\mathrm{final}}$.

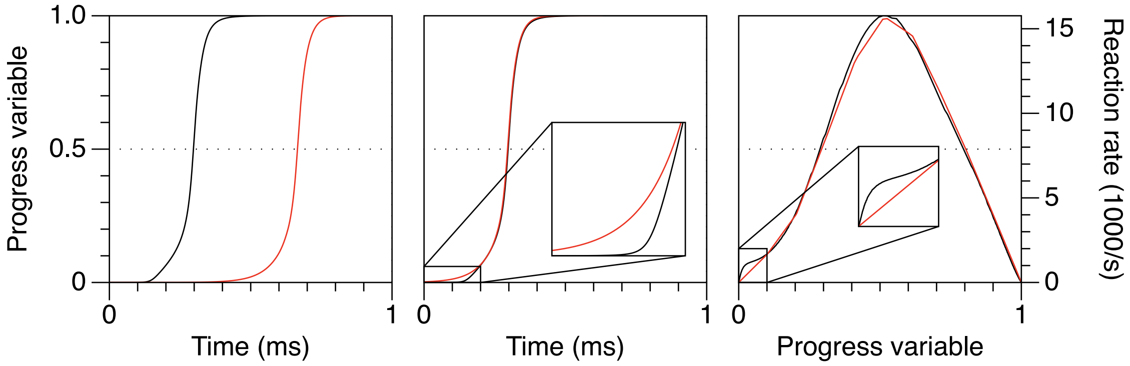

Figure 4.12: Solution of Equation 4.92 for $Z = 0.2$ over time; red: CFD solution; black: solution from CMC code. First panel: comparison of $c(t)$ as calculated by CFD and CMC code. Second panel: CFD solution time-shifted to show difference in profile of $c(t)$. Third panel: $\dot{\omega}_c$ vs c, showing lookup table interpolation error.

established: Z, t. Provided $c(t)$ is monotonic there exists a bijection from (Z, t) space to (Z, c) space.

Hence, the 1D CFD problem described above should be able to exactly reproduce the laminar flamelet solution by directly integrating $c(t)$ according to Equation 4.92. However, it was found to be unable to do so. Figure 4.11 shows a solution of Equation 4.92 as calculated by the CFD code. The fluctuations in c exhibited in Figure 4.11 are due to errors in the ignition delay time of a mixture at a given mixture fraction. To understand why, Equation 4.92 is integrated directly for $Z = 0.2$. The figures show that there is a large error (over 100%) in the ignition delay time as calculated from the integration of c versus the flamelet solution. Once the ignition occurs, the two follow solutions the same trajectory. The cause of this is the error in the interpolation of the reaction rates for $c < 0.1$, which were stored in a table with only 11 points in progress variable space. The calculation is highly sensitive to the reaction rates during the initial stages of ignition, which were not captured well by the coarse table used here. Replacing the reaction rates for $c < 0.1$ with those from the flamelet solution, or performing the same integration using a table with 51 points in progress variable space, both resulted in an accurate ignition delay time prediction. However, this highlights the sensitivity of the problem to the progress variable in the early reaction phase. This sensitivity was found to be lowest at around $Z = 0.2$, as shown here; for both leaner and richer mixture fractions, the sensitivity was higher and increasing the resolution of the table (within reasonable limits — up to 101 points in progress variable space) was insufficient to obtain accurate ignition delay time estimates.

It should be noted that this does not pose a problem for the CMC code, as the use of full chemistry to characterise the ignition mitigates the problem of numerical accuracy, since radical concentrations are accurately accounted for. This also explains the behaviour seen in Figure 4.11: the dissipation term in the CMC equations uses a second order central difference scheme to calculate the second derivative in the diffusion term. This scheme produces fluctuations in the source terms and therefore fluctuations in the species mass fraction profiles. The employed scalar dissipation rate model amplifies these fluctuations around $Z = 0.5$ and diminishes them towards the boundaries. During the initial stages of the CMC solution, where the mass fraction profiles are close to linear, the amplitude of the contribution from these fluctuations is relatively large, resulting in small errors in the total RHS around $Z = 0.5$ which manifest as highly fluctuating ignition delay times in this region. This explains the almost correct behaviour for $Z < 0.3$ in Figure 4.11, where the mixture ignites sooner and therefore these errors are less important, and the incorrect behaviour around $Z = 0.5$.

A sensitivity study was performed by directly integrating Equation 4.92 for $Z = 0.6$. The results are shown in Figure 4.13. The progress variable initial condition was set to three different values close to zero. The ignition delay time is strongly affected by the initial value: an error in the initial value of 0.01% (relative to $c = 1$) produces roughly a 125% error in ignition delay time; an error in the initial value of 0.0001% produces an ignition delay time error of around 50%.

The sensitivity of the time integration of c to small changes in initial conditions poses a problem with using c as a reference variable for an autoignition calculation. There are many sources of both modelling and numerical error in CFD simulations, and the inability to eliminate all error makes the sensitivity of the reaction rate of c a concern. Error in ignition delay time prediction will directly affect the prediction of lift-off height in autoignition stabilised flames.

Fundamentally, this sensitivity stems from the slow rate of change of c during the early stages of autoignition. The progress variable is characterised by a very shallow gradient initially, followed by a short period of rapid change before levelling off again. This has the desirable property that the composition changes though the reaction are well characterised in c-space. For premixed flames which are driven by the diffusion of heat ahead of the flame (the preheat zone) this is not an issue as the premixed flame is

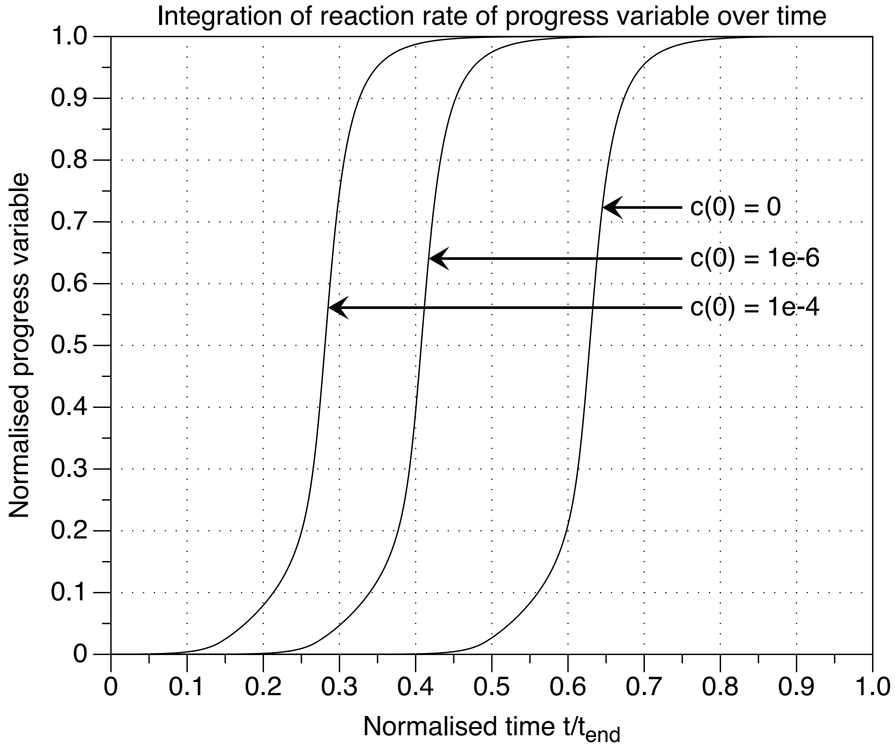

Figure 4.13: Integration of reaction rate of progress variable over time, showing sensitivity of homogeneous reactor to initial conditions of c.

captured by the diffusion of progress variable ahead of the flame front. However, for an auto-igniting flame this is not the case: the reaction is driven by the accumulation of radical species before ignition.

Thus it is desirable to make use of a reference variable that can account for the changes in thermochemical state during the pre-ignition phase. One way to increase the gradient of the progress variable near $c = 0$ — and therefore reduce the sensitivity — would be to choose a definition of progress variable including weighted mass fractions of species which are present during this initial phase. Species such as HO_2 and H_2O_2 are important precursors to ignition. However their mass fractions are strongly non-monotonic though the reaction, unlike the mass fractions of products CO_2 and H_2O, which makes preservation of monotonicity of the progress variable troublesome.

The residence time-based reference parameter a presented in Chapter 2 was developed in order to avoid this problem. The direct integration of the case described above and shown in Figure 4.13 was performed using reference variables a and b. The results are shown in Figure 4.14. It is seen that the use of either a or b as a reference parameter successfully removed the sensitivity to initial conditions which is inherent in using a progress variable based on species mass fractions.

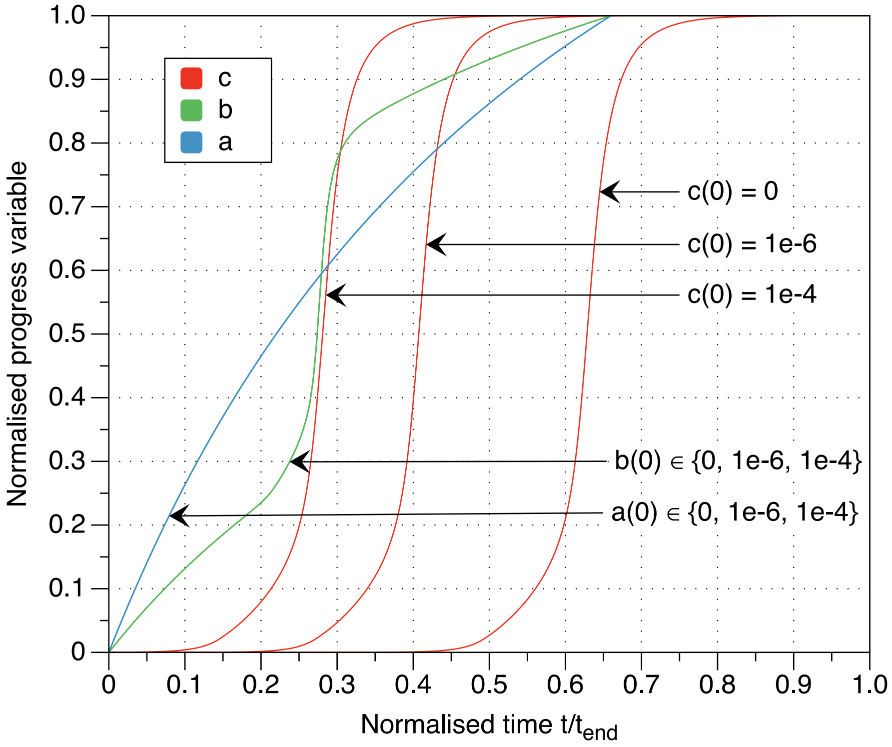

Figure 4.14: Integration of reference variables a, b and c over time. Use of c as a reference variable shows strong sensitivity of ignition delay time to initial conditions, whereas both a and b remain insensitive to the initial condition.

4.7 Summary and Application

This chapter has developed the numerical implementation and the application of the concepts developed in Chapter 3. A robust and accurate framework for integration of scalars over a given joint-pdf was developed, which is capable of handling presumed distributions including analytical joint distributions, presumed marginal distributions combined with presumed copulas, or empirical distributions. This method was then applied to the calculation of the upper and lower bounds of covariance, an important step in the population of a regular turbulent flamelet table where covariance or an equivalent quantity is a parameter. Such a parameter was developed, referred to as the min/max scaled covariance and given the notation σ^*_{XY} for random variables X and Y. The numerical implementation of this method draws on the previously developed numerical integration techniques. Some specifics of the Plackett copula, in particular sampling methods and the determination of the odds parameter, were explored, and a new approach to linking odds parameter with covariance was presented. Finally, a sampling method appropriate for application to sprays was given which is applicable to both analytical distributions and empirical distributions. The numerical methods developed here will be used in the implementation in proceeding chapters.

Chapter 5

Results I: *A-priori* analysis of one-point pdfs in partially-premixed flames

Chapters 2 and 3 described a modelling approach for joint distributions of reference variables. This took the form of combining established presumed marginal distributions for each reference variable and then modelling the dependence between the two by using a presumed copula. Previous work (Darbyshire and Swaminathan 2012; Ruan et al. 2014) has studied the mixture fraction–progress variable joint distribution and modelled dependence using a Plackett copula. It remains to be seen whether this form of the presumed copula is capable of capturing accurately the dependence between these two variables in a wide variety of partially premixed flames. In this chapter, joint distributions extracted from a variety of direct numerical simulations (DNS) and experimental datasets are examined, and a new technique for studying the copula in isolation is developed to assess the suitability of a particular presumed copula for modelling the given joint distribution.

The focus here is on the joint distribution of mixture fraction and progress variable from a selection of direct numerical simulations (DNS) and laboratory experiments spanning a range of partially-premixed combustion regimes However, the techniques developed for the *a-priori* analysis of presumed pdfs are applicable to any set of reference variables. The dependence between mixture fraction and progress variable in DNS data is revealed by considering the underlying copula, which gives more insight into the dependence structure than the correlation alone would allow. Where appropriate, the presumed pdf and the Plackett copula model performance is evaluated against the DNS data, both in terms of goodness of fit metrics on the distributions, and in terms of accuracy of the prediction of statistical quantities that appear in turbulent reacting flow models (especially the temperature T and mean reaction rate $\dot{\omega}$). It is found that the efficacy of the improved presumed joint-pdf depends strongly on the flame type.

It was suggested in (Darbyshire and Swaminathan 2012) that deviation from independence was strongest in regions of high equivalence ratio stratification. Here, two DNS cases are investigated: one with an equivalence ratio stratified slot Bunsen configuration, involving combustion mostly by flame propagation; and a lifted autoigniting jet flame which exhibits strong stratification near the flame base. In addition, experimental data from the Sandia flame series is examined, exhibiting extinction and reignition phenomenon within a nominally non-premixed jet flame.

5.1 Methodology

The modelling approach taken here is to presume the marginal distributions are known and focus on modelling the copula. Both the marginal pdfs and the joint distribution are obtained from the DNS or experimental data. The aim of this study is to look for and quantify dependence between mixture fraction and progress variable in partially-premixed combustion.

5.1.1 Removal of marginals via the inversion method

Bivariate dependence can be isolated and investigated by removing the influence of the marginal distributions from the bivariate distribution. This is done by transforming the marginal distributions P_Z and P_c into uniform distributions U_Z and U_c , while preserving the copula C which relates them. For reference, see (Nelsen 1999, p50). A given bivariate distribution function P_{Zc} can be expressed in terms of its marginal distributions P_Z and P_c and the copula C which joins them:

$$P_{Zc}(\eta, \zeta) = C[P_Z(\eta), P_c(\zeta)] \tag{5.1}$$

It is possible to invert this relationship to study the copula in isolation:

$$C(u, v) = P_{Zc}(P_Z^{-1}(u), P_c^{-1}(v)) \tag{5.2}$$

where

$$\begin{aligned} u &= P_Z(\eta) \\ v &= P_c(\zeta) \end{aligned} \tag{5.3}$$

are the values of the marginal distributions. By replacing the marginal distributions with uniform distributions denoted U_Z and U_c, a new bivariate distribution U_{Zc} is obtained having the same copula as P_{Zc} but with uniform marginal distributions:

$$U_{Zc}(\eta, \zeta) = C\left[U_Z(\eta), U_c(\zeta)\right] \tag{5.4}$$

$$= C\left[P_Z(P_Z^{-1}(\eta)), P_c(P_c^{-1}(\zeta))\right] \tag{5.5}$$

In this study, the distribution functions P_{Zc}, P_Z, and P_c and their inverses, are estimated by their empirical counterparts E_{Zc}, E_Z, and E_c, calculated from DNS or experimental data.

The process of transforming the marginal distributions into uniform random variates is essentially the reverse of the inversion method for the generation of random numbers with a given distribution. The key steps for the inversion method for random number generation using the inversion method are as follows:

1. Take the CDF $P(x)$ and its inverse $P^{-1}(y)$ of the desired distribution,
2. Generate a set of n uniform random variates y_i,
3. Let $x_i = P^{-1}(y_i)$.

Following this procedure, the random variates x_i are distributed with the CFD $F(x)$. The de-marginalisation process is the reverse of this algorithm. It has the following steps:

1. Take samples x_i from the physical system,
2. Calculate the empirical CDF $E(x)$ from the samples,
3. Let $y_i = E(x_i)$.

The resulting values y_i will be uniformly distributed. For a pair of scalars ϕ_1 and ϕ_2, pairs of samples of these scalars may be denoted $(\phi_{1,i}, \phi_{2,i})$ where i indicates the ith sample. Performing the above process simultaneously on these pairs will give a set of pairs $(\psi_{1,i}, \psi_{2,i})$ where each random variable ψ_1 or ψ_2 is uniformly distributed:

$$\psi_{1,i} = E_{\phi_1}(\phi_{1,i}) \tag{5.6}$$

$$\psi_{2,i} = E_{\phi_2}(\phi_{2,i}) \tag{5.7}$$

For example, taking the distribution of H mass fraction versus OH mass fraction in Figure 5.1 for the stratified flame introduced in Section 5.2, which is strongly correlated, it is difficult to discern how much of the structure is due to the dependence between variables and how much is solely due to the marginal pdfs. By removing the influence of the marginal pdfs, the underlying copula may be visualised and it is seen that there

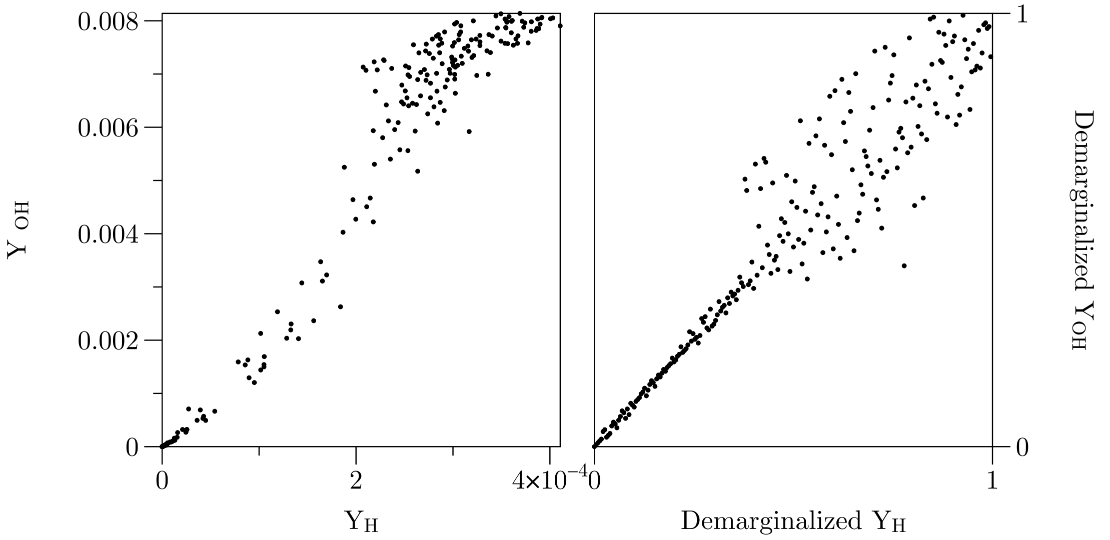

Figure 5.1: Left: H mass fraction versus OH mass fraction in the stratified flame. Right: H mass fraction versus OH mass fraction in the stratified flame after being normalised by their respective marginal distributions.

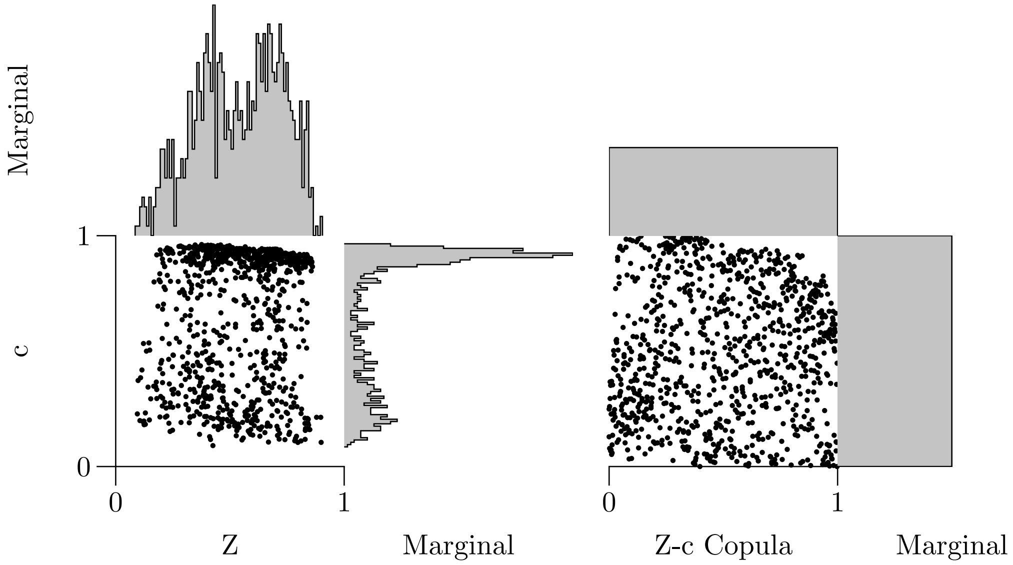

Figure 5.2: Showing the bivariate distributions (scatter plots) and marginal pdfs (histograms) of mixture fraction and progress variable before (left) and after (right) the process of de-marginalisation. Data are for the stratified flame introduced in Section 5.2.

is indeed a strong dependence in this case. This is illustrated in the second panel of Figure 5.1. With the influence of the marginals removed, only the dependence structure remains, showing strong tail dependence — samples are more correlated at the lower end of the distribution and less correlated towards the upper end.

While Figure 5.1 demonstrates this process for two strongly dependent quantities (H and OH mass fractions), Figure 5.2 illustrates this process for mixture fraction and progress

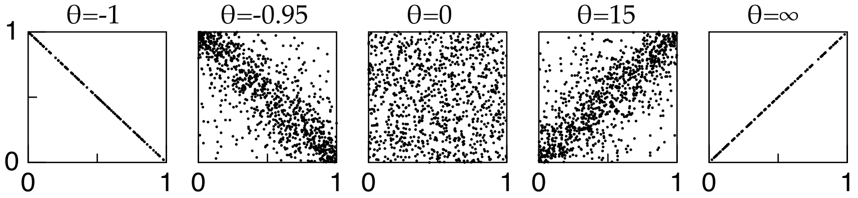

Figure 5.3: Examples of distributions with uniform marginal distributions and a Plackett copula with the given odds parameter θ. Plots range from perfectly negatively correlated (far left) through independent (centre) to perfectly positively correlated (far right).

variable at the same location. Plots of the marginal pdfs of each variable are included for clarification, before and after the above process is applied. The left hand side (scatter plot of the original data) shows some coherent clustering of data points. When the influence of the marginals is removed while preserving the dependence structure, the distribution U_{Zc} (scatter plot on the right hand side) reveals that very little of this coherence is due to dependence between the two variables. At this point in the flow the dependence between mixture fraction and progress variable is very weak, and the sample plot of U_{Zc} looks very close to that of an independent distribution.

This can be seen by comparison to Figure 5.3, which demonstrates the appearance of a range of Plackett copulas ranging from perfectly negatively correlated to perfectly positively correlated. Each scatter plot in Figure 5.3 has uniform marginal distributions. Depicted centrally is a set of samples from the independent distribution, which exhibits no inherent pattern, unlike the other examples which are partially and fully dependent.

5.1.2 Error measurement

To assess the suitability of a copula for modelling the joint distribution of c, Z, a measurement of error is needed. Two such measures are presented here. The first is the L_2-norm of the error between the presumed pdf and the empirical pdf from experiment or DNS. The L_2-norm is defined as

$$||\mathbf{x}||_2 := \sqrt{\sum_i x_i^2} \tag{5.8}$$

where $\mathbf{x}$ is a vector to which the norm is applied and i is the vector component index. The metric referred to from here on as the “L_2-norm of the pdf” is defined as

$$||p_{\text{empirical}}(\eta_i, \zeta_i) - p_{\text{presumed}}(\eta_i, \zeta_i)||_2 \tag{5.9}$$

where (η_i, ζ_j) is the ith sample (typically from the empirical distribution, i.e. the observed quantities from the DNS or experiment). Hence, $p_{\text{empirical}}(\eta_i, \zeta_i) = 1/N$ where

N is the number of samples and the presumed pdf $p_{\text{presumed}}(\eta_i, \zeta_i)$ is evaluated at the points observed in the DNS.

Another appropriate assessment of presumed pdf performance is the ability to predict mean quantities. Such mean quantities are available from the experimental or DNS for comparison. For a scalar ϕ, the mean value $\overline{\phi}$ can be calculated as

$$\overline{\phi} = \int_{\Omega} \phi(\eta) p(\eta) d\eta \tag{5.10}$$

where Ω is the domain of the pdf $p(\eta)$, and η is the state vector. Additionally, given a finite set of samples ϕ_i, the mean $\overline{\phi}$ can be calculated though:

$$\overline{\phi} = \frac{1}{N} \sum_{i=0}^{N} \phi_i \tag{5.11}$$

The same averaging procedure can be done for samples generated from a presumed distribution. However, samples generated from a bivariate Z, c distribution do not directly specify ϕ, and hence the reaction rate cannot be calculated. This poses a problem for calculation of both mean mass fractions and mean reaction rates. Instead, a relationship must be found for the scalar ϕ as a function of mixture fraction and progress variable:

$$\phi = \phi(Z, c) \tag{5.12}$$

This relationship is provided by a flamelet library appropriate for each case.

The same definition of progress variable is used in all of the studies presented in this chapter, so it is presented here. The progress variable c is based on the mass fractions of products:

$$Y_c = Y_{\mathrm{CO_2}} + Y_{\mathrm{H_2O}} + Y_{\mathrm{CO}} + Y_{\mathrm{H_2}} \tag{5.13}$$

$$c = \frac{Y_c}{Y_c^{\max}(Z)} \tag{5.14}$$

The maximum value of the scalar Y_c for a given mixture fraction, $Y_c^{\max}(Z)$, is calculated in an appropriate way for each individual case.

5.1.3 Odds parameter for DNS samples

The Plackett family of copulas, introduced in Section 3.2.3.2, is parametrised by a single variable θ, which is loosely referred to as the odds parameter. The relationship between the odds parameter and the correlation is discussed in Section 4.4. Due to the difficulty in finding a correct mapping between the two, throughout this chapter the correlation is not used as a means of determining the odds parameter when a Plackett copula is

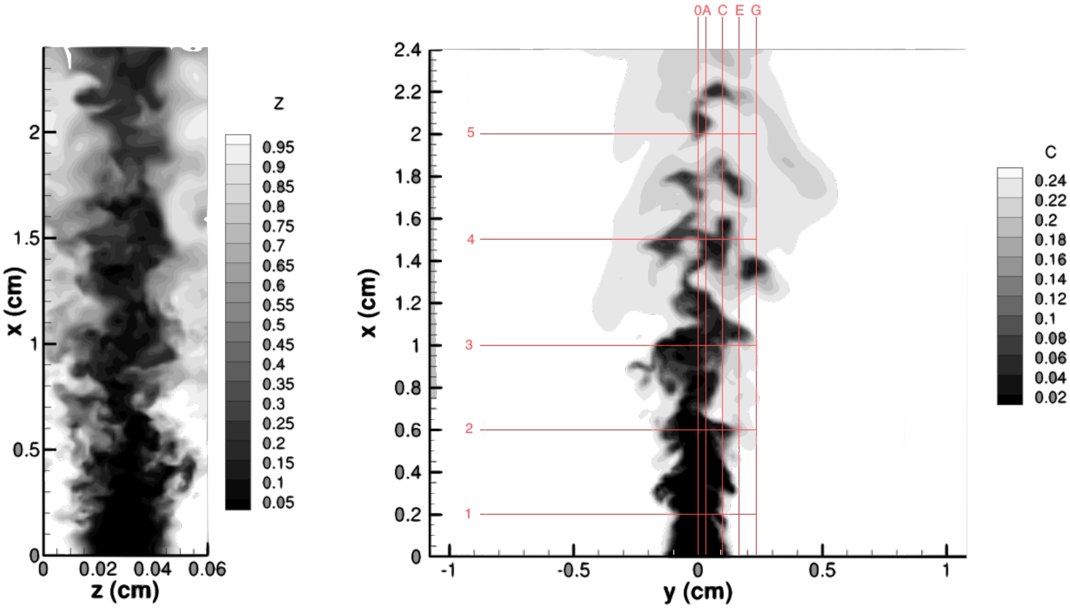

Figure 5.4: Overview of case C2. Left: A central ($y = 0$) span-wise slice showing the variation in equivalence ratio (mixture fraction) along the inlet. Right: An yx-plane slice at the point where the inlet is richest ($z = 0$, $Z_{inlet} = 1$) showing a contour plot of progress variable (unscaled). Sample locations (listed in Table 5.1) are shown in red.

employed; rather, the odds parameter is calculated directly from the available DNS samples. This has its own drawbacks in that one of the contingency diagram quadrants (A, B, C or D) could potentially be zero depending on the choice of midpoint (x_0, y_0). This is mitigated by choosing (x_0, y_0) as the median values of x and y, which is the optimal choice for reducing the asymptotic error in the parameter estimation (Mardia 1970). This ensures that there is always a finite odds parameter with the exception of the trivial case where one of the marginal distributions is a delta distribution.

5.2 Stratified flame DNS

5.2.1 Description of DNS

The first two cases studied are from a series of direct numerical simulations of premixed methane slot flames (Richardson and Chen 2016). Premixed fuel and air flow into the domain through a slot surrounded by a coflow, which consists of hot burned products. The inlet composition is taken from a 2D laminar stratified flame solution.

There are three flames in this series, referred to as C1, C2 and C3. Case C1 is completely premixed with equivalence ratio $\phi = 0.7$. Case C2 is weakly stratified; the equivalence ratio varies from $\phi = 0.41$ to $\phi = 1$ along the direction parallel to the flame. The

Span-wise Location	A	B	C	D	E	F	G
y (mm)	0.317	0.651	0.986	1.320	1.654	1.988	2.323
Stream-wise Location	1	2	3	4	5		
x (mm)	2	6	10	15	20		

Table 5.1: Span-wise and stream-wise locations for case C2

composition of both the coflow (fully burned) and jet (fully unburned) vary in this spanwise direction. Case C3 is similar to C2, but with stronger stratification and an equivalence ratio which varies between $\phi = 0$ and $\phi = 1.46$. In all three cases the global equivalence ratio is $\phi = 0.7$. The original interest in these simulations was to investigate the physics which govern the mixing and dissipation time-scales in "stratified" flames, i.e. flames with a gradient of equivalence ratio.

Cold reactants are injected through the 1.8mm slot at 100m/s into a co-flow of burned products at 25m/s, giving a jet Reynolds number of 2,100. The inlet equivalence ratio is stratified along the z direction, ranging from richer at the outer edge to lean at the centre. The simulation was performed on a $1200 \times 600 \times 360$ grid, which is stretched in the y direction to limit the influence of lateral boundary conditions and periodic in the z direction. A subset of these locations is shown in Figure 5.4, in which every second location in the y direction has been omitted for clarity.

Statistics were collected for a range of points across the domain for 120 time steps over 8 flow through times to ensure that statistics collected were not influenced by large scale motions of the flow field. Sampling began after the flow had reached statistically steady state. Since the stratified flames have reflective symmetry in two of their axes, each set of statistics could be compiled from four self-similar points in each quadrant of the domain, giving a total of $120 \times 4 = 460$ samples for each point. In each of the four similar quarters of the domain, 7 locations in the span-wise direction were selected. In each of these span-wise directions, 5 locations in the stream-wise direction were selected, giving a total of 35 locations of interest, listed in Table 5.1. These sample locations were chosen to capture a wide range of mean mixture fractions (along the cross-stream dimension) and mean progress variables (in the stream-wise dimension).

Mixture fraction is transported as a conserved scalar in the DNS. The mixture fraction at the inlet is normalised such that $Z(\phi = 1) = 1$ and $Z(\phi = 0.41) = 0$. The scaling of the progress variable is between the unburned condition and the equilibrium condition as determined by a series of laminar premixed flamelet calculations over the appropriate range of equivalence ratios.

The flamelet table used for calculating mean quantities is based on premixed laminar flamelets generated by the code PREMIX (Kee et al. 1985). There were 26 methane flamelets run over the range of equivalence ratios found in the DNS, which were all within

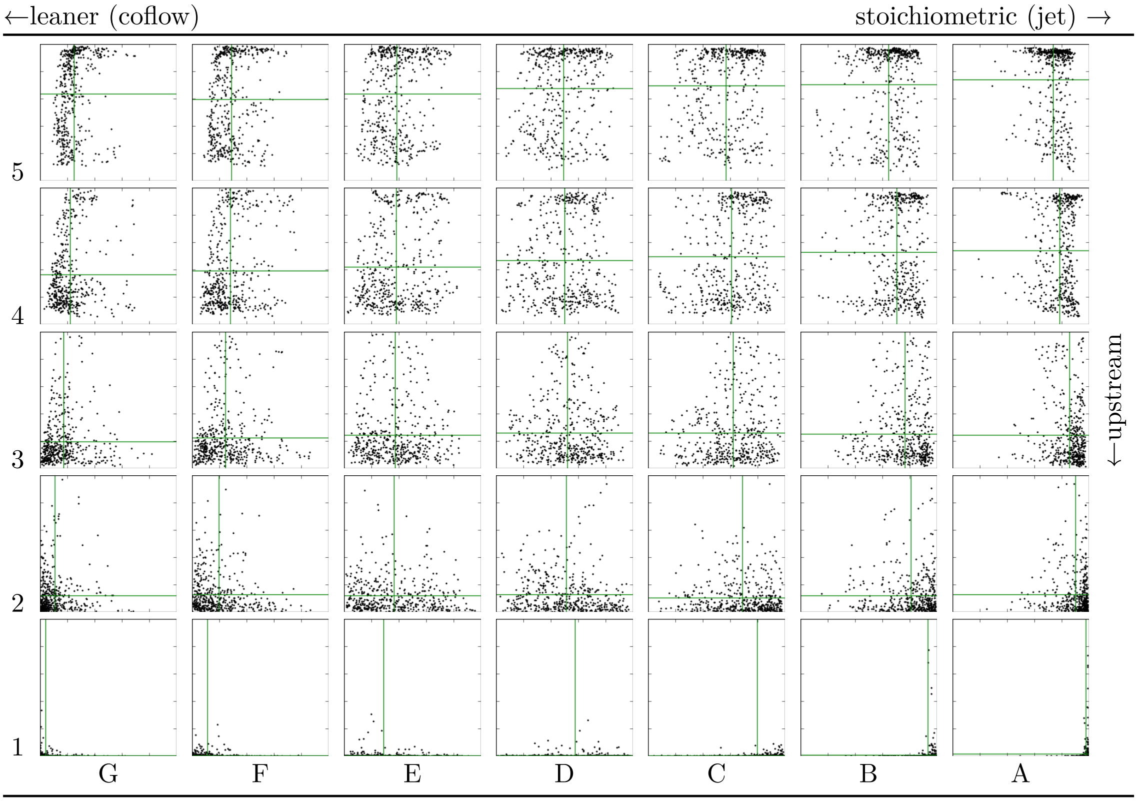

Figure 5.5: c vs Z distributions from the C2 stratified flame DNS for spanwise locations A-G and streamwise locations 1-5, as defined in Table 5.1 and shown in Figure 5.4. Green lines indicate the mean values of Z and c.

the flammability limits (case C2). Due to adaptive mesh refinement, the resolution of each flamelet varies between 100 and 140 points.

5.2.2 Results and Discussion

Figures 5.5 and 5.6 show the results of the analysis for case C2. The corresponding transformed samples (illustrating the shape of the copula with uniform marginals) are shown in Figure 5.6. For each of the individual plots, the horizontal and vertical axes span the range $[0, 1]$ and represent mixture fraction and progress variable, respectively. For this case, $Z = 0$ and $Z = 1$ indicate lean ($\phi = 0.41$) and stoichiometric mixture, respectively.

In the tables, each row and column heading refers to the location where the sample was taken, illustrated on Figure 5.4. Therefore, leftmost columns correspond to locations towards the centre of the of the DNS domain, where the inlet composition is lean; rightmost columns are for locations at the outer edge of the DNS domain (z-axis) where the inlet is stoichiometric. For each of the physical locations identified in Figure 5.4 there is one scatter plot in Figure 5.5, showing the values of the DNS samples (Z, c) at that

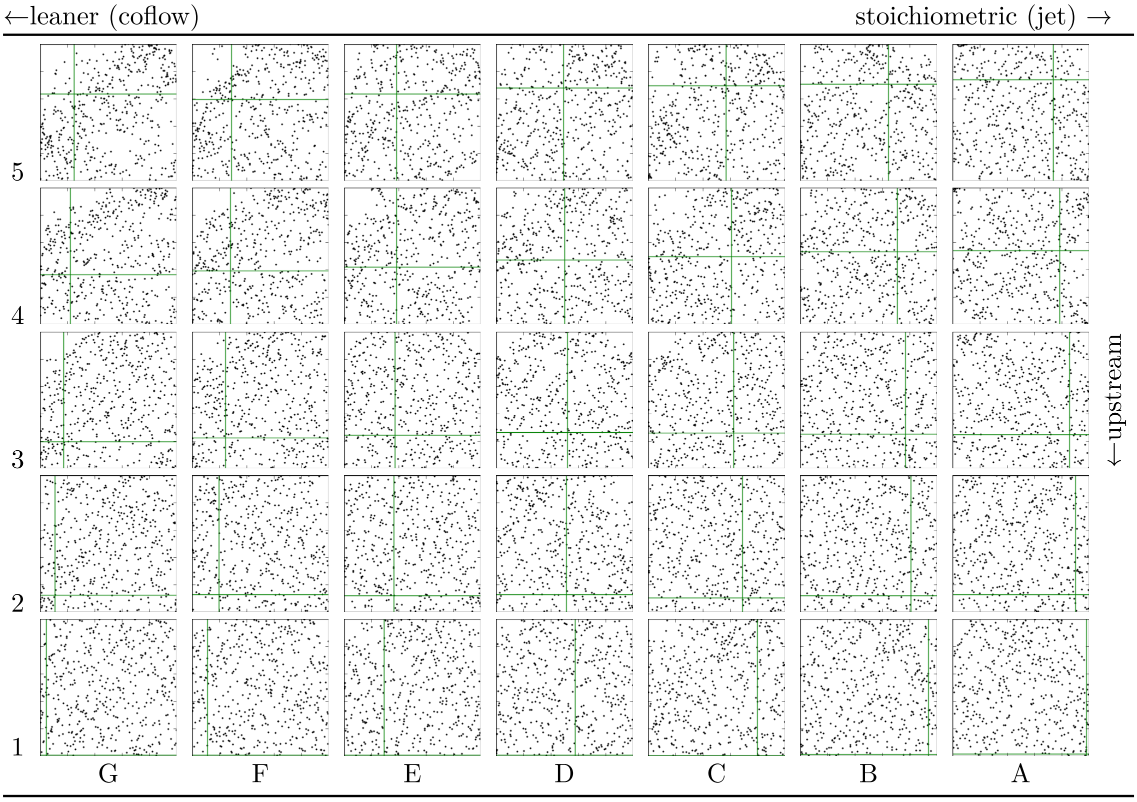

Figure 5.6: Transformed data $(P_Z(Z), P_c(c))$ corresponding to the DNS samples (Z, c) shown in Figure 5.5.

location, and another scatter plot in Figure 5.6 showing the corresponding transformed values $(P_Z(Z), P_c(c))$.

Close to the inlet (row 1, $x = 0.2cm$) the pdf is initially completely independent, due to the coflow being completely burned and the inlet being completely unburned. This is illustrated by the DNS samples lying along the $c = 0$ and $Z = 1$ axes, and is reflected in the scatter plot of the empirical copula which exhibits no obvious dependence (compare with Figure 5.3).

In the intermediate downstream locations (rows 2 and 3, $x = 0.6cm, 1.0cm$) the pdf becomes less singular as mixing and combustion begin to effect significant proportions of the sampled states, broadening the marginal distributions in Z and c space respectively and the movement of each mean $\overline{Z}$ and $\bar{c}$ away from the origin. However, this process happens without introducing any obvious dependence appearing in the copula plots at those locations. The plots of the copula still appear to indicate complete independence of the two parameters by exhibiting no apparent structure in the scatter.

In the final downstream location (row 5, $x = 2.0cm$) there is some weak dependence exhibited in the copula structure, indicated by the absence of samples around the corners $(P_Z(Z), P_c(c)) = (0, 1)$ (top left of scatter plot) and $(P_Z(Z), P_c(c)) = (1, 1)$ (top right) corresponding to fully burned gas which is either very lean or very close to stoichiometric.

Note that these locations on the copula plot should *not* be interpreted as $(Z, c) = (0, 1)$ and $(Z, c) = (1, 1)$ i.e. fully burned mixture at $Z = 0$ and $Z = 1$, respectively. Rather, $(P_Z(Z), P_c(c)) = (0, 1)$ indicates the highest value of c paired with the highest value of Z observed at this location. The absence of samples around $(P_Z(Z), P_c(c)) = (0, 1)$ would then indicate that the leanest samples observed were never fully burned. Similarly, the lack of samples around $P_Z(Z), (P_c(c)) = (1, 1)$ would indicate that the richest samples observed never reach maximum c observed at this location.

In the copula plots for locations G3, G4 and G5, the region around $(P_Z(Z), P_c(c)) = (0, 1)$ (top left corner of each scatter plot) is weakly populated. Moving from each of these locations towards the coflow (horizontal towards column A), this feature is slowly lost as very few samples in column A are approaching the lean flammability limit. The leanest samples never reach the value of Y_c given by the normalisation curve for progress variable $Y_{\mathrm{eq}}(Z)$. Therefore this observed dependence structure – unpopulated upper left corner – is a result of the chosen normalisation of progress variable. This serves to illustrate that the dependence seen is a function of the chosen progress variable normalisation; the same analysis based on a different choice of equilibrium curve would produce different results.

The dependence exhibited in the copulas above are not particularly strong, at any location. As expected, it was found that the mean values calculated from the flamelet table did not depend strongly on the choice of copula (Plackett, independent and Clayton copulas (Nelsen 1999; Clayton 1978) were tested). As such, the results are not presented here, save the mention that there was no observable difference (beyond statistical error) between the means calculated using Plackett copula and the means calculated assuming independence.

5.3 Sandia flame series (experiment)

5.3.1 Description of experiment

Sandia flames C, D, E and F are piloted methane air flames characterised at Sandia National Laboratories using a burner developed by University of Sydney (Barlow and Frank 1998). All flames in the series are partially-premixed methane flames in which the fuel stream is rich (25% CH_4, 75% Air) and the jet velocity is varied between cases, producing a range of Damköhler numbers. The level of local extinction and re-ignition increases from case C up to F, which is very close to blow-off. Local extinction provides a mechanism that can potentially affect the dependence between Z and c, as apparent in the comparison between Figure 5.7 and Figure 5.8, which show the non-normalised progress variable Y_c vs mixture fraction Z for flames D and F, respectively.

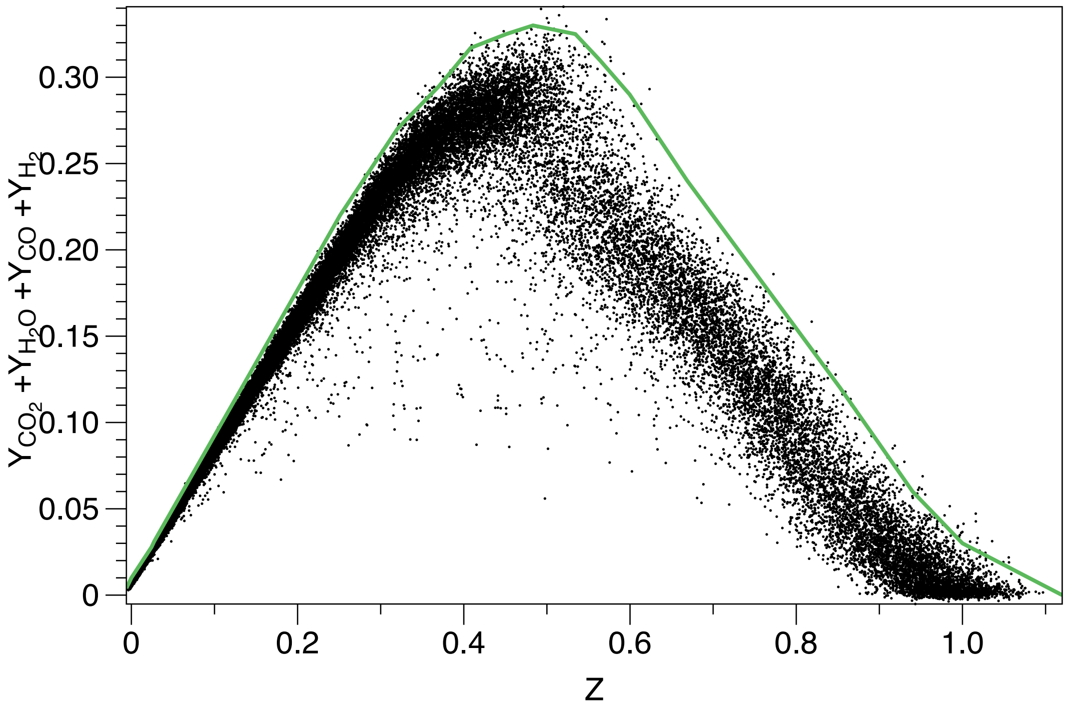

Figure 5.7: Scatter plot of Sandia D, unscaled progress variable vs. mixture fraction. The green line shows the curve $Y_{c,\mathrm{max}}(Z)$ used to normalise the progress variable.

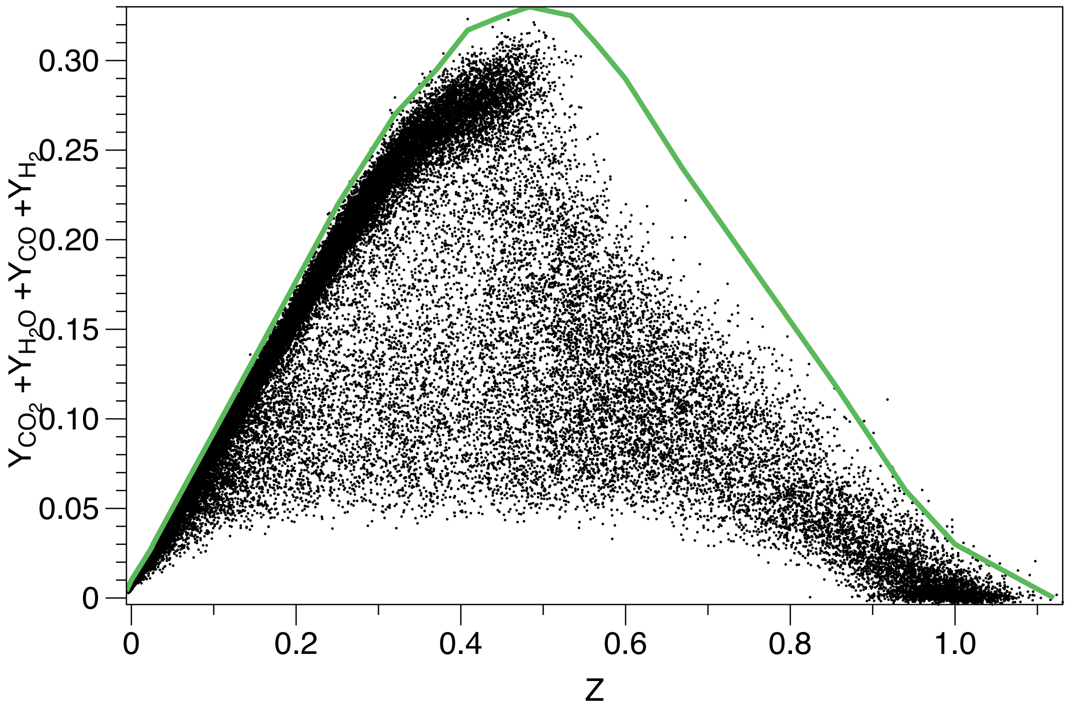

Figure 5.8: Scatter plot of Sandia F, unscaled progress variable vs. mixture fraction. The green line shows the curve $Y_{c,\mathrm{max}}(Z)$ used to normalise the progress variable.

Mixture fraction is experimentally measured (Barlow and Frank 1998) and based on Bilger's definition of mixture fraction (Bilger 1989b). The normalisation of progress variables is shown in Figure 5.7 and Figure 5.8. The maximum value of $Y_{c,\mathrm{max}}(Z)$ is based on the convex hull of the experimental data, with significant outliers removed, and the same curve is used for all Sandia flame cases. The flamelet table for this case was generated from a series of opposed diffusion flamelets in mixture fraction space, generated by FlameMaster (Pitsch 1998) using the GRI 3.0 mechanism (Smith et al. 1999) over a range of equivalence ratios. The solutions were then interpolated onto a mixture fraction progress variable grid. The use of non-premixed flamelets was required to accurately predict scalars outside of the flammability limits of premixed flames.

5.3.2 Results and Discussion

5.3.2.1 Sandia D

Figure 5.9 includes scatter plots showing data (Z, c) sampled at selected radial locations and at the axial positions $x/D = 30$ through $x/D = 75$, where D is the jet diameter. Each plot shows mixture fraction on the horizontal axis and normalised progress variable on the vertical axis. The radial positions, denoted r_i for the ith radial location, are determined by the experimental setup. Higher row number i indicates greater radial position. However, radial positions vary depending on axial position and therefore figures on the same row are not directly comparable. The exact radial locations for flames D and F are shown in Table 5.2.

One notable feature of the experimental samples is that there is very little variation in Z-c space at $x/D = 60$ and $x/D = 75$, because the mixture is by that point very lean and nearly fully burned. At $x/D = 30$ a little more variance is shown. Figure 5.10 shows the corresponding transformed data $U_{Zc}(Z, c) = C[U_Z(Z), U_c(c)]$ (Equation 5.4), illustrating the underlying copulas. Mean quantities $\overline{Z}$ and $\overline{c}$ are marked on each plot, to give a sense of the marginal distributions through their first moment.

Radial locations towards the coflow (r_9 and r_{11}, and r_7 at $x/D = 75$) exhibit tail dependence in the distribution, manifesting as a higher correlation in samples at one of the extremes of the distribution. However, there is very little fuel present at each of these locations and therefore the mean mixture fraction is close to zero. These structures are again artefacts of the progress variable normalisation curve close to $Z = 0$. On the copula plots, the points $P_Z(Z) = 0.5$ and $P_c(c) = 0.5$ represent the median of the observed sample values. The distribution of the samples above the median values (i.e. the scatter observed in the region $P_Z(Z) > 0.5$, $P_c(c) > 0.5$) appears largely independent. Only in the leanest cases (for example, r_{11} at $x/D = 60$) does this region of distribution space display noticeable correlation.

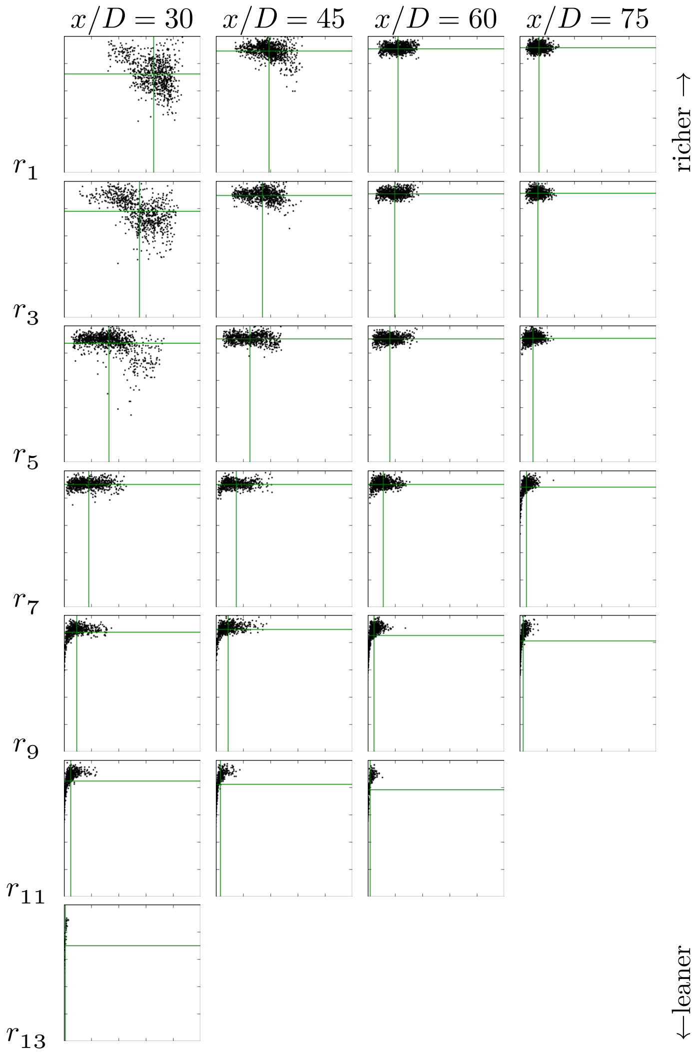

Figure 5.9: Empirical samples of (Z, c) for Sandia D at a selection of axial and radial positions. The mean values $\overline{Z}$ and $\overline{c}$ are marked in each plot.

Moving away from the locations where the mean mixture fraction is extremely low, the downstream locations $x/D = 60$ and $x/D = 70$ are essentially independent across r_1, r_3 and r_5. The region of interest, in which there is significant variance of both mixture fraction and progress variable, lie between r_1 and r_5 at $x/D = 30$. Here there is a deviation from independence, shown by the non-uniform distribution of points in the scatter plot. Location r_5 at $x/D = 30$ (and also r_1 at $x/D = 45$) also exhibits tail dependence. Furthermore, it does not appear that the structures exhibited at these locations can be described by a Plackett copula, which has a particular form as demonstrated in Figure 5.3.

At $x/D = 30$, there is a trend in the correlation with radial direction. Near the centreline (r_1), where the mixture is richer, the overall correlation appears to be negative. Further out (r_9), towards leaner mixture, the correlation becomes positive. This is reflective of the general trend in correlation that might be expected looking at Figure 5.7.

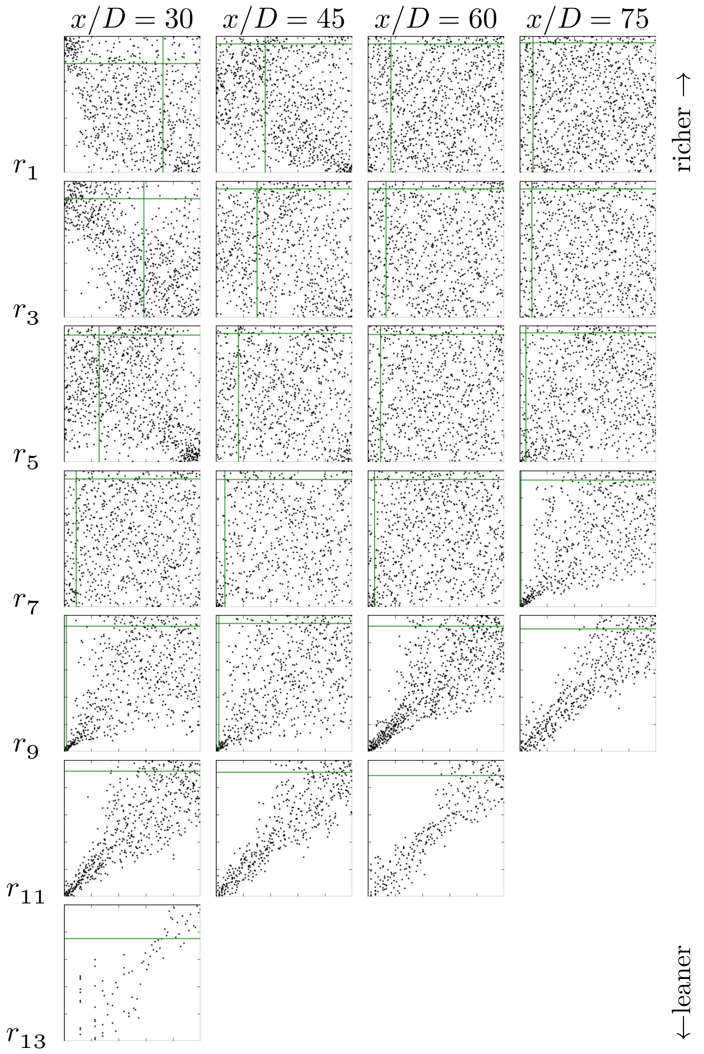

Figure 5.10: Transformed values $(P_Z(Z), P_c(c))$ for Sandia D. The mean values $\overline{Z}$ and $\overline{c}$ are marked in each plot.

5.3.2.2 Sandia F

Scatter plots of (Z, c) for Sandia F are shown in Figure 5.11 and the corresponding copula scatter plots in Figure 5.12. The axial locations chosen for Sandia F are the same as those for Sandia D, but radial locations again differ by experiment and therefore do not correspond directly to the locations analysed for Sandia D.

Overall, the trends observed in this flame are very similar to those observed for Sandia D. There is significantly more local extinction evident in the progress variable scatter, particularly at $x/D = 30$ and $x/D = 45$ (see Figure 5.11). This results in a more pronounced dependence between Z and c in the richer, upstream locations as seen in the case of Sandia D (r_{1-5} at $x/D = 30$ on both copula scatter figures): some areas of $(P_Z(Z), P_c(c))$ space are now totally unpopulated, whereas in Sandia D they were simply less populated. The same structure of a bivariate progress variable distribution for the

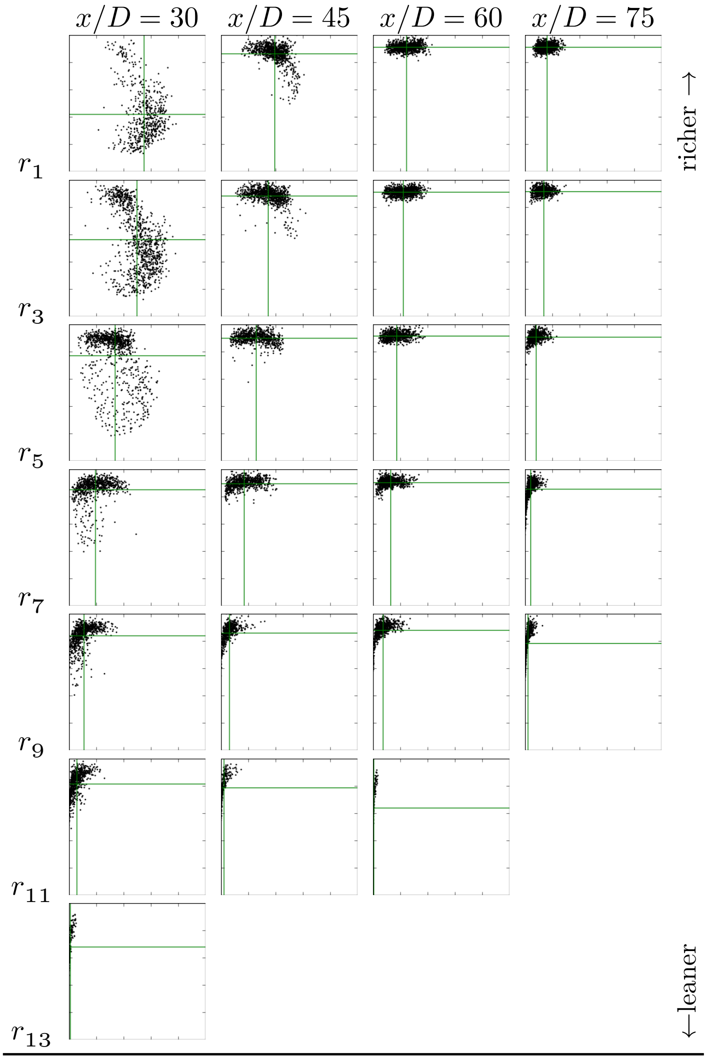

Figure 5.11: Empirical samples of (Z, c) for Sandia F at a selection of axial and radial positions. The mean values $\overline{Z}$ and $\overline{c}$ are marked in each plot.

leanest samples and a univariate progress variable distribution for the richest samples, is displayed here, manifesting as a ">" shape in plots r_1 and r_3 at $x/D = 30$ in Figure 5.12. Recall that the actual marginal distributions of these plots is a uniform distribution. Again, this is a structure that the Plackett copula is not capable of describing.

Weaker dependence is also observed at locations r_7 at $x/D = 45$ and $x/D = 60$ in Figure 5.12, which was not seen at similar locations in Figure 5.10. Strong tail dependence is again exhibited for most of the higher (very lean) radial locations.

To quantitatively compare the accuracy of the copula joint distribution model relative to the distribution, the error metrics and mean quantities discussed in Section 5.1.2 were calculated for Sandia D and F. The quantities considered are the L_2-norm of the joint pdf, and the Favre mean reaction rate, mass fraction of fuel, and temperature, and the results are shown in Figures **??** and **??**. Four locations were chosen from each of Sandia

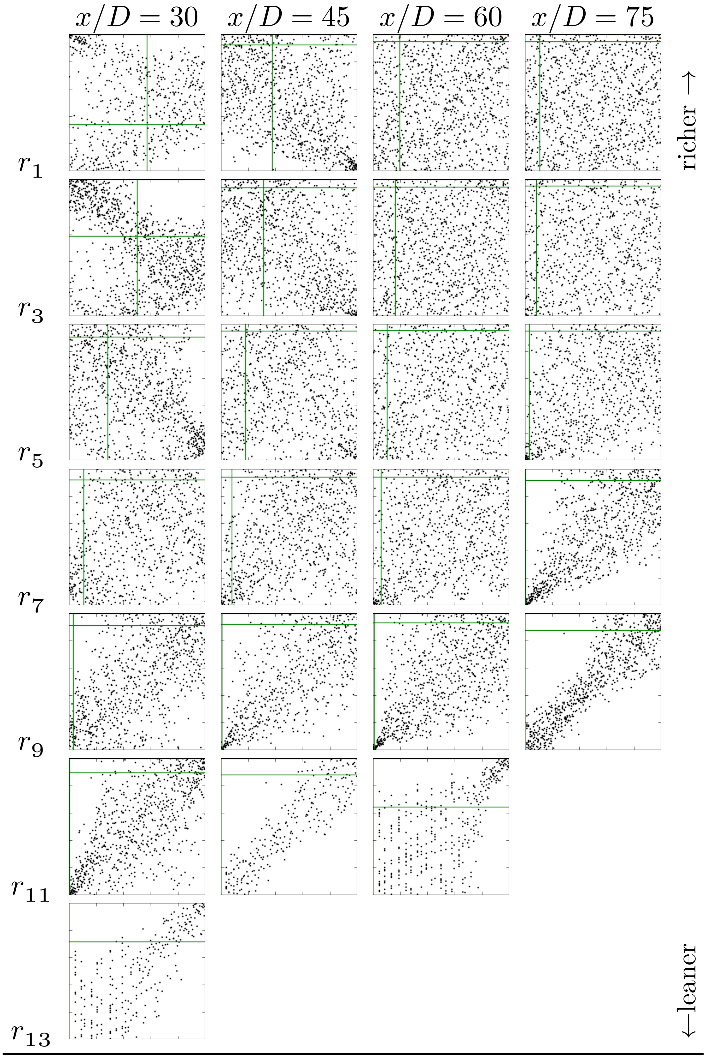

Figure 5.12: Transformed values $(P_Z(Z), P_c(c))$ for Sandia F at a selection of axial and radial positions corresponding to Figure 5.11. The mean values $\overline{Z}$ and $\overline{c}$ are marked in each plot.

D and F, specifically r_1, r_3 and r_5 for $x/D = 30$ and r_1 for $x/D = 45$, which showed the most complex dependence structures for copula modelling to capture.

The Favre averaged quantities were computed by integrating the instantaneous quantities from the laminar flamelet table over the relevant joint distributions. In this way, three different joint-distributions (the empirical joint-pdf from experimental observations; the independent copula combined with empirical marginal distributions; and the Plackett copula combined with empirical marginal distributions) were used to calculate the values of mean quantities and then compared. The integration was performed using a Monte Carlo method, in which (Z, c) samples were generated from each distribution and the corresponding laminar flamelet values averaged.

The L_2 norm of the difference between the empirical pdf and the modelled pdf is a direct comparison of the presumed pdf to experimental data, without considering the

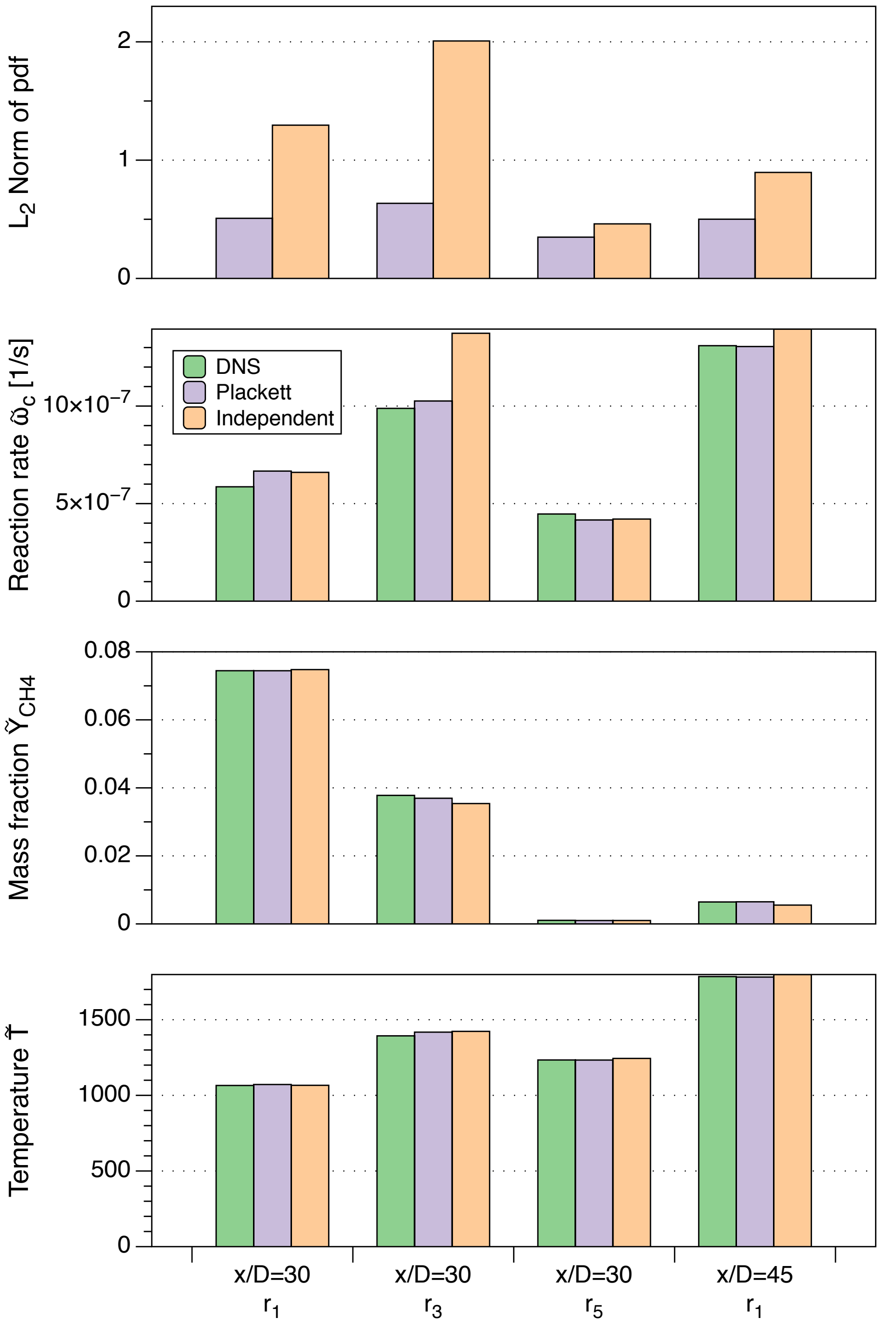

Figure 5.13: Comparison between predictive capability of Plackett and Independent copulas from Sandia D flame at 4 selected locations. From top to bottom: L_2-norm of error in pdf; Mean reaction rate of progress variable; Mean mass fraction Y_{CH_4}; mean temperature $\widetilde{T}$.

effect on mean quantities. For Sandia D (Figure 5.13), the Plackett copula shows strong potential for reducing the error in the joint distribution. Use of the Plackett copula resulted in lower error values at each of the four points of interest, the most significant improvement over the independent copula being for r_3, $x/D = 30$.

However, this general trend of more accurate pdf modelling does always have a significant effect on mean quantities. At r_3, $x/D = 30$, which showed the highest reduction in the L_2-norm of the error, the modelled mean reaction rate is significantly more accurate when a Plackett copula is applied. However, there is only a marginal improvement in fuel mass fraction and temperature improvements at this point. At each of the other locations, the use of a Plackett copula has only a minor affect on the mean quantities predicted, although in most instances it offers a marginal *improvement* over the independent copula. This insensitivity to dependence in the joint distribution is likely due to the fact that the one-point distributions are so compact in Z-c space that the scalar values from the laminar flamelet table do not vary greatly within the region where most of the probability lies.

The results for Sandia F (Figure **??**) show similar trends. Despite significant reductions in the L_2-norm of the error in the pdf for some locations (at r_3, $x/D = 30$ for example) was significantly reduced relative to the use of independent Z-c. Location r_5 at $x/D = 30$ showed no improvement in modelling the joint pdf, since the distribution at that location is close to independent. With regard to mean quantity calculations, there was no significant improvement in accuracy at any of the locations shown for any of the mean quantities considered.

Considering these results, it is concluded that while the joint distributions encountered in the Sandia flame series can by modelled more accurately by the Plackett copula than the independent copula (as shown by lower L_2-norm of error), the importance of this modelling improvement on the prediction of mean quantities of interest is small.

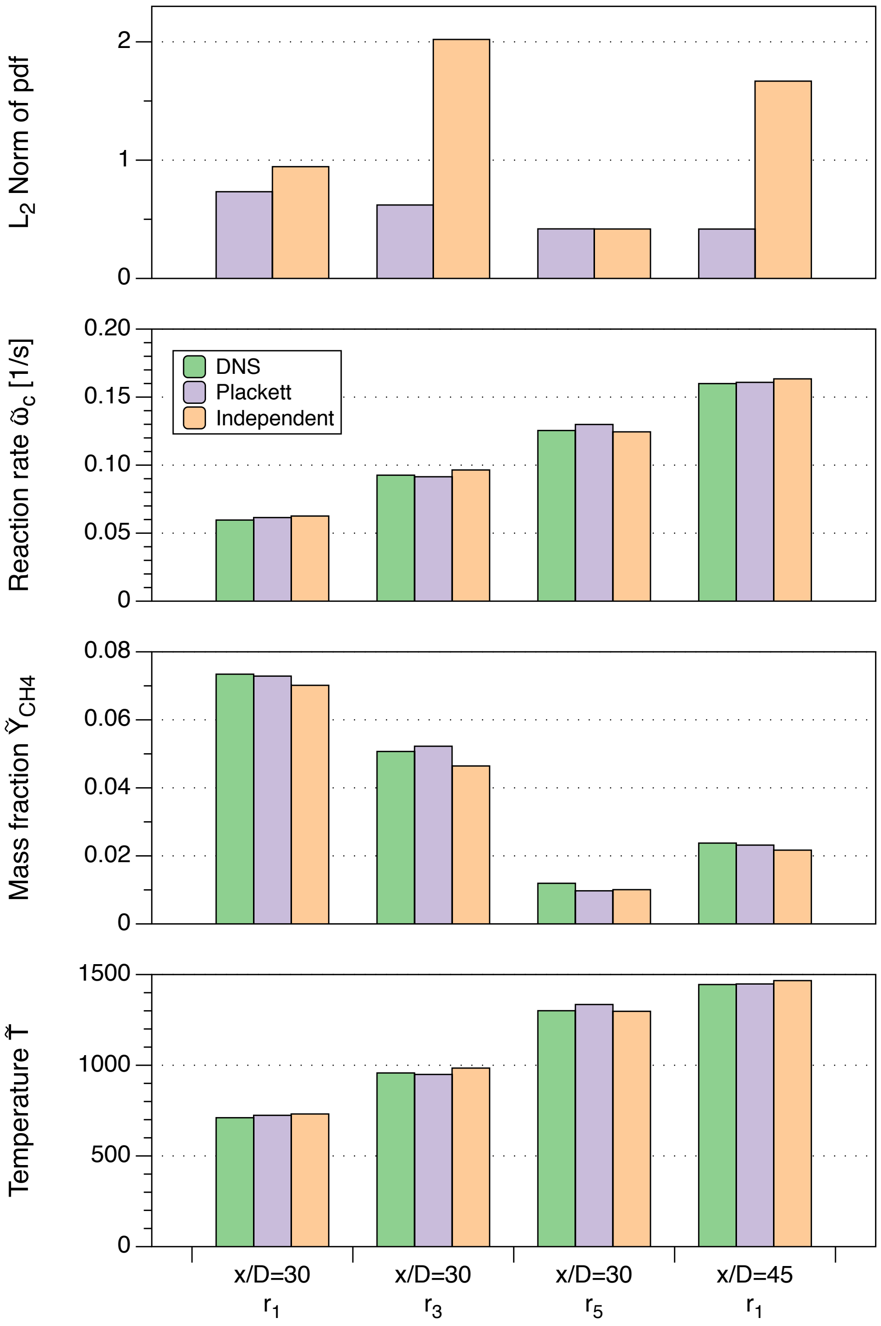

Figure 5.14: Comparison between predictive capability of Plackett and Independent copulas from Sandia F flame at 4 selected locations. From top to bottom: L_2-norm of error in pdf; Mean reaction rate of progress variable; Mean mass fraction Y_{CH_4}; mean temperature $\widetilde{T}$.

	Sandia D						Sandia F					
x	0.75	15	30	45	60	75	0.75	15	30	45	60	75
r_{-3}	-20											
r_{-2}	-2	-4	-6	-4	-10	-10	-1	-4	-6			
r_{-1}	-1	-2	-3	-8	-5	-5	-2	-2	-3	-5	-5	-10
r_0	0	0	0	0	0	0	0	0	0	0	0	0
r_1	1	2	3	4	5	5	1	2	3	4	5	10
r_2	2	4	6	8	10	10	2	4	6	8	10	20
r_3	3	6	9	12	15	20	3	6	9	12	15	30
r_4	4	8	12	16	20	30	4	8	12	16	20	40
r_5	5	10	15	20	25	40	5	10	15	20	30	50
r_6	6	12	18	24	30	50	6	12	18	24	40	60
r_7	7	14	21	28	40	60	7	14	21	28	50	70
r_8	8	16	24	32	50	70	8	16	27	32	60	80
r_9	9	18	27	40	60	80	9	18	33	40	70	
r_{10}	10	20	30	48	70		10	20	39	48		
r_{11}	11	22	36	56			11	22		56		
r_{12}	12		42				12					
r_{13}	14						14					
r_{14}	16						16					

Table 5.2: Radial locations (mm) for Sandia D and F.

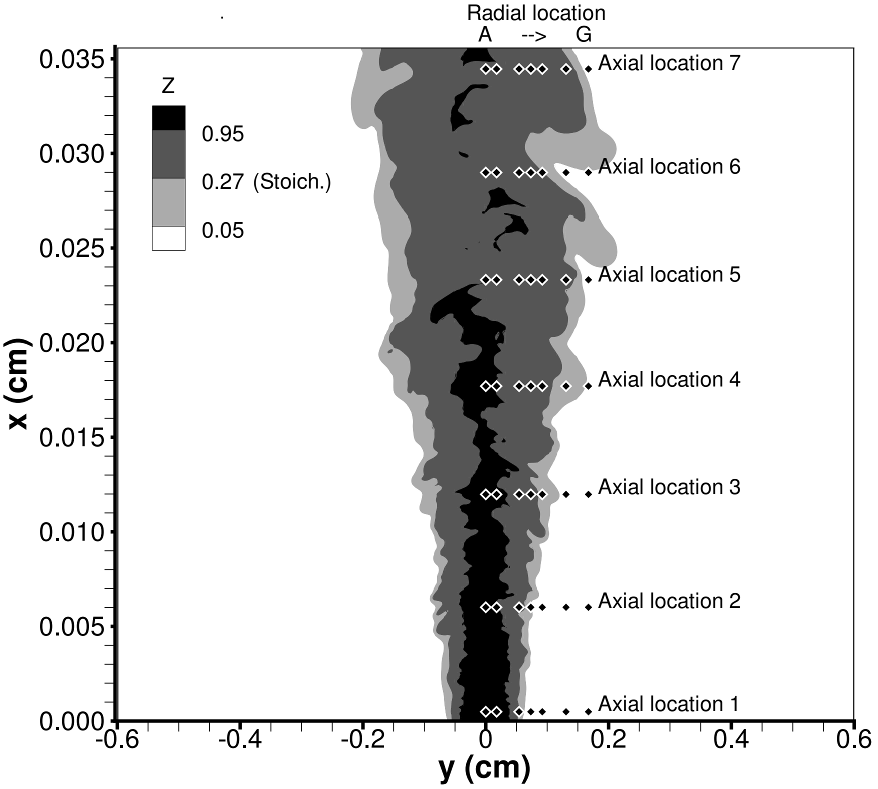

Figure 5.15: A yx-plane cross section of the full DNS domain of the lifted ethylene flame. The contour plot of mixture fraction is shown with sample locations marked.

5.4 Autoignition stabilised lifted flame DNS

5.4.1 Description of DNS

This DNS case (Knudsen, Richardson, Chen, et al. 2011; Yoo, Richardson, et al. 2011), shown in Figure 5.15, is of an auto-igniting ethylene slot jet flame surrounded by a hot (1550K) air coflow. The bulk velocity of the jet is 204m/s, and the coflow velocity 20m/s. The composition of the slot jet is 82% N_2 and 18% C_2H_4 by volume and the temperature is 550K. Sample locations are marked in Figure 5.15 as black diamonds (the corresponding reflections in the line $y = 0$ are not marked). Each sample location has an axial and radial location identifier (e.g. “A4”).

Mixture fraction is based on the mass fraction of nitrogen:

$$Z = \frac{Y_{N_2} - Y_{N_2}^{coflow}}{Y_{N_2}^{jet} - Y_{N_2}^{coflow}} \tag{5.15}$$

such that $Z = 1$ in the jet and $Z = 0$ in the coflow, giving a stoichiometric mixture fraction of $Z_{st} = 0.27$.

5.4.2 Flamelet table and normalisation of progress variable

This flame is stabilised by autoignition promoted by the hot oxidiser stream, and therefore the flamelet table used for estimating the mean quantities is calculated from an unsteady auto-igniting flamelet computed in mixture fraction space. This calculation is done with the unsteady zero dimensional conditional moment closure (CMC) code described in Section 2.1.4.5 on a uniform mixture fraction grid with 201 points, with the same chemical mechanism as applied in the DNS (Yoo, Richardson, et al. 2011). The AMC model (O'Brien and Jiang 1991) is used to describe the scalar dissipation rate as a function of mixture fraction with the maximum value given as $2000s^{-1}$. This corresponds to about 60% of the critical value at which autoignition is prevented and representative of the peak conditional scalar dissipation rate seen in the DNS. The same CMC code is used with a peak conditional scalar dissipation rate of $1s^{-1}$ to calculate a steady state fully-burned solution which is used as the burned limit in order to normalise progress variable as a function of mixture fraction.

5.4.3 Results and Discussion

Figure 5.16 shows kernel density estimation plots of the mixture fraction progress variable joint-pdf. In this plot, and all subsequent plots, only valid pdfs, where $\overline{Z}$ and $\overline{c}$ are within the range $[0.01, 0.99]$ are shown, to exclude pdfs which are delta functions in at least one marginal and therefore essentially univariate. This removes locations close to the inlet, where the fluid has not had time to mix. The leftmost plot corresponds to locations along the centreline, while the rightmost is the outermost location.

The initial stages of an autoignition process may be observed at location E3, where the composition around the most reactive mixture fraction has begun to ignite. Moving downstream, the autoignition continues until it reaches the fully burned state at the stoichiometric mixture fraction at E6. The majority of mixture never reaches its fully burned state corresponding to $c = 1$: fully burned mixture is almost always found close to the stoichiometric mixture fraction $Z = 0.27$ for this case, as fluid with richer or leaner equivalence ratios are slower to ignite and are convected out of the domain before doing so.

At locations where the majority of the mixture is rich (e.g. columns A, B, and C), the Z-c correlation is negative. In column F the mean mixture fraction is close to stoichiometric and the pdf takes a triangular shape. In column G, featuring locations with the leanest conditions, the correlation is positive. Further analysis of the covariance observed in this DNS case is presented in the following section (5.5), which reveals that the sign of Z-c correlation switches around the mean stoichiometric mixture fraction line.

Figure 5.17 shows the transformed distributions corresponding to the joint pdfs shown in Figure 5.16. The locations with richer mixture, specifically columns A through D,

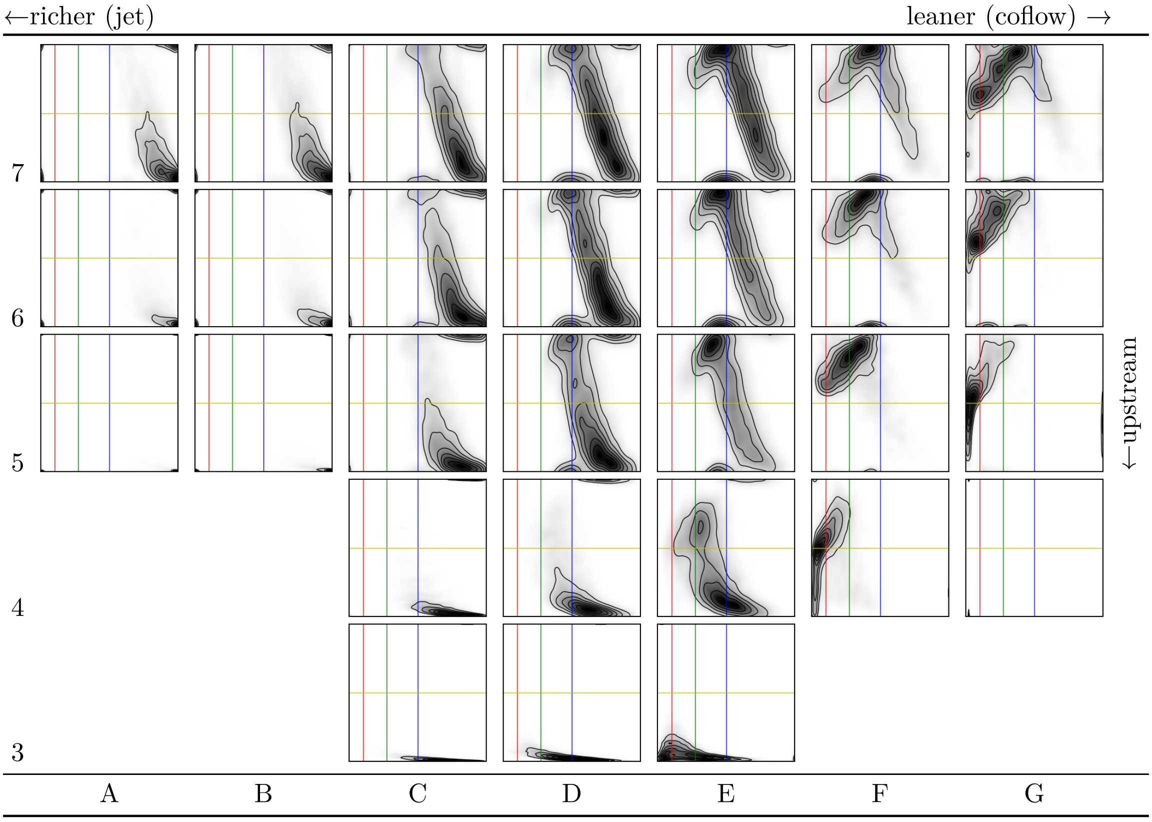

Figure 5.16: Mixture fraction-progress variable joint-pdfs for the lifted flame. Sample locations with singular pdfs have been omitted. Dark indicates high probability, light low probability. Green line: stoichiometric mixture fraction; Red line: approximate value of most reactive mixture fraction; blue line: $Z = 0.5$; yellow line: $c = 0.5$.

indeed exhibit significant negative correlation between mixture fraction and progress variable. Furthermore, they show simple dependence structures which could reasonably be expected to be well captured by a Plackett copula. Locations where most of the samples are lean or stoichiometric (columns F and G), the distribution takes on a trimodal shape, wherein there is a linear region of high probability which indicates that Z and c will be correlated, but an additional region of high probability at an opposing corner. For example, case F2 has a region of high probability spanning a linear stretch in P_Z, P_c space from $(0, 0)$ to around $1, 0$, indicating that for the approximate range $P_Z \in [0, 0.9]$ (i.e. the leaner 90% of observed samples) there is a positive correlation between Z and c. However, there is also a region of high probability at $(P_Z, P_c) = (0, 1)$ which indicates that for the richest observed samples ($P_Z \approx 1$) the distribution of c is bimodal, with a significant proportions of the observed values being very close to the maximum and minimum observed values of c at that sample location ($P_c \in \{0, 1\}$. In column E, where mean mixture fraction is slightly richer than stoichiometric, even more intricate dependence structures are observed, sometimes showing up to 6 local maxima of the transformed distribution. At location E5 for example, there is positive correlation for the leaner samples ($P_Z < P_Z(0.5)$) but negative correlation for the richer samples

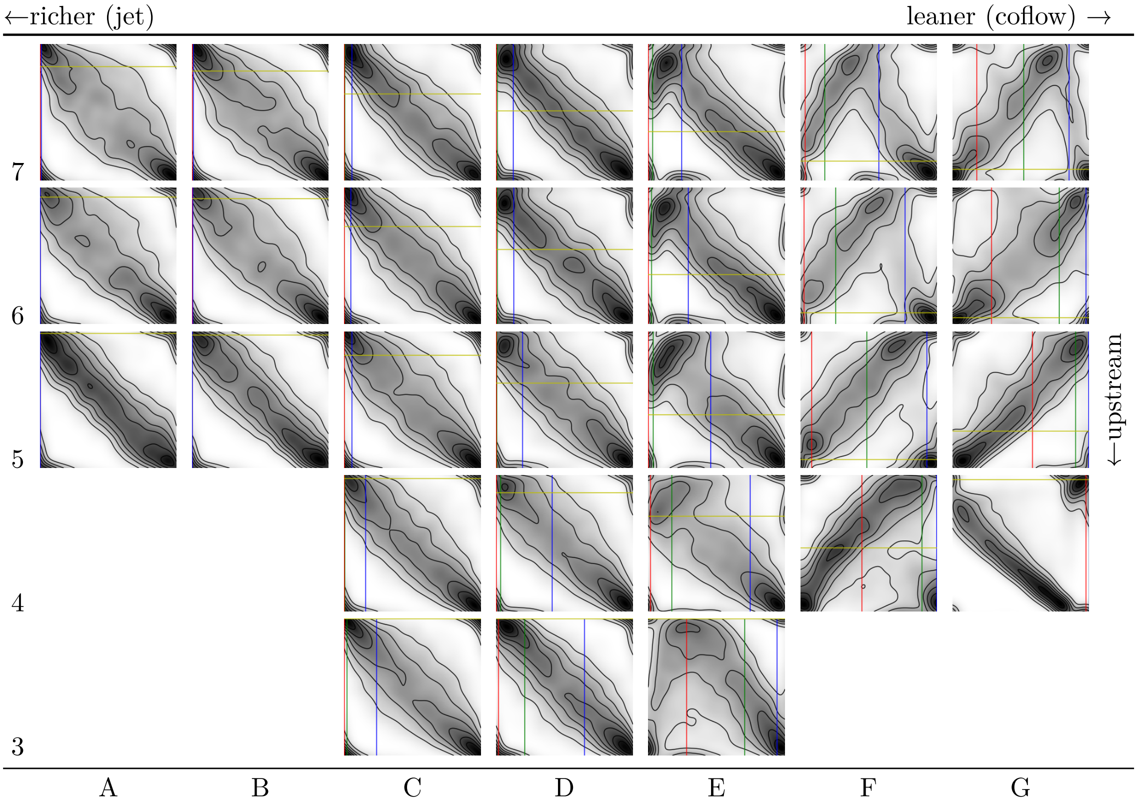

Figure 5.17: Kernel density estimation plot of $(P_Z(Z), P_c(c))$. Dark indicates high probability, light low probability. Green line: $P_Z(Z_{st})$; Red line: $P_Z(Z_{mr})$, where Z_{mr} is the approximate value of the most reactive mixture fraction; blue line: $P_Z(0.5)$; yellow line: $P_c(0.5)$.

$(P_Z > P_Z(0.5))$ while also suggesting that the leaner samples tend to be the most burned $(P_c > P_c(0.5))$ while the richer samples tend to be the least burned $(P_c < P_c(0.5))$. This results in the appearance of a "T" shaped distribution, rotated 45° anticlockwise, in which the "top half" and "bottom half" of the "T" are enclosed by the lines $P_Z(0.5)$ and $P_c(0.5)$ (blue and yellow lines on the plot, respectively).

It is therefore apparent that the dependence structures exhibited in rows E through F (where the mixture is typically lean or stoichiometric) can not be well captured by a Plackett copula, due to the restricted form of the dependence it can describe.

This restriction on the form of the dependence is show in Figure 5.18, which shows the presumed joint pdf constructed from uniform marginals and a Plackett copula with the same odds parameter as the DNS data. In the majority of locations it appears superficially to be a very good fit to the original transformed pdfs shown in Figure 5.17. As expected, the trimodal shape of the pdf is not captured in columns F and G, where the exact positioning and weighting of the three high probability regions of the joint pdf effect the value of the calculated odds parameter. As a result, the Plackett copula variously presents a band of positive or negative correlation in this region. At any location in which the odds parameter is close to 1 (independence), there is no obvious

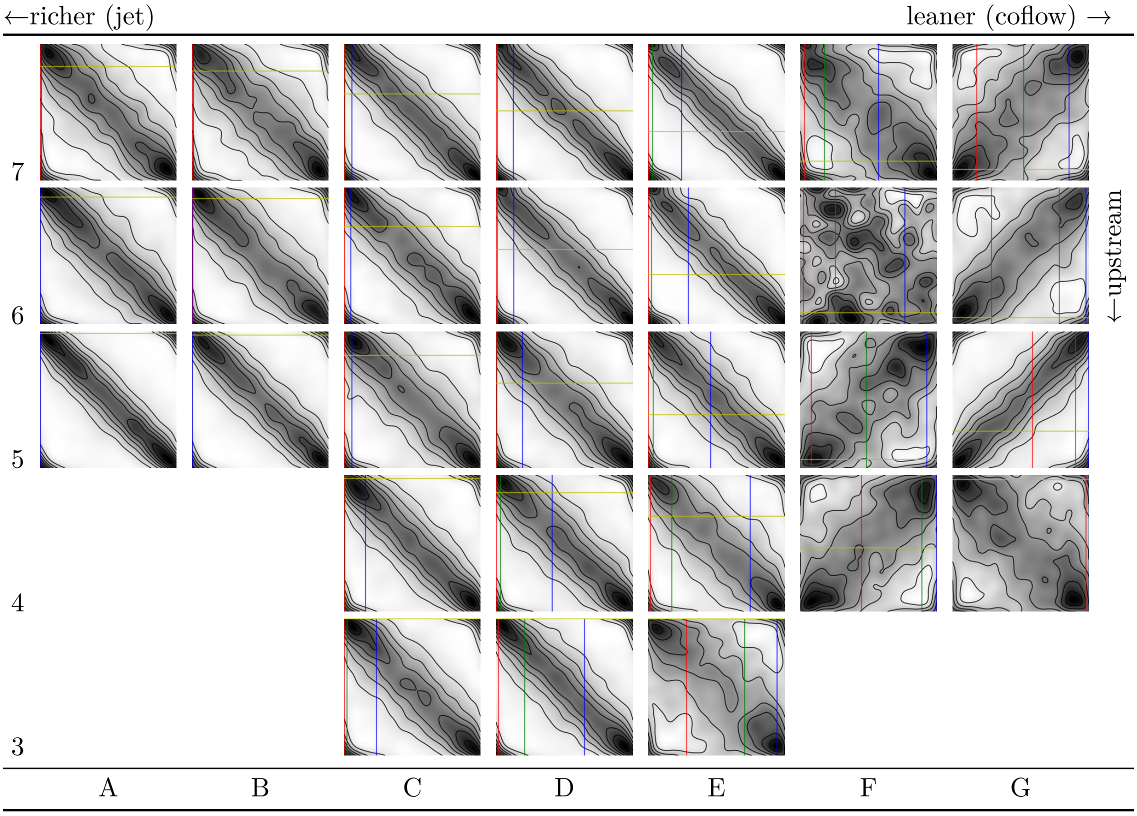

Figure 5.18: Kernel density estimation plot produced by the Plackett copula. For legend, see Figure 5.17.

large scale structure in the contours and only noise is observed. In particular, location F6 looks close to independent, but from Figure 5.17 we see that it should not be. In the richer region (columns A-E) the original transformed pdfs show slightly more tail dependence than the Plackett copula distributions but are otherwise well modelled by it.

For reference, both the Plackett copula and the empirical copula plots from Figures 5.17 and 5.18 are reproduced in Tables B.1 to B.5 in Appendix B, along with relevant statistical quantities.

Figure 5.19 shows the values of mean temperature obtained by integrating the flamelet table using the joint-pdf from the DNS, and using the marginal pdfs from the DNS in conjunction with the Plackett copula or the independent copula. The error in the predicted mean temperature is almost always lower in the case of the Placket copula than in the independent pdf, indicating that the Plackett copula offers a significant modelling improvement over the assumption of independence. This is even more evident in the case of the reaction rate of progress variable (Figure 5.20). The Plackett copula offers substantial improvement in the predictions for most of the samples in columns A through D where the dependence structure is simple. In locations where it performs more poorly than the assumption of independence, for example D6 and D7, this is due to

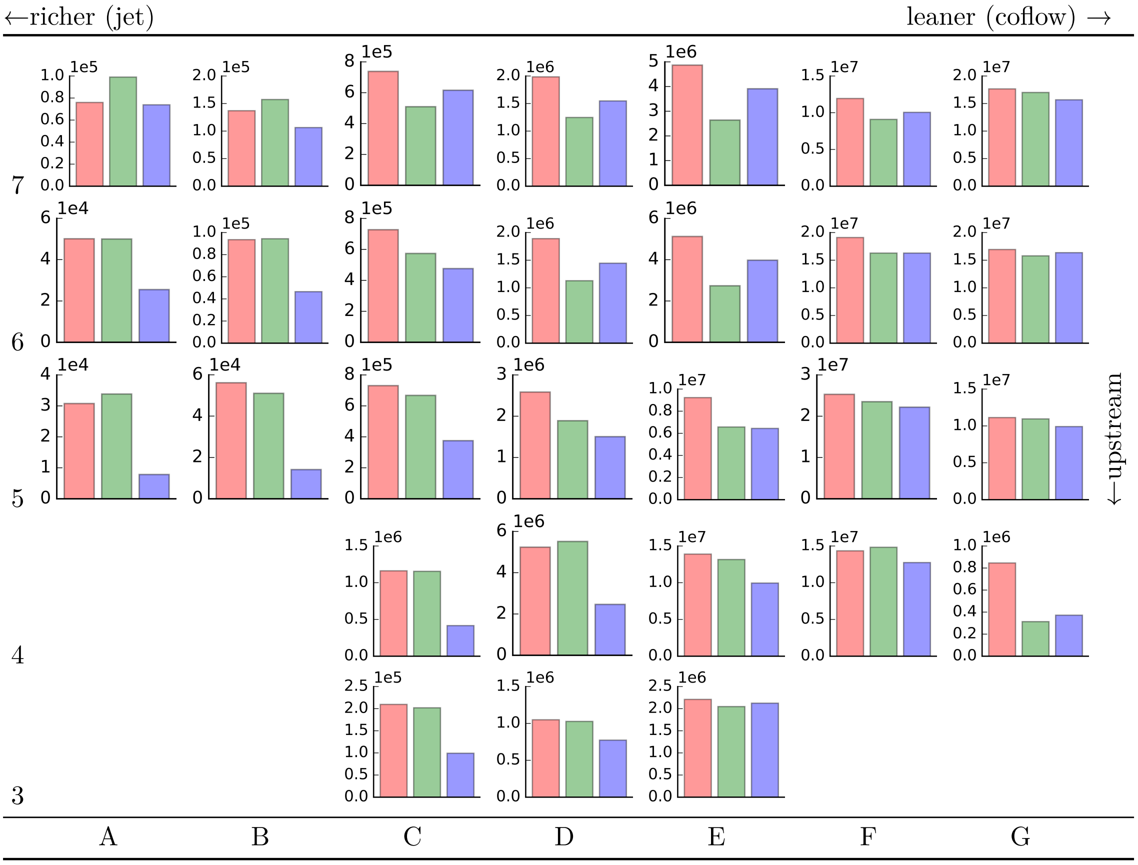

Figure 5.20: Mean reaction rate of progress variable $(1/s)$ predicted by the flamelet table with different presumed pdfs. Red: pdf from DNS; green: Plackett copula; blue: independent.

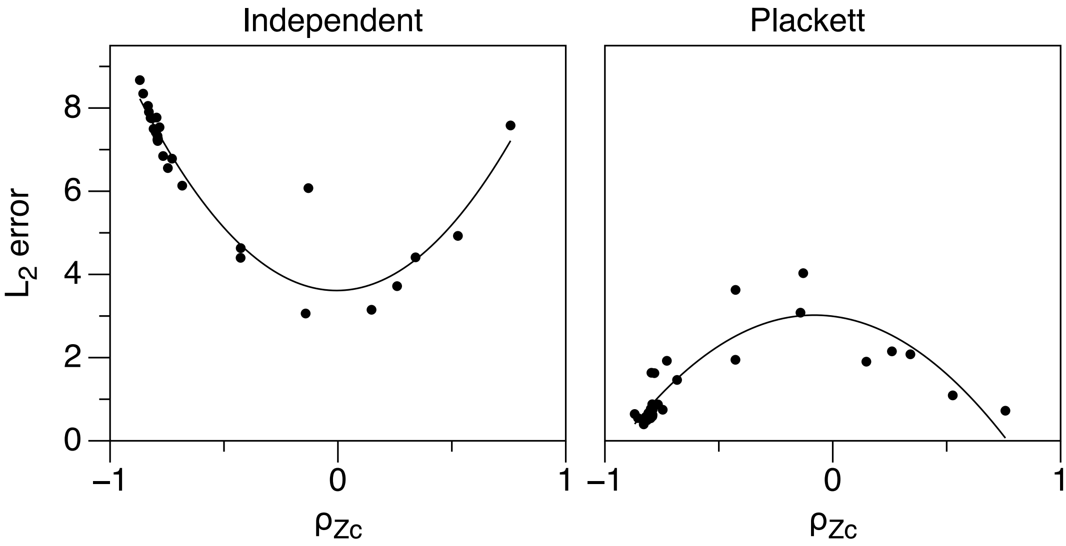

Figure 5.21: L_2 norm of error between empirical and modelled pdfs for empirical pdfs with a range of Pearson correlation coefficients. The error is shown for independent and Plackett-based modelled pdfs. The trend lines shown are quadratic curves for illustration purposes only.

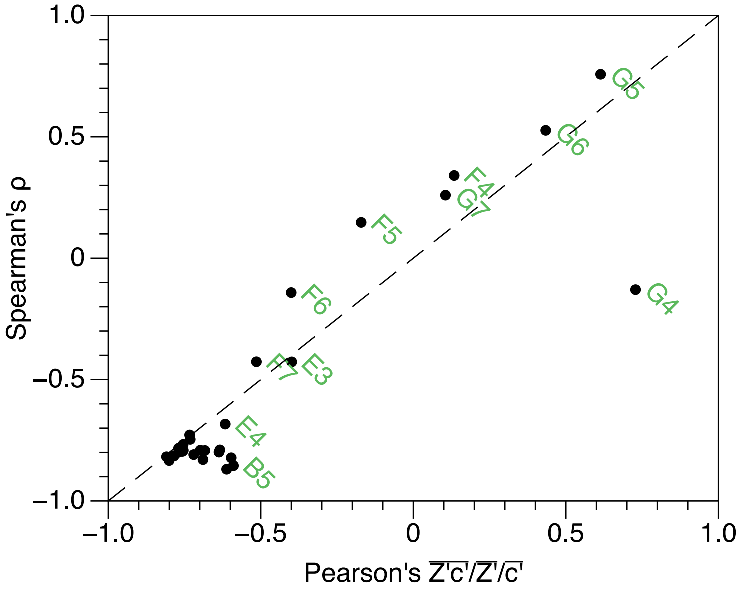

Figure 5.22: Pearson correlation coefficient r_{Zc} versus Spearman's ρ_{Zc} for DNS samples at labelled locations. The line $\rho_{Zc} = r_{Zc}$ is included for comparison.

as G4, where Spearman's ρ_{Zc} is much higher than the Pearson correlation, indicate a non-linear but still monotonic dependence between parameters. Substantial differences between these two measures of dependence is an indication that the dependence between the Z and c is more complex than can be described by a single parameter, and the modelling of such pdfs requires the use of joint distribution models with additional reference variables. However, the Plackett copula provides an improvement across a wide range of conditions encountered in Sections 5.2-5.4 and adding further complexity to the joint-pdf model in the form of additional statistical reference variables is expected to yield limited improvement in the predictions of pdf-integrated reaction rates, or other required source terms.

5.5 Further details of ethylene, contour lines, FGC

The relationship of the observed Z-c correlation to the stoichiometric mixture fraction for the lifted ethylene case discussed in the previous section can be further explored by considering the contours of mean mixture fraction and correlation Z-c in the DNS. To do so, quantities averaged in both time and the z-direction are calculated from the DNS data for each point in the x-y plane. These averaged quantities are given by

$$\tilde{\phi}(x,y) = \frac{1}{\bar{\rho}} \frac{1}{60{,}000} \sum_{i=1}^{400} \sum_{j=1}^{150} \rho\phi(x,y,z_i,t_j) \tag{5.16}$$

where over Z_i is one of 400 locations in the z direction over the range $[0, 3H]$ and t_j is one of 150 timesteps over the same range as above, giving a total of 60,000 samples per grid point. The progress variable c, in the context of this analysis, is normalised by the maximum value of $Y_c(Z)$ found in the entire domain.

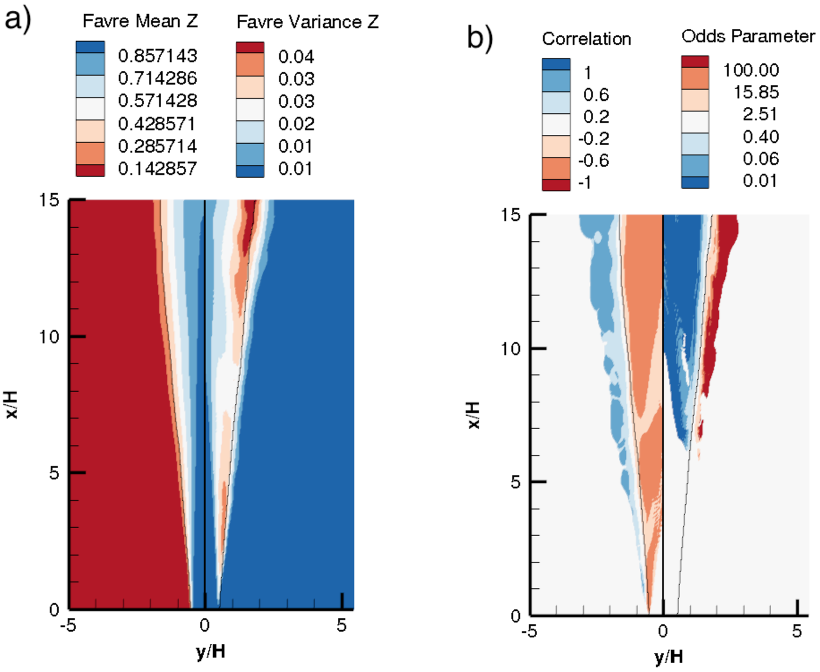

Figure 5.23: x-y plane values of a) Mean (left) and variance (right) of mixture fraction; b) Z-c correlation and odds parameter. Black line shows the contour of stoichiometric mean mixture fraction.

Contours of Favre mean and variance of mixture fraction and progress variable are shown in Figure **??**. The Z-c correlation (Figure 5.23b, left) has significant values all the way back to the inlet, whereas the odds parameter (Figure 5.23b, right) has significant values only around locations of high mixture fraction and progress variable variance. The correlation is clearly separated into regions of positive and negative correlation on either side of the stoichiometric mean mixture fraction line.

The strong correlations seen in the DNS can be explained using the CMC solution. Figure 5.24 shows the CMC solution values of $\langle c|\eta\rangle$ for several values of a, which represents a non-linear function of the solution time. Initially it is seen that, in terms of normalised progress variable c, the dependence between Z and c is negative for lean mixtures, as lean values of dc/dt are higher – this is due to the fact that the difference in Y_c between $c = 0$ and $c = 1$ at these locations in Z-space is very small. Additionally, for rich mixtures there is no strong dependence of $\langle c|\eta\rangle$ on mixture fraction. Thus, reaction is happening around the most reactive mixture fraction and the stoichiometric mixture fraction and the diffusion to the lean and rich regions to either side will receive roughly the same diffusion source term, however it has considerably higher effect on the lean region since the peak Y_c value is that much smaller. Hence the rapid increase of c for $Z < 0.2$ during the early stages of ignition.

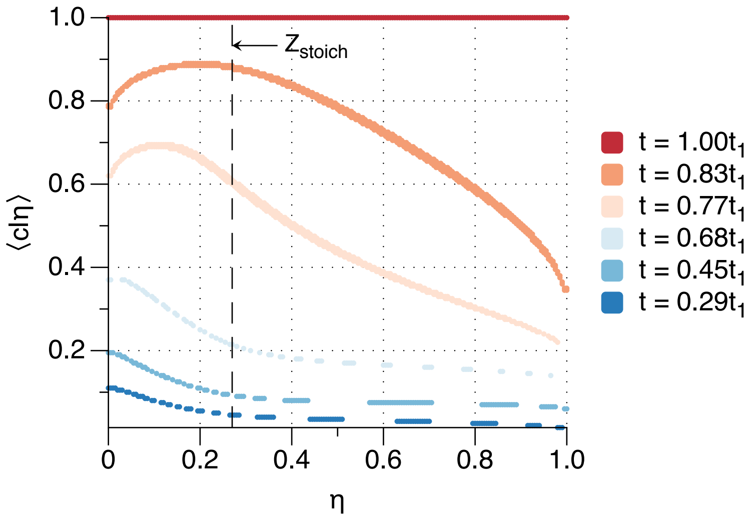

Figure 5.24: Plots of $\langle c|\eta\rangle$ from a 0D-CMC with $\chi = 3000/s$ at selected times, where t_1 is the final time of the CMC simulation.

However, as the reaction progresses the shape of $\langle c|\eta\rangle$ changes to convex-up, and the peak value moves closer to Z_{st}. The lean side now shows a negative relationship between Z and c while the rich side shows a positive one. Furthermore, since this effect is only observed once c achieves suitably large values, these values will have a stronger effect on the covariance than the smaller positively correlated lean and negatively correlated rich conditions found at earlier times.

This provides an explanation for the strong adherence of the sign of the correlation to the stoichiometric mean mixture fraction contour. Lean mixtures are again seen to be positively correlated, while rich mixtures are strongly negatively correlated. The negative correlations in the rich region are the first to appear in terms of streamwise location, suggesting that, although the ignition occurs at the most reactive mixture fraction to the lean side of stoichiometry, and so we would expect the lean mixtures to be more burnt at an earlier stage, the switching of the dependence of c on Z from negative to positive in this region results in strong correlations taking longer to develop, unlike in the rich region where the dependence is always negative or neutral.

5.6 Flamelet Generated Copula

As seen in the previous section, the covariance of Z and c found in the DNS of a lifted autoigniting jet flame is partitioned into positive and negative regions by the mean stoichiometric mixture fraction contour, with rich fluid regions tending to have negative covariance and lean fluid regions tending to have positive covariance. This suggests that fluid close to stoichiometric tends to be more reacted than either rich or lean mixtures, resulting in the statistical dependence of c on Z. This behaviour is also observed in an

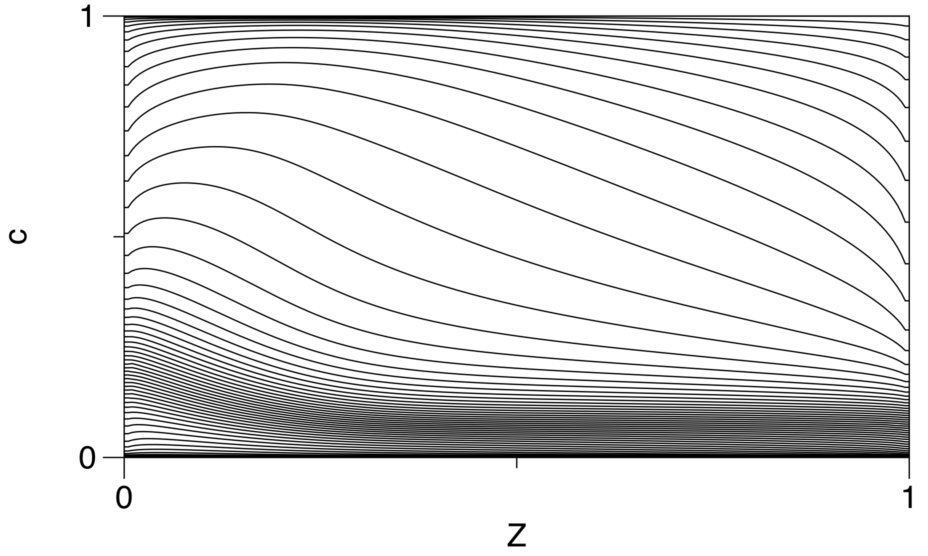

Figure 5.25: Lines of constant a_M vs mixture fraction Z in an autoigniting ethylene flamelet with peak scalar dissipation rate 3000/s. Each line represents a different time in the flamelet solution.

unsteady autoigniting laminar non-premixed flamelet, in which the ignition starts at the most reactive mixture fraction and then quickly propagates towards the stoichiometric mixture fraction. Regions around stoichiometry rapidly approach the peak progress variable; points in mixture fraction space away from this region eventually reach the fully burned solution though a combination of reaction and diffusion in mixture fraction space, but at a slower rate. For a significant time, then, there is a positive gradient dc/dZ for $Z < Z_{st}$ and a negative gradient for $Z > Z_{st}$. This is illustrated in Figure 5.25.

It is a common modelling assumption (Kostka et al. 2009) to relate the thermochemical state in a turbulent autoigniting jet flame to the thermochemical state in an autoigniting flamelet in terms of mixture fraction and progress variable. In the autoigniting flamelet solution there is a unique mapping between progress variable at a given mixture fraction and the solution time, referred to as fuel-age a_M. Properties of the distribution of fluid age in a statistically-stationary turbulent jet are reported by Shin *et al.* (Shin et al. 2016) indicating that a range of distribution shapes are possible. For purposes of illustration, consider a hypothetical point in a turbulent flow with a delta-function pdf of fuel-age, implying that the thermochemical state sampled in the turbulent flow is modelled by the thermochemical states along one fuel-age line in Figure 5.25. In this situation, the statistical dependence of Z and c is governed by the shape of fuel-age contour in Z-c space in the flamelet solution. More generally, the fuel-age exhibits a finite variance and the statistical dependence of Z and c inferred from the flamelet solution depends on the joint-distribution of Z and fuel-age.

The temporal information represented by the contours in Figure 5.25 therefore contains information resulting from physical mechanisms producing a dependence between Z and

c. However, this temporal information is lost when the thermochemical state is tabulated in terms of Z-c, and it is not contained in any presumed copula. This motivates the concept of a Flamelet Generated Copula, in which dependence information is extracted from the temporal evolution of a relevant autoigniting flamelet.

In order to construct a Flamelet Generated Copula, the joint age density function $\alpha_{zc}(Z,c)$ is defined based on the autoigniting flamelet solution data over the range of times $t \in [0, t_{\text{end}}]$, given by,

$$\alpha_{zc}(Z,c) = \frac{1}{t_{\text{end}}} \frac{\partial^2 a_M}{\partial Z \partial c}. \tag{5.17}$$

The cumulative age density function is given by integration of $\alpha(Z,c)$ in Z-c space,

$$\mathrm{A}_{zc}(Z,c) = \int_0^c \int_0^Z \frac{\partial^2 \alpha_{zc}(Z,c)}{\partial Z \partial c} dz dc. \tag{5.18}$$

The copula of the joint age density function is evaluated numerically from the joint cdf. First the marginal age cdfs for mixture fraction and progress variable are computed,

$$\mathrm{A}_Z(Z) = \int_0^1 \int_0^Z \frac{\partial^2 \alpha_{zc}(Z,c)}{\partial Z \partial c} dz dc \tag{5.19}$$

and

$$\mathrm{A}_c(c) = \int_0^c \int_0^1 \frac{\partial^2 \alpha_{zc}(Z,c)}{\partial Z \partial c} dz dc. \tag{5.20}$$

Each of these quantities may be evaluated as a post processing step from transient flamelet data, since a_M is known. Subsequently the Flamelet Generated Copula is given by the inversion method described in Section 5.1.1.

$$C(u,v) = P^e(P_Z^{e-1}(u), P_c^{e-1}(v)) \tag{5.21}$$

Plots of the age density function and the Flamelet Generated Copula obtained from an autoigniting ethylene-air flamelet are shown in Figure 5.27. The corresponding marginal age cdfs are shown in Figure 5.26.

The age density function is a deterministic function, rather than a probability density function. However, based on similarity of the underlying physics driving the Z-c dependence in the igniting flamelet and in an autoigniting non-premixed jet flame, it is hypothesised that the Z-c dependence is similar in both, and therefore propose to model the Z-c copula in the turbulent flame with the Flamelet Generated Copula. Implicit in this modelling are two strong assumptions. First that the Z-c dependence in an igniting flamelet is the same as in the turbulent jet flame, thereby neglecting effects of physical mechanisms, such as flame propagation, that are not present in the autoigniting flamelet. The second implicit assumption is that there is no dependence in the mixture

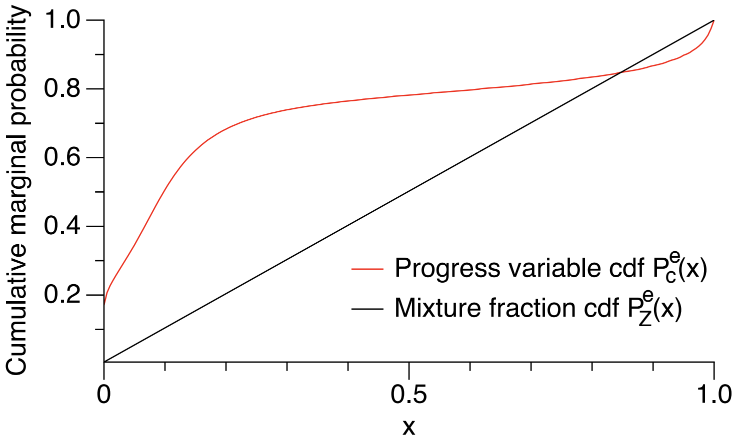

Figure 5.26: Empirical marginal age distribution functions for Z and c from a flamelet calculation of ethylene autoignition with peak scalar dissipation rate $3000/s$.

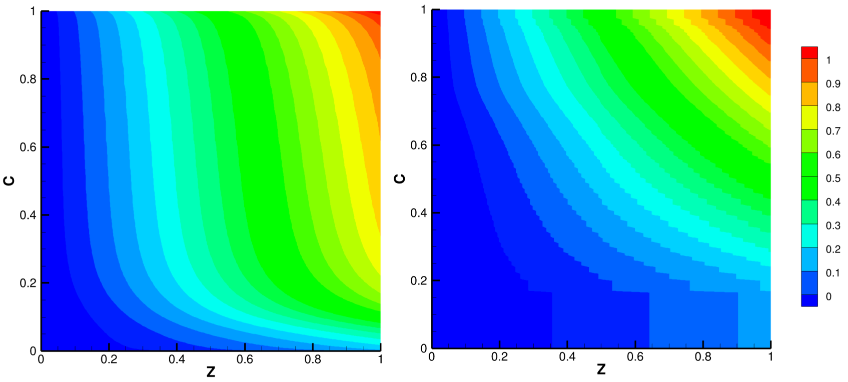

Figure 5.27: Left; Empirical age cdf $\mathrm{A}_{zc}(Z, c)$; Right: Empirical copula $C(u, v)$. Computed from a flamelet solution of ethylene autoignition with peak scalar dissipation rate $3000/s$.

fraction-age distribution in the turbulent flow, which is not generally true (Shin et al. 2016).

It may be possible to reduce the severity of these approximations, for example by using two-dimensional flamelets including transport in progress variable space (Nguyen et al. 2010), or by also accounting for the dependence of mixture fraction and fuel-age (e.g. based on the data of Shin et al. (2016)), however the basic Flamelet Generated Copula described above serves as a starting point for evaluating how the underlying concept performs.

The copula shown in Figure 5.27 was tested in a RANS simulation of the lifted ethylene flame. It was found to produce the same trend in covariance through mixture fraction space — positive covariance for lean mixtures and negative covariance for rich mixtures — as displayed in the DNS. However, the strength of the dependence is much reduced.

5.7 Conclusions

The importance of including dependence in the presumed pdf model was evaluated for three different cases: a stratified flame DNS, a piloted flame experiment, and a lifted auto-igniting flame DNS. For both the piloted experiment and the lifted auto-igniting DNS the performance of the joint-pdf model was directly assessed in terms of the L_2 error relative to the observed distribution, and in the calculation of mean quantities using the pdf. The usefulness of the Plackett copula was assessed for each case.

For the stratified DNS, very little dependence between mixture fraction and progress variable was observed. Therefore no improvement can be made by the use of more advanced models for the one-point pdf for given marginal distributions, since the assumption of independence is the most appropriate choice.

For the piloted jet flame experimental results, a variation of dependence structures was observed. Downstream, strong dependence with positive correlation between mixture fraction and progress variable was seen for increasing radial position; towards the centreline the distribution tended towards independence. Further upstream (circa $x/D = 30$), centreline pdfs showed weak dependence with negative correlation between Z and c. Moving from centreline to increasing radius transitions the pdf from negative correlation through independence to positive correlation. In many of the locations where dependence is observed, it takes the form of tail dependence, a feature which cannot be captured with the Plackett copula. The Plackett copula results in a greatly reduced error in the presumed pdf. However, this improvement does not lead to an improvement in the calculated mean quantities for this case. This is because the mean values of T and ω_c obtained depend also on the functional dependence of T or ω_c on c and Z.

For the lifted flame, strong dependence between Z and c is observed in most sampled locations. The observed copula is well approximated by the Plackett copula, which greatly reduces the error in both the pdf and in the calculated mean quantities. The importance of the Z-c dependence in the auto-igniting lifted jet flame is attributed to the significant Z-c covariance generated in lifted turbulent flames. Because fuel tends to be more reacted in the region of most reactive or stoichiometric mixture fraction, there tends to be a positive Z-c correlation for lean mixture and a negative correlation for rich mixture. An alternative to the presumed copula method, the Flamelet Generated Copula method was introduced and the underlying mathematical model presented. The Plackett copula provides a reasonably accurate model for the Z-c dependence throughout the majority of the lifted auto-igniting flow. In the vicinity of $\overline{Z} = Z_{st}$, the Z-c dependence has two branches, across which the Plackett copula performs less well. Hence it is necessary to perform *a posteriori* evaluation of the joint distribution model performance to assess the impact of this discrepancy on flame simulations in practice.

Chapter 6

Results II: Presumed-pdf modelling of an autoigniting ethylene jet flame

6.1 Introduction

Based on the results of the *a-priori* analysis in Chapter 5, the most challenging combustion feature for presumed pdf methods is the stabilisation of lifted flames. As suggested in the conclusions of that section, this is likely due to the stronger mean gradients in both mixture fraction and progress variable resulting in a large gradient production term in the covariance equation. As a result their dependence has a greater impact on flame prediction in this region. Therefore an auto-igniting lifted flame is used as a test case for further a posteriori analysis of the mixture fraction progress variable presumed pdf approach.

In this chapter, a series of RANS simulations of the autoigniting lifted ethylene jet flame of Yoo, Richardson, et al. (2011) are performed, varying the following global parameters: the peak conditional scalar dissipation rate, A; the choice of marginal pdf, taken as either the top-hat pdf or the beta pdf; and the formulation of the joint-pdf, either assuming independence or applying the Plackett copula.

The scalar dissipation rate is an important control parameter for tabulated chemistry, especially in the case of auto-igniting non-premixed flames, and has been incorporated into the turbulent flamelet table in other studies (Knudsen, Richardson, Chen, et al. 2011). Here, a single conditional scalar dissipation rate profile is taken for the entire flow, in a manner analogous to a zero dimensional CMC. The mean scalar dissipation rate can be ascertained from the whole domain, or from a subsection of the domain upstream of the lift-off height, using volume averaging or pdf-weighted averaging. However, this does not fully account for the effect of the instantaneous scalar dissipation rate on the instantaneous reaction rate and so cannot be expected to give accurate predictions of the autoignition. The peak conditional scalar dissipation rate A may be calculated (O'Brien and Jiang 1991) from either the DNS or RANS quantities as

$$A = \frac{\tilde{\chi}}{\int G(\eta) p_Z(\eta) d\eta} \tag{6.1}$$

where

$$G(\eta) = \exp\left(-2(\mathrm{erf}^{-1}(2\eta - 1))^2\right), \tag{6.2}$$

$\tilde{\chi}$ is the Favre average scalar dissipation rate, p_Z is the mixture fraction pdf and η is the state space variable for mixture fraction. Application of Equation 6.1 to the lifted ethylene DNS data indicates that the A is of the order of $9000/s$ in the region close to the jet inlet, and as low as $50/s$ further downstream. Conditional mean scalar dissipation rates presented for this case in Yoo, Richardson, et al. (2011) confirm a similar range, with peak values around $3000/s$ at $x/H = 3$. The purpose of this parametric study is not to suggest that the variation of scalar dissipation rate between jet exit and lift-off height can be described by a constant value, but to demonstrate the sensitivity of the results to an assumed value of A in comparison to the other parameters.

The choice of marginal pdf is an important question to answer, not least because of the cost and complexity of accurately integrating the beta pdf. Floyd et al. (2009) argue for the use of the top-hat distribution in LES due to its acceptable accuracy, simplicity and computational cost. Here we investigate its application in a RANS context, together with the integration methods developed in Section 4.2. The Reynolds averaged formulation was chosen because the sub-grid pdf is expected to be more difficult to model than the sub-filter pdf in a well resolved LES. While such LES are reported increasingly often in research journals for relatively low Reynolds number laboratory flame tests, simulation of industrial combustion systems typically achieves much lower resolution of flame structures and often employ RANS. Both the variance and covariance are expected to be larger in the case of RANS. Finally, the effect of assuming an independent pdf versus a copula-based pdf is studied in order to determine the importance of avoiding the independence assumption relative to the other parameters.

6.2 Tabulation approaches for auto-igniting flows

Autoignition presents a particular challenge for tabulated chemistry approaches because progress variables based on major reactant or product species or temperature change very little during the early stages of autoignition. This makes tabulated chemistry simulations of auto-igniting flows that use progress variables sensitive to numerical error. A suitable test case to check that the lookup table is functioning correctly is to use the full tabulated chemistry CFD implementation to simulate the 1D autoignition process that was used to generate the lookup tables. This was achieved by initialising a 1D simulation domain $x \in [0,1]$ with a linear gradient of mixture fraction $\widetilde{Z} = x$, with an unburnt composition $\tilde{c} = 0$ and imposing constant zero values for velocity, mixture fraction variance and progress variable variance and keeping pressure constant. The results of this CFD simulation, given as a function of mixture fraction $Z = \widetilde{Z} = x$, are then expected to reproduce the CMC solution that was used to generate the table, with any deviation being due to numerical error.

The autoigniting laminar flamelet used for the flamelet table was generated using the CMC code described in Section **??** which was developed for this application. In Equation 2.59, the second derivative is discretised using a second order central difference scheme. The system of equations is integrated implicitly using the DVODPK solver with a relative tolerance of 1×10^{-6} and an absolute tolerance of 1×10^{-12}. The peak scalar dissipation rate A used in the AMC model was one of the parameters varied in this study. The code was used to perform an autoigniting ethylene flamelet on a regular mixture fraction grid of 201 points. A regular grid was chosen to avoid an unnecessary interpolation during the generation of the turbulent flamelet table, and was verified to produce the correct solution by comparison with a mixture fraction grid clustered around stoichiometry, as recommended by Mastorakos (2009). The boundary conditions for each autoigniting flamelet were chosen to match the conditions of the inlet streams of the DNS – the oxidiser boundary condition ($Z = 0$) is 1550K with a composition of $Y_{O_2} = 0.233$ and $Y_{N_2} = 0.767$; the fuel boundary condition ($Z = 1$) is 550K with a composition of $Y_{C_2H_4} = 0.18$, $Y_{O_2} = 0$ and $Y_{N_2} = 0.82$, and the pressure is at a constant 1 bar. For the initial conditions, species and enthalpy were linearly interpolated between their boundary conditions, representing an inert mixing solution, and resulting in a slightly non-linear initial temperature profile. The ethylene chemical mechanism used was the same as in the DNS case, a 22 species reduced mechanism by Luo et al. (2012). The autoigniting flamelet solution was run until steady state was reached, and the final state was used as the definition of the maximum value of non-normalised progress variable Y_c. A typical such solution is illustrated in Figure 6.1.

The progress variable c is based on a linear combination of mass fractions Y_c and is normalised as a function of mixture fraction.

$$Y_c = Y_{H_2O} + Y_{CO_2} \tag{6.3}$$

$$c(Z) = \frac{Y_c}{Y_c^{\max}(Z)} \tag{6.4}$$

where $Y_c^{\max}(Z) = \langle Q_c^{\max} | \eta \rangle$ is determined by the steady state of the CMC solution. It was confirmed in all cases that the unscaled progress variable Y_c was a monotonic function of time for all Z. We define the conditional source term $\langle \dot{S}_c | \eta \rangle$ for the normalised progress variable c by the contribution from its reactive source term and diffusion source

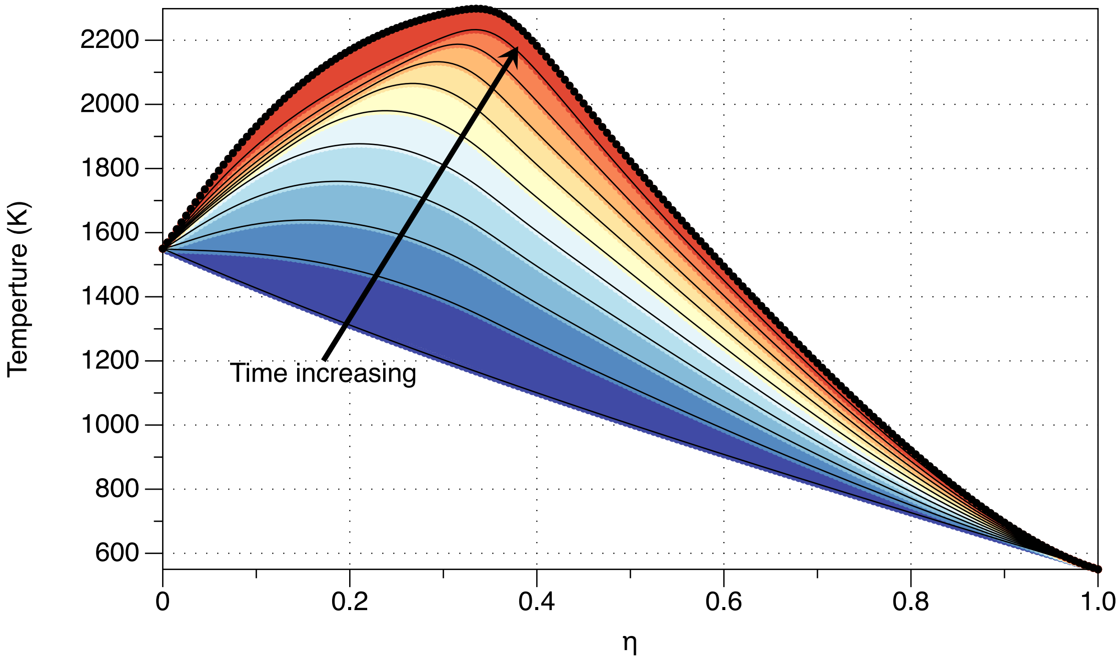

Figure 6.1: Autoignition of ethylene from CMC code with $\chi_{max} = 3000/s$. Solid lines indicate progress variable $c = i/10$ for $i = 1 \dots 10$.

term, i.e.

$$\langle \dot{S}_c|\eta\rangle = \frac{1}{\langle Q_c^{\mathrm{max}}|\eta\rangle}\frac{\partial\langle Q_c|\eta\rangle}{\partial t} \tag{6.5}$$

$$= \frac{1}{\langle Q_c^{\mathrm{max}}|\eta\rangle}\left(\langle N|\eta\rangle\frac{\partial^2\langle Q_c|\eta\rangle}{\partial x_k}^{2}\eta + \langle\dot{\omega}_{H_2O}|\eta\rangle + \langle\dot{\omega}_{CO_2}|\eta\rangle\right). \tag{6.6}$$

Once a solution $\langle Q_k|\eta\rangle\,(t)$ is calculated, it is then remapped to a two dimensional uniform grid in mixture fraction and the control parameter c using a linear interpolation, providing a final set of values $\langle Q|\eta,\zeta\rangle$ which are used to generate the turbulent lookup table.

The quantities in the turbulent lookup table are Favre averaged quantities given by

$$\widetilde{Q}\,(\Theta) = \overline{\rho}\int_0^1\int_0^1 \frac{\langle Q|\eta,\zeta\rangle}{\rho\,(\eta,\zeta)}\widetilde{p}\,(\eta,\zeta;\Theta)\,d\eta d\zeta \tag{6.7}$$

where $\tilde{p}\,(\eta,\zeta;\Theta)$ is the Favre pdf and Θ is a vector of control moments (for example $\Theta = \{\widetilde{Z}, \widetilde{Z''^2}, \tilde{c}, \widetilde{c''^2}, \widetilde{Z''c''}\}$).

6.3 CFD set-up

The simulations presented in this section are two-dimensional steady-state RANS calculations performed using StarCD (CD-adapco 2016). The mean momentum (Equation 2.21), continuity (Equation 2.20) and turbulence quantities (Equation 2.24 and Equation 2.25) were solved by the built-in methods in the software. The transport equations for the Favre averaged reference variables (Equations 2.61-2.72), source terms for the transport equations, the subroutines to interpolate Favre averaged quantities from the turbulent lookup table, and setting of the temperature field, were implemented as user defined functions in Fortran 90. The mean density field was calculated from the mean temperature and mean species mass fractions using the ideal gas law.

The size of the computational domain is $30H \times 30H$ in the x, y dimensions, where $H = 2mm$ is the jet width, with a symmetry plane at $y = 0$ corresponding to the mid-plane of the jet. This domain size is greater than the original DNS dimensions of $15H \times 20H$ in order to minimise any effect of the simulation boundaries on the flow, since the DNS and RANS boundary conditions do not correspond exactly. The grid dimensions are 300×300 with the smallest grid point in each direction being $0.1mm$, giving approximately 10 points across the jet inlet which is sufficient to capture the tanh inlet profile of the DNS.

The inlet boundary condition for the coflow and jet inlets is described as follows. Velocity component $\tilde{u}$, density $\overline{\rho}$, mean mixture fraction $\widetilde{Z}$, turbulent kinetic energy $\tilde{k}$ and turbulent dissipation ε profiles are specified as a function of the cross-stream coordinate y:

$$\begin{aligned}\widetilde{Z} &= \frac{1}{2}\left[\tanh\left(\frac{y+H/2}{2\delta}\right) - \tanh\left(\frac{y-H/2}{2\delta}\right)\right], \text{ where } \delta = 0.05H \\ u &= u_{\text{coflow}} + (u_{\text{jet}} - u_{\text{coflow}})\widetilde{Z} \\ u' &= uI\widetilde{Z}\end{aligned}$$

as in the DNS. Inlet values of k and ε are estimated to be

$$\begin{aligned}k &= \frac{3}{2}u^2 I^2 \\ \varepsilon &= \frac{k^{3/2}}{L_t}\end{aligned}$$

where turbulent intensity $I = 10\%$ and integral length scale $L_t = H/2 = 1mm$ are the same as specified in the DNS turbulent inlet conditions. Density is calculated from the ideal gas law using the enthalpy and composition as functions of mixture fraction. It is important to specify both velocity and density at the inlet so that the correct mass flux profile can be calculated. This step is performed only once, at the simulation initialisation. Boundary value for the control parameters are fixed at the inlet, equal to zero except for $\widetilde{Z}$.

The turbulent properties specified above are inconsistent: since the inlet table specifies k and ε which cannot be zero for the standard k-ε model, the laminar coflow is given a non-zero turbulent intensity of 10%. This is a limitation of the RANS model used to simulate the flow and could be avoided by applying a more advanced model which can account for laminar regions. That the turbulence intensity is set equal to 10% across both the jet ($u = 204m/s$) and coflow ($u = 20m/s$), whereas the DNS imposed a laminar coflow, implies that the turbulent kinetic energy in the jet is two orders of magnitude greater than in the coflow. Sensitivity studies reducing I in proportion to u demonstrated that the RANS solution is insensitive to the value of I used in the coflow for $4\% < I < 10\%$. This insensitivity to I_{coflow} may be because $k_{\text{coflow}} \ll k_{\text{jet}}$ in all cases.

A slip wall condition is applied at the outer $y = 30H$ boundary and $y = 0$ is a symmetry plane. At the outlet boundary the pressure is fixed and the velocity, scalar and turbulent property outlet boundary conditions are zero-gradient.

The turbulence model used is the realisable k-ε model (Shih et al. 1995), with the default coefficients. The realisable k-ε model has been shown to give better results for round and planar jets over the standard k-ε model and was found to accurately capture the spreading rate of this jet. No energy equation is solved; the mixture fraction transport equation is sufficient to capture the enthalpy field in the absence of heat loss, such as from radiation. There were no sources of heat loss in the original DNS simulation, and therefore this is a valid assumption.

Gravity is set to zero as in the DNS. The flow density is provided by the lookup table. Molecular viscosity is assumed constant since this is negligible compared to the turbulent viscosity. Each simulation was initialised by extrapolating the inlet conditions across the whole domain.

The SIMPLE algorithm (Patankar 1980) is used to solve the flow field and scalar quantities as given in Section 2.1.4.6. The maximum residual tolerance of 10^{-5} was applied. Only the u and v components of the momentum equations are solved for. Relaxation factors of 0.7 and 0.3 were applied to velocity and pressure respectively. An under-relaxation factor of 0.8 is applied to each of the mean control moments $\widetilde{Z}$, $\tilde{c}$, $\widetilde{Z''^2}$, $\widetilde{c''^2}$, $\widetilde{Z''c''}$ in order to improve convergence, since the density can change rapidly with minor changes to the control moments. Gradient calculations for u, v, k, ε, and all scalar quantities are done using an upwind differencing scheme. With these parameters, a typical simulation on the grid described above takes around 800 iterations to converge. The integration of the turbulent table is described in Section 4.2.

6.4 Validation of the flow field

In this section, the flow field upstream from the RANS will be compared with the flow field from the DNS, upstream of the ignition point. After ignition, the flow field is significantly distorted by the expansion caused by the temperature rise. Since the lift-off height and post-ignition temperature field in the RANS both depend on the choice of modelling options, downstream comparison of the flow field between RANS and DNS further is difficult. Therefore, in the following figures the RANS case is an inert simulation, where the reaction rate of progress variable is set to zero and therefore $c = 0$ everywhere.

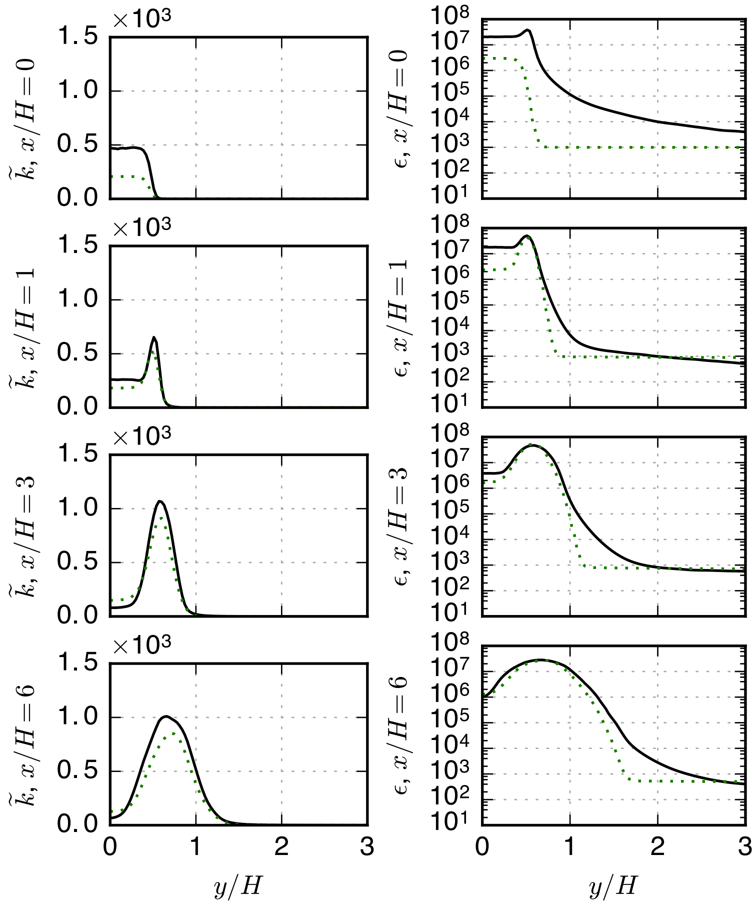

Figure 6.2: Radial profiles of turbulence quantities for a typical RANS simulation with no reaction at selected downstream locations. Solid black: DNS; Dotted green: RANS.

Figure 6.2 compares the cross-stream profiles of the turbulence quantities from the RANS with those calculated from the DNS data. The turbulence inlet quantities were not matched with the DNS, but rather selected to give good downstream predictions. This is because the synthetic turbulence used in the DNS jet decays rapidly, as seen in the streamwise plot of turbulent kinetic energy in Figure 6.3. Therefore the turbulence kinetic energy at the inlet is set artificially low at the inlet. The turbulence dissipation

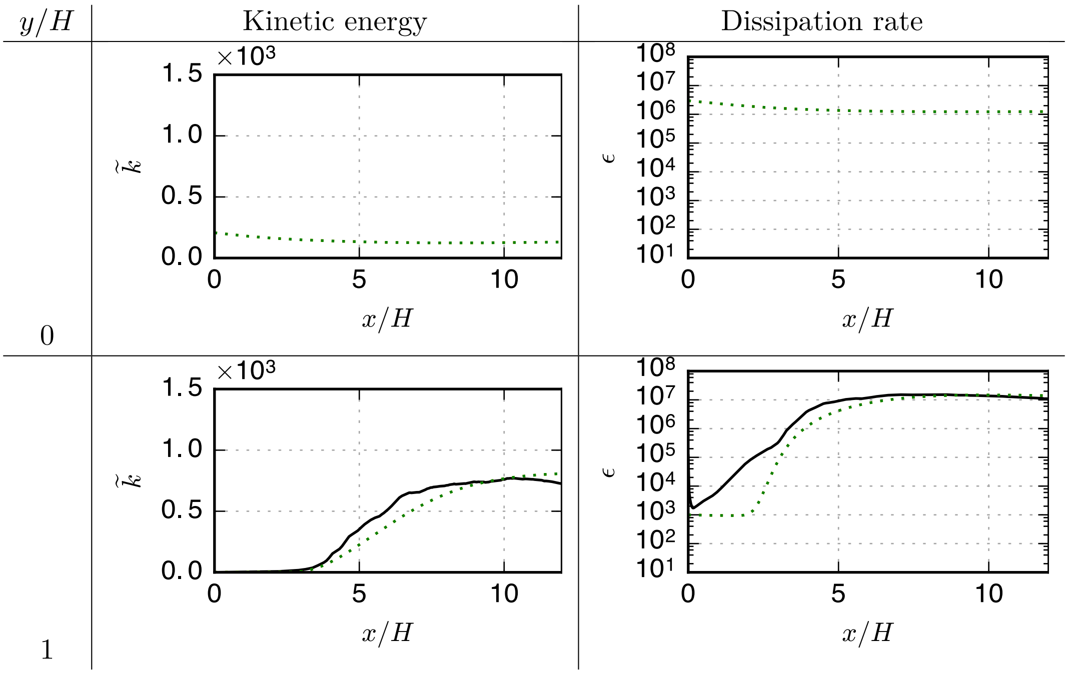

Figure 6.3: Streamwise profiles of turbulence quantities for a typical RANS simulation with no reaction at selected downstream locations. Solid black: DNS; Dotted green: RANS.

rate at the inlet is based on k. Both the k and ε cross-stream profiles at $x/H = 3$ match the DNS results well, and at $x/H = 6$, close to where ignition occurs, the profiles are still matched reasonably well. Streamwise profiles at the cross-stream location $y/H = 1$ show that the turbulent kinetic energy generated by the shear layer matches closely that of the DNS. The turbulent dissipation rate in this profile can be seen to be under predicted by the RANS, again due to the artificially high dissipation rate of the DNS.

The centreline values of the streamwise velocity component (Figure 6.5) shows that there is a distinct potential core apparent in the DNS which ends around $x/H = 6.5$. The DNS centreline velocity initially decays more slowly than that of the RANS simulation. The sharp change in the $d\tilde{u}/dx$ seen in the both streamwise velocity and mixture fraction plots is caused by ignition in the DNS. After this point the DNS profiles become broader and the centreline values lower due to the increased turbulence (see Figure 6.3).

Temperature and density inlet profiles are shown in Figure 6.6. Given that the mixture fraction spans $[0, 1]$ across the inlet, correspondence of the temperature profile with the DNS indicates that the unburned conditional temperature in DNS corresponds well with the unburned condition in the CMC used to generate the table. The matching both the velocity and density profiles at the inlet implies that the total momentum flux of the jet is correct.

The preceding figures show that the base RANS simulation, shown here without chemical reaction, is a sufficiently good fit to the DNS flow field to make comparisons valid.

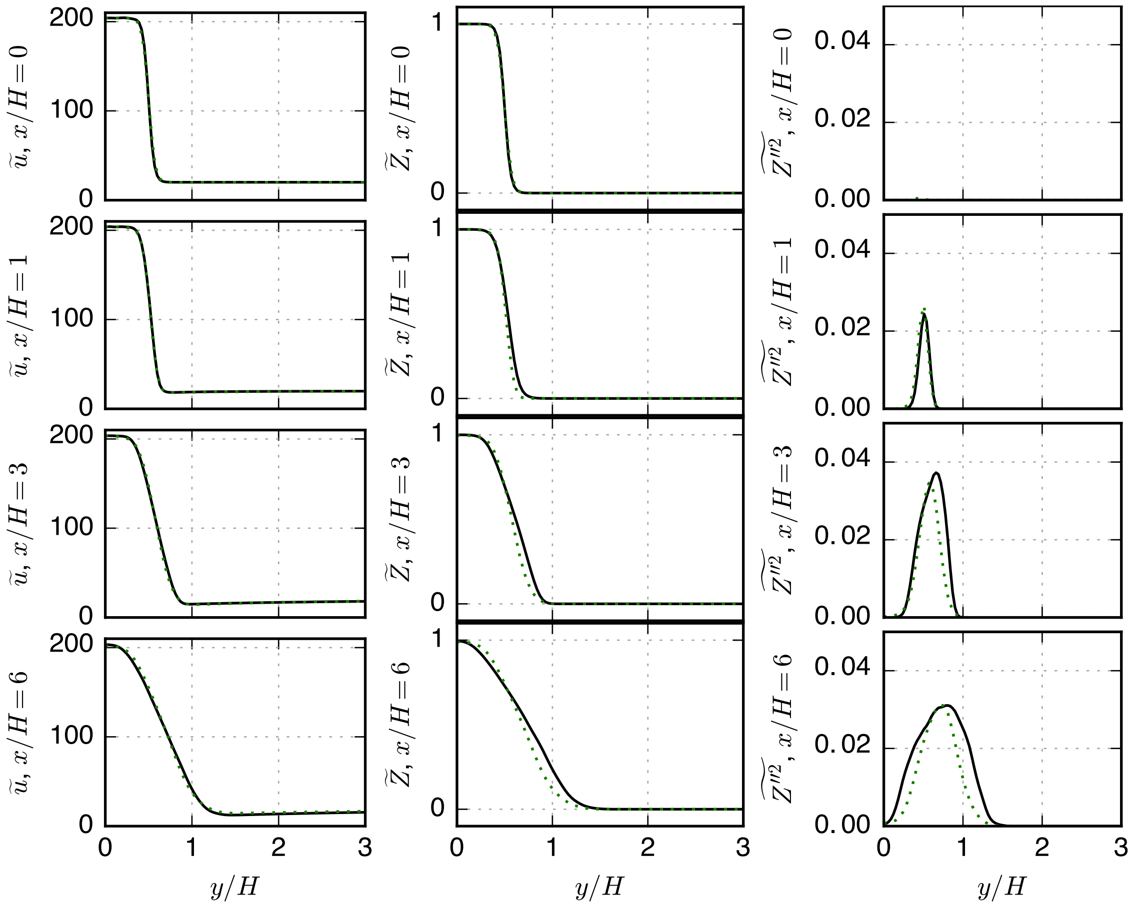

Figure 6.4: Cross-stream profiles of streamwise velocity, mixture fraction and mixture fraction variance for a typical RANS simulation with no reaction at selected downstream locations. Solid black: DNS; Dotted green: RANS.

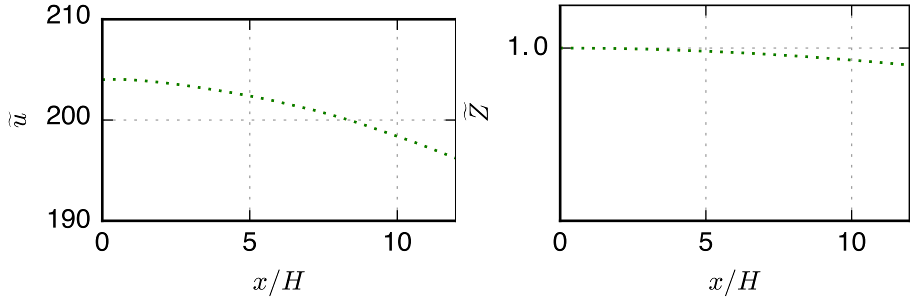

Figure 6.5: Centreline profiles of streamwise velocity and mixture fraction. Solid black: DNS; Dotted green: RANS.

In the following sections, the downstream results from reacting RANS simulations are compared directly with the values from the DNS in order to assess the importance of each modelling decision listed in Section 6.1. The full set of parameters for the reacting RANS simulations performed is presented in 6.1.

The lift-off height for each simulation, defined as the most upstream point where $\widetilde{Y}_{\mathrm{OH}}$ reaches 4% of its maximum value, are shown in Figure 6.7. It is clear that the peak

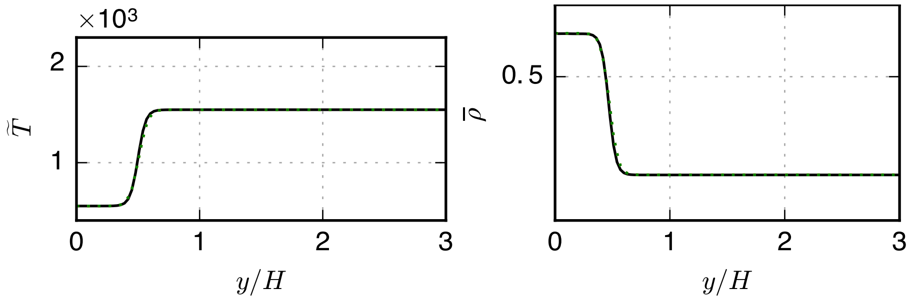

Figure 6.6: Cross-stream profiles of temperature and density inlet conditions for a typical RANS simulation. Solid black: DNS; Dotted green: RANS.

Ref. Var.	Marginal	JPDF	A (1/s)	Section
a	Top-hat	4D	3000	6.5
a	Beta	4D	3000	6.5
b	Top-hat	4D	3000	6.5
b	Beta	4D	3000	6.5
c	Top-hat	4D	3000	6.5
c	Beta	4D	3000	6.5
c	Top-hat	4D	2000	6.6
c	Top-hat	4D	2500	6.6
c	Top-hat	4D	3000	6.6
c	Top-hat	4D	3175	6.6
c	Top-hat	4D	3250	6.6
c	Top-hat	4D	3375	6.6
c	Top-hat	4D	3375	6.6
c	Top-hat	3D	3000	6.7
c	Top-hat	4D	3000	6.7
c	Top-hat	5D	3000	6.7

Table 6.1: Table of simulations and modelling choices.

scalar dissipation rate A is the most significant quantity affecting the lift-off height. The rate of change of lift-off height with respect to scalar dissipation rate is low for scalar dissipation rates around $A = 2000/s$, and becomes increasingly large for higher scalar dissipation rates as they approach the extinction limit of the laminar flamelet. The choice of marginal pdf (beta or top-hat distribution) is clearly seen to have a negligible effect on the lift-off height. The use of a residence time based reference quantity to quantify the reaction progress is seen to have a significant effect on the lift-off height, and the sensitivity to the peak scalar dissipation rate is becomes more linear than with the use of a progress variable. The difference in predicted lift-off height is considerably lower between reference parameters a and b than between either one and c. Therefore there is no benefit of using a purely time-based quantity such as a as opposed to a combined time/reaction rate quantity such as b, which can provide improved resolution in state space for mean quantities.

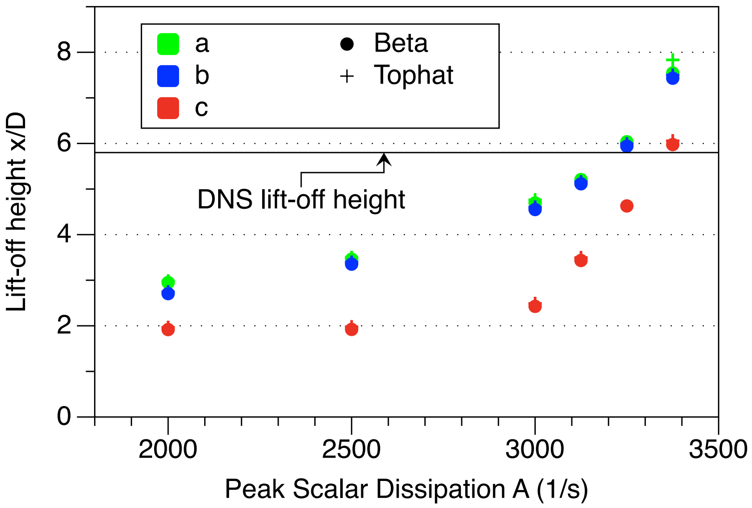

Figure 6.7: Lift-off heights for lifted ethylene jet flame simulations.

6.5 Choice of marginal distribution and reference variable

The RANS simulations presented in this section employ a table with peak scalar dissipation rate $A = 3000/s$ and an assumption of independence between the Z and c pdfs. Here, the choice of marginal distribution (top-hat vs. beta) and the choice of control parameter are compared between the Z and c pdfs. The control parameters tested are the normalised progress variable c, the residence-time based parameter a and the combination of the two, $b = (a + c)/2$.

Figure 6.8 shows velocity, mean mixture fraction and mixture fraction variance cross-stream profiles for various downstream locations, ranging from near the flame base at $x/H = 6$ to $x/H = 12$. The velocity and mixture fraction fields are not significantly affected by either choice of marginal distribution or choice of progress variable. The spreading rate of each closely matches that of the DNS, and the peak values are reasonably well captured. For both variables, the centreline values are slightly under-predicted by the RANS while the values on the edge of the jet are slightly over predicted, indicating that the RANS is slightly too diffusive. The mixture fraction cross-stream profile of the DNS is expanded radially outwards around $y/H = 1$ due to a combination of the increased scalar transport caused by higher turbulence, and the expansion around the flame driving an outward flow component. This flow feature is not captured in the RANS and is not seen in the corresponding velocity profiles. The mixture fraction variance, important for the determination of mean quantities, is over predicted by the RANS at upstream locations. At the furthest downstream location ($x/H = 12$) the peak values from the RANS simulations are much closer to the DNS, particularly for reference variables b and c. This indicates that the development of the shear layer is delayed, possibly due to the scalar dissipation rate model used. Nevertheless, the peak value of mixture fraction variance is correctly located inside the shear layer and on the rich

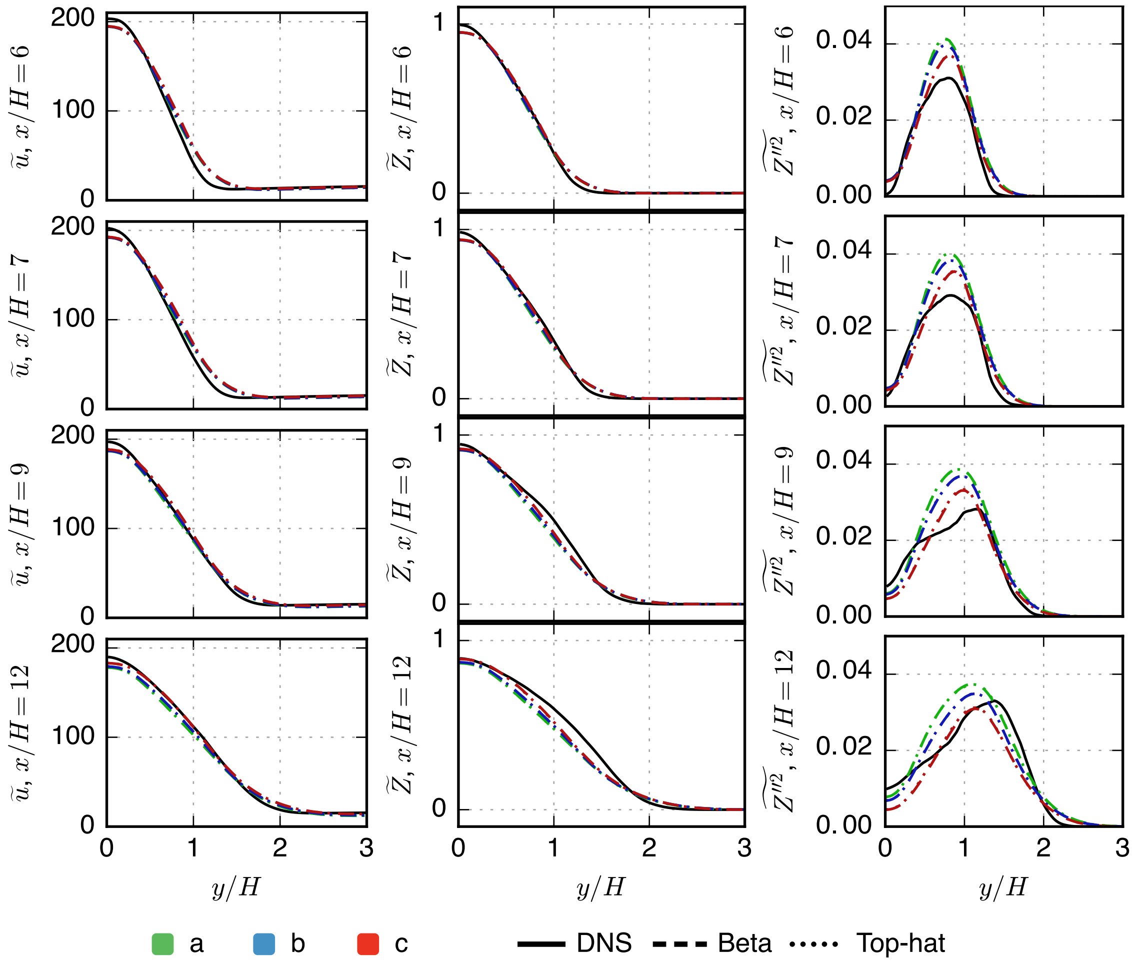

Figure 6.8: Cross stream profiles of mean velocity, mixture fraction and mixture fraction variance for $x/H \in \{6, 7, 9, 12\}$

side of the mean stoichiometric mixture fraction contour, and the width of the mixture fraction variance profile is comparable to that of the DNS at all downstream locations. Simulations using progress variable c as a reference parameter tend to have lower peak values of mixture fraction variance. In general though, it is concluded that the mean mixture fraction its variance are sufficiently well captured by the RANS simulations for the purposes of turbulent flamelet table lookup.

Figure 6.9 shows the cross-stream profiles for the reactedness reference variable $\phi \in \{a, b, c\}$ for the same downstream locations. These indicate that the lift-off height is over predicted, as shown by the profiles of a, b or c, which show fully burning compositions even at $x/H = 6$. The DNS, in contrast, begins to ignite around $x/H = 6$ and becomes increasingly burned moving towards $x/H = 12$. This is confirmed by Figure 6.7, which shows lift-off heights for each case and in which this case corresponds to $A = 3000/s$. This under-prediction is most likely due to the use of a fixed peak scalar dissipation rate; whereas in the DNS the dissipation rate near the jet exit is high and inhibits autoignition, this is not captured in the RANS simulations. Progress variable from the DNS (shown in

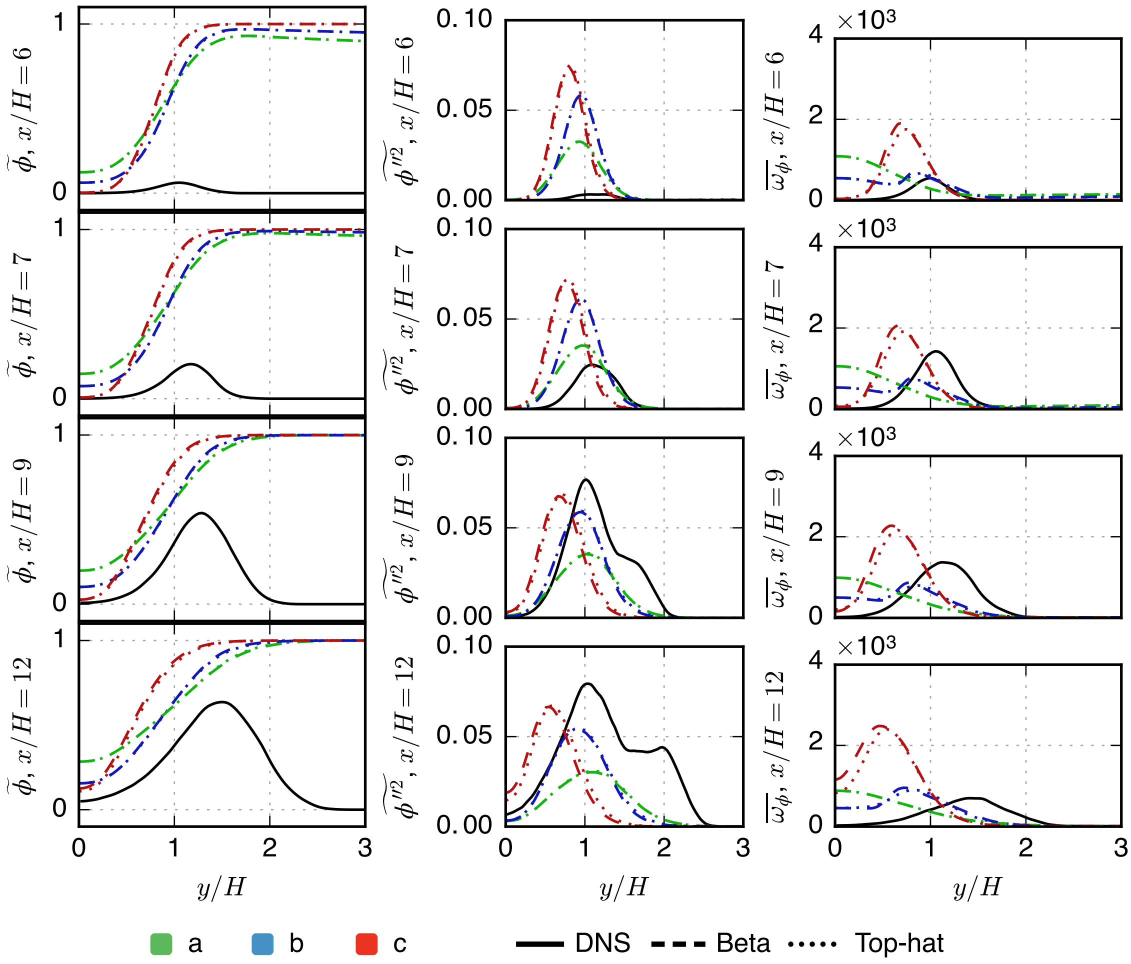

Figure 6.9: Cross-stream profiles of reaction reference variable Favre mean $\tilde{\phi}$, variance $\widetilde{\phi''^2}$ and source term $\overline{\omega_\phi}$ for $x/H \in \{6, 7, 9, 12\}$ and $\phi \in \{a, b, c\}$. The source term has units of $1/s$.

black) is not directly comparable to the RANS case, since it is normalised based on the Y_c^max found in the DNS domain, not by the final solution of the CMC. Therefore only qualitative comparisons may be made. The RANS progress variables take the value of 1 in the coflow at this point, however this does not affect the composition of the coflow for which $c = 0$ and $c = 1$ are equivalent. The radial profiles of the residence-time based reference quantities are broader than those of the progress variable: in burning regions both a and b are slower to reach the value of one compared to the progress variable due to the reduced source term ω_a as $a \to 1$; and along the centreline the values of both a and b move away from zero due to this source term, unlike c which remains close to zero. Each of these effects is more pronounced for a than for b.

Similarly, the three choices of reference variable exhibit significantly different radial profiles. Initially ($x/H = 6$) each has a bell-shaped profile, where the maximum value is strongly dependent on the maximum gradient of the respective mean. In each case the peak variance decreases downstream as the shear layer develops. A direct comparison to the DNS quantities is not possible due to the under-prediction of the lift-off height. Over these locations, the peak progress variable variance in the DNS grows from the ignition point up to a fixed maximum value which is maintained between $x/H = 9$ and $x/H = 12$; each of the RANS simulations appears to maintain the peak value reached as the profiles broaden downstream.

The source term for each reference variable (labelled ω_c in Figure 6.7) illustrates the difference between the three. The reaction rate of progress variable c is non-zero everywhere that $c \notin \{0, 1\}$ and is highest around $c \approx 0.4$. In contrast, ω_a and ω_b are non-zero everywhere that a,$b \neq 1$. The source term for a is highest when $a \approx 0$, and ω_b has its peak value sometimes around $b = 0$ and sometimes around $b = 0.4$. At $x/H = 12$, the y location where ω_b is maximum does not correspond to the y location where ω_c is maximum, purely as a result of the different mean and variance profiles of b and c. In general, the peak mean reaction rate of progress variable from the DNS is lower than that observed in the RANS simulation using c as a reference variable.

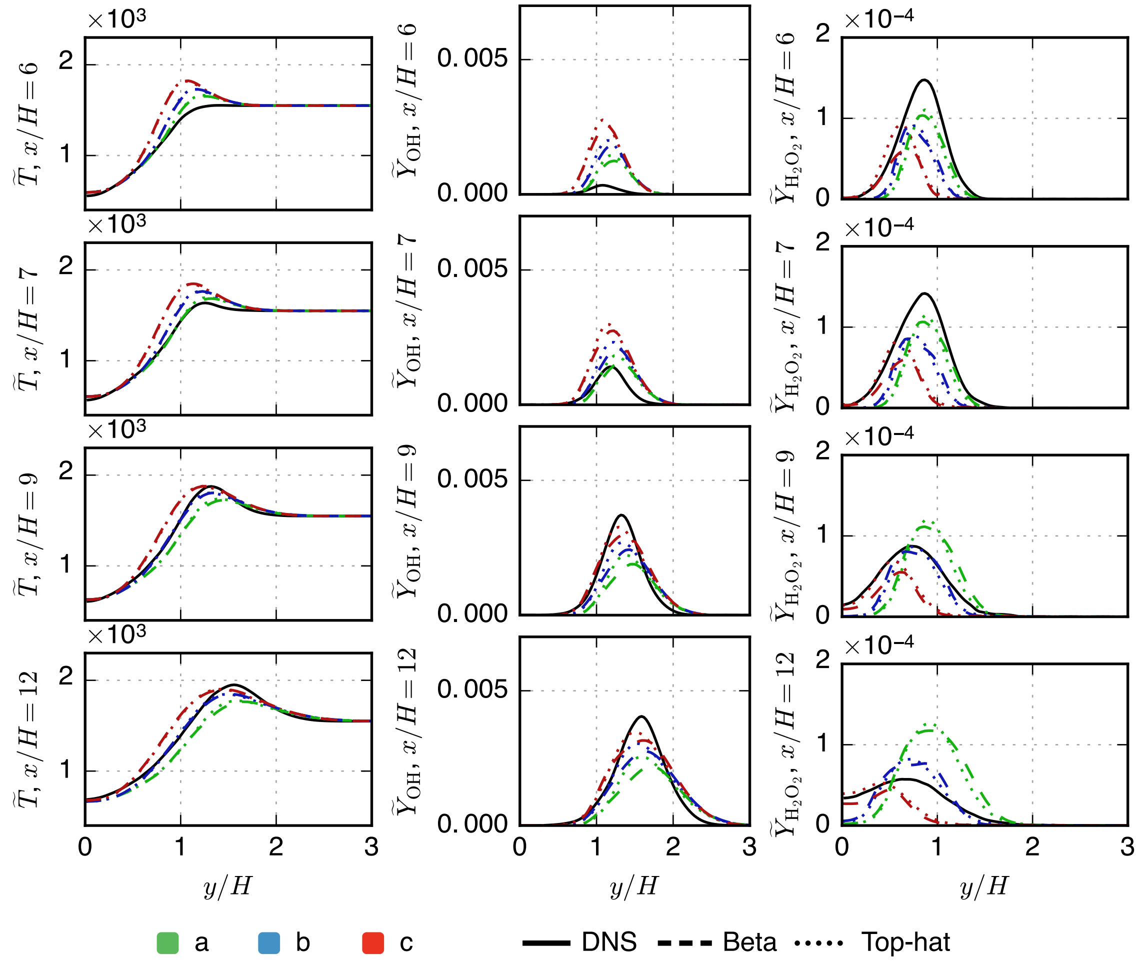

Figure 6.10: Cross-stream profiles of temperature, OH and H_2O_2 mass fraction for $x/H \in \{6, 7, 9, 12\}$.

Figure 6.10 shows the corresponding cross-stream profiles for temperature, $\widetilde{Y}_{\mathrm{OH}}$ and $\widetilde{Y}_{\mathrm{H_2O_2}}$. The temperature and $\widetilde{Y}_{\mathrm{OH}}$ plots again indicate that the flame lift-off height is under-predicted in each case. For progress variable c, which under-predicts lift-off height by the greatest amount, peak temperature at $x/H = 6$ is around $y/H = 1$. In contrast, the DNS peak temperature shortly after ignition ($x/H = 7$) is further out at $y/H \approx 1.2$. This is due to the broadening of the jet moving downstream, and this effect is also seen in the peak temperatures for a and b at $x/H = 6$ which are further out than $y/H = 1$. In each respective case (a, b, c and DNS) the location of peak temperature moves outwards as the flame brush broadens, towards $y/H \approx 1.5$. By $y/H = 12$ each RANS case exhibits a peak temperature lower than that of the DNS.

For all reference variables the Favre averaged mass fraction of OH, an indicator of flame location, is over-predicted relative to the DNS at upstream locations due to the under-prediction of lift-off heights. The DNS profiles show a clear progression which corresponds strongly to the progress variable radial profiles. The radial profiles of $\widetilde{Y}_{\mathrm{H_2O_2}}$, a which is present during the early stages of autoignition, are captured best by the reference variable a over the range $x/H = 6, 7$. However, where the DNS profiles show decreasing peak values and broadening profiles moving downstream, this is not captured by the parameter a, for which the peak value actually increases over this range. In this respect the parameter b performs better, capturing the both the decreasing peak value and broadening profile of $\widetilde{Y}_{\mathrm{H_2O_2}}$ between $x/H = 6$ and $x/H = 12$.

There is no significant difference between the use of a beta distribution vs. top-hat distribution in any of the results. Slight differences can be seen in $\widetilde{Y}_{\mathrm{OH}}$ and $\widetilde{Y}_{\mathrm{H_2O_2}}$ plots, where the top-hat distribution seems to produce marginally narrower profiles. However in the velocity, mixture fraction, mixture fraction variance and temperature profiles there is no observable difference between the two.

6.6 Effect of peak scalar dissipation rate

Figure 6.11 shows mixture fraction variance, temperature and $\widetilde{Y}_{\mathrm{OH}}$ profiles for a range of peak scalar dissipation rates A using progress variable c as the reference variable. The velocity and mixture fraction fields proved insensitive to A over the ranges considered, so plots of these quantities are not included. Mixture fraction variance is also only slightly more sensitive to this parameter, which is to be expected since the effect of A on $\widetilde{Z''^2}$ is only indirectly through the flow field. For the temperature predictions, the highest peak scalar dissipation rate of $3375/s$ gave the most accurate prediction of lift-off height for progress variable, whereas $3250/s$ gave the most accurate prediction with both a and b (see Figure 6.7). This is also seen in temperature and $\widetilde{Y}_{\mathrm{OH}}$ profiles at $x/H = 6$. This is due to the high presumed mean scalar dissipation rate better matching the conditions upstream of the flame, which determine the autoignition process. However it performs

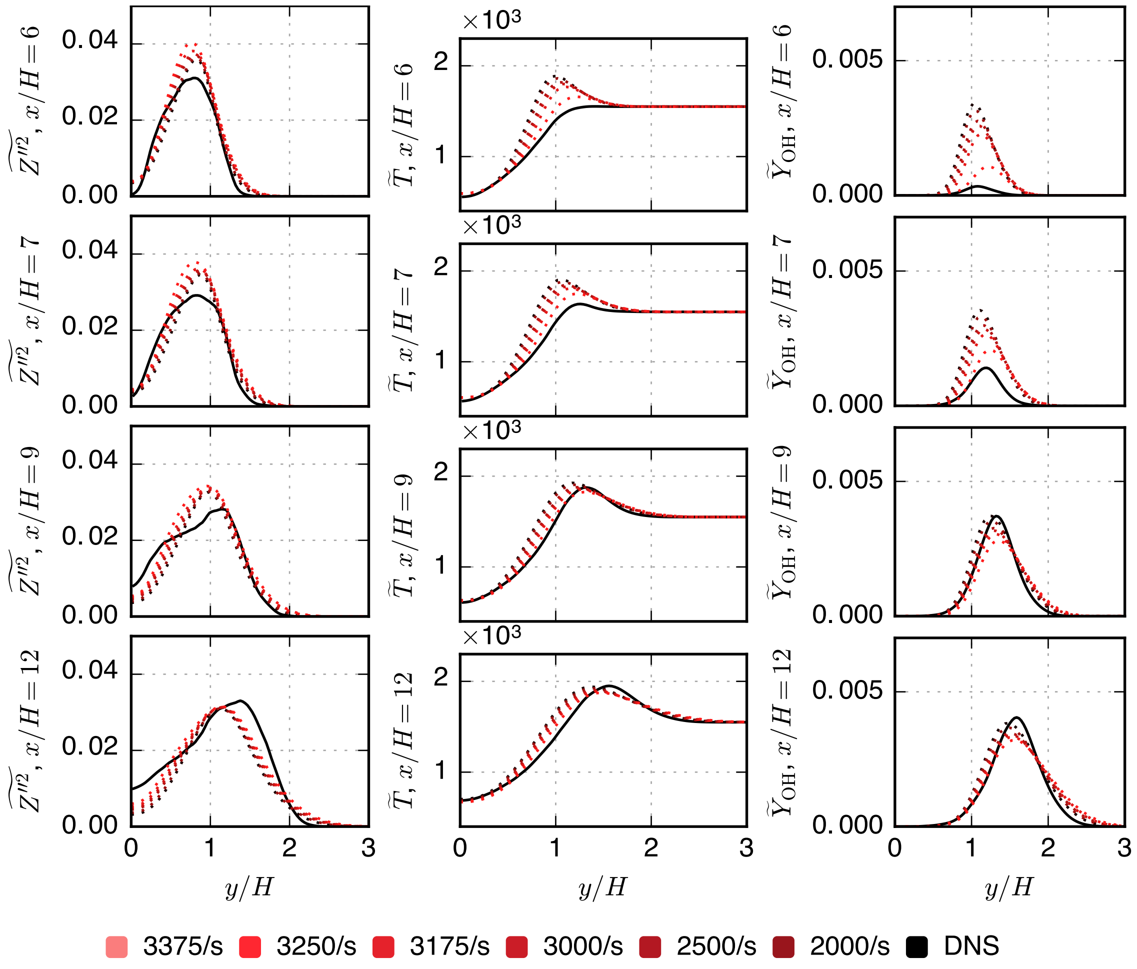

Figure 6.11: Cross-stream profiles of mixture fraction variance, temperature and $\widetilde{Y}_{\mathrm{OH}}$ for a range of scalar dissipation rates at $x/H \in \{6, 7, 9, 12\}$

worst further downstream, where it fails to match the peak temperature achieved by using a lower scalar dissipation rate which is closer to the downstream DNS conditions, and as a result has a lower peak temperature than the DNS. The temperature and $\widetilde{Y}_{\mathrm{OH}}$ profiles both tell the same story in this regard. This downstream effect is less pronounced than the variation caused at $x/H = 6$ by the lift-off height variation, but this can be explained as a result of the sharp gradient of temperature and $\widetilde{Y}_{\mathrm{OH}}$ in this region; high dT/dx combined with error in the lift-off height (measured in the x direction) causes a large error in the predicted temperature at this location.

6.7 Comparison of 3D, 4D and 5D tables

This section compares the effect of the number of free parameters included in the joint mixture fraction progress variable pdf, specifically:

- Continuous marginal pdf for Z, Dirac delta marginal distribution for c (3D);

- Continuous marginal pdf for both Z and c, with independence assumed (4D);
- Continuous marginal pdf for both Z and c, using a Plackett copula (5D).

The odds parameter for the Plackett copula is determined using a transport equation for $\widetilde{Z''c''}$ together with the methods laid out in Chapter 4.

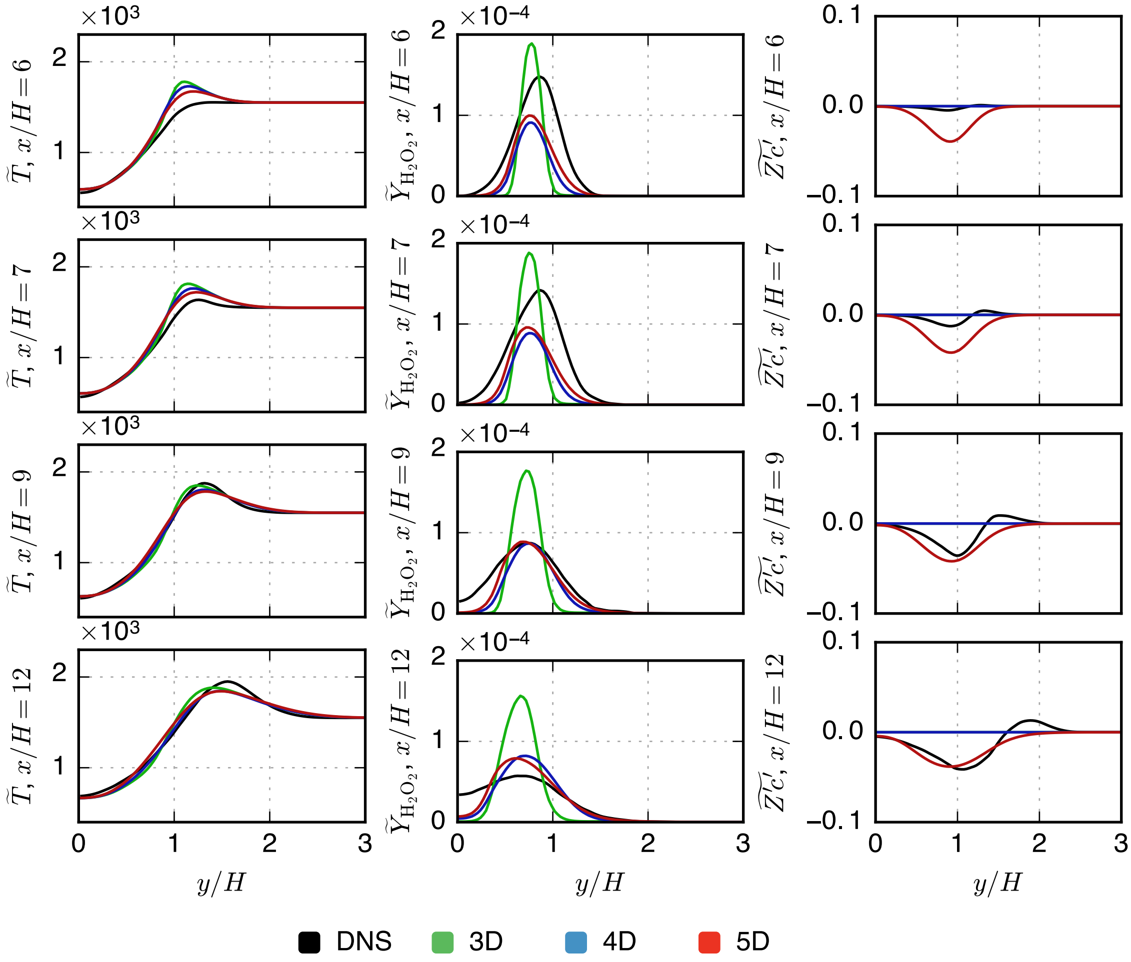

Figure 6.12: Cross-stream profiles of $\widetilde{T}$, $\widetilde{Y}_{\mathrm{H_2O_2}}$ and $\widetilde{Z''c''}$ for 3D, 4D and 5D presumed pdfs at $x/H \in \{6, 7, 9, 12\}$.

Radial profiles comparing the influence of the 3D, 4D and 5D presumed pdf models for $\widetilde{T}$, $\widetilde{Y}_{\mathrm{H_2O_2}}$ and $\widetilde{Z''c''}$ are showin in Figure 6.12. The profiles of $\widetilde{Z''^2}$ and $\widetilde{c''^2}$ show no significant differences between the models and so are omitted. The temperature profiles indicate that all three models over-predict the lift-off height. The peak temperature from the 3D model (delta distribution for c) is higher than that of the 4D and 5D models. The temperature profile of the 4D (independent) model is initially higher, indicating that it slightly over-predicts the lift-off height, and downstream the 4D and 5D models predict very similar temperatures. This suggests that the 5D model gives an improved model for reaction rates, but has little direct effect on $\widetilde{T}$. In terms of prediction of $\widetilde{Y}_{\mathrm{H_2O_2}}$, the 3D model gives a significant over-prediction and fails to account for the consumption of $\widetilde{Y}_{\mathrm{H_2O_2}}$ moving downstream. Both the 4D and 5D models significantly under-predict $\widetilde{Y}_{\mathrm{H_2O_2}}$ around $x/H = 7, 9$ but over-predict it downstream at $x/H = 12$. Relative to this effect, the difference in profiles from the 4D and 5D models is much less significant. Finally, the plots of $\widetilde{Z''c''}$ compare the covariance observed in the DNS with the covariance modelled by the RANS transport equation. While these are not exactly comparable due to the normalisation of progress variable differing between the two, the general agreement is good, with negative values of covariance being accurately captured downstream. However, upstream the covariance appears over-predicted and the transport equation fails to capture the positive covariance observed on the lean side of the stoichiometric line observed in the DNS.

6.8 DNS data copula vs independent

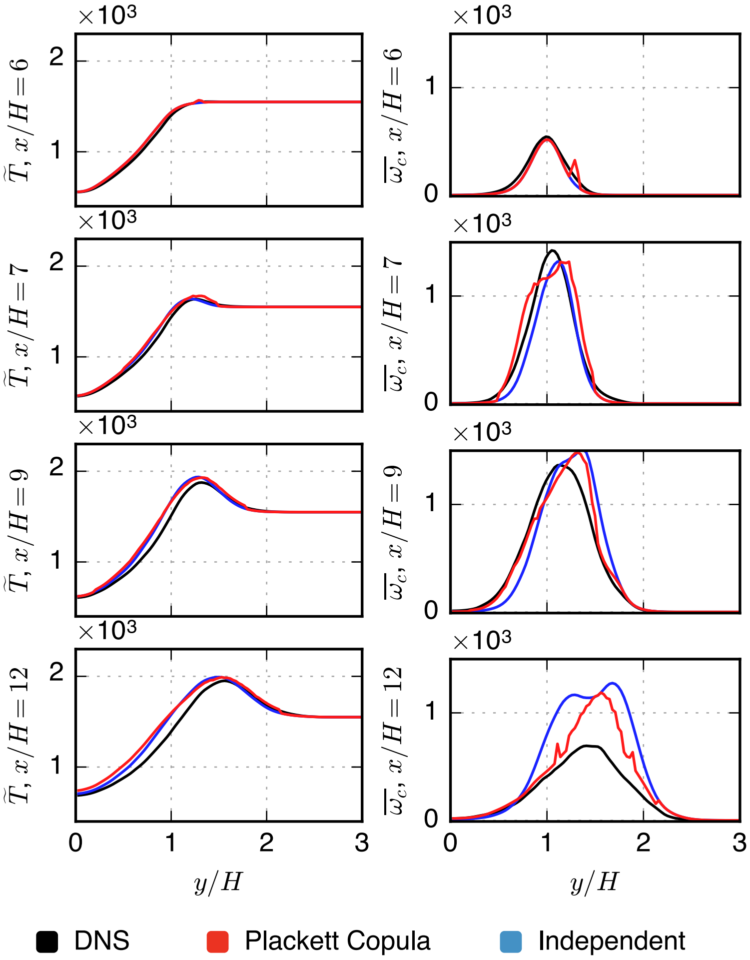

Figure 6.13: Radial profiles of temperature and reaction rate of progress variable computed from DNS quantities with presumed pdfs.

To confirm that the 5D model has little direct effect on predicted temperature, conditional mean quantities $\langle \omega_c | \eta, \zeta \rangle$ were extracted from the entire DNS domain, and used

Turbulent table dimension	Lift-off height x/H
3D	4.64
4D	4.54
5D	4.97

Table 6.2: Lift-off heights predicted by 3D, 4D and 5D turbulent flamelet tables.

for the to the calculation of mean and Favre averaged quantities via

$$\overline{\omega_c}(\mathbf{x},t) = \int_0^1 \int_0^1 \langle \omega_c | \eta, \zeta \rangle p(\eta,\zeta) d\eta d\zeta \tag{6.8}$$

$$\widetilde{T}(\mathbf{x},t) = \int_0^1 \int_0^1 \langle T | \eta, \zeta \rangle \widetilde{p}(\eta,\zeta) d\eta d\zeta. \tag{6.9}$$

where p is the presumed pdf to be analysed. This approach differs from the use of a flamelet table to provide conditional quantities, as applied in Section 5.4, as the temperature and reaction rate come directly from the DNS and include information about the effect of scalar dissipation rate on conditional quantities.

Figure 6.13 compares the mean temperature and reaction rate from the DNS with the respective quantities computed from the conditional averages and a presumed pdf. The error associated with the use of a presumed pdf, illustrated by the deviation of the integrated mean values from the DNS solution, is significant and of the order of 20% at some locations for temperature, and higher for the reaction rate. The assumption of independence has no significant effect on the calculation of the mean temperature, and the sensitivity to this assumption is at any rate small in comparison to the use of presumed pdfs in the first place; the use of this particular copula does not significantly reduce the error in prediction of the mean temperature. A similar result was observed for all of the major species mass fractions. The mean reaction rate, however, exhibits a stronger dependence on correlation. The temperature differences observed in the RANS simulations attributed to different predictions of the mean reaction rates resulting in different $\tilde{c}$ and $\widetilde{c''^2}$ fields.

6.9 Conclusions

In this chapter, several RANS simulations of the ethylene slot jet were performed. Several modelling options were tested, including: choice of marginal presumed pdf; formulation of the presumed joint-distribution; value of the peak scalar dissipation rate; and choice of control variable. Scalar dissipation rate was confirmed to be an important parameter in autoigniting flames which should be accounted for in a turbulent combustion model. The prediction of Favre averaged quantities was found to be insensitive to the choice of marginal distributions tested (top-hat and beta) however the top-hat pdf (Floyd et al. 2009) provided a substantial decrease in computation time needed to generate the lookup table. The significance of this depends on the case to be simulated: for the RANS simulations presented in this chapter, the computational cost of table generation for the 5D table containing all species mass fractions and source terms greatly exceeded the that of running the RANS. The use of a residence-time based reference variable a was found to offer improved predictive capability in some situations and the reference variable b was found to exhibit behaviour between that shown by the use of a and c as a reference variable.

Variance of progress variable was considerable, the inclusion of the Plackett copula over the assumption of independence was found to offer moderate improvements in prediction of mean profiles. The mechanism by which the dependence in the presumed joint-distribution affects the mean reaction rates is explained by evaluating the mean reaction rates and temperatures from the joint-distribution and conditional quantities of the DNS data, reconfirming that correlation has little direct effect on temperature but a significant effect on reaction rates. It is concluded that the temperature profiles in the RANS differ due to modified progress variable mean and variance fields produced by the different mean reaction rate and variance source terms. Hence it is shown that the use of the Plackett copula to model the joint distribution in a lifted autoigniting flame offers only marginal modelling improvement.

Given the added computational cost of turbulent table calculation involved in including the scaled covariance as a parameter in the table, it is recommended that scalar dissipation rate be included as a tabulation parameter before some measure of the dependence. With the size of a 5-dimensional turbulent flamelet table already exceeding several gigabytes when all species and source terms are tabulated, extending beyond 5 table parameters will require more advanced data structures such as those employed in In Situ Adaptive Tabulation (Pope 1997).

Chapter 7

Results III: Multivariate presumed-pdf modelling for spray-fuelled combustion

A key step in the prediction of spray combustion is modelling the evaporation of fuel droplets. As noted in Sections 2.2.1 and 2.2.3, the evaporation rate of a droplet depends on the seen properties of the surrounding flow, such as the temperature, composition and relative velocity. Each of these seen quantities exhibit turbulent fluctuations, and these influence the instantaneous and, potentially, the averaged evaporation rate within a spray. In the context of Lagrangian spray modelling, it is common to account for seen velocity fluctuations by assuming they have a normal distribution, and De *et al.* (De, Lakshmisha, et al. 2011) have recently demonstrated a presumed beta distribution mixture fraction probability density function approach which accounts for independent fluctuations in the seen composition. This chapter presents a further development of presumed-probability density function (pdf) modelling which also accounts for the correlation between fluctuations of seen velocity, temperature and composition. The new approach uses stochastic sampling of copula-based presumed joint-distributions.

Section 7.1 presents two numerical investigations on the effect of turbulent fluctuations in seen quantities on the mean evaporation rate. The Plackett copula is used to model the joint-distribution of selected seen quantities, and the effect of seen quantity correlations on the mean evaporation rate is investigated. This is done first for the mixture fraction-velocity joint-distribution (Section 7.1.2), and then for the mixture fraction-progress variable joint-distribution (Section 7.1.3). In Section 7.2 the influence of the seen mixture fraction-progress variable joint-distribution on overall spray combustion behaviour is studied by application to a RANS simulation of an autoigniting turbulent spray.

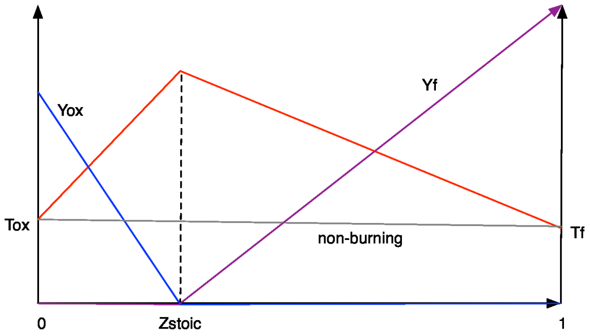

Figure 7.1: The generic Burke-Schumann limit for a diffusion flame

7.1 Effects of seen property fluctuations on evaporation rate statistics

7.1.1 General Formulation for statistically homogeneous spray

In mixture fraction-based spray combustion modelling (Bilger 2011), the evaporation rate contributes to source terms in both the mean and variance equations for mixture fraction. The source term for the mean mixture fraction is related to the volumetrically-averaged evaporation rate of the spray (found using Equation 2.91). In the following numerical studies, the influence of the joint-distribution of seen quantities on mean evaporation rate is investigated by evaluating the steady-state evaporation rates for a spray consisting of boiling droplets under a range of turbulence and mixing conditions. In order to isolate the influence of the droplets' seen properties from the droplets own properties, we report the average of the steady-state evaporation parameter ($\overline{\lambda}_{st}$), which is proportional to the mean evaporation rate for a given droplet population.

Droplet evaporation and seen quantities are discussed in Sections 2.2.1 and 2.2.3, respectively, and the steady state evaporation rate λ_{st} is given by Equation 2.92. Sampling from presumed joint-distributions is described in Section 4.5; here, the method of Johnson (Johnson 2013) is used to sample from a Plackett copula, and presumed marginal distributions are applied for each of the seen quantities. For velocity fluctuations, a Gaussian distribution is assumed, and for mixture fraction and progress variable a beta distribution is assumed. The evaluation of seen quantities such as temperature and fuel mass fraction depends on the choice of control parameters.

For mixture fraction-velocity fluctuations, the functional dependence of the temperature and fuel mass fraction on mixture fraction is modelled by the Burke-Schumann diffusion flame structure, as plotted in Figure 7.1 (Burke and Schumann 1948). The simple structure of the Burke-Schumann diffusion flame in Figure 7.1 is idealised, but is still sufficient for the purposes of demonstrating the effects of seen mixture fraction fluctuations on droplet evaporation. In general, more advanced models which account for

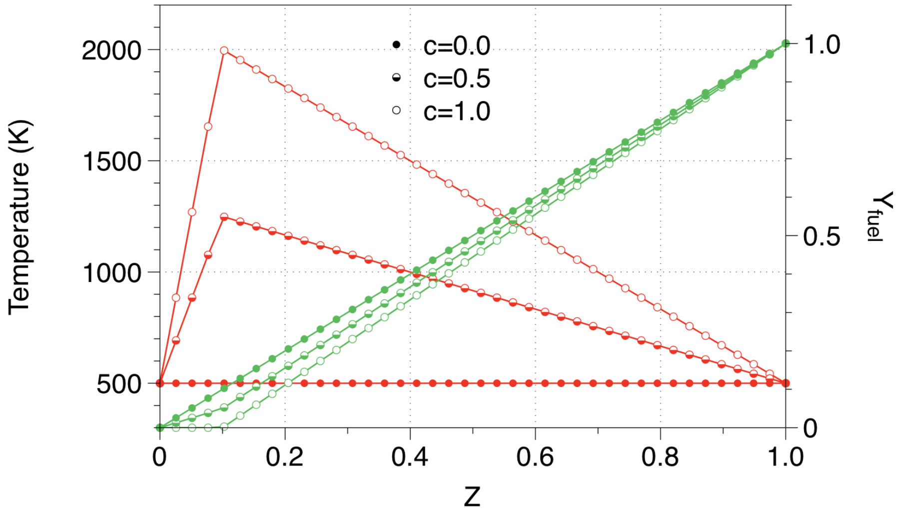

Figure 7.2: The extension of the Burke-Schumann limit for partially-premixed combustion employed in this study. Red: temperature, green: fuel mass fraction.

effects of finite rate chemistry on the relationship between the seen mixture fraction and the seen composition could be applied — for example the steady laminar flamelet model (Peters 1984a). The fuel and air are modelled using property models for n-heptane evaporation in air specified in (Chin and Lefebvre 1983). Evaporation predictions are reported for combustion with evaporated-fuel and air temperatures of 500K, and a flame temperature of 2000K at an assumed stoichiometric mixture fraction of 0.1. The mean evaporation rate $\overline{\lambda}_{st}$ is reported in terms of the mixture fraction segregation, rather than the variance, where the segregation g is defined by,

$$g = \frac{\overline{Z'^2}}{\overline{Z}\left(1 - \overline{Z}\right)} \tag{7.1}$$

such that it varies between zero and unity. A constant mean slip velocity of $6ms^{-1}$ is specified for all tests. The Ranz-Marshall correlation (Equation **??**) only depends on the magnitude of the droplet slip velocity, and not its sign, therefore a non-zero mean slip velocity is needed in order to see any effect of correlation between mixture fraction and velocity.

For mixture fraction-progress variable fluctuations, the Burke-Schumann limit is no longer applicable, since it is parametrised by mixture fraction only. A simple extension can be made by a linear interpolation between the burning (progress variable $c = 1$) and unburned ($c = 0$) states, as shown in Figure 7.2. The definition chosen for this analysis is based on the mass fraction of CO_2:

$$c = \frac{Y_{CO_2} - Y_{CO_2}^{\text{unburned}}(Z)}{Y_{CO_2}^{\text{burned}}(Z) - Y_{CO_2}^{\text{unburned}}(Z)} \tag{7.2}$$

$$= \frac{Y_{CO_2}}{Y_{CO_2}^{\text{burned}}(Z)} \tag{7.3}$$

Here we assumed that $Y_{CO_2}^{\text{unburned}} = 0$.

The mean steady-state evaporation parameter $\overline{\lambda}_{st}$ is evaluated according to Equation 2.92 by drawing a large number of samples (here, 10,000) from the appropriate joint-distribution of control parameters. These samples from the joint-distribution of control parameters are then used to determine the seen temperature and composition. For each sample, a steady state evaporation rate λ_{st} is then found. From these the mean steady state evaporation rate $\overline{\lambda}_{st}$ is calculated. This sampling procedure is equivalent to ensemble-averaging in a statistically stationary turbulent flow.

7.1.2 Velocity/mixture fraction results and discussion

Results for the mixture fraction-velocity study are presented for correlation values of -0.5, 0, and 0.5, and for kinetic energy values of 0, 0.135, 0.54 and 2.16 m^2s^{-2} which correspond to turbulence intensities I of 0%, 5%, 10% and 20%. In the case where the correlation is zero, the joint-distribution reverts to independent distributions of mixture fraction and velocity.

Figure 7.3 shows the effect of the mean mixture fraction and velocity fluctuation on the mean steady state evaporation coefficient $\overline{\lambda}_{st}$. It is observed that the mean evaporation rate for the laminar case ($k = 0$, $g = 0$) peaks at $Z = 0.25$ after rising rapidly with the temperature in the region below stoichiometry. Between $Z = 0.1$ and $Z = 0.25$ the mean evaporation rate continues to increase due to the disproportionate effect of higher temperatures on evaporation rates in the logarithm in Equation 2.92.

Introducing velocity fluctuations only ($g = 0$ and $k > 0$ in Figure 7.3) increases the evaporation rate across the entire range of mixture fractions by a small amount. This is due increased spread of the velocity distribution and the $Re^{1/2}$ non-linear dependence of evaporation rate on seen velocity. The shape of the evaporation profile is preserved.

Introducing mixture fraction fluctuations only ($g = 0.02$ and $g = 0.2$ in Figure 7.4) the increase in segregation results in a decrease in evaporation rate, particularly in the region surrounding stoichiometry, as a higher proportion of seen mixture fractions lie close to zero. The shape of the evaporation rate profile is no longer preserved, indicating that the dependence on the mean temperature profile is lessened as a wider range of temperatures is experienced by the droplets.

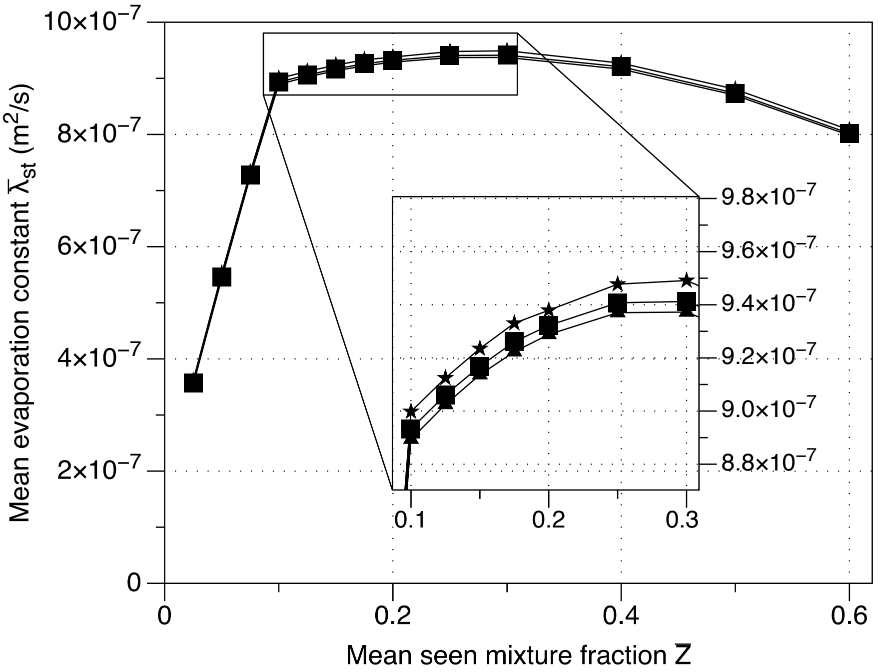

Figure 7.3: Effect of velocity fluctuations on evaporation rate with g=0 and (○): $k = 0 m^2/s^2$; (▲): $k = 0.135 m^2/s^2$; (■): $k = 0.54 m^2/s^2$; ($\star$): $k = 2.16 m^2/s^2$

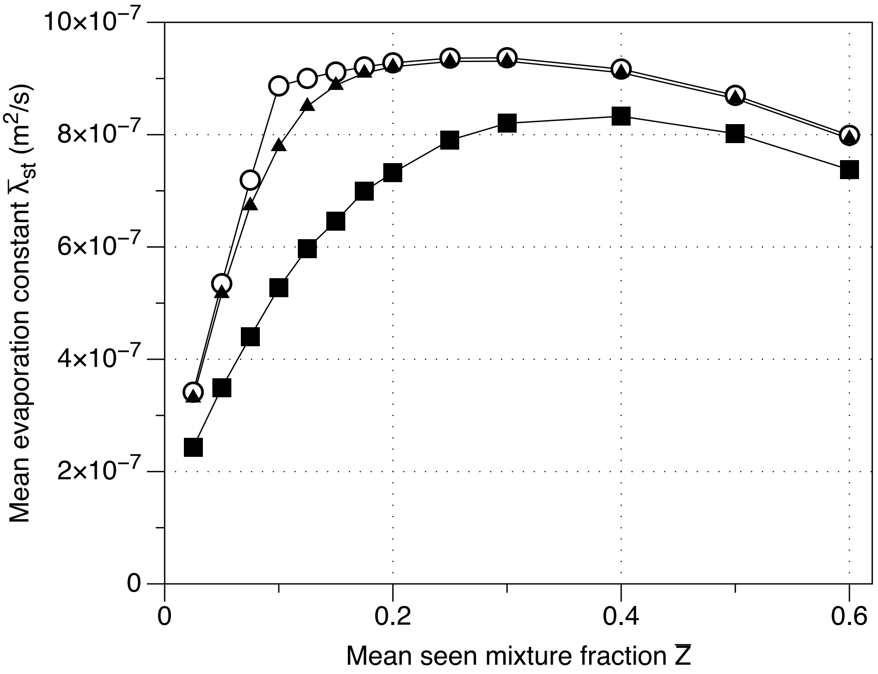

Figure 7.4: Effect of mixture fraction fluctuations on evaporation rate with $k = 0$ and (○): $g = 0$; (△): $g = 0.02$; (□): $g = 0.2$

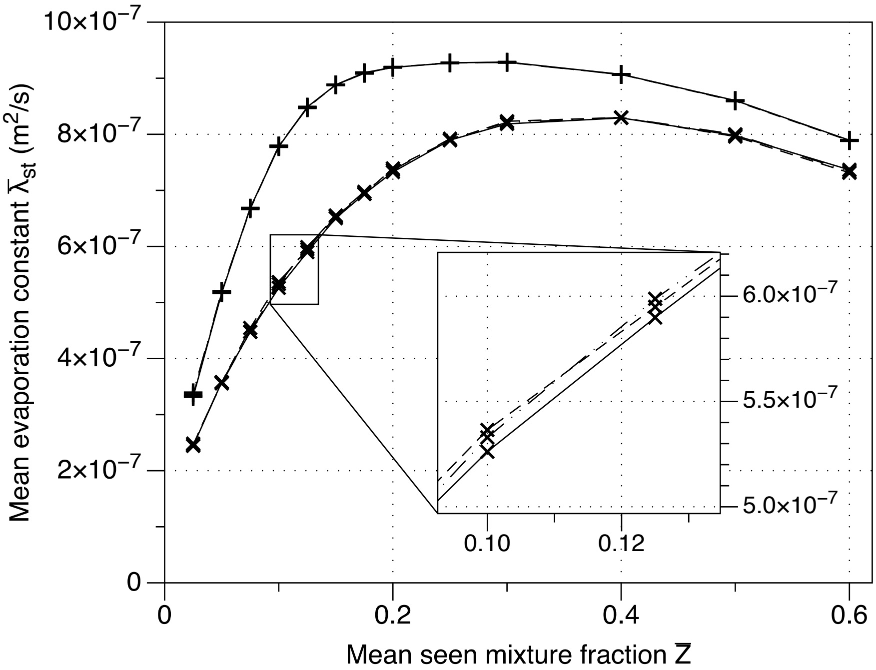

Figure 7.5: Effect of correlation on evaporation rate at $k = 2.16 m^2/s^2$ with (+):$g = 0.02$; and (×):$g = 0.2$. Solid line: zero correlation. Dashed line: correlation = 0.5. Dotted line: correlation = -0.5.

The combination of both mixture fraction and velocity fluctuations (Figure 7.5) shows little difference from the inclusion of mixture fraction only, due to the relatively small effect of velocity fluctuations as compared with the effect of mixture fraction fluctuations. For low values of segregation $g = 0.02$ no effect is seen of the correlation between mixture fraction and Reynolds number; the lines are indistinguishable. For higher segregation $g = 0.2$ there is an observable effect on the order of 4%, although it is not clear whether this is due to a lack of statistical convergence. In the region around stoichiometry $Z \in [0, 0.3]$, both positively and negatively correlated fluctuations enhance evaporation rate while in the region above $Z = 0.4$ both forms of correlation inhibit evaporation.

7.1.3 Mixture fraction-progress variable distribution results

The results of Section 7.1.2 indicate that in the burning case, turbulent velocity fluctuations do not have a significant effect on the evaporation rate of a droplet in steady state evaporation. In particular, the dependence of λ_{st} on $\mathrm{Re}_d^{\frac{1}{2}}$ is only weakly non-linear at conditions of practical interest. This suggests that the covariance $\overline{u'Z'}$ was a poor choice to investigate, as the correlation should not be expected to have a significant impact unless both of the quantities in question exhibit a significant effect on evaporation.

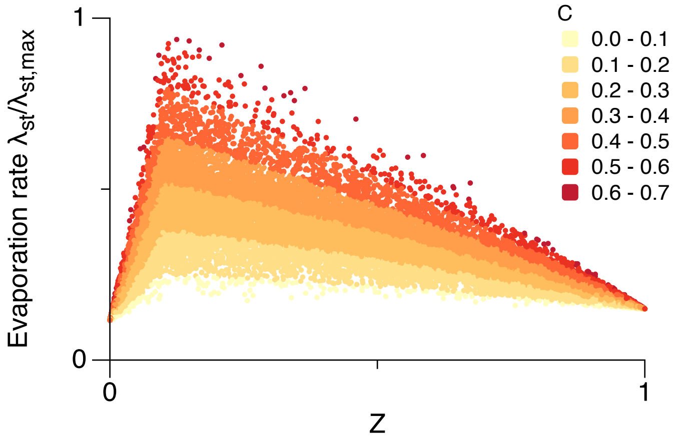

Figure 7.6: Samples of instantaneous steady state evaporation rate as a function of mixture fraction and progress variable.

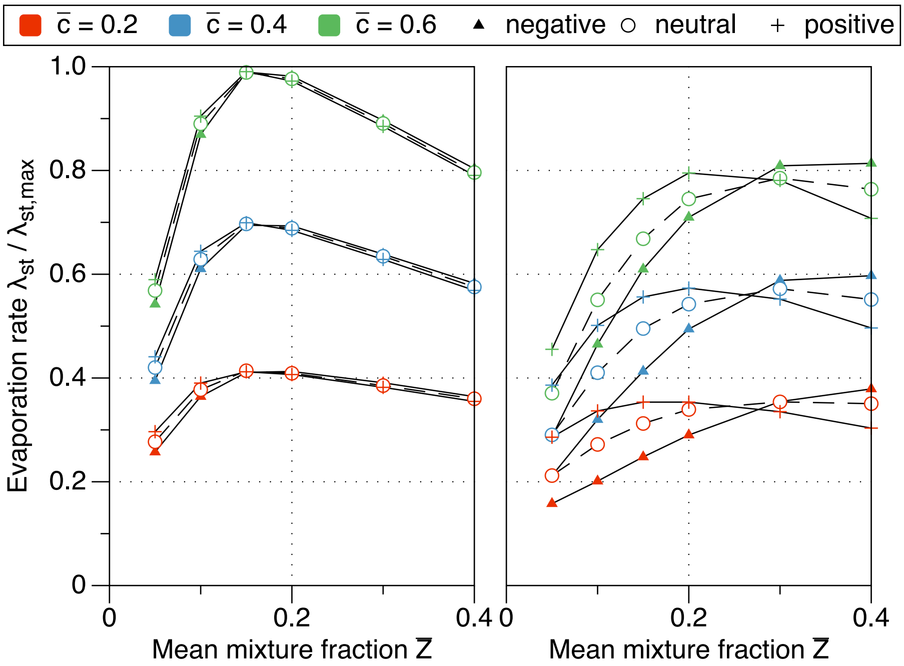

Figure 7.7: Mean steady state evaporation rate as a function of mean mixture fraction. Left: $g = 0.02$, Right: $g = 0.2$.

The modified Burke-Schumann limit shown in Figure 7.2 produces the instantaneous evaporation rate shown in Figure 7.6. The strong dependence of the evaporation parameter on the seen temperature is evident though the similarity of this figure to Figure 7.2. The effect of mixture fraction and progress variable fluctuations is summarised in Figure 7.7: for a selection of mean progress variable values $\bar{c} \in \{0.2, 0.4, 0.6\}$, mean mixture fractions $\overline{Z}$, and segregations $g \in \{0.02, 0.2\}$, the effect of correlation on the mean evaporation rate is presented. The covariances investigated correspond to the minimum and maximum values possible by the given marginal distributions, plus the independent assumption. For very low segregation ($g = 0.02$), there is very little effect

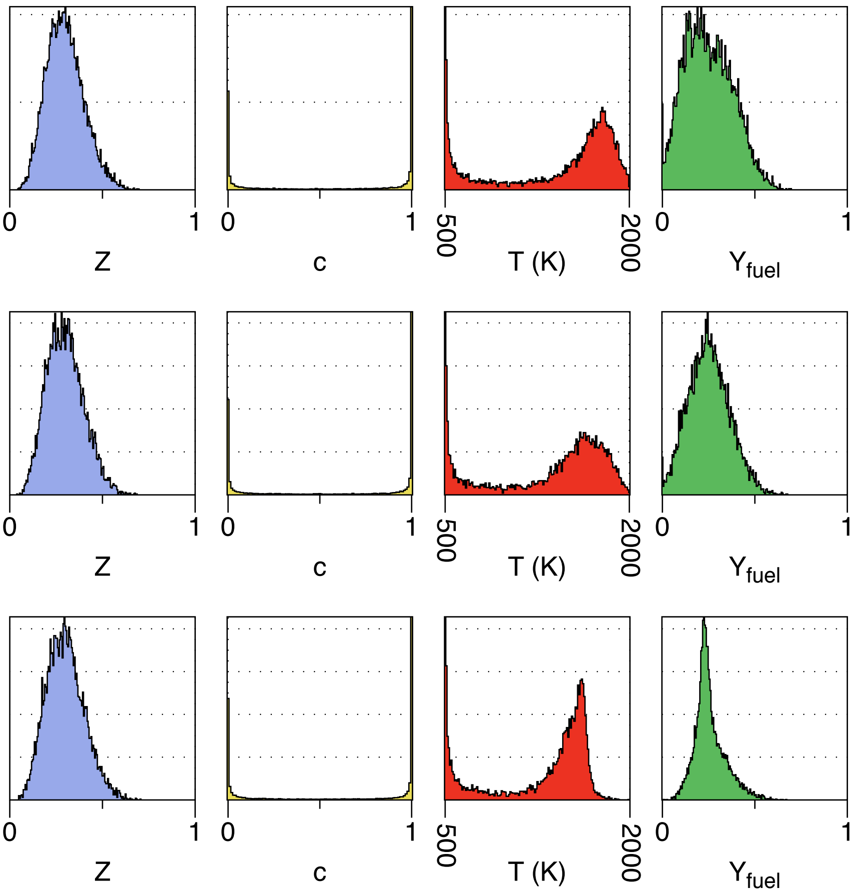

Figure 7.8: Seen mixture fraction, progress variable, temperature and fuel mass fraction probability density functions for negatively correlated ($\theta = 0.1$, top), independent ($\theta = 1$, centre), and positively correlated ($\theta = 100$, bottom).

of the Z-c correlation on the evaporation rate for any of the mean mixture fractions. For moderate values of the segregation, however, the covariance has a significant effect on the evaporation rate. For mean mixture fractions below ≈ 0.3, positive covariance enhances the evaporation rate while negative covariance inhibits evaporation. This trend switches for $Z > 0.3$, where positive covariance inhibits evaporation and negative covariance increases evaporation. This is perhaps unexpected, as the stoichiometric mixture fraction is specified as $Z_{st} = 0.1$ in the modified Burke-Schumann profile.

The influence of Z-c correlation on the evaporation rate can be understood by considering the marginal distributions of T and Y_{fuel}. These marginal distributions, together with the marginal distributions of Z and c, are presented in Figure 7.8 for negative, neutral and positive covariances (these distributions are obtained by sampling the Plackett copula, in which these covariances correspond to odds parameters of $\theta = 0.1$, $\theta = 1$ (independent) and $\theta = 100$, respectively). The marginal distributions of Z and c are given by $\overline{Z} = 0.3$, $\overline{Z'^2} = 0.01$, $\overline{c} = 0.6$ and $\overline{c'^2} = 0.2$. It is observed that the inclusion of correlation has no effect on the mixture fraction and progress variable distributions, as expected, whereas significantly different temperature and fuel mass fraction distributions are observed. Since ultimately temperature and fuel mass fraction are parameters that affect the evaporation rate, this gives insight into how the inclusion of Z-c dependence on evaporation rates has a significant effect.

7.1.4 Summary of seen property effects on evaporation

Using a zero dimensional evaporating spray problem, the sensitivity of the mean steady state evaporation rate of liquid n-heptane to both mixture fraction – velocity dependence and mixture fraction – progress variable dependence were studied. The approach developed uses Plackett copulas to generate presume joint-pdfs with specified first and second moments. This method has been demonstrated for a beta-Gaussian joint-pdf and an efficient sampling algorithm has been developed. Mixture fraction – velocity correlations were found to have no significant effect on the mean evaporation rate, whereas mixture fraction – progress variable correlations were found to have a significant effect on evaporation rate, of up to 20%. Further, whether correlation enhanced or inhibited the evaporation rate was found to be a dependent on the mean mixture fraction, and the point where correlation had no significant effect was found to lie around $Z = 0.3$, considerably higher than the stoichiometric mixture fraction. While this analysis was performed by considering an idealised temperature and fuel mass fraction dependence on Z and c, this result is expected to be observed in real flames where the temperature and fuel mass fraction are related to Z and c through more complex models, such as the laminar flamelet model. These results therefore suggest that the inclusion of a presumed pdf model which can capture mixture fraction and progress variable dependence is important for the numerical simulation of Reynolds averaged flows with evaporating dispersed spray in which the spray is found in regions where such correlations are present.

7.2 Assessment of presumed joint-pdf modelling in the simulation of an autoigniting n-heptane spray

Building on the results of the *a priori* analysis done in the previous section, this following section sets out to test the stochastic evaporation model *a posteriori* in a 3D axisymmetric RANS simulation in conditions relevant to diesel engines.

7.2.1 Experimental configuration

Spray autoignition data from the Sandia National Laboratories' optically-accessible constant volume combustion chamber are used as a basis for investigating the presumed-pdf

Case name	Temperature	Pressure	X_{O_2}	X_{N_2}	X_{CO_2}	X_{H_2O}
X21	1000K	42bar	0.21	0.6933	0.0611	0.0356
X12	1000K	42bar	0.12	0.7806	0.0628	0.0365

Table 7.1: Initial conditions for Spray H

modelling of spray combustion. This equipment is designed to reproduce the thermodynamic conditions found inside a diesel engine. A schematic diagram of the combustion vessel is reproduced from (Idicheria and Pickett 2007b) in Figure 7.9. The combustion chamber has a cubic shape and sufficient volume that the pressure rise during combustion may be neglected. The spray is mounted centrally and directed towards the centre of the chamber so that the whole spray is visible through a 108mm optical window. Full details of the experimental configuration are given in (Idicheria and Pickett 2007b; M. Pickett 2016) and references therein. A range of operating parameters have been investigated experimentally including fuel type, injection pressure, injection nozzle diameter, and temperature, density and dilution of the oxidiser (giving between 8% and 21% oxygen by volume). The initial high pressure and temperature is achieved by burning a lean charge of a premixed hydrocarbon fuel blend, in order to achieve the desired pre-ignition composition and temperature. The vessel walls are heated and the vessel contents are stirred in order to reduced thermal inhomogeneity in the charge, however the background flow is sufficiently weak that the fluid can be considered quiescent prior to fuel injection.

The experimental cases simulated in this Chapter are all for n-heptane fuel, known as *Sandia Spray-H*, with 0.1mm diameter single hole injector and a 6ms injection duration. The fuel mass flow rate specified in the simulations is fitted to experimetnal measurements is given in Fig. 7.10 (M. Pickett 2016). The two initial oxygen levels are used, as specified in Table 7.1. The key metrics used for comparison with the experimental are the ignition delay time (IDT) and lift-off length (LOL), as defined and reported in (M. Pickett 2016). The experimental ignition delay time is based on the system pressure measurement and the experimental lift-off length is based on OH* chemiluminescence observations. In the simualtions, IDT was defined as the time after the start of injection with the maximum rate of change of peak temperature in the system and the lift-off length is estimated from the most upstream location of a threshold value of OH mass fraction, in accordance with guidance from the Engine Combustion Network (ECN) (M. Pickett 2016).

7.2.2 Numerical details

The spray configuration is statistically axisymmetric and it is modelled with unsteady RANS (URANS) simulations are performed on an axisymmetric domain as described in (Bolla 2013). The domain is a 2D wedge of 1° with cyclic boundary conditions with

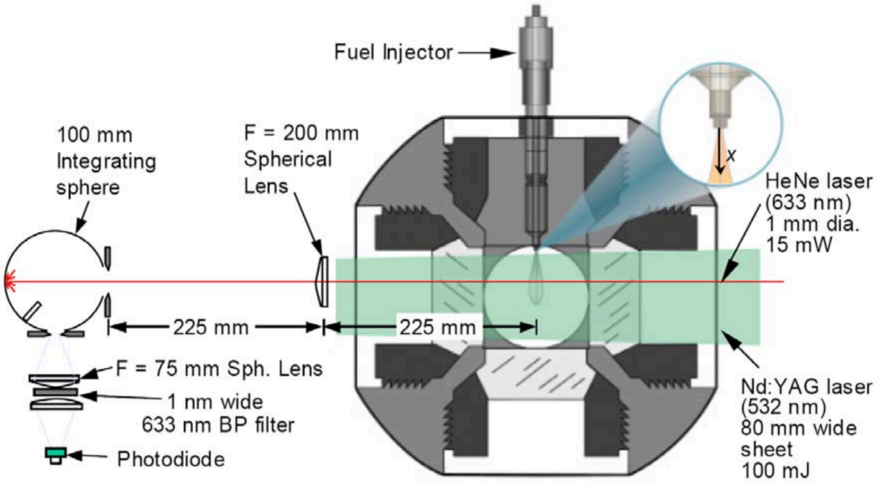

Figure 7.9: Burner configuration for spray cases, reproduced from (Idicheria and Pickett 2007b)

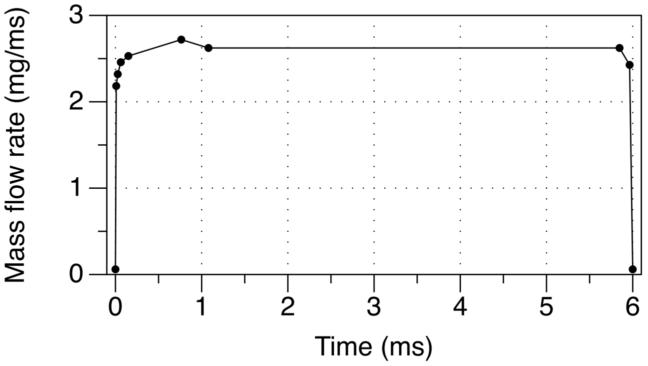

Figure 7.10: Spray mass flow rate temporal profile

a uniform grid resolution of $0.5mm \times 0.5mm$ in the region of the spray. This level of resolution is consistent with previous studies (Bolla 2013; Lucchini et al. 2009; Novella et al. 2011) and with ECN recommendations (M. Pickett 2016).

This same configuration was studied previously by De Paola (Paola 2007) and Bolla (Bolla 2013) in the context of CMC and the FGM/presumed-pdf method has been applied to this spray by Bekdemir *et al.* (Bekdemir, Somers, et al. 2009; Bekdemir, Rijk, et al. 2010).

The numerical implementation for this case is essentially the same as described in Section 6.3, with the addition of the Lagrangian spray model described in Equations 2.74-2.76.

Density is given by the ideal gas equation of state using the mean mass fractions and local pressure, neglecting gravitational effects. Other thermodynamic properties are modelled as functions of temperature and composition.

Chemical reaction is modelled using the reduced n-heptane mechanism by S. Liu et al. (2004), involving 22 species according to 18 global steps. The mechanism has been applied successfully in several n-heptane spray ignition studies. Bolla (2013) reports that the mechanism gives correct trends with varying oxygen levels, giving relatively good agreement for higher oxygen levels but tending to overpredict ignition delay for higher dilution levels. Overall the kinetic model is an adequate basis for the present investigation of the presumed-pdf modelling sensitivities. The definition of progress variable for this case is given in Equation **??**.

The turbulence model employed is the $k-\varepsilon$ model with the standard coefficients. The fluid is initialised with ambient temperature 1000K ($Z=0$) and turbulence quantities $k=1.25m^2/s^2$ and $\varepsilon=125m^2/s^3$. The solution method is PISO (Issa 1986) with a constant timestep of $1\times10^{-6}s$. Simulations were performed over the entire 6ms injection time interval.

The liquid phase mass-transfer is given by the same boiling model present in Star-CD, modified via a user defined function to apply stochastically sampled seen quantities from the presumed pdf:

$$\frac{\partial m_d}{\partial t} = -2\pi \frac{k_g}{c_{p,g}} D_d \left(1 + 0.23\mathrm{Re}_d^{\frac{1}{2}}\right) \log\left[1 + \frac{c_{p,g}(T_g - T_d)}{L_v}\right] \tag{7.4}$$

where m_d, D_d and T_d are the mass, diameter and temperature of the droplet, k_g and $c_{p,g}$ are the thermal conductivity and specific heat at constant pressure of the gas phase, and L_v is the latent heat of vaporization. The droplet Reynolds number Re_d is calculated as

$$\mathrm{Re}_d = \frac{\rho_g |\mathbf{u}_{rel}| D_d}{\mu_{\mathrm{film}}} \tag{7.5}$$

where the relative velocity $u_{i,rel}$ is based on the stochastic seen velocity. Subscripts are used to differentiate between gas-phase/seen quantities (g), droplet quantities (d) and film quantities ($film$). In the case of no fluctuations, T_g, ρ_g and $Y_{fuel,g}$ are interpolated from the CFD. Where the stochastic evaporation model is employed, values of Z and c are sampled from the presumed joint-pdf and then the seen temperature T_g, density ρ_g and fuel mass fraction $Y_{fuel,g}$ are obtained from the flamelet table assuming $\widetilde{Z} = \tilde{c} = 0$, parametrized by Z and c. If the droplet temperature exceeds the critical temperature T_{crit} it evaporates immediately.

Liquid n-heptane at a temperature of $373K$ is injected into the domain as an axisymmetric jet of diameter $0.1mm$ and cone angle of 10°. The mass flow rate of the nozzle is given in Figure 7.10. The liquid phase injection is represented by 2×10^7 parcels/s. The Reitz-Diwakar atomization and breakup models are applied (Reitz and Diwaker 1986), in order to model the transition from the continuous injection conditions into discrete droplets and therefore avoid the need to specify the droplet size distribution as an input parameter.

7.2.3 Results and discussion

Time-series plots are presented for $\widetilde{Z}$, $\tilde{c}$, $\widetilde{Y}_{\mathrm{H_2O_2}}$, and $\widetilde{T}$ in Figures 7.11-7.14 for the base case X12. Only a subsection of the domain closest to the axis is shown for the x direction. Figure 7.11 shows the evolution of mixture fraction over time. The spray begins to evaporate almost immediately after injection, and momentum transfer from the injected spray to the surrounding gas phase and the resulting inertia carries the vapour downstream where it mixes with the turbulent oxidiser. The stoichiometric mixture fraction line is marked (black line), as is a contour of $\widetilde{Y_{OH}}$ which indicates the position of the flame. At all times after ignition the $\widetilde{Y_{OH}}$ contour follows the stoichiometric mixture fraction line. Figure 7.12 shows the same time-series for Favre mean progress variable $\tilde{c}$. Ignition occurs after 0.94ms on the lean side of the stoichiometric mixture fraction line. This is in agreement with the laminar flamelet used to generate the lookup table, in which the most reactive mixture fraction was found to be on the lean side of stoichiometric. Once autoignition has occurred, the flame kernel grows via progress variable diffusion and begins to propagate along the stoichiometric mixture fraction line by the same mechanism. In this manner it propagates back along the stoichiometric mixture fraction line until eventually a balance is reached between reaction and advection and the flame stabilises at the lift-off height. The lift-off height can be defined by the minimum height of a Y_{OH} contour; here $Y_{OH} = 0.0001$ was chosen, but the measurement of the lift-off height is insensitive to the exact value. While this propagation along the stoichiometric mixture fraction is happening, the progress variable also diffuses orthogonally to the mixture fraction contours. This results in the entire upper region shown in Figure 7.12 being burned, and is an artefact of the dissipation term in the laminar flamelet being included in the source term for the lookup table. In reality the scalar dissipation rate in this region is low, which would prevent the diffusion of product mass fractions into regions of mixture fraction space close to the oxidiser boundary condition.

Figure 7.13 shows time-series contour plots of $\widetilde{Y}_{\mathrm{H_2O_2}}$, which is an important quantity in pre-ignition chemistry. The contour plots show that it is initially concentrated in the regions of rich fluid with the longest residence times, up until ignition occurs at which point it is rapidly consumed. As the mean progress variable propagates downstream the small patch of $\widetilde{Y}_{\mathrm{H_2O_2}}$ moves down ahead of it to reside in the rich mixture at the base of the flame.

The time-series of temperature plots, shown in Figure 7.14, displays much the same trend as the progress variable. Initial low temperature in the region of evaporation is caused by the transfer of heat to the spray, captured here by the low temperature of the fuel boundary condition in the laminar flamelet. The temperature contours follow the progress variable propagation downstream but have a much narrower profile, with highest values around the stoichiometric mixture fraction line.

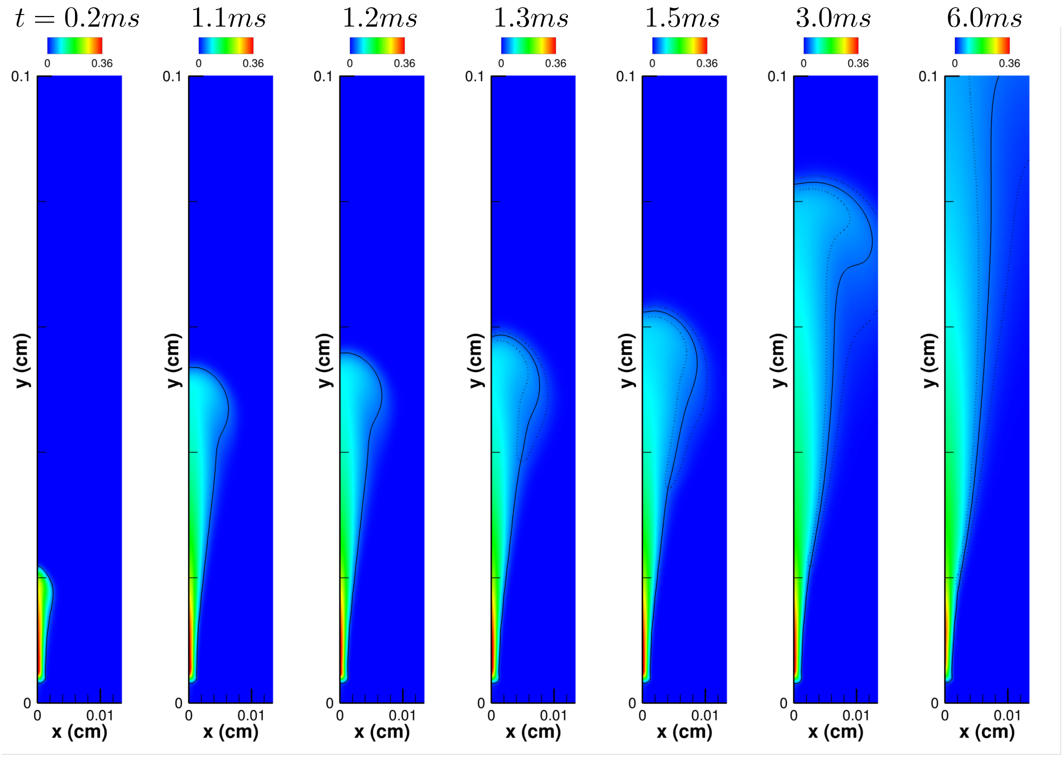

Figure 7.11: Overview of base case (X12) $\widetilde{Z}$ over time. Stoichiometric mixture fraction line (black) and $Y_{OH} = 0.0001$ contour (dotted).

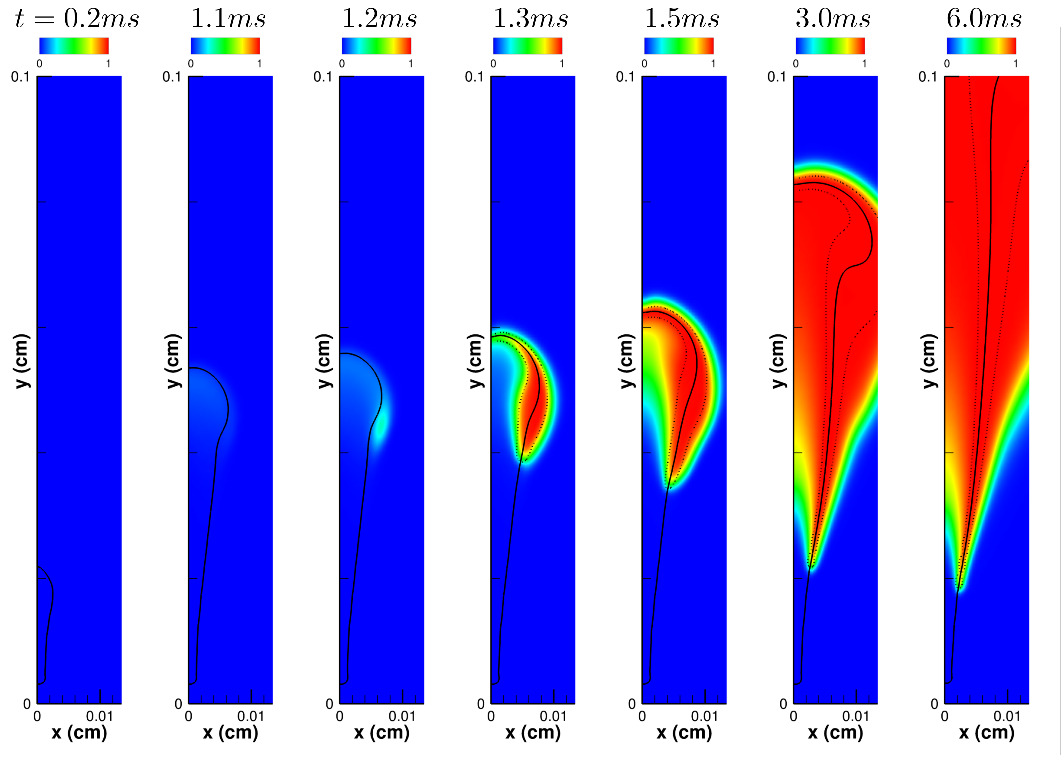

Figure 7.12: Overview of base case (X12) $\tilde{c}$ over time. Stoichiometric mixture fraction line (black) and $Y_{OH} = 0.0001$ contour (dotted).

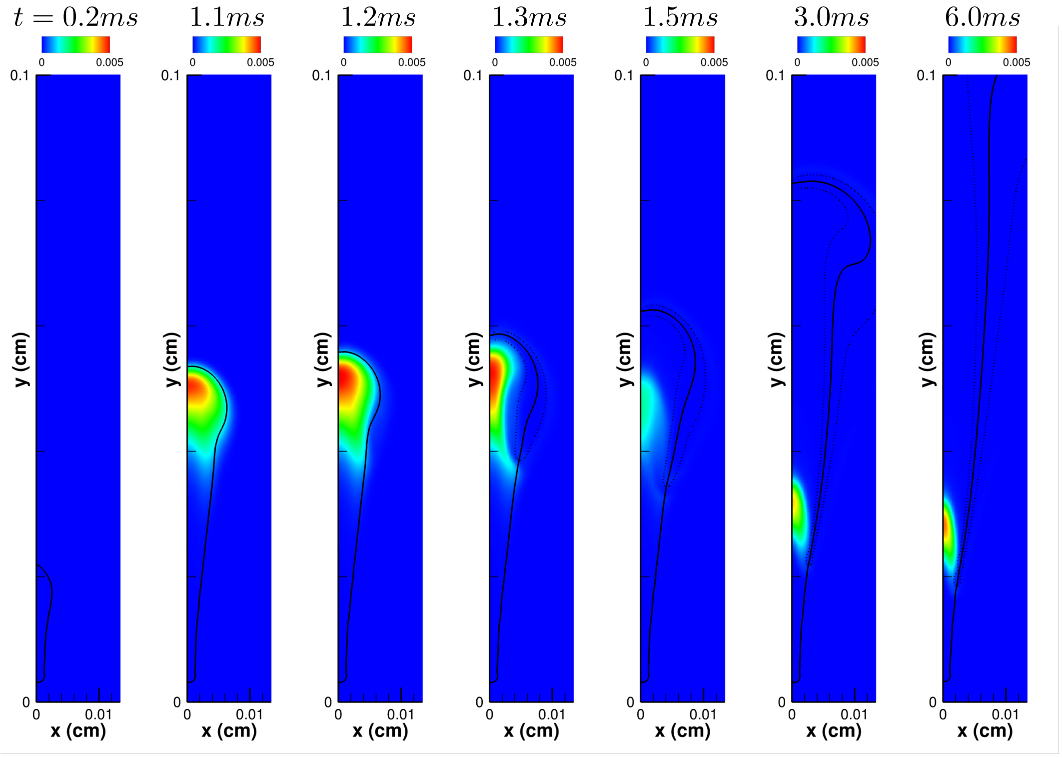

Figure 7.13: Overview of base case (X12) $\widetilde{Y}_{\mathrm{H_2O_2}}$ over time. Stoichiometric mixture fraction line (black) and $Y_{OH} = 0.0001$ contour (dotted).

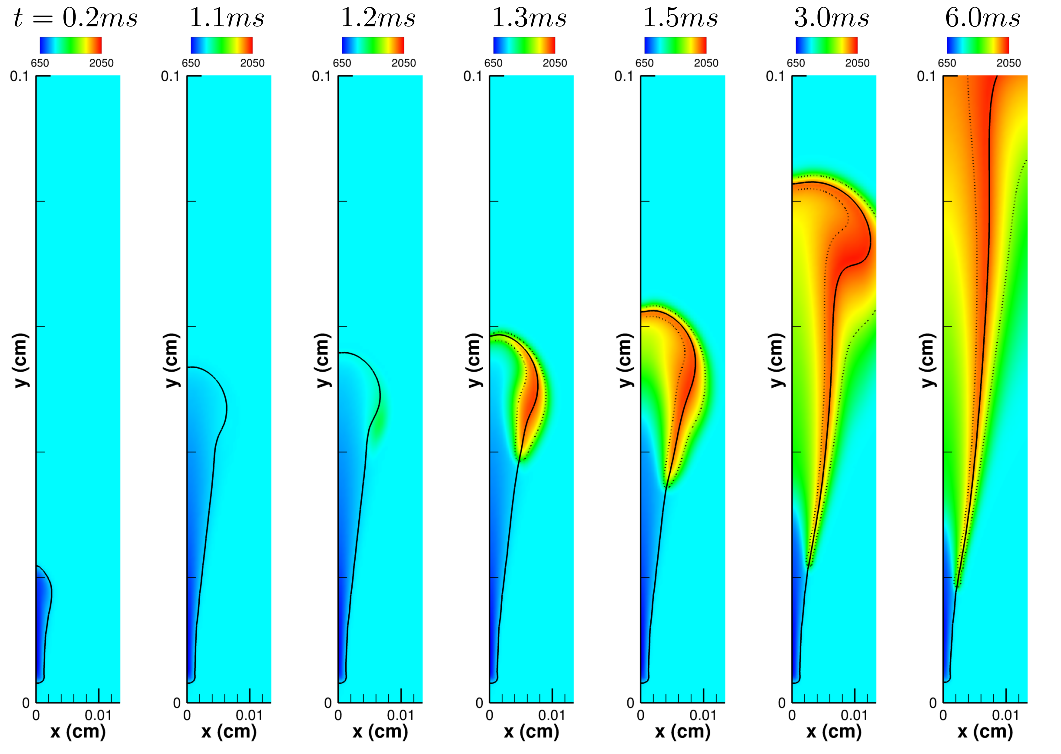

Figure 7.14: Overview of base case (X12) $\widetilde{T}$ (K) over time. Stoichiometric mixture fraction line (black) and $Y_{OH} = 0.0001$ contour (dotted).

Figure 7.15 shows contour plots for Favre mean reference variables, temperature, $\widetilde{Y}_{\mathrm{H_2O_2}}$ and the peak scalar dissipation rate A (modelled via Equation 6.1 assuming a beta distribution for mixture fraction) shortly after ignition. The value of A changes very little between just after ignition and the final steady state of the flow (Figure 7.16). The value is extremely high next to the spray region ($\approx 800/s$) due to the high mixture fraction gradient and turbulence generated by the spray. It rapidly decreases away from this location but remains slightly higher on the lean side of the stoichiometric mixture fraction line. Around the region where ignition occurs it has values of around $18/s$. Using a scalar dissipation rate this low in the laminar flamelet results in far too low ignition delay time and rapid propagation of the mean progress variable, and the flame becomes attached. When generating the flamelet table, it is important to restrict the choice of peak scalar dissipation rate to be high enough such that autoignition does not occur in the region where A is above the critical value for the fuel ($200/s$), which would be physically unrealistic.

Figure 7.16 shows the same fields at the steady state condition, at $t = 6ms$. Upstream mixture fraction and mixture fraction variance fields remain much the same, and progress variable variance has followed the progress variable contours upstream to the lift-off height. This is unfortunate as, despite the mixture fraction variance around the region of spray, there is no progress variable variance upstream of the stabilisation point, and therefore the Z-c covariance upstream of this location is expected to be zero, as indeed was observed. This makes this test case unsuitable for determining the effect of mixture fraction progress variable correlation on the evaporation rate using the stochastic evaporation model developed. This simulation was run for a variety of modelling parameters (listed in Table 7.2) including the gas phase copula model of Darbyshire *et al.* (Darbyshire and Swaminathan 2012) and the copula-based stochastic model developed in this thesis, but while the use of the copula to model the gas phase joint-pdf may present some improvement downstream, after ignition and away from the location of the spray, this is expected to have no effect on the lift-off height or ignition delay time. Similarly the copula based stochastic evaporation model is expected to have no effect on the evaporation rates for this configuration, because there is no direct interaction of the spray with the flame front.

Nevertheless, some results for lift-off length are presented in Table 7.2, which lists observed lift-off lengths and ignition delay times for each configuration run. Ignition delay time is defined as the time at which $\overline{C} \geq 0.05$ and lift-off length is given by $Y_{OH} \geq 0.0001$. The case with oxidiser $X_{O_2} = 0.12$ with a peak conditional scalar dissipation rate of $50/s$ is taken as a base case, in which the gas phase presumed pdf is modelled with a copula and no stochastic evaporation model is employed for the dispersed phase. From this base case, variants are run with one of the following changes: peak conditional scalar dissipation rate $A = 150/s$; independent presumed pdf for the gas phase; stochastic evaporation model; and ambient oxygen concentration $X_{O_2} = 0.21$.

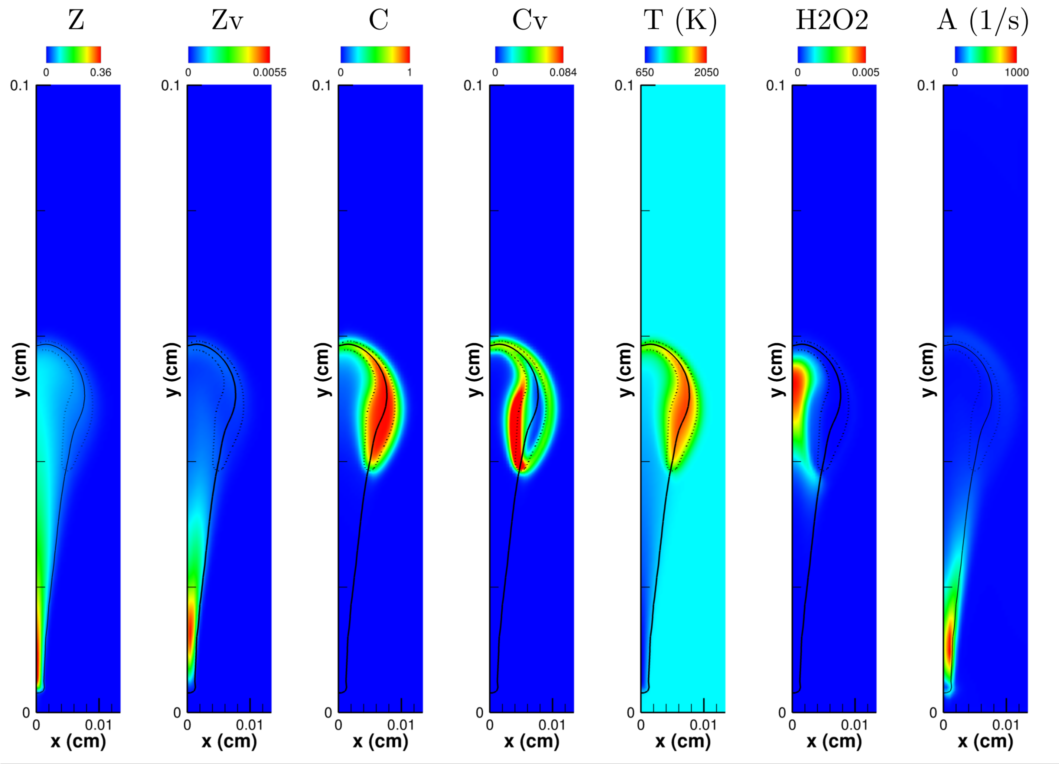

Figure 7.15: Selected Favre averaged quantities just after ($t = 1.3ms$) ignition time for base case (X12). Stoichiometric mixture fraction line (black) and $Y_{OH} = 0.0001$ contour (dotted). Zv and Cv denote mixture fraction and progress variable variance, respectively. H2O2 is the Favre averaged mass fraction $\widetilde{Y}_{\mathrm{H_2O_2}}$.

X_{O_2}	Peak SDR	Copula?	Stoch.?	Experiment		Simulation	
				LOL	IDT	LOL	IDT
0.12	50	Yes	No	29.2	0.947	18.9	0.94
	150	Yes	No			19.1	1.36
	50	No	No			18.7	0.7
	50	Yes	Yes			18.6	0.94
0.21	50	Yes	No	17.0	0.53	8.4	0.15

Table 7.2: Spray lift-off lengths (mm) and ignition delay times (ms) predicted for various modelling options. Peak scalar dissipation rate (SDR) has units of s^{-1}.

The base case ($X_{O_2} = 0.12$, $A = 50/s$) matches the ignition delay time to within 1%. Increasing the peak scalar dissipation rate to $150/s$ results in a greatly increased ignition delay time but very minor difference in the lift-off length; this is because the lift-off length is determined by the balance between reaction and advection, and the reaction rates in the higher SDR laminar flamelet are not significantly lower once autoignition has occurred, whereas the ignition delay time is longer. Using the independent presumed joint-pdf for the gas phase results in a 25% shorter ignition delay time, emphasising the importance influence of the mixture fraction-progress variable dependence on the reaction rate statistics in this flow.

Using a stochastic evaporation model results in no difference in the ignition delay time, and a very slight change in lift-off length. This indicates that stochastic fluctuations have a small effect in this flame, but since the progress variable variance is near-zero in the region of the spray the same result is found by assuming independent fluctuations, or by not considering progress variable fluctuations at all. Effectively, the stochastic process is modelling the fluctuations in seen temperature and fuel mass fraction, where such inhomogeneities are caused solely evaporation, including locally-rich mixtures and heat loss to the evaporating fluid. Finally, the case with ambient oxygen concentration $X_{O_2} = 0.21$ results in a significant under-predictions in both lift-off length and ignition delay time. Again, this can be attributed to the omission of spatial variations in scalar dissipation rate in the present tests, combined with the increased reactivity of the mixture due to the presence of extra oxygen.

7.3 Summary and Discussion

The effect of seen quantity correlations on the mean evaporation rate of a boiling spray in partially-premixed combustion are studied by means of two statistically-homogeneous spray simulations using an idealised combustion model. It is shown that mixture fraction-velocity correlations have no significant effect on the mean evaporation rate due to the negligible effect of velocity fluctuations on the mean evaporation rate. Mixture fraction-progress variable dependence was found to significantly enhance or inhibit mean evaporation rate, depending on the value of mean mixture fraction. The mechanism for this phenomenon is explained through the resulting joint distribution of temperature and fuel mass fraction.

Finally, simulations of an auto-igniting spray bomb (M. Pickett 2016) spray were performed giving poor agreement with experimental results, attributed to the lack of scalar dissipation rate variation in the combustion model. This emphasises the fact that the scalar dissipation rate is a key reference variable for autoigniting flow. Extension of the current modelling to also include mean scalar dissipation rate as a control parameter is possible and should be expected to greatly improve quantitative predictions. However the simulations presented serve as an adequate basis for examining the sensitivity to the other presumed-pdf modelling aspects.

The stochastic joint-distribution model based on a Plackett copula was tested and found to have no significant effect on the flame structure, due to the region in which the majority of evaporation occurs being away from the flame, resulting in low progress variable variance in the region of evaporation. High oxidizer temperatures also result in rapid evaporation and render the effects of mixture fraction fluctuations on the droplet negligible.

The absence of spray-combustion-turbulence interactions in the n-heptane spray case is itself an important observation. This demonstrates that the mixture fraction fluctuations in the non-reacted region in which the spray evaporates do not have a substantial influence: the dependence of evaporation rate on temperature and the dependence of temperature on mixture fraction upstream of the stabilisation point are both approximately linear, so that fluctuations of mixture fraction do not have a net effect on the mean reaction rate.

Heye et al. (2015) also show very limited effects of spray-combustion-turbulence interactions in transported-pdf modelling of an auto-igniting methanol spray (Sydney series), including a coupling method which pairs representative fluid particles with gas phase Lagrangian pdf particles to provide a model for the seen quantities. Where as Jones et al. (2011), employing a stochastic coupling similar to Heye et al. (2015) but in the context of stochastic fields implementation of the transported pdf, and De, Lakshmisha, et al. (2011) in the context of cold spray jets do observe a significant contribution from spray-combustion-turbulence interactions. A pre-requisite for the occurrence of spray-combustion-turbulence interactions is for there to be some overlap between the spray and the flame. In general, this is more likely to occur when droplet (or solid fuel particle) life times are relatively large compared to their convection times, and this is likely the case under colder conditions, with larger droplets or with solid fuel particles.

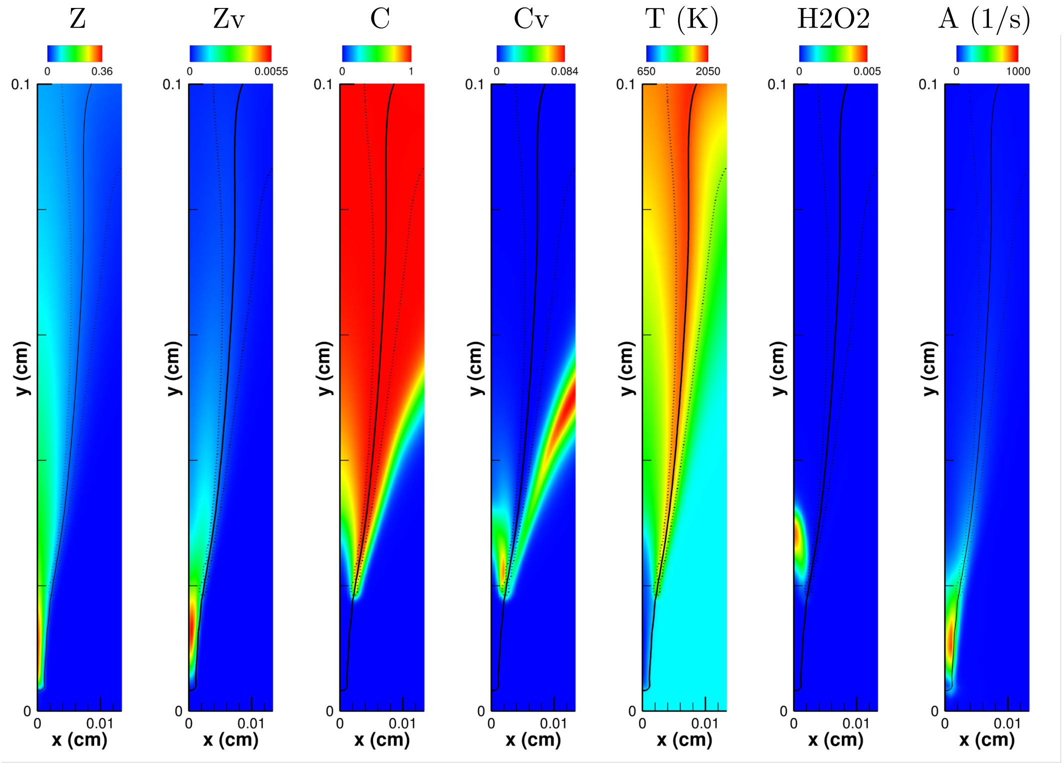

Figure 7.16: Selected Favre averaged quantities at steady state ($t = 6ms$) for base case (X12). Stoichiometric mixture fraction line (black) and $Y_{OH} = 0.0001$ contour (dotted). Zv and Cv denote mixture fraction and progress variable variance, respectively. H2O2 is the Favre averaged mass fraction $\widetilde{Y}_{\mathrm{H_2O_2}}$.

Chapter 8

Conclusions

The aims of this thesis are to investigate and model the statistical dependence between mixture fraction and progress variable in partially-premixed combustion, and to develop a presumed-pdf computer code that can model gas and spray-fuelled combustion. This requires some care in the numerical implementation, and an appropriate numerical formulation is developed through Chapters 2-4. The nature of the mixture fraction-progress variable dependence is investigated in a range of archetypal partially-premixed combustion configurations in Chapter 5, showing that the effect of their dependence has a significant impact on mean reaction rate predictions in the stabilisation region of lifted jet flames. In Chapter 6, the sensitivities of the presumed-pdf modelling are investigated with reference to direct numerical simulation (DNS) data for a gas-fuelled lifted autoigniting jet flame. Last, in Chapter 7, stochastic modelling for evaporation processes based on the presumed joint-pdf of mixture fraction and progress variable is developed and analysed. The joint-pdf modelling in the present work provides a numerical and theoretical basis which can be applied in RANS and LES of a wide range of gas, liquid and potentially also solid-fuelled combustion systems.

8.1 Presumed-pdf formulation and numerical implementation

In Chapter 2, two new reference variables, denoted a and b, were introduced based on a non-linear residence time and in combination with a mass fraction-based progress variable, respectively. The instantaneous and mean transport equations for these new quantities are presented in Chapter 2. These were then applied to an autoigniting homogeneous reactor in order to characterise the numerical sensitivity of autoignition delay time using each reference variable (Section 4.6). The parameters a and b were found to offer an improvement over the progress variable c in terms of numerical accuracy of the prediction of autoignition delay time. It is suggested that a progress variable based on major species mass fractions is unsuitable for accurately resolving pre-ignition chemistry in autoigniting flames, due to the initial period of slow production of major species mass fractions, and hence predictions of autoignition time are highly sensitive to small fluctuations caused by numerical errors, such as integration error, in the progress variable. The use of a as a reference variable resolves this problem by introducing a source term which is linear for small values of a. However a is unsuitable for modelling flame propagation since the source term of a has no dependence on the extent of reaction. The hybrid variable $b = \frac{1}{2}(a + c)$ is therefore recommended for systems in which autoignition and flame propagation are both influential.

In Chapter 4, a general method for the integration of joint-distributions with a scalar in the context of turbulent combustion is developed, making use of the known joint-distribution function (cdf), which can be applied to both empirical joint-distributions and the functional forms of presumed joint-distributions containing singularities. The application of this method is presented for one- and two-dimensional distribution functions, and the extension to higher dimensions is simple. It is demonstrated in Section 4.3 that the upper and lower bounds of the covariance of a joint-distribution are determined by the marginal pdfs, and that the bounds $\{-1, 1\}$ of the Pearson correlation coefficient are rarely attainable in practice. This result is already known in statistical literature, but has been previously neglected in the context of turbulent combustion modelling. Knowledge of these upper and lower bounds is important for tabulation of chemistry with a joint-moment as a parameter. A robust method for numerically evaluating these bounds is presented, making use of the integration method developed in this thesis. A numerical method for linking copula parameters to known joint-moments from CFD (covariance) is developed and applied to the Plackett copula parameter θ. An alternative method for finding θ based on Spearman's ρ is suggested which avoids the use of sampling or lookup tables to obtain the odds parameter, thereby improving the computational efficiency of the method to enable its application to the stochastic modelling of seen quantities in Lagrangian sprays. A generic method for sampling from a joint distribution is presented, which is optimized for generation of small numbers of samples for application to the short-lived seen quantity joint-distributions to stochastic modelling of sprays.

An alternative approach to the presumed copula method is suggested, based on mixture fraction-residence time information from a laminar flamelet or other canonical combustion experiment. This approach (referred to here as the Flamelet Generated Copula approach) constructs a copula from the joint-distribution of reference variables in the laminar flamelet, which has the potential to characterise reference variable dependence without the use of a transport equation for joint-moments.

8.2 *a priori* analysis of statistical dependence between reference variables

In Chapter 5, a priori analysis of one-point joint Z-c distributions is applied to a range of test cases including: partially premixed stratified DNS case of (Richardson and Chen 2016), the Sandia series of piloted methane jet flames with local extinction (Barlow and Frank 1998), and the lifted autoigniting ethylene jet DNS of (Yoo, Richardson, et al. 2011). A methodology is developed for the analysis of the underling copula from an empirical joint-pdf obtained from the DNS or experiment. The methodology involved the removal of the influence of the marginal joint-distributions in order to isolate the underlying empirical copula of the two reference variables. A general dependence of the copula on the mean values of the reference variables was observed in all cases where it had a significant effect.

The validity of the Plackett and independent copulas as models for the statistical dependence between Z and c was also examined based on the empirically-observed pdfs. Using the empirical marginals, the two presumed copulas (Plackett and independent) were used to construct joint-distributions and then compared with the empirical joint distribution. It was found that the Placket copula offers a general improvement in the representation of the empirical joint distribution in most cases. This was determined though comparison of the L_2 norm between the empirical joint pdf and the reconstructed joint pdf with modelled copula. However, it was seen that the same joint-distributions when used to calculate mean scalar quantities gave no significant difference in the case of the Sandia flame series, but significant differences in mean reaction rate for the lifted ethylene DNS.

8.3 *a posteriori* analysis of presumed-pdf modelling

In Chapter 6, RANS simulations of the ethylene slot jet were performed. Several modelling options were tested, including: choice of marginal presumed pdf; formulation of the presumed joint-distribution; value of the peak scalar dissipation rate; and choice of control variable. Scalar dissipation rate was confirmed to be an important parameter in autoigniting flames which should be accounted for in a turbulent combustion model. The prediction of Favre averaged quantities was found to be insensitive to the choice of marginal distributions tested (top-hat and beta) however the top-hat pdf (Floyd et al. 2009) provided a substantial decrease in computation time needed to generate the lookup table. The use of a residence-time based reference variable a was found to offer improved predictive capability in some situations and the reference variable b was found to exhibit behaviour between that shown by the use of a and c as a reference variable.

Variance of progress variable was considerable, the inclusion of the Plackett copula over the assumption of independence was found to offer moderate improvements in prediction of mean profiles. The mechanism by which the dependence in the presumed joint-distribution affects the mean reaction rates is explained by evaluating the mean reaction rates and temperatures from the joint-distribution and conditional quantities of the DNS data, reconfirming that correlation has little direct effect on temperature but a significant effect on reaction rates. It is concluded that the temperature profiles in the RANS differ due to modified progress variable mean and variance fields produced by the different mean reaction rate and variance source terms. Hence it is shown that the use of the Plackett copula to model the joint distribution in a lifted autoigniting flame is a significant modelling improvement.

8.4 presumed-pdf modelling for gas-phase properties *seen* by droplets

In Chapter 7, the effect of seen quantity correlations on the mean evaporation rate of a boiling spray in partially-premixed combustion was studied by means of two statistically-homogeneous spray simulations using an idealised combustion model. It is shown that mixture fraction-velocity correlations have no significant effect on the mean evaporation rate due to the negligible effect of velocity fluctuations on the mean evaporation rate. Mixture fraction-progress variable dependence was found to significantly enhance or inhibit mean evaporation rate, depending on the value of mean mixture fraction. The mechanism for this phenomenon is explained through the resulting joint distribution of temperature and fuel mass fraction.

Finally, in Chapter 7, *a priori* evaluation of droplet evaporation times demonstrated that the correlation in mixture fraction – progress variable fluctuations has a significant effect on seen quantity distributions resulting in a significant effect on mean steady-state evaporation rate. In Section 7.2, simulations of an auto-igniting spray bomb (M. Pickett 2016) were performed giving poor agreement with experimental results, attributed to the lack of scalar dissipation rate modelling in the combustion model. The stochastic joint-distribution model based on a Plackett copula was tested and found to have no significant effect on the flame structure, due to the region in which the majority of evaporation occurs being away from the flame, resulting in low progress variable variance in the region of evaporation. High oxidizer temperatures also result in rapid evaporation and render the effects of mixture fraction fluctuations on the droplet negligible.

8.5 Summary and future work

The main contributions of this thesis may be summarised as follows:

- The systematic *a priori* analysis of mixture fraction – progress variable dependence across multiple high quality empirical datasets.
- A novel technique for analysing dependence between reference variables, by removing the influence of marginal distributions to studying the underlying copula in isolation.
- Improved numerical methods for the integration of and sampling from presumed pdfs.
- The application of presumed pdfs with non-zero correlation to existing stochastic evaporation models for seen quantities, and demonstration of the effect on evaporation rate.
- The introduction of two new reference variables based on non-linear residence time, which are appropriate for tabulated chemistry approaches and avoid the demonstrated issue of numerical sensitivity exhibited by the use of a mass fraction-based progress variable.
- The flamelet generated copula method, allowing the generation of copulas from laminar flamelet solutions and hence the ability to capture dependence between reference variables without the need to transport joint moments.

The flamelet generated copula approach, while promising the inclusion of real combustion physics into the model for the joint-distribution, should be extended in a manner that can account for $\tilde{c}$ and $\widetilde{Z}$, in order to account for the variation of the copula throughout the flow field observed in Chapter 5. It remains to be seen whether this approach is capable of capturing the majority of dependence between Z and c without the use of joint moments. Preliminary application of the resultant copula (with no dependence on mean reference variables) shows promising qualitative ability to give the general trend of covariance observed in the ethylene jet DNS, but the dependence produced is not strong enough to manifest in the mean quantity predictions.

The stochastic evaporation model developed should be applied to a more appropriate laboratory scale spray flame in which the droplets interact with the flame directly, in order to confirm the results of Section 7.1.

Appendix A

Derivation of upper and lower bounds for specific distributions

A.1 Known bounds for covariance and variance

The variance of a function is given by

$$\sigma^2(x) = \int (x-\mu)^2 f(x)dx$$

where

$$\mu = \int x f(x)dx$$

is the mean.

$$\begin{aligned}\sigma^2(x) &= \int \left(x^2 - 2\mu x + \mu^2\right) f(x)dx \\ &= \int x^2 f(x)dx - 2\mu \int x f(x)dx + \mu^2 \int f(x)dx\end{aligned}$$

Since f is a pdf we have the identity $\int f(x)dx = 1$:

$$\begin{aligned}\sigma^2 &= \int x^2 f(x)dx - 2\mu^2 + \mu^2 \\ &= \int x^2 f(x)dx - \mu^2\end{aligned}$$

For a given μ, the maximum value of σ^2 is obtained when $\int x^2 f(x)dx$ is maximised. For $x \in [0,1]$ and the requirement that $f(x) \geq 0$, we have

$$\int x^2 f(x)dx \leq \int x f(x)dx = \mu$$

$$\therefore \sigma^2 \leq \mu - \mu^2$$

This gives the upper bound for the variance. This upper bound is achieved when

$$\int x^2 f(x)dx = \int xf(x)dx$$
$$\int \left(x^2 - x\right) f(x)dx = 0$$

What does this tell us about the function $f(x)$? The expression $x^2 - x$ is negative everywhere in $(0, 1)$ and is zero at $x = 0, 1$. Therefore $(x^2 - x)f(x)$ is zero at $x = 0, 1$ so does not contribute to the integral. The contribution from $(x^2 - x)f(x)$ on $x \in (0, 1)$ must also be zero. Since $f(x) \geq 0$ and $(x^2 - x) < 0$ on this interval, we have that $f(x) = 0$ in $x \in (0, 1)$. Therefore

$$f(x) = c_0\delta(x) + c_1\delta(x - 1)$$

where $\delta(x)$ is a Dirac delta. The coefficients are found by

$$\begin{aligned}
\mu &= \int xf(x)dx \\
&= \int x \left(c_0\delta(x) + c_1\delta(x - 1)\right) dx \\
&= c_0 \int x\delta(x)dx + c_1 \int x\delta(x - 1)dx \\
&= c_1 \\
1 &= \int f(x)dx \\
&= c_0 \int \delta(x)dx + c_1 \int \delta(x - 1)dx \\
&= c_0 + c_1 \\
c_0 &= 1 - \mu
\end{aligned}$$

So the distribution function $f(x)$ which maximises the variance and has mean μ is

$$f(x) = (1 - \mu)\delta(x) + \mu\delta(x - 1)$$

■.

The covariance of two random variables X and Y with joint probability distribution $f(X,Y)$ is defined as

$$\begin{aligned}
\overline{X'Y'} &= \int\int \left(x-\overline{X}\right)\left(y-\overline{Y}\right) f(x,y)dxdy \\
&= \int\int \left(xy-\overline{X}y+x\overline{Y}-\overline{XY}\right) f(x,y)dxdy \\
&= \int\int xyf(x,y)dxdy - \int\int \overline{X}yf(x,y)dxdy + \int\int x\overline{Y}f(x,y)dxdy - \int\int \overline{XY}f(x,y)dxdy \\
&= \int\int xyf(x,y)dxdy - \overline{X}\int\int yf(x,y)dxdy + \overline{Y}\int\int xf(x,y)dxdy - \overline{XY}\int\int f(x,y)dxdy \\
&= \int\int xyf(x,y)dxdy - \overline{X}\,\overline{Y} + \overline{Y}\,\overline{X} - \overline{X}\,\overline{Y} \\
&= \int\int xyf(x,y)dxdy - \overline{X}\,\overline{Y} \\
&= \overline{XY} - \overline{X}\,\overline{Y}
\end{aligned}$$

Again, the maximum value of the covariance (for random variables with means that are known) is determined by the maximum value of the integral $\int\int xyf(x,y)dxdy$. Since $x,y \in [0,1]$ we have

$$\begin{aligned}
&\int\int xyf(x,y)dxdy \le \int\int xf(x,y)dxdy = \int \overline{X}dy = \overline{X} \\
\text{and } &\int\int xyf(x,y)dxdy \le \int\int yf(x,y)dxdy = \int yf_y(y)dy = \overline{Y} \\
\therefore &\int\int xyf(x,y)dxdy \le \min\left(\overline{X},\overline{Y}\right)
\end{aligned}$$

where $f_Y(y)$ is the marginal distribution of f. Hence the covariance has an upper bound given by

$$\begin{aligned}
\overline{X'Y'} &\le \min\left(\overline{X},\overline{Y}\right) - \overline{X}\,\overline{Y} \\
&= \min\left(\overline{X}\left(1-\overline{Y}\right),\overline{Y}\left(1-\overline{X}\right)\right)
\end{aligned}$$

(As a sanity check, consider $\overline{X'X'} = \sigma_X^2$

$$\begin{aligned}
\overline{X'X'} &\le \min(\overline{X},\overline{X}) - \overline{X}\,\overline{X} \\
&= \overline{X} - \overline{X}\,\overline{X} \\
&= \overline{X}\left(1-\overline{X}\right)
\end{aligned}$$

which is what we expect.)

$$\min\left(\overline{X},\overline{Y}\right)-\overline{X}\,\overline{Y}=\begin{cases}\overline{X} & \overline{X}\leq\overline{Y}\\ \overline{Y} & \overline{X}>\overline{Y}\end{cases}-\overline{X}\,\overline{Y}$$

$$=\begin{cases}\overline{X}\left(1-\overline{Y}\right) & \overline{X}\leq\overline{Y}\\ \overline{Y}\left(1-\overline{X}\right) & \overline{X}>\overline{Y}\end{cases}$$

$$\frac{\partial}{\partial\overline{X}}\left(\cdots\right)=\begin{cases}\frac{\partial}{\partial\overline{X}}\overline{X}\left(1-\overline{Y}\right) & \overline{X}\leq\overline{Y}\\ \frac{\partial}{\partial\overline{X}}\overline{Y}\left(1-\overline{X}\right) & \overline{X}>\overline{Y}\end{cases}$$

$$=\begin{cases}1-\overline{Y} & \overline{X}\leq\overline{Y}\\ \overline{Y} & \overline{X}>\overline{Y}\end{cases}$$

If $x<y$ then there is a stationary point at $\overline{Y}=1$, and if $x>y$ there is a stationary point at $\overline{Y}=0$. However, because the function min is not defined on the line $\overline{X}=\overline{Y}$, we have not searched this line for the maximum. Setting $\overline{X}=\overline{Y}$ gives

$$f(x,y)=\overline{X}-\overline{X}^2$$

which has a stationary point at $\overline{X}=0.5$. The second derivative $\partial^2 f/\partial x^2=-2$ indicates that the function is convex on the domain and therefore $(\overline{X},\overline{Y})=(0.5,0.5)$ is indeed a maximum. Hence, the maximum covariance occurs when $\overline{X}=\overline{Y}=0.5$ and therefore $\overline{X'Y'}=0.5-0.5^2=0.25$. Note that the maximum covariance does not depend directly on the variances of X and Y, only on their mean values.

Similarly, the minimum value of the covariance is determined by the minimum value of the integral, which is zero:

$$\int\int xyf(x,y)dxdy\geq 0$$

$$\therefore\overline{X'Y'}\geq-\overline{X}\,\overline{Y}$$

A.2 Upper bound on correlation from quadruple-delta distribution

The covariance of two distributions is limited by the upper bound found in the denominator of the definition of the Pearson correlation coefficient:

$$\text{Correlation}=\frac{\sigma_{xy}}{\sqrt{\sigma_x^2}\sqrt{\sigma_y^2}}\tag{A.1}$$

Figure A.1: a) Numerically calculated minimum and maximum covariance for all distributions in the

The covariance can never be greater than $\sqrt{\sigma_x^2}\sqrt{\sigma_y^2}$. However, for some given marginal distributions this upper limit can not be achieved.

This is demonstrated in Figure A.1 using the joint-pdfs from the gas phase table. For each joint-pdf specified by a particular set of control parameters

To illustrate, consider the case where both marginal distributions have segregation 1 (two double delta distributions). Specifically, look at

$$\begin{aligned}\mu_x &= 0.25\\ \mu_y &= 0.75\\ s_x = s_y &= 1\end{aligned}$$

Where s is a segregation and the distributions have domain $[0,1]$ unless stated otherwise. They have the corresponding pdfs:

$$\begin{aligned}f_x(\eta) &= (1-\mu_x)\,\delta(\eta-0)+\mu_x\delta(\eta-1)\\ &= 0.75\delta(\eta-0)+0.25\delta(\eta-1)\\ f_y(\psi) &= \left(1-\mu_y\right)\delta(\psi-0)+\mu_y\delta(\psi-1)\\ &= 0.25\delta(\psi-0)+0.75\delta(\psi-1)\end{aligned}$$

The x distribution has a mean closer to $x=0$ and therefore the delta distribution at $\delta(x-0)$ is weighted more heavily, etc. The joint distribution with these two marginals will be a quadruple delta distribution, with one Dirac delta at each of the corners of the domain $[0,1]^2$. The weighting of each of these four deltas is unknown and depends on both the weightings of the deltas in the marginals and the copula of the joint-pdf, i.e. on the covariance.

$$\begin{aligned}\mathrm{jpdf}(\eta,\psi) &= \frac{\partial^2 C}{\partial x\partial y}\left[f_x(\eta),f_y(\psi)\right]\\ &= w_{00}\delta(\eta-0,\psi-0)+w_{01}\delta(\eta-0,\psi-1)+w_{10}\delta(\eta-1,\psi-0)+w_{11}\delta(\eta-1,\psi-1)\end{aligned}$$

where $\delta(a,b)=\delta(a)\,\delta(b)$. This is a pdf:

$$\begin{aligned}\int w\delta(\eta,\psi)\,d\eta d\psi &= w\\ \int \mathrm{jpdf}(\eta,\psi)\,d\eta d\psi &= w_{00}+w_{01}+w_{10}+w_{11}=1\end{aligned}$$

The conditions that the weights sum to 1 has not been proven but is a requirement of jpdf being a pdf. For independent marginals, the joint distribution is simply the product of the two marginals:

$$\begin{aligned}
\operatorname{jpdf}(\eta,\psi) &= f_x(\eta)\, f_y(\psi) \\
&= \left[(1-\mu_x)\,\delta(\eta-0)+\mu_x\delta(\eta-1)\right]\times\left[\left(1-\mu_y\right)\delta(\psi-0)+\mu_y\delta(\psi-1)\right] \\
&= (1-\mu_x)\left(1-\mu_y\right)\delta(\eta-0,\psi-0) \\
&+ (1-\mu_x)\,\mu_y\delta(\eta-0,\psi-1) \\
&+ \mu_x\left(1-\mu_y\right)\delta(\eta-1,\psi-0) \\
&+ \mu_x\mu_y\delta(\eta-1,\psi-1)
\end{aligned}$$

Proof that this is a joint-pdf:

$$\begin{aligned}
\int \operatorname{jpdf}(\eta,\psi)\,d\eta d\psi &= (1-\mu_x)\left(1-\mu_y\right)+(1-\mu_x)\,\mu_y+\mu_x\left(1-\mu_y\right)+\mu_x\mu_y \\
&= 1-\mu_x-\mu_y+\mu_x\mu_y+\mu_y-\mu_x\mu_y+\mu_x-\mu_x\mu_y+\mu_x\mu_y \\
&= 1
\end{aligned}$$

In the case of perfect positive correlation ($C[u,v]=\max(u+v-1,0)$), we have $w_2 = w_3 = 0$ and therefore $w_1 + w_4 = 1$ and w_1 and w_4 are determined by the marginal distributions

$$\begin{aligned}
f_x(0) &= (1-\mu_x)\,\delta(0) = w_{00}\delta(0) \\
f_x(1) &= \mu_x\delta(0) = w_{11}\delta(0) \\
f_y(0) &= \left(1-\mu_y\right)\delta(0) = w_{00} \\
f_y(1) &= \mu_y\delta(0) = w_{11}
\end{aligned}$$

The marginal distributions can be expressed in terms of the joint distribution

$$\begin{aligned}
f_x(\eta) &= \int \operatorname{jpdf}(\eta,\psi)\, d\psi \\
&= \int w_{00}\delta(\eta-0,\psi-0)\, d\psi \\
&+ \int w_{01}\delta(\eta-0,\psi-1)\, d\psi \\
&+ \int w_{10}\delta(\eta-1,\psi-0)\, d\psi \\
&+ \int w_{11}\delta(\eta-1,\psi-1)\, d\psi \\
&= (w_{00}+w_{01})\,\delta(\eta-0) + (w_{10}+w_{11})\,\delta(\eta-1) \\
f_y(\psi) &= \int \operatorname{jpdf}(\eta,\psi)\, d\eta \\
&= \int w_{00}\delta(\eta-0,\psi-0)\, d\eta \\
&+ \int w_{01}\delta(\eta-0,\psi-1)\, d\eta \\
&+ \int w_{10}\delta(\eta-1,\psi-0)\, d\eta \\
&+ \int w_{11}\delta(\eta-1,\psi-1)\, d\eta \\
&= (w_{00}+w_{10})\,\delta(\psi-0) + (w_{01}+w_{11})\,\delta(\psi-1)
\end{aligned}$$

Therefore we have these equations to solve

$$\begin{aligned}
w_{00}+w_{01}+w_{10}+w_{11} &= 1 \\
w_{00}+w_{01} &= (1-\mu_x) \\
w_{10}+w_{11} &= \mu_x \\
w_{00}+w_{10} &= \left(1-\mu_y\right) \\
w_{01}+w_{11} &= \mu_y
\end{aligned}$$

In matrix form,

$$\begin{pmatrix} 1 & 1 & 0 & 0 \\ 0 & 0 & 1 & 1 \\ 1 & 0 & 1 & 0 \\ 0 & 1 & 0 & 1 \end{pmatrix} \begin{pmatrix} w_{00} \\ w_{01} \\ w_{10} \\ w_{11} \end{pmatrix} = \begin{pmatrix} 1-\mu_x \\ \mu_x \\ 1-\mu_y \\ \mu_y \end{pmatrix}$$

Which has determinant 0 so the system cannot be solved.

The covariance is given by

$$
\begin{aligned}
\sigma_{xy} &= \int \eta\psi \mathrm{jpdf}\left(\eta,\psi\right) d\eta d\psi - \mu_x\mu_y \\
&= \int \eta\psi \left[w_{00}\delta\left(\eta-0,\psi-0\right) + w_{01}\delta\left(\eta-0,\psi-1\right) + w_{10}\delta\left(\eta-1,\psi-0\right) + w_{11}\delta\left(\eta-1,\psi-1\right)\right] d\eta d\psi - \mu_x\mu \\
&= \int \eta\psi w_{00}\delta\left(\eta-0,\psi-0\right) d\eta d\psi \\
&+ \int \eta\psi w_{01}\delta\left(\eta-0,\psi-1\right) d\eta d\psi \\
&+ \int \eta\psi w_{10}\delta\left(\eta-1,\psi-0\right) d\eta d\psi \\
&+ \int \eta\psi w_{11}\delta\left(\eta-1,\psi-1\right) d\eta d\psi - \mu_x\mu_y \\
&= w_{11} - \mu_x\mu_y
\end{aligned}
$$

Which gives us $w_{11} = \sigma_{xy} + \mu_x\mu_y$. For known $\mu_x\mu_y$, the covariance depends only on w_{11}. This relation can be used to make the linear system invertible:

$$
\begin{pmatrix} 1 & 1 & 0 & 0 \\ 0 & 0 & 1 & 1 \\ 1 & 0 & 1 & 0 \\ 0 & 0 & 0 & 1 \end{pmatrix}
\begin{pmatrix} w_{00} \\ w_{01} \\ w_{10} \\ w_{11} \end{pmatrix}
=
\begin{pmatrix} 1-\mu_x \\ \mu_x \\ 1-\mu_y \\ \sigma_{xy}+\mu_x\mu_y \end{pmatrix}
$$

with solution

$$
\begin{aligned}
w_{00} &= 1-\mu_x-\mu_y+\mu_x\mu_y+\sigma_{xy} \\
w_{01} &= \mu_y-\mu_x\mu_y-\sigma_{xy} \\
w_{10} &= \mu_x-\mu_x\mu_y-\sigma_{xy} \\
w_{11} &= \mu_x\mu_y+\sigma_{xy}
\end{aligned}
$$

It is easily seen that the additional constraint $w_{00}+w_{01}+w_{10}+w_{11}=1$ is satisfied. However, the above result does not help us find the maximum because covariance now we have a circular expression involving σ_{xy}.

The variances for the marginal distributions are given by

$$
\begin{aligned}
\sigma_x^2 &= \int \left(\eta-\mu_x\right)^2 f_x\left(\eta\right) d\eta \\
&= \int \left[\left(\eta-\mu_x\right)^2 \left\{\left(1-\mu_x\right)\delta\left(\eta-0\right)+\mu_x\delta\left(\eta-1\right)\right\}\right] d\eta \\
&= \int \left[\left(\eta^2-2\eta\mu_x+\mu_x^2-\eta^2\mu_x+2\eta\mu_x^2-\mu_x^3\right)\delta\left(\eta-0\right)+\left(\eta^2\mu_x-2\eta\mu_x^2+\mu_x^3\right)\delta\left(\eta-1\right)\right] d\eta \\
&= \left(\mu_x^2-\mu_x^3\right)+\left(\mu_x-2\mu_x^2+\mu_x^3\right) \\
&= \mu_x-\mu_x^2
\end{aligned}
$$

and similarly $\sigma_y^2 = \mu_y - \mu_y^2$. Hence, for the univariate distribution the known upper limit of the variance is realisable, using a double delta distribution. Is the known upper limit for the covariance also realisable for all potential marginal distributions? Assume that the covariance is equal to the upper bound stated above, and consider the quadruple-delta distribution again:

$$\begin{aligned}
\sigma_{xy}^2 &= \sigma_x^2 \sigma_y^2 \\
\left(w_{11} - \mu_x \mu_y\right)^2 &= \left(\mu_x - \mu_x^2\right)\left(\mu_y - \mu_y^2\right) \\
w_{11}^2 - 2\mu_x\mu_y w_{11} + \mu_x^2\mu_y^2 &= \mu_x\mu_y - \mu_x\mu_y^2 - \mu_x^2\mu_y + \mu_x^2\mu_y^2 \\
w_{11}^2 - 2\mu_x\mu_y w_{11} + \left(-\mu_x\mu_y + \mu_x\mu_y^2 + \mu_x^2\mu_y\right) &= 0
\end{aligned}$$

This is a quadratic in w_{11} and hence

$$w_{11} = \mu_x\mu_y + \sqrt{\left(1-\mu_x\right)\mu_x\left(1-\mu_y\right)\mu_y}$$

substituting back into the covariance equation confirms that

$$\sigma_{xy} = \sqrt{\left(1-\mu_x\right)\mu_x\left(1-\mu_y\right)\mu_y} = \sqrt{\sigma_x^2}\sqrt{\sigma_y^2}$$

Further, since σ_{xy} is known, then so are all the weights $w_{..}$:

$$\begin{aligned}
w_{00} &= 1 - \mu_x - \mu_y + \mu_x\mu_y + \sqrt{\sigma_x^2}\sqrt{\sigma_y^2} \\
w_{01} &= \mu_y - \mu_x\mu_y - \sqrt{\sigma_x^2}\sqrt{\sigma_y^2} \\
w_{10} &= \mu_x - \mu_x\mu_y - \sqrt{\sigma_x^2}\sqrt{\sigma_y^2} \\
w_{11} &= \mu_x\mu_y + \sqrt{\sigma_x^2}\sqrt{\sigma_y^2}
\end{aligned}$$

A specific example reveals a problem: choose $\mu_x = 0.25$, $\mu_y = 0.75$, $\sigma_x^2 = \sigma_y^2 = .1875$, and hence $\sigma_{xy} = .1875$:

$$\begin{aligned}
w_{00} &= 1 - 0.25 - 0.75 + 0.25 \cdot 0.75 + 0.1875 = 0.375 \\
w_{01} &= 0.75 - 0.25 \cdot 0.75 - 0.1875 = 0.375 \\
w_{10} &= 0.25 - 0.25 \cdot 0.75 - 0.1875 = -0.125 \\
w_{11} &= 0.25 \cdot 0.75 + 0.1875 = 0.375
\end{aligned}$$

While these values do fit the "sum to 1" criteria, they are not suitable because w_{10} is negative which would make the pdf negative at the point $(x, y) = (1, 0)$. (To see that this problem is caused by the covariance imposed on the distribution, note that the values found in the independent case are all positive: $w_{00} = 0.1875$, $w_{01} = 0.5625$, $w_{10} = 0.0625$ and $w_{11} = 0.1875$.)

Hence the covariance $\sigma_{xy} = \sigma_x \sigma_y$ cannot be achieved with these marginal distributions and there must be a smaller upper limit on the value of the covariance than the one we are currently applying. The restriction that each $w_{..} \geq 0$ can be used to find restrictions on both the upper (positive) and lower (negative) bounds of covariance:

$$\begin{aligned}
w_{01} :& \sigma_{xy} \leq \mu_y - \mu_x \mu_y \\
w_{10} :& \sigma_{xy} \leq \mu_x - \mu_x \mu_y \\
\therefore & \sigma_{xy} \leq \min \left[\mu_y \left(1 - \mu_x\right),\ \mu_x \left(1 - \mu_y\right) \right]
\end{aligned}$$

$$\begin{aligned}
w_{00} :& \ \sigma_{xy} \geq \mu_x + \mu_y - \mu_x \mu_y - 1 \\
w_{11} :& \ \sigma_{xy} \geq -\mu_x \mu_y \\
\therefore & \sigma_{xy} \geq \max \left[\mu_x + \mu_y - \mu_x \mu_y - 1,\ -\mu_x \mu_y \right]
\end{aligned}$$

Note: the lower limits $\sigma_{xy} \geq \max \left(\mu_x + \mu_y - \mu_x \mu_y - 1,\ -\mu_x \mu_y \right)$ seem intricately related to the existing limit:

$$\begin{aligned}
\sigma_{xy} &\geq -\sigma_x \sigma_y \\
&\geq -\sqrt{\mu_x \left(1 - \mu_x\right) \mu_y \left(1 - \mu_y\right)} \\
&= -\sqrt{\mu_x \mu_y \left(1 - \mu_x\right) \left(1 - \mu_y\right)} \\
&= -\sqrt{\left(\mu_x \mu_y - \mu_x^2 \mu_y\right) \left(1 - \mu_y\right)} \\
&= -\sqrt{\left(\mu_x \mu_y - \mu_x^2 \mu_y - \mu_x \mu_y^2 + \mu_x^2 \mu_y^2\right)} \\
&= -\sqrt{\left(-\mu_x \mu_y\right) \left(\mu_x + \mu_y - \mu_x \mu_y - 1\right)}
\end{aligned}$$

The complete set of restrictions is then

$$\begin{aligned}
\sigma_{xy} &\leq \min \left[\mu_y \left(1 - \mu_x\right),\ \mu_x \left(1 - \mu_y\right),\ \sigma_x \sigma_y \right] \\
\sigma_{xy} &\geq \max \left[\mu_x + \mu_y - \mu_x \mu_y - 1,\ -\mu_x \mu_y,\ \sigma_x \sigma_y \right]
\end{aligned} \tag{A.2}$$

Presumably, this upper limit (for the case of positive covariance) is found when the quadruple delta joint-pdf is actually a double-delta pdf, with weights only at $(0, 0)$ and $(1, 1)$. Similarly, for the maximum negative covariance we would expect the joint-pdf to be nonzero at $(1, 0)$ and $(0, 1)$. Consider the positive covariance case:

$$\begin{aligned}
w_{00} &= 0 \\
w_{01} &= \mu_y - \mu_x\mu_y - \sigma_{xy} \\
w_{10} &= 0 \\
w_{11} &= \mu_x\mu_y + \sigma_{xy} \\
&= \mu_y - w_{01}
\end{aligned}$$

and also

$$\begin{aligned}
w_{01} + w_{11} &= 1 \\
\Rightarrow \mu_y &= 1 \\
\Rightarrow w_{01} &= 1 - \mu_x - \sigma_{xy} \\
\Rightarrow w_{11} &= 1 - w_{01}
\end{aligned}$$

the maximum σ_{xy} will occur when $w_{01} = 0$ and therefore $w_{11} = 1$, $\sigma_{xy} = \mu_x - 1$. Similarly, in the case of greatest negative covariance:

$$\begin{aligned}
w_{00} &= 1 - \mu_x - \mu_y + \mu_x\mu_y + \sigma_{xy} \\
w_{01} &= 0 \\
w_{10} &= \mu_x - \mu_x\mu_y - \sigma_{xy} \\
w_{11} &= 0
\end{aligned}$$

and also

$$\begin{aligned}
w_{00} + w_{11} &= 1 \\
\Rightarrow \mu_y &= 0 \\
\Rightarrow w_{00} &= 1 - \mu_x + \sigma_{xy} \\
\Rightarrow w_{10} &= 1 - w_{00}
\end{aligned}$$

These are not satisfactory solutions because when $\mu_y = 0$ or 1 one of the distributions is a delta distribution and hence its variance is zero, and by the original upper bound the covariance is also zero. This is why these expressions for covariance only depend on the other marginal.

A.3 Distributions with one continuous marginal

Now consider the case where one of the marginal pdfs is not a double delta distribution, but is instead an arbitrary continuous distribution $f_x(\eta)$ and the other given by

$$f_y(\zeta) = \left(1-\mu_y\right)\delta(\zeta) + \mu_y\delta(1-\zeta)$$

The joint-pdf can now be written in the form

$$\mathrm{jpdf}(\eta,\zeta) = \left(1-\mu_y\right)\delta(\zeta)\, f_{x0}(\eta) + \mu_y\delta(1-\zeta)\, f_{x1}(\eta)$$

where $f_{x0}(\eta)$ and $f_{x1}(\eta)$ are the distributions of $f_x(\eta)$ conditioned on $y = 0, 1$ respectively (in the case of independence, f_{x0} is a scalar multiplication of f_{x1}). The marginal distribution of x must still be $f_x(\eta)$, hence

$$\begin{aligned}
f_x(\eta) &= \int \mathrm{jpdf}(\eta,\zeta)\, d\zeta \\
&= \left(1-\mu_y\right) f_{x0}(\eta) \int \delta(\zeta)\, d\zeta + \mu_y f_{x1}(\eta) \int \delta(1-\zeta)\, d\zeta \\
&= \left(1-\mu_y\right) f_{x0}(\eta) + \mu_y f_{x1}(\eta)
\end{aligned}$$

The covariance is given by

$$\begin{aligned}
\sigma_{xy} &= \int\int \eta\zeta\,\mathrm{jpdf}(\eta,\zeta)\, d\eta d\zeta - \mu_x\mu_y \\
\sigma_{xy} + \mu_x\mu_y &= \int\int \eta\zeta\left(1-\mu_y\right)\delta(\zeta)\, f_{x0}(\eta)\, d\eta d\zeta + \int\int \eta\zeta\mu_y\delta(1-\zeta)\, f_{x1}(\eta)\, d\eta d\zeta \\
&= \left(1-\mu_y\right)\int \zeta\delta(\zeta)\left\{\int \eta f_{x0}(\eta)\, d\eta\right\} d\zeta + \mu_y \int \zeta\delta(1-\zeta)\left\{\int \eta f_{x1}(\eta)\, d\eta\right\} d\zeta \\
&= \left(1-\mu_y\right)\int \zeta\delta(\zeta)\,\mu_{x0} d\zeta + \mu_y \int \zeta\delta(1-\zeta)\,\mu_{x1} d\zeta
\end{aligned}$$

where μ_{x0} and μ_{x1} are the expected values of the conditional distributions f_{x0} and f_{x1}.

$$\begin{aligned}
\sigma_{xy} + \mu_x\mu_y &= \left(1-\mu_y\right)\mu_{x0}\int \zeta\delta(\zeta)\, d\zeta + \mu_y\mu_{x1}\int \zeta\delta(1-\zeta)\, d\zeta \\
&= \mu_y\mu_{x1} \\
\sigma_{xy} &= \mu_y\left(\mu_{x1} - \mu_x\right)
\end{aligned}$$

How are μ_x and μ_{x1} related? We can look at the expected value of the marginal distribution f_x:

$$\begin{aligned}
\mu_x &= \int \eta f_x(\eta)\, d\eta \\
&= \int \eta \left[\left(1-\mu_y\right) f_{x0}(\eta) + \mu_y f_{x1}(\eta)\right] d\eta \\
&= \left(1-\mu_y\right) \int \eta f_{x0}(\eta)\, d\eta + \mu_y \int \eta f_{x1}(\eta)\, d\eta \\
&= \left(1-\mu_y\right) \mu_{x0} + \mu_y \mu_{x1}
\end{aligned}$$

As an interesting aside, a similarly structured expression is obtained from the variance of the continuous marginal:

$$\begin{aligned}
\sigma_x^2 &= \int \eta^2 f_x(\eta)\, d\eta - \mu_x^2 \\
&= \int \eta^2 \left[\left(1-\mu_y\right) f_{x0}(\eta) + \mu_y f_{x1}(\eta)\right] d\eta - \mu_x^2 \\
&= \left(1-\mu_y\right) \int \eta^2 f_{x0}(\eta)\, d\eta + \mu_y \int \eta^2 f_{x1}(\eta)\, d\eta - \mu_x^2 \\
\sigma_x^2 + \mu_x^2 &= \left(1-\mu_y\right)\left(\sigma_{x0}^2 + \mu_{x0}^2\right) + \mu_y\left(\sigma_{x1}^2 + \mu_{x1}^2\right)
\end{aligned}$$

Substituting the value of μ_x into σ_{xy}:

$$\begin{aligned}
\sigma_{xy} &= \mu_y\left(\mu_{x1} - \left(1-\mu_y\right)\mu_{x0} - \mu_y\mu_{x1}\right) \\
&= \mu_y\left(\mu_{x1} - \mu_{x0} + \mu_y\mu_{x0} - \mu_y\mu_{x1}\right) \\
&= \mu_y\left(1-\mu_y\right)\left(\mu_{x1} - \mu_{x0}\right) \\
&= \sigma_y^2\left(\mu_{x1} - \mu_{x0}\right)
\end{aligned}$$

Here we have made use of the fact that f_y is a double delta distribution and therefore $\sigma_y^2 = \mu_y\left(1-\mu_y\right)$.

Since the parameters μ_{x0} and μ_{x1} are not known, we would like to express this in terms of the means and variances of the marginals instead. The maximum positive covariance possible for this type of distribution will occur when as much of the probability mass of f_{x1} lies as close as possible to the point $(\eta, \zeta) = (1, 1)$ and as much as possible of the probability mass of f_{x0} lies as close as possible to $(0, 0)$. Since both are (not strictly) positive, this corresponds to the piecewise functions

$$f_{x0}\left(\eta\right) = \begin{cases} f_x\left(\eta\right) & \eta < \eta_d \\ 0 & \eta > \eta_d \end{cases}$$

$$f_{x1}\left(\eta\right) = \begin{cases} 0 & \eta < \eta_d \\ f_x\left(\eta\right) & \eta > \eta_d \end{cases}$$

i.e. the marginal is simply cut at the point $\eta = \eta_d$ and part given to each partial marginal. Hence the relation with the f_x is preserved by

$$\begin{aligned} f_x &= \left(1-\mu_y\right) f_{x0}\left(\eta\right) + \mu_y f_{x1}\left(\eta\right) \\ &= \left(1-\mu_y\right) \begin{cases} f_x\left(\eta\right) & \eta < \eta_d \\ 0 & \eta > \eta_d \end{cases} + \mu_y \begin{cases} 0 & \eta < \eta_d \\ f_x\left(\eta\right) & \eta > \eta_d \end{cases} \\ &= \begin{cases} \left(1-\mu_y\right) f_x\left(\eta\right) & \eta < \eta_d \\ \mu_y f_x\left(\eta\right) & \eta > \eta_d \end{cases} \end{aligned}$$

Aside: the variance of f_x can be written

$$\begin{aligned} \sigma_x^2 &= \int \left(\eta-\mu_x\right)^2 f_x\left(\eta\right) d\eta \\ &= \int \left(\eta-\mu_x\right)^2 \begin{cases} \left(1-\mu_y\right) f_x\left(\eta\right) & \eta < \eta_d \\ \mu_y f_x\left(\eta\right) & \eta > \eta_d \end{cases} d\eta \\ &= \int_0^{\eta_d} \left(\eta-\mu_x\right)^2 \left(1-\mu_y\right) f_x\left(\eta\right) d\eta + \int_{\eta_d}^1 \left(\eta-\mu_x\right)^2 \mu_y f_x\left(\eta\right) d\eta \\ &= \left(1-\mu_y\right) \int_0^{\eta_d} \left(\eta-\mu_x\right)^2 f_x\left(\eta\right) d\eta + \mu_y \int_{\eta_d}^1 \left(\eta-\mu_x\right)^2 f_x\left(\eta\right) d\eta \\ &= \left(1-\mu_y\right) \left|\sigma_x^2\right|_{\eta_d} + \mu_y \left(\sigma_x^2 - \left|\sigma_x^2\right|_{\eta_d}\right) \\ &= \left|\sigma_x^2\right|_{\eta_d} - 2\mu_y \left|\sigma_x^2\right|_{\eta_d} + \mu_y \sigma_x^2 \\ &= \left(1-2\mu_y\right) \left|\sigma_x^2\right|_{\eta_d} + \mu_y \sigma_x^2 \\ &= \frac{1-2\mu_y}{1-\mu_y} \left|\sigma_x^2\right|_{\eta_d} \end{aligned}$$

or

$$\begin{aligned}
\sigma_x^2 + \mu_x^2 &= \int \eta^2 f_x(\eta)\, d\eta \\
&= \int \eta^2 \begin{cases} (1-\mu_y) f_x(\eta) & \eta < \eta_d \\ \mu_y f_x(\eta) & \eta > \eta_d \end{cases} d\eta \\
&= \int_0^{\eta_d} \eta^2 (1-\mu_y) f_x(\eta)\, d\eta + \int_{\eta_d}^1 \eta^2 \mu_y f_x(\eta)\, d\eta \\
&= (1-\mu_y) \int_0^{\eta_d} \eta^2 f_x(\eta)\, d\eta + \mu_y \int_{\eta_d}^1 \eta^2 f_x(\eta)\, d\eta \\
&= \int_0^{\eta_d} \eta^2 f_x(\eta)\, d\eta - \mu_y \int_0^{\eta_d} \eta^2 f_x(\eta)\, d\eta + \mu_y \int_{\eta_d}^1 \eta^2 f_x(\eta)\, d\eta
\end{aligned}$$

where

$$\left|\sigma_x^2\right|_{\eta_d} = \int_0^{\eta_d} (\eta - \mu_x)^2 f_x(\eta)\, d\eta$$

is the “partial variance of f_x.” Since the integrand here is positive or zero, this value is a monotonically increasing function of η_d which tends towards σ_x^2 as $\eta_d \to 1$. However, σ_x^2 should not depend on η_d which implies that η_d must depend on μ_y:

$$\left|\sigma_x^2\right|_{\eta_d} = \frac{1-\mu_y}{1-2\mu_y}\sigma_x^2$$

This is only positive for $\mu_y < 0.5$. This implies a contradiction.

The question now is what are the extreme values of the covariance permitted by this form.

We need to relate the values of μ_{x0} and μ_{x1} to known quantities, the means and variances of the marginal distributions. This will most likely be through the expression for covariance. Considering the definition of covariance, which involves an integral of the joint pdf (which in this case is only nonzero on $\zeta = 0$ or $\zeta = 1$) multiplied by $\eta\zeta$: on the $\zeta = 0$ axis there will be no contribution to the covariance from f_{x0}, but on the $\zeta = 1$ axis there will be a finite positive contribution from f_{x1}. Hence the covariance is maximised as $\eta_d \to 0$. But the mean μ_y places a restriction on the value of ξ_d:

$$\begin{aligned}
\int_{\xi_d}^1 f_x(\xi)\, d\xi &= \mu_y \\
\int_0^{\xi_d} f_x(\xi)\, d\xi &= 1 - \mu_y
\end{aligned}$$

Each of these leads to the same expression for ξ in terms of the cumulative density function F_x:

$$\begin{aligned} F_x\left(\xi_d\right) &= 1-\mu_y \\ \therefore \xi_d &= F_x^{-1}\left(1-\mu_y\right) \end{aligned}$$

Now we can see why the maximum covariance depends on the variance of X (a phenomenon which was observed numerically). As the mean μ_y approaches 1, ξ_d approaches zero, and the domain of f_{x1} increases towards the whole $[0,1]$ interval. A fixed μ_y (and μ_x) determines ξ_d, but the value of the integration from ξ_d to 1 depends on the marginal pdf f_x. Since we have

$$\begin{aligned} \sigma_{xy}+\mu_x\mu_y &= \int_0^1\int_0^1 \eta\zeta f\left(\eta,\zeta\right)d\eta d\zeta \\ &= \int_{\xi_d}^1 \eta f_x\left(\eta\right)d\eta \\ &= \int_{F_x^{-1}\left(1-\mu_y\right)}^1 \eta f_x\left(\eta\right)d\eta \end{aligned}$$

we are able to evaluate this once we know the marginal distributions. The integration can be done numerically. Often the marginal distribution f_x will have singularities at 0 and/or 1. We would like to avoid the numerical issues that this causes by transforming the above integral into a form where the integrand is always finite over the integration interval, i.e.:

$$\sigma_{xy}+\mu_x\mu_y = \mu_x - \int_0^{F_x^{-1}\left(1-\mu_y\right)} \eta f_x\left(\eta\right)d\eta$$

For the minimum covariance, let

$$\begin{aligned} f_{x0}\left(\eta\right) &= \begin{cases} 0 & \eta<\eta_d \\ f_x\left(\eta\right) & \eta>\eta_d \end{cases} \\ f_{x1}\left(\eta\right) &= \begin{cases} f_x\left(\eta\right) & \eta<\eta_d \\ 0 & \eta>\eta_d \end{cases} \end{aligned}$$

The restrictions placed on ξ_d by the mean μ_y are now

$$\begin{aligned} \int_{\xi_d}^1 f_x\left(\xi\right)d\xi &= 1-\mu_y \\ \int_0^{\xi_d} f_x\left(\xi\right)d\xi &= \mu_y \end{aligned}$$

which, in terms of the CDF, are

$$\begin{aligned} F_x\left(\xi_d\right) &= \mu_y \\ \therefore \xi_d &= F_x^{-1}\left(\mu_y\right) \end{aligned}$$

and finally

$$\begin{aligned} \sigma_{xy} + \mu_x \mu_y &= \int_0^1 \int_0^1 \eta \zeta f\left(\eta, \zeta\right) d\eta d\zeta \\ &= \int_0^{\xi_d} \eta f_x\left(\eta\right) d\eta \\ &= \int_0^{F_x^{-1}\left(\mu_y\right)} \eta f_x\left(\eta\right) d\eta \end{aligned}$$

If needed, these upper and lower limits are may be computed numerically.

Appendix B

Additional statistics for lifted ethylene DNS case

#	$\overline{Z}$	$\bar{c}$	$\overline{Z''c''}$	r_{Zc}	ρ_{Zc}	θ_{Zc}	L_2	*Empirical*	*Plackett*
C3	0.629	0.014	-0.002	-0.720	-0.809	0.063	0.669	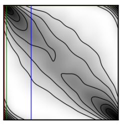	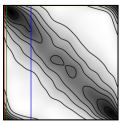
D3	0.431	0.036	-0.004	-0.690	-0.830	0.046	0.395	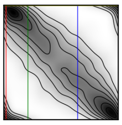	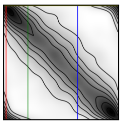
E3	0.212	0.067	-0.004	-0.399	-0.427	0.224	1.94	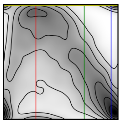	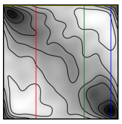

Table B.1: DNS Row 3: Statistical properties of lifted flame sample locations, including the mean mixture fraction, mean progress variable, covariance, Pearson correlation, Spearman's ρ_{Zc}, odds parameter, and calculated L_2 norm of error.

#	$\overline{Z}$	$\overline{c}$	$\overline{Z''c''}$	r_{Zc}	ρ_{Zc}	θ_{Zc}	L_2	*Empirical*	*Plackett*
C4	0.668	0.083	-0.012	-0.597	-0.822	0.050	0.568	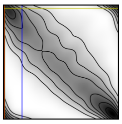	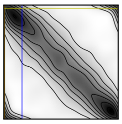
D4	0.544	0.193	-0.021	-0.637	-0.799	0.057	0.768	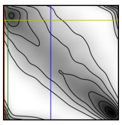	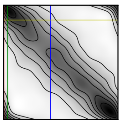
E4	0.407	0.335	-0.023	-0.617	-0.683	0.090	1.46	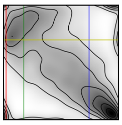	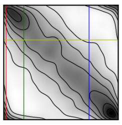
F4	0.137	0.485	0.003	0.134	0.341	3.459	2.07	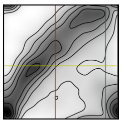	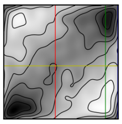
G4	0.025	0.083	0.003	0.728	-0.130	0.331	4.02	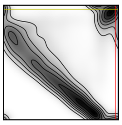	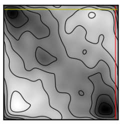

Table B.2: DNS Row 4: Statistical properties of lifted flame sample locations, including the mean mixture fraction, mean progress variable, covariance, Pearson correlation, Spearman's ρ_{Zc}, odds parameter, and calculated L_2 norm of error.

#	$\overline{Z}$	$\overline{c}$	$\overline{Z''c''}$	r_{Zc}	ρ_{Zc}	θ_{Zc}	L_2	*Empirical*	*Plackett*
A5	0.914	0.040	-0.006	-0.612	-0.869	0.020	0.644	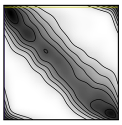	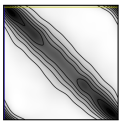
B5	0.879	0.062	-0.009	-0.590	-0.855	0.035	0.546	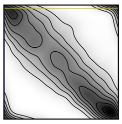	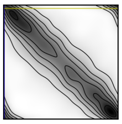
C5	0.711	0.245	-0.026	-0.698	-0.791	0.066	0.625	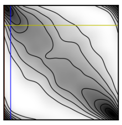	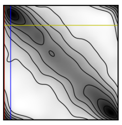
D5	0.625	0.416	-0.033	-0.754	-0.792	0.056	0.586	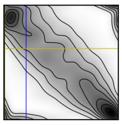	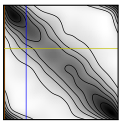
E5	0.522	0.580	-0.032	-0.733	-0.728	0.053	1.92	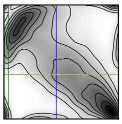	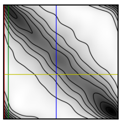
F5	0.289	0.756	-0.004	-0.171	0.147	2.692	1.90	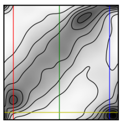	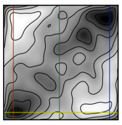
G5	0.110	0.611	0.013	0.614	0.758	18.696	0.723	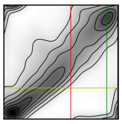	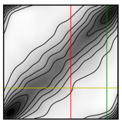

Table B.3: DNS Row 5: Statistical properties of lifted flame sample locations, including the mean mixture fraction, mean progress variable, covariance, Pearson correlation, Spearman's ρ_{Zc}, odds parameter, and calculated L_2 norm of error.

#	$\overline{Z}$	$\overline{c}$	$\overline{Z''c''}$	r_{Zc}	ρ_{Zc}	θ_{Zc}	L_2	*Empirical*	*Plackett*
A6	0.866	0.141	-0.013	-0.634	-0.790	0.059	0.756	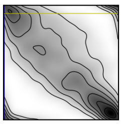	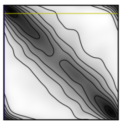
B6	0.846	0.162	-0.016	-0.683	-0.792	0.072	0.878	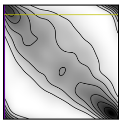	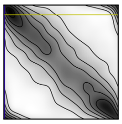
C6	0.734	0.346	-0.031	-0.770	-0.799	0.061	0.541	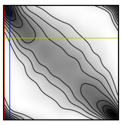	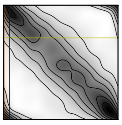
D6	0.661	0.478	-0.036	-0.785	-0.815	0.042	0.494	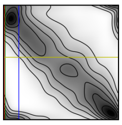	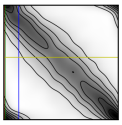
E6	0.581	0.614	-0.036	-0.770	-0.783	0.034	1.62	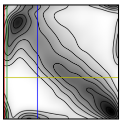	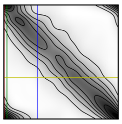
F6	0.384	0.781	-0.012	-0.400	-0.142	0.899	3.08	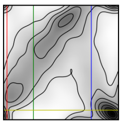	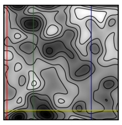
G6	0.188	0.763	0.009	0.434	0.527	6.451	1.09	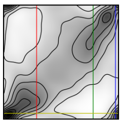	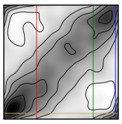

Table B.4: DNS Row 6: Statistical properties of lifted flame sample locations, including the mean mixture fraction, mean progress variable, covariance, Pearson correlation, Spearman's ρ_{Zc}, odds parameter, and calculated L_2 norm of error.

#	$\overline{Z}$	$\overline{c}$	$\overline{Z''c''}$	r_{Zc}	ρ_{Zc}	θ_{Zc}	L_2	*Empirical*	*Plackett*
A7	0.833	0.259	-0.020	-0.731	-0.746	0.090	0.746	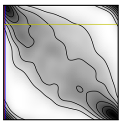	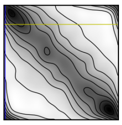
B7	0.821	0.284	-0.022	-0.754	-0.767	0.090	0.874	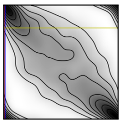	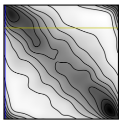
C7	0.737	0.416	-0.033	-0.809	-0.818	0.049	0.544	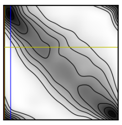	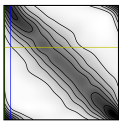
D7	0.677	0.512	-0.036	-0.801	-0.834	0.036	0.517	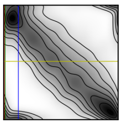	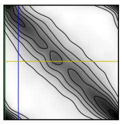
E7	0.608	0.611	-0.037	-0.757	-0.796	0.032	1.63	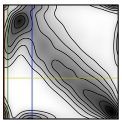	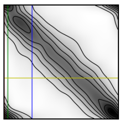
F7	0.458	0.741	-0.022	-0.514	-0.427	0.234	3.62	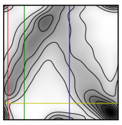	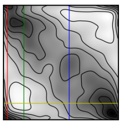
G7	0.287	0.747	0.004	0.105	0.260	3.905	2.15	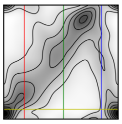	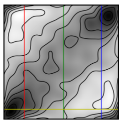

Table B.5: DNS Row 7: Statistical properties of lifted flame sample locations, including the mean mixture fraction, mean progress variable, covariance, Pearson correlation, Spearman's ρ_{Zc}, odds parameter, and calculated L_2 norm of error.

Bibliography

CD-adapco (2016). *Star-CD website.* URL: `http://www.cd-adapco.com/products/star-cd` (visited on 03/01/2016).

Arghode, V.K. and A.K. Gupta (2010). “Effect of flow field for colorless distributed combustion (CDC) for gas turbine combustion”. In: *Applied Energy* 87.5, pp. 1631–1640. ISSN: 0306-2619. DOI: `http://dx.doi.org/10.1016/j.apenergy.2009.09.032`. URL: `http://www.sciencedirect.com/science/article/pii/S0306261909004243`.

Avellana, Carlos María Cuadras (2006). “The importance of being the upper bound in the bivariate family”. In: *SORT: statistics and operations research transactions* 30.1, pp. 55–84.

Barlow, R.S. and J.H. Frank (1998). “Effects of turbulence on species mass fractions in methane/air jet flames”. In: *Symposium (International) on Combustion* 27.1. Twenty-Seventh Sysposium (International) on Combustion Volume One, pp. 1087–1095. ISSN: 0082-0784.

Bekdemir, C., E. Rijk, B. Somers, P. de Goey, and B. Albrecht (2010). *On the application of the Flamelet Generated Manifold (FGM) approach to the simulation of an igniting diesel spray.* Tech. rep. SAE Technical Paper.

Bekdemir, C., T. Somers, and L.P.H. de Goey (2009). “First application of the flamelet generated manifold (fgm) approach to the simulation of an igniting diesel spray”. In: *19th International Multidimensional Engine Modeling User’s Group Meeting at the SAE Congress, Detroit, Michigan.*

Bentley, J.L. and J.B. Saxe (1980). “Generating sorted lists of random numbers”. In: *ACM Transactions on Mathematical Software (TOMS)* 6.3, pp. 359–364.

Berntsen, J., T.O. Espelid, and A. Genz (1991). “An adaptive algorithm for the approximate calculation of multiple integrals”. In: *ACM Transactions on Mathematical Software (TOMS)* 17.4, pp. 437–451.

Bilger, R.W. (1975). “A Note on Favre Averaging in Variable Density Flows”. In: *Combustion Science and Technology* 11.5-6, pp. 215–217.

– (1977). “Reaction rates in diffusion flames”. In: *Combustion and Flame* 30, pp. 277–284. ISSN: 0010-2180. DOI: `http://dx.doi.org/10.1016/0010-2180(77)90076-1`. URL: `http://www.sciencedirect.com/science/article/pii/0010218077900761`.

– (1989a). “The structure of turbulent nonpremixed flames”. In: *Symposium (International) on Combustion.* Vol. 22. 1. Elsevier, pp. 475–488.

Bilger, R.W. (1989b). “The structure of turbulent nonpremixed flames”. In: *Symposium (International) on Combustion* 22.1, pp. 475–488. ISSN: 0082-0784.

– (2011). “A mixture fraction framework for the theory and modeling of droplets and sprays”. In: *Combustion and Flame* 158.2, pp. 191–202.

Bilger, R.W., S.B. Pope, K.N.C. Bray, and J.F. Driscoll (2005). “Paradigms in turbulent combustion research”. In: *Proceedings of the Combustion Institute* 30.1, pp. 21–42. ISSN: 1540-7489.

Bolla, M. (2013). “Modeling Soot Formation in Diesel Engines Using Conditional Moment Closure”. PhD thesis. ETH Zurich.

Borghi, R. and P. Moreau (1977). “Turbulent combustion in a premixed flow”. In: *Acta Astronautica* 4.3–4, pp. 321–341. ISSN: 0094-5765.

BP Statistical Review of World Energy June 2015 (2015).

Bray, K.N.C., M. Champion, P.A. Libby, and N. Swaminathan (2006). “Finite rate chemistry and presumed PDF models for premixed turbulent combustion”. In: *Combustion and Flame* 146.4, pp. 665–673. ISSN: 0010-2180.

Bray, K.N.C., P. Domingo, and L. Vervisch (2005). “Role of the progress variable in models for partially premixed turbulent combustion”. In: *Combustion and flame* 141.4, pp. 431–437.

Brown, B.W., J. Lovato, and K. Russell (2002). *CDFLIB90 Fortran 95 routines for cumulative distribution functions, their inverses and more.* Tech. rep. Technical Report, Department of Biomathematics, The University of Texas MD Anderson Cancer Center, Houston.

Buckmaster, J. (1996). “Edge-Flames and Their Stability”. In: *Combustion Science and Technology* 115.1-3, pp. 41–68.

Burke, S.P. and T.E.W. Schumann (1948). “Diffusion flames”. In: *Proceedings of the Symposium on Combustion.* Vol. 1. Elsevier, pp. 2–11.

Bushe, W.K. (1996). “Conditional Moment Closure Methods for Autoignition Problems”. PhD thesis. University of Cambridge.

Cabra, R., J.-Y. Chen, R.W. Dibble, A.N. Karpetis, and R.S. Barlow (2005). “Lifted methane–air jet flames in a vitiated coflow”. In: *Combustion and Flame* 143.4. Special Issue to Honor Professor Robert W. Bilger on the Occasion of His Seventieth Birthday, pp. 491–506. ISSN: 0010-2180.

Carslaw, D.C. et al. (2011). *Trends in NOx and NO2 emissions and ambient measurements in the UK.* URL: `http://uk-air.defra.gov.uk/assets/documents/reports/cat05/1108251149_110718_AQ0724_Final_report.pdf` (visited on 03/01/2016).

Cavaliere, A. and M. Joannon (2004). “Mild Combustion”. In: *Progress in Energy and Combustion Science* 30.4, pp. 329–366. ISSN: 0360-1285.

Cha, C.M. and H. Pitsch (2002). “Higher-order conditional moment closure modelling of local extinction and reignition in turbulent combustion”. In: *Combustion Theory and Modelling* 6.3, pp. 425–437.

Chang, C-H., Y-K. Tung, and J-C. Yang (1994). “Monte Carlo simulation for correlated variables with marginal distributions”. In: *Journal of Hydraulic Engineering* 120.3, pp. 313–331.

Chen, C.S., K-C. Chang, and J-Y. Chen (1994). “Application of a robust β-pdf treatment to analysis of thermal NO formation in nonpremixed hydrogen-air flame”. In: *Combustion and Flame* 98.4, pp. 375–390.

Chin, S. and H. Lefebvre (1983). “Steady-state evaporation characteristics of hydrocarbon fuel drops”. In: *AIAA journal* 21.10, pp. 1437–1443.

Clayton, G. (1978). “A model for association in bivariate life tables and its application in epidemiological studies of familial tendency in chronic disease incidence”. In: *Biometrika* 65.1, pp. 141–151.

Climate Analysis Indicators Tool (2009). World Resources Institute. URL: `http://cait.wri.org` (visited on 03/01/2009).

Cran, W., J. Martin, and E. Thomas (1977). “Remark AS R19 and Algorithm AS 109: A Remark on Algorithms: AS 63: The Incomplete Beta Integral AS 64: Inverse of the Incomplete Beta Function Ratio”. In: *Journal of the Royal Statistical Society. Series C (Applied Statistics)* 26.1, pp. 111–114.

Darbyshire, O.R. and N. Swaminathan (2012). “A Presumed Joint pdf Model for Turbulent Combustion with Varying Equivalence Ratio”. In: *Combustion Science and Technology* 184.12, pp. 2036–2067.

De, S. and S. Kim H. (2013). “Large eddy simulation of dilute reacting sprays: Droplet evaporation and scalar mixing”. In: *Combustion and Flame* 160.10, pp. 2048–2066.

De, S. and S.H. Kim (2013). “Large eddy simulation of dilute reacting sprays: Droplet evaporation and scalar mixing”. In: *Combustion and Flame* 160.10, pp. 2048–2066. ISSN: 0010-2180.

De, S., K.N. Lakshmisha, and R.W. Bilger (2011). “Modeling of nonreacting and reacting turbulent spray jets using a fully stochastic separated flow approach”. In: *Combustion and Flame* 158.10, pp. 1992–2008.

Demirtas, H. and D. Hedeker (2011). “A practical way for computing approximate lower and upper correlation bounds”. In: *The American Statistician* 65.2, pp. 104–109.

Demoulin, F.X. and R. Borghi (2000). “Assumed PDF modeling of turbulent spray combustion”. In: *Combustion science and technology* 158.1, pp. 249–271.

Domingo, P. and L. Vervisch (1996). “Triple flames and partially premixed combustion in autoignition of non-premixed turbulent mixtures”. In: *Symposium (International) on Combustion* 26.1, pp. 233–240. ISSN: 0082-0784.

Dooren, P. Van and L. de Ridder (1976). “An adaptive algorithm for numerical integration over an N-dimensional cube”. In: *Journal of Computational and Applied Mathematics* 2.3, pp. 207–217.

Doran, E.M. (2012). “A multi-dimensional flamelet model for ignition in multi-feed combustion systems”.

Dukic, V.M. and N. Marić (2013). “Minimum correlation in construction of multivariate distributions”. In: *Physical Review E* 87.3, p. 032114.

Dukowicz, J.K. (1980). “A particle-fluid numerical model for liquid sprays”. In: *Journal of Computational Physics* 35.2, pp. 229–253.

Duret, B., G. Luret, J. Réveillon, T. Ménard, A. Berlemont, and F. Demoulin (2012). “DNS analysis of turbulent mixing in two-phase flows”. In: *International Journal of Multiphase Flow* 40, pp. 93–105.

Epstein, A.H. (2012). “Aircraft engines’ needs from combustion science and engineering”. In: *Combustion and Flame* 159.5, pp. 1791–1792.

Floyd, J., A.M. Kempf, A. Kronenburg, and R.H. Ram (2009). “A simple model for the filtered density function for passive scalar combustion LES”. In: *Combustion Theory and Modelling* 13.4, pp. 559–588.

Fox, R.O. (2003). *Computational Models for Turbulent Reacting Flows*. Cambridge Books Online. Cambridge University Press. ISBN: 9780511610103.

Fréchet, M. (1951). “Généralisations de la loi de probabilité de Laplace”. In: *Annales de l’institut Henri Poincaré*. Vol. 12. 1, pp. 1–29.

Fredricks, G.A. and R.B. Nelsen (2007). “On the relationship between Spearman’s rho and Kendall’s tau for pairs of continuous random variables”. In: *Journal of Statistical Planning and Inference* 137.7, pp. 2143–2150. ISSN: 0378-3758.

Gampert, M., K. Kleinheinz, N. Peters, and H. Pitsch (2013). “Experimental and Numerical Study of the Scalar Turbulent/Non-Turbulent Interface Layer in a Jet Flow”. In: *Flow, Turbulence and Combustion* 92.1, pp. 429–449. ISSN: 1573-1987.

Gao, Y., N. Chakraborty, and N. Swaminathan (2015). “Scalar Dissipation Rate Transport and Its Modeling for Large Eddy Simulations of Turbulent Premixed Combustion”. In: *Combustion Science and Technology* 187.3, pp. 362–383.

Ge, H-W. and E. Gutheil (2008). “Simulation of a turbulent spray flame using coupled PDF gas phase and spray flamelet modeling”. In: *Combustion and Flame* 153.1–2, pp. 173–185. ISSN: 0010-2180.

Gentle, J.E. (2003). *Random number generation and Monte Carlo methods*. Springer.

Ghirelli, F. and B. Leckner (2004). “Transport equation for the local residence time of a fluid”. In: *Chemical engineering science* 59.3, pp. 513–523.

Girimaji, S.S. (1991). “Assumed -pdf Model for Turbulent Mixing: Validation and Extension to Multiple Scalar Mixing”. In: *Combustion Science and Technology* 78.4-6, pp. 177–196.

Glassman, I., A. Yetter, and G. Glumac (2014). *Combustion*. Academic press.

Goldin, G.M. (1996). “PhD Thesis”. In:

Goldin, G.M. and S. Menon (1997). “A scalar pdf construction model for turbulent non-premixed combustion”. In: *Combustion science and technology* 125.1-6, pp. 47–72.

– (1998). “A comparison of scalar PDF turbulent combustion models”. In: *Combustion and flame* 113.3, pp. 442–453.

Gopalakrishnan, V. and J. Abraham (2004). “Effects of multicomponent diffusion on predicted ignition characteristics of an n-heptane diffusion flame”. In: *Combustion and Flame* 136.4, pp. 557–566.

Grout, R.W.S. (2009). “Combustion modeling with conditional source-term estimation and laminar flamelet decomposition”. PhD thesis.

Heye, C., V. Raman, and A.R. Masri (2015). “Influence of spray/combustion interactions on auto-ignition of methanol spray flames”. In: *Proceedings of the Combustion Institute* 35.2, pp. 1639–1648. ISSN: 1540-7489.

Hoeffding, W. (1940). *Massstabinvariante korrelationstheorie.* Teubner.

Hollmann, C. and E. Gutheil (1996). “Modeling of turbulent spray diffusion flames including detailed chemistry”. In: *Symposium (international) on combustion.* Vol. 26. 1. Elsevier, pp. 1731–1738.

Idicheria, A. and M. Pickett (2007a). “Effect of EGR on diesel premixed-burn equivalence ratio”. In: *Proceedings of the Combustion Institute* 31.2, pp. 2931–2938.

– (2007b). *Quantitative mixing measurements in a vaporizing diesel spray by Rayleigh imaging.* Tech. rep. SAE Technical Paper.

Ihme, M., C.M. Cha, and H. Pitsch (2005). “Prediction of local extinction and re-ignition effects in non-premixed turbulent combustion using a flamelet/progress variable approach”. In: *Proceedings of the Combustion Institute* 30.1, pp. 793–800. ISSN: 1540-7489.

Ihme, M. and H. Pitsch (2008a). “Prediction of extinction and reignition in nonpremixed turbulent flames using a flamelet/progress variable model: 1. A priori study and presumed {PDF} closure”. In: *Combustion and Flame* 155.1–2, pp. 70–89. ISSN: 0010-2180.

– (2008b). “Prediction of extinction and reignition in nonpremixed turbulent flames using a flamelet/progress variable model: 2. Application in {LES} of Sandia flames D and E”. In: *Combustion and Flame* 155.1–2, pp. 90–107. ISSN: 0010-2180.

Issa, I. (1986). “Solution of the implicitly discretised fluid flow equations by operator-splitting”. In: *Journal of computational physics* 62.1, pp. 40–65.

Johnson, E. (2013). *Multivariate statistical simulation: A guide to selecting and generating continuous multivariate distributions.* John Wiley & Sons.

Jones, W.P., S. Lyra, and S. Navarro-Martinez (2011). “Large Eddy Simulation of a swirl stabilized spray flame”. In: *Proceedings of the Combustion Institute* 33, pp. 2153–2160.

Kampen, N.G. Van (1992). *Stochastic processes in physics and chemistry.* Vol. 1. Access Online via Elsevier.

Kee, J., F. Grcar, D. Smooke, A. Miller, and E. Meeks (1985). *PREMIX: a Fortran program for modeling steady laminar one-dimensional premixed flames.*

Kerkemeier, S.G., E. Frouzakis, G. Tomboulides, E. Mastorakos, and K. Boulouchos (2009). “Autoignition of a diluted hydrogen jet in a heated 2-D turbulent air flow”. In: *Proceedings of the European Combustion Meeting, Vienna, Austria.* Citeseer.

Kerstein, A.R. (1988). “Fractal dimension of turbulent premixed flames”. In: *Combustion science and technology* 60.4-6, pp. 441–445.

Kerstein, A.R. (1991). “Linear-eddy modelling of turbulent transport. Part 6. Microstructure of diffusive scalar mixing fields”. In: *Journal of Fluid Mechanics* 231, pp. 361–394.

Klimenko, A.Y. and R.W. Bilger (1999). “Conditional moment closure for turbulent combustion”. In: *Progress in energy and combustion science* 25.6, pp. 595–687.

Knudsen, E., S.H. Kim, and H. Pitsch (2010). “An analysis of premixed flamelet models for large eddy simulation of turbulent combustion”. In: *Physics of Fluids (1994-present)* 22.11, p. 115109.

Knudsen, E., E.S. Richardson, J.H. Chen, and H. Pitsch (2011). “LES of an auto-igniting C2H4 flame DNS”. In: *Annual Research Briefs*.

Knudsen, E., E.S. Richardson, E.M. Doran, H. Pitsch, and J.H. Chen (2012). “Modeling scalar dissipation and scalar variance in large eddy simulation: Algebraic and transport equation closures”. In: *Physics of Fluids (1994-present)* 24.5, p. 055103.

Kolla, H., J.W. Rogerson, N. Chakraborty, and N. Swaminathan (2009). “Scalar Dissipation Rate Modeling and its Validation”. In: *Combustion Science and Technology* 181.3, pp. 518–535.

Kolmogorov, A.N. (1991). “The local structure of turbulence in incompressible viscous fluid for very large Reynolds numbers”. In: *Proceedings of the Royal Society of London Series A* 434, pp. 9–13.

Kostka, M., E. Knudsen, and H. Pitsch (2009). “Towards regime identification and appropriate chemistry tabulation for computation of autoigniting turbulent reacting flows”. In: *Center of Turbulence Research (CTR) Annual Research Briefs* 2009, pp. 199–207.

Laurie, D. (1997). “Calculation of Gauss-Kronrod quadrature rules”. In: *Mathematics of Computation of the American Mathematical Society* 66.219, pp. 1133–1145.

Lentini, D. (1994). “Assessment of The Stretched Laminar Flamelet Approach For Nonpremixed Turbulent Combustion”. In: *Combustion Science and Technology* 100.1-6, pp. 95–122.

Levenspiel, O. (1999). *Chemical Reaction Engineering*. New York, NY: Wiley.

Libby, P.A. and F.A. Williams (2000). “A presumed PDF analysis of partially premixed turbulent combustion”. In: *Combustion Science and technology* 161.1, pp. 351–390.

Liew, S.K., K.N.C. Bray, and J.B. Moss (1984). “A stretched laminar flamelet model of turbulent nonpremixed combustion”. In: *Combustion and Flame* 56.2, pp. 199–213. ISSN: 0010-2180.

Lin, G.D., X. Dou, S. Kuriki, and J. Huang (2014). “Recent developments on the construction of bivariate distributions with fixed marginals”. In: *Journal of Statistical Distributions and Applications* 1.1, p. 14.

Linan, A. (1974). “The asymptotic structure of counterflow diffusion flames for large activation energies”. In: *Acta Astronautica* 1.7, pp. 1007–1039.

Liu, F., H. Guo, G.J. Smallwood, ÖL Gülder, and M.D. Matovic (2002). “A robust and accurate algorithm of the β-pdf integration and its application to turbulent methane–air diffusion combustion in a gas turbine combustor simulator”. In: *International journal of thermal sciences* 41.8, pp. 763–772.

Liu, S., J.C. Hewson, J.H. Chen, and H. Pitsch (2004). “Effects of strain rate on high-pressure nonpremixed n-heptane autoignition in counterflow”. In: *Combustion and Flame* 137.3, pp. 320–339. ISSN: 0010-2180.

Liu, Z., C. Zheng, and L. Zhou (2002). “A joint PDF model for turbulent spray evaporation/combustion”. In: *Proceedings of the Combustion Institute* 29.1, pp. 561–568.

Lozier, D.W. and F.W.J. Olver (1994). “Numerical evaluation of special functions”. In: *AMS Proceedings of Symposia in Applied Mathematics*. Vol. 48, pp. 79–125.

Lucchini, T., G. D’Errico, D. Ettorre, and G. Ferrari (2009). “Numerical Investigation of Non-Reacting and Reacting Diesel Sprays in Constant-Volume Vessels”. In: *SAE International Journal of Engines* 1.2, pp. 966–975.

Luo, Z., C.S. Yoo, E.S. Richardson, J.H. Chen, C.K. Law, and T. Lu (2012). “Chemical explosive mode analysis for a turbulent lifted ethylene jet flame in highly-heated coflow”. In: *Combustion and Flame* 159.1, pp. 265–274. ISSN: 0010-2180.

Lurie, P.M. and M.S. Goldberg (1998). “An approximate method for sampling correlated random variables from partially-specified distributions”. In: *Management Science* 44.2, pp. 203–218.

Majumder, L. and P. Bhattacharjee (1973). “Algorithm AS 63: The incomplete beta integral”. In: *Journal of the Royal Statistical Society. Series C (Applied Statistics)* 22.3, pp. 409–411.

Marchisio, D.L., R.D. Vigil, and R.O. Fox (2003). “Quadrature method of moments for aggregation–breakage processes”. In: *Journal of Colloid and Interface Science* 258.2, pp. 322–334. ISSN: 0021-9797.

Mardia, V. (1970). “Families of Bivariate Distributions (Charles Griffin and Co., London)”. In:

Markides, C.N. and E. Mastorakos (2010). “Experimental Investigation of the Effects of Turbulence and Mixing on Autoignition Chemistry”. In: *Flow Turbulence and Combustion* 86, pp. 585–608.

Masri, A.R. (2015). “Partial premixing and stratification in turbulent flames”. In: *Proceedings of the Combustion Institute* 35.2, pp. 1115–1136. ISSN: 1540-7489.

Mastorakos, E. (2009). “Ignition of turbulent non-premixed flames”. In: *Progress in Energy and Combustion Science* 35.1, pp. 57–97.

Mastorakos, E., T.A. Baritaud, and T. Poinsot (1997). “Numerical simulations of autoignition in turbulent mixing flows”. In: *Combustion and Flame* 109.1, pp. 198–223.

McGrath, M. (2014). “EU Commission launches legal action over UK air quality”. In: *BBC News*. URL: `http://www.bbc.co.uk/news/science-environment-26257703`.

Mortensen, M. (2005). “Consistent modeling of scalar mixing for presumed, multiple parameter probability density functions”. In: *Physics of Fluids* 17.1, 018106.

Mortensen, M. and B. Andersson (2006). “Presumed Mapping Functions for Eulerian Modelling of Turbulent Mixing”. In: *Flow, Turbulence and Combustion* 76.2, pp. 199–219. ISSN: 1573-1987.

Nelsen, R.B. (1999). *An introduction to copulas.* Springer.

Nguyen, P-D., L. Vervisch, V. Subramanian, and P. Domingo (2010). “Multidimensional flamelet-generated manifolds for partially premixed combustion”. In: *Combustion and Flame* 157.1, pp. 43–61. ISSN: 0010-2180.

Novella, R., A. García, M. Pastor, and V. Domenech (2011). “The role of detailed chemical kinetics on CFD diesel spray ignition and combustion modelling”. In: *Mathematical and Computer Modelling* 54.7, pp. 1706–1719.

O’Brien, E.E. and T-L. Jiang (1991). “The conditional dissipation rate of an initially binary scalar in homogeneous turbulence”. In: *Physics of Fluids A: Fluid Dynamics (1989-1993)* 3.12, pp. 3121–3123.

Opat, R., Y. Ra, M.A. Gonzalez, R. Krieger, R.D. Reitz, D.E. Foster, R.P. Durrett, and R.M. Siewert (2007). *Investigation of mixing and temperature effects on HC/CO emissions for highly dilute low temperature combustion in a light duty diesel engine.* Tech. rep. SAE Technical Paper.

Paola, G. De (2007). “Conditional Moment Closure for Autoignition in Turbulent Flows”. PhD thesis. University of Cambridge.

Patankar, S. (1980). *Numerical heat transfer and fluid flow.* CRC press.

Peters, N. (1984a). “Laminar diffusion flamelet models in non-premixed turbulent combustion”. In: *Progress in energy and combustion science* 10.3, pp. 319–339.

– (1984b). “Laminar diffusion flamelet models in non-premixed turbulent combustion”. In: *Progress in Energy and Combustion Science* 10.3, pp. 319–339. ISSN: 0360-1285.

– (2000). *Turbulent combustion.* Cambridge university press.

Pickett, L.M. (2005). “Low flame temperature limits for mixing-controlled Diesel combustion”. In: *Proceedings of the Combustion Institute* 30.2, pp. 2727–2735. ISSN: 1540-7489.

Pickett, M. (2016). *ECN website.* URL: `http://www.sandia.gov/ecn/dieselSprayCombustion.php` (visited on 03/01/2016).

Pitsch, H. (1998). *FlameMaster v3. 1: a C++ computer program for 0D combustion and 1D laminar flame calculations.*

Plackett, R.L. (1965). “A class of bivariate distributions”. In: *Journal of the American Statistical Association* 60.310, pp. 516–522.

Poinsot, T. and D. Veynante (2005). *Theoretical and numerical combustion.* RT Edwards Incorporated.

Pope, S.B. (1979). “The Statistical Theory of Turbulent Flames”. In: *Philosophical Transactions of the Royal Society of London. Series A, Mathematical and Physical Sciences* 291.1384, pp. 529–568. ISSN: 00804614.

– (1985). “PDF methods for turbulent reactive flows”. In: *Progress in Energy and Combustion Science* 11.2, pp. 119–192.

– (1994). “Lagrangian PDF methods for turbulent flows”. In: *Annual review of fluid mechanics* 26.1, pp. 23–63.

– (1997). “Computationally efficient implementation of combustion chemistry using in situ adaptive tabulation”. In: *Combustion Theory and Modelling* 1.1, pp. 41–63. DOI: `10.1080/713665229`.

– (2000). *Turbulent flows*. Cambridge university press.

– (2013). “Small scales, many species and the manifold challenges of turbulent combustion”. In: *Proceedings of the Combustion Institute* 34.1, pp. 1–31. ISSN: 1540-7489.

Prins, M.J., K.J. Ptasinski, and F.J.J.G. Janssen (2007). “From coal to biomass gasification: Comparison of thermodynamic efficiency”. In: *Energy* 32.7, pp. 1248–1259. ISSN: 0360-5442. DOI: `http://dx.doi.org/10.1016/j.energy.2006.07.017`. URL: `http://www.sciencedirect.com/science/article/pii/S0360544206002106`.

Raman, V., H. Pitsch, and R.O. Fox (2005). “Hybrid large-eddy simulation/Lagrangian filtered-density-function approach for simulating turbulent combustion”. In: *Combustion and Flame* 143.1, pp. 56–78.

Reitz, D. and R. Diwaker (1986). *Effect of drop breakup on fuel sprays*. Tech. rep. Fluid Mechanics Dept., GM Research Labs., Warren, MI.

Réveillon, J. and L. Vervisch (2000). “Spray vaporization in nonpremixed turbulent combustion modeling: a single droplet model”. In: *Combustion and Flame* 121.1, pp. 75–90.

Richardson, E.S. and J.H. Chen (2016). “Analysis of turbulent flame propagation in equivalence ratio-stratified flow”. In: *Submitted to Proceedings of the Combustion Institute.*

Ruan, S., N. Swaminathan, and R. Darbyshire (2014). “Modelling of turbulent lifted jet flames using flamelets: a priori assessment and a posteriori validation”. In: *Combustion Theory and Modelling* 18.2, pp. 295–329.

Sandberg, M. (1981). “What is ventilation efficiency?” In: *Building and environment* 16.2, pp. 123–135.

Sanders, J. P. H. and I. Gökalp (1998). “Scalar dissipation rate modelling in variable density turbulent axisymmetric jets and diffusion flames”. In: *Physics of Fluids* 10.4, pp. 938–948.

Sazhin, S.S. (2006). “Advanced models of fuel droplet heating and evaporation”. In: *Progress in Energy and Combustion Science* 32.2, pp. 162–214. ISSN: 0360-1285. DOI: `http://dx.doi.org/10.1016/j.pecs.2005.11.001`. URL: `http://www.sciencedirect.com/science/article/pii/S0360128505000535`.

Schiller, L. and A. Naumann (1933). “Über die grundlegenden Berechnungen bei der Schwerkraftaufbereitung”. In: *Z. Ver. Dtsch. Ing* 77.12, pp. 318–320.

Seiser, R., H. Pitsch, K. Seshadri, W.J. Pitz, and H.J. Gurran (2000). “Extinction and autoignition of n-heptane in counterflow configuration”. In: *Proceedings of the Combustion Institute* 28.2, pp. 2029–2037. ISSN: 1540-7489.

Shih, T.H., W.W. Liou, A. Shabbir, Z. Yang, and J. Zhu (1995). “A New Eddy-Viscosity Model for High Reynolds Number Turbulent Flows – Model Development and Validation”. In: *Computers Fluids* 24, p. 3.

Shin, D., R. Sandberg, and S. Richardson (2016). “Self-similarity of fluid residence time statistics in a turbulent round jet”. In: *Submitted to Journal of Fluid Mechanics.*

Sirignano, W.A. (2010). *Fluid dynamics and transport of droplets and sprays.* Cambridge University Press.

Sklar, M. (1959). *Fonctions de répartition à n dimensions et leurs marges.* Université Paris 8.

Smith, G.P. et al. (1999). “GRI 3.0 Mechanism”. In: *Gas Research Institute (http://www. me. berkeley. edu/gri_mech).*

Spalding, B. (1953). “The combustion of liquid fuels”. In: *Symposium (International) on Combustion.* Vol. 4. 1. Elsevier, pp. 847–864.

Sparrow, E.M. and J.L. Gregg (1958). “The variable fluid property problem in free convection”. In: *Trans. ASME* 80.4, pp. 879–886.

StarCD 4.20 Methodology Manual (2013). CD-adapco.

Subramaniam, S. and S.B. Pope (1998). “A mixing model for turbulent reactive flows based on Euclidean minimum spanning trees”. In: *Combustion and Flame* 115.4, pp. 487–514.

Sutherland, J.C. and A. Parente (2009). “Combustion modeling using principal component analysis”. In: *Proceedings of the Combustion Institute* 32.1, pp. 1563–1570. ISSN: 1540-7489. DOI: `http://dx.doi.org/10.1016/j.proci.2008.06.147`. URL: `http://www.sciencedirect.com/science/article/pii/S1540748908002630`.

Swaminathan, N. and K.N.C. Bray (2005). “Effect of dilatation on scalar dissipation in turbulent premixed flames”. In: *Combustion and Flame* 143.4. Special Issue to Honor Professor Robert W. Bilger on the Occasion of His Seventieth Birthday, pp. 549–565. ISSN: 0010-2180.

Tsui, H.P. and W.K. Bushe (2014). “Linear-Eddy Model Formulated Probability Density Function and Scalar Dissipation Rate Models for Premixed Combustion”. In: *Flow, Turbulence and Combustion* 93.3, pp. 487–503. ISSN: 1573-1987.

Veynante, D. and L. Vervisch (2002). “Turbulent combustion modeling”. In: *Progress in Energy and Combustion Science* 28.3, pp. 193–266. ISSN: 0360-1285.

Vreman, B., B. Geurts, and H. Kuerten (1995). “Subgrid-modelling in LES of compressible flow”. In: *Applied Scientific Research* 54.3, pp. 191–203. ISSN: 1573-1987. DOI: `10.1007/BF00849116`. URL: `http://dx.doi.org/10.1007/BF00849116`.

Wall, T.F. (2007). “Combustion processes for carbon capture”. In: *Proceedings of the Combustion Institute* 31.1, pp. 31–47. ISSN: 1540-7489. DOI: `http://dx.doi.org/10.1016/j.proci.2006.08.123`. URL: `http://www.sciencedirect.com/science/article/pii/S1540748906003865`.

Williams, F.A. (1958). “Spray Combustion and Atomization”. In: *Physics of Fluids* 1.6, pp. 541–545.

Wright, Y.M., G. De Paola, K. Boulouchos, and E. Mastorakos (2005). “Simulations of spray autoignition and flame establishment with two-dimensional CMC”. In: *Combustion and Flame* 143.4. Special Issue to Honor Professor Robert W. Bilger on the Occasion of His Seventieth Birthday, pp. 402–419. ISSN: 0010-2180.

Yao, M., Z. Zheng, and H. Liu (2009). “Progress and recent trends in homogeneous charge compression ignition (HCCI) engines”. In: *Progress in Energy and Combustion Science* 35.5, pp. 398–437. ISSN: 0360-1285.

Yoo, C.S., E.S. Richardson, R. Sankaran, and J.H. Chen (2011). “A DNS study on the stabilization mechanism of a turbulent lifted ethylene jet flame in highly-heated coflow”. In: *Proceedings of the Combustion Institute* 33.1, pp. 1619–1627. ISSN: 1540-7489.

Yoo, C.S., R. Sankaran, and J.H. Chen (2009). “Three-dimensional direct numerical simulation of a turbulent lifted hydrogen jet flame in heated coflow: flame stabilization and structure”. In: *Journal of Fluid Mechanics* 640, pp. 453–481.

Yun, S., M.F. Lightstone, and M.J. Thomson (2005). “An evaluation of beta PDF integration using the density-weighted PDF and the un-weighted PDF”. In: *International journal of thermal sciences* 44.5, pp. 421–428.